Experimental Study of Control Laws for Supercavitating Vehicles

A DISSERTATION
SUBMITTED TO THE FACULTY OF THE GRADUATE SCHOOL
OF THE UNIVERSITY OF MINNESOTA
BY

Arnar Hjartarson

IN PARTIAL FULFILLMENT OF THE REQUIREMENTS
FOR THE DEGREE OF
DOCTOR OF PHILOSOPHY

Gary J. Balas, Adviser
Roger E. A. Arndt, Adviser

March 2012

Acknowledgments

I want to thank my advisors Professor Gary Balas and Professor Roger Arndt for their guidance and support throughout my studies. I am very grateful for having had the opportunity to work with them, and for having had the ability to draw on their great expertise and experience. They taught me a great deal. I also want to thank Professor Demoz Gebre-Egziabher and Professor William Garrard for serving on my examination committee and providing me with valuable feedback.

I want to thank the members of the Dynamics and Control Center, both past and present, for creating a fun working environment that fostered many excellent discussions on control theory, research and life in general. I especially want to thank Balint, Paw, Rohit and Abhijit for their friendship, valuable advice and insights. Their enthusiasm and impressive work ethic is exemplary, and had a strong impact on me. I also want to thank Abhijit for his help in my dedicated efforts to enrich the Starbucks corporation.

The experimental work for this thesis was done at the St. Anthony Falls Laboratory. I want to thank the laboratory staff for their help with the experimental setup, and I am particularly grateful to Ellison and Hamid for all of their help in setting up and executing my experiments.

At last, I want to thank my family and Pather for their unwavering support and encouragements throughout my studies. Thank you Pather for your love and understanding. I dedicate this dissertation to my parents, who enabled me to pursue my ambitions at home and abroad.

Dedicated to my parents

Abstract

Supercavitation is when a cavity is made to envelop a submerged body. Supercavitation can be used to achieve an order of magnitude reduction in drag on underwater vehicles. Supercavitating vehicles can reach unprecedented speeds underwater. Supercavitation has reportedly been used to create underwater vehicles that reach speeds of 370 km/h, which is significantly faster than the fastest traditional submarine vehicles.

Methods and technologies to control and maneuver supercavitating vehicles are actively being researched. The efforts to develop control strategies and assess the effectiveness of control effectors are hampered by a lack of access to working test beds and operational vehicles. This thesis describes the development and testing of an experimental test bed for validating the performance of control strategies for supercavitating vehicles. The test bed addresses the need for an experimental platform that enables researchers to test candidate control algorithms and associated technologies on a real, physical, supercavitating system.

The test bed was used to evaluate the performance of feedback control systems on a model supercavitating vehicle in a water tunnel. Two controllers were developed using H_∞ control design techniques and evaluated on the test bed. The validity of the hydrodynamic model that the control designs were based on was established, and a comparison and partial validation of their performance was obtained in water tunnel experiments. The experiments demonstrated that a test bed of this kind can be used to evaluate control algorithms, and study the effects of active control systems on a supercavitating vehicle.

Contents

List of Tables

List of Figures

Nomenclature

List of Abbreviations and Acronyms

CoSCIS	Control surface-cavity interaction simulator
I/O	Input/output
cRIO	National instruments compact reconfigurable input/output
DOF	Degree of freedom
LTI	Linear time invariant
RHP	Right half plane
CG	Center of gravity
CM	Center of measurement
AoA	Angle-of-attack

List of Symbols

α	Angle-of-attack	(rad)
q	Pitch rate	(rad/s)
θ	Pitch angle	(rad)
A_z	Acceleration in the z_{body}-axis	(m/s^2)
δ_c	Cavitator deflection angle	(rad)
α_c	Cavitator angle-of-attack	(rad)
x_{body}, y_{body}, z_{body}	Body centric coordinate system	
x_{sensor}, y_{sensor}, z_{sensor}	Load-cell centric coordinate system	
u, v, w	Velocity in the body coordinate system	(m/s)
I_{xx}, I_{yy}, I_{zz}	Vehicle moment of inertia	($kg \cdot m^2$)
T_x, T_z	Thrust force in x_{body}, and z_{body} axis	(N)
T_d	Time delay	(sec)
L_c	Lift on the cavitator	(N)
D_c	Drag on the cavitator	(N)
C_L	Coefficient of lift on the cavitator	
C_D	Coefficient of drag on the cavitator	
d_c	diameter of cavitator	(m)
A_c	Area of cavitator	(m^2)
Q	Ventilation rate	(L/min)

$\bar{q}_c$	Dynamic pressure	(Pa)
σ	Cavitation number	
Fr	Froude number	
P	Pressure	(Pa)
h	Height of a point in a fluid	(m)
V_∞	Ambient flow velocity in a fluid	(m/s)
V	Water tunnel flow velocity	(m/s)
V_c	Flow velocity about cavitator	(m/s)
m	Mass of vehicle	(kg)
g	Acceleration of gravity	(m/s^2)
l_c	Distance between vehicle CG and cavitator	(m)
l_t	Distance between vehicle CG and the aft end	(m)
l_f	Distance between vehicle CG and fins	(m)
L_{body}	Total length of vehicle body	(m)
$L_{cylinder}$	Length of simulated vehicle body cylinder	(m)
L_{cone}	Length of simulated vehicle body cone	(m)
R_{body}	Radius of vehicle body	(m)
k_1	C_{D_c} approximation constant	
k_2	C_{D_c} approximation constant	($1/rad^2$)
k_3	C_{L_c} approximation constant	(1/rad)
ρ_{water}	Mass density of water	(kg/m^3)
ρ_{body}	Mass density of simulated vehicle	(kg/m^3)
W	Weighting matrix in H_∞ control synthesis	
G	Linear time invariant system model	
A, B, C, D	State space matrices	
K	State-space model of a controller	
γ	H_∞ norm of weighted H_∞ synthesis interconnection	
F	Force	(N)
M	Moment	(N)
l_{sensor}	Distance from load-cell CM to cavitator	(m)
Δ	Measurement uncertainty	
ϕ_s	Rotation of servo motor shaft	(counts)
n	Ratio between cavitator and servo shaft deflections	
Ω	Standard deviation of a measurement	

Chapter 1

Introduction

1.1 Overview

Supercavitation is when a cavity is made to envelop an underwater vehicle in an effort to reduce the drag forces on it. Supercavitation has been used to create underwater vehicles that reportedly reach speeds of 370 km/h [1, 2]. The fastest non-supercavitating underwater vehicles in existence, such as high speed attack submarines and torpedoes, are limited to speeds less than 150 km/h [3–5]. Effective use of the supercavitation phenomenon allows these supercavitating vehicles to reach unprecedented speeds underwater.

Methods and technologies to control and maneuver supercavitating vehicles are actively being researched [1, 6–13]. These research efforts include: hydrodynamic modeling of supercavitating vehicles and associated cavity dynamics, development of control effectors for supercavitating vehicles and the modeling of their effects on the cavity, and development of control strategies to stabilize and maneuver the vehicle. The efforts to develop control strategies and assess the effectiveness of control effectors are hampered by a lack of access to working test beds and operational vehicles.

This thesis describes the development and testing of an experimental test bed for validating the performance of control strategies for supercavitating vehicles. The test bed addresses the need for an experimental platform that enables researchers to test candidate control algorithms and associated technologies on a real, physical,

supercavitating system.

1.2 Supercavitating Vehicles

Cavitation occurs when the pressure in a fluid falls below vapor pressure and it undergoes a phase transformation into gas. An example of this effect are the cavitation bubbles that are commonly seen around boat propellers. A small bubble of water vapor is formed when the pressure at some point in the fluid falls below vapor pressure. Supercavitation is an application of this phenomenon, where a cavity is formed around the surface of a body that is traveling through water. The formation of the supercavity replaces the fluid around the body with water vapor, which significantly reduces its skin friction drag. Supercavitation can be used to reduce the total drag on a submerged self propelled vehicle by roughly 80% [9].

Two examples illustrate the application of the supercavitation phenomenon to vehicle systems. The *Ghost* is shown in Figure 1.1. It is built by Juliet Marine Systems, and uses supercavitation to reduce the drag on its catamaran hull [14, 15]. In this case supercavitation is used to lower the drag on the submerged components of a surface vehicle.

Figure 1.1: The Ghost supercavitating vehicle [picture courtesy of [15]].

The focus of this work is on supercavitating submarine vehicles. An example of this is the Russian built *Shkval* torpedo, shown on the left in Figure 1.2. It is a supercavitating vehicle that is fully encapsulated by a supercavity. The Shkval is reportedly capable of traveling at 370 km/h [1, 2], which is significantly faster than the fastest traditional submarine vehicles [3–5]. The Shkval has a long slender cylindrical body, and the supercavity is formed at a disk surface at the front that is

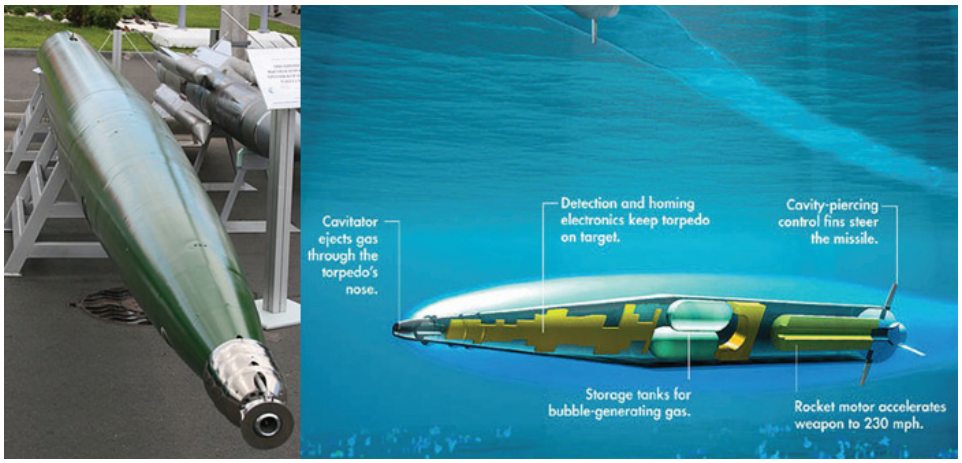

Figure 1.2: Left: The Shkval supercavitating vehicle. Right: An artists rendering of a generic supercavitating vehicle traveling underwater. [pictures courtesy of [16,17]]

called a *cavitator*. The formation and sustenance of the cavity is aided by pumping gas into it, referred to as *ventilation*. The shape of the Shkval is conventionally used as the assumed configuration of a generic supercavitating vehicle, as shown on the right in Figure 1.2, and this work will follow that tradition. The supercavitating vehicles considered in this thesis correspond to submerged vehicles similar to the Shkval.

A unique feature of supercavitating vehicles is that only parts of them are in contact with the water. The cavitator at the front is in contact with the water and creates the supercavity. If no other surface is in contact with the water, this places the center of pressure at the tip of the vehicle, and ahead of the center of gravity. This is an unstable configuration, and the aft of the vehicle is often assumed to house cavity piercing fins, skids, or a thrust vectoring system to allow for a stable configuration. These control effectors are used to stabilize the vehicle and maneuver it. When the body of the vehicle comes into contact with the liquid, it is called *planing*.

There are unique challenges associated with the control of supercavitating vehicles. The cavitator at the front forms the cavity, yet it can potentially be used as a control surface. Hence, the shape of the cavity is affected when it is used for control. The shape of the cavity is also dependent on the time-history of the cavitator deflections, and position in space. The cavity is formed around the cavitator and its shape will depend on where the cavitator has been positioned in the liquid. This effect adds a

layer of complexity to efforts to model a supercavitating vehicle. The cavity shape is very important to the prediction of planing, since the timing and depth of immersion is critical to modeling the planing forces correctly. Another benefit to modeling the cavity shape correctly, is that the fins need to pierce the cavity and come into contact with the water to be effective as control surfaces. The forces and moments that the fins generate are dependent on the depth of their immersion, which is a function of the cavity shape. The portion of the fins that is in contact with the water has the potential to generate its own supercavity. The fin supercavities affect the force and moment generation by the fins, and the interaction between the fin supercavities and the main body supercavity represents a further challenge in the modeling effort. An understanding of all of these issues and the ability model them accurately is imperative to any control design effort.

1.3 Challenges in Supercavitating Vehicle Control System Development

The control of supercavitating vehicles is an active area of research [1, 11, 13], but current efforts to develop control architectures and practical control effector combinations for supercavitating vehicles are restricted to simulations. Stabilization and control of supercavitating vehicles requires accurate models of their dynamics, and an understanding of how active control will influence the dynamics.

Modeling the influence of the cavitator and fin surface on the shape and stability of the cavity is an open research question. The stability of the cavity can be affected by the dynamic use of these surfaces. Previous efforts at the St. Anthony Falls Laboratory have successfully demonstrated active control of a supercavitating fin in a water tunnel experiment [10]. Those experiments showed that fast fin actuation rates can destabilize the cavity and cause it to collapse. Results of equivalent experiments studying the fast actuation of cavitators are not available.

The cavity shape, the forces on the control surfaces, and the forces due to planing, are predicted by models that are derived analytically, from computational fluid dynamics simulations, or from static water tunnel experiments. It is of interest to determine if these models are valid when the control surfaces are being actively used for control. The effects of dynamic cavitator and fin control surfaces, and the

potential interaction between the two when they are used at the same time, need to be studied because control designs rely heavily on them to effect control. There is a clear need for a test bed to study issues related to active control of supercavitating vehicles, and give researchers the ability to test candidate control architectures on a real system. This thesis presents the development of a test bed to address these needs.

1.4 Research Objectives

This work presents the development of a test bed that enables active control of a supercavitating vehicle model in a water tunnel. This test bed will be used to experimentally validate the performance of control algorithms and dynamic control effectors, and study the effect that active control has on the supercavity.

The goal is to validate a proposed control design on the test bed, and demonstrate the capability to validate the performance of candidate control architectures in experiment. This research has the potential to yield valuable insights into the practicality of proposed control strategies, and help identify deficiencies in the modeling efforts.

1.5 Organization of Dissertation

A brief survey of the design objectives and motivation for the development of the Control Surface-Cavity Interaction Simulator (CoSCIS) test bed is given in Chapter 2. The design of the test bed and component hardware are discussed. The issues encountered when the design was built and assembled in the water tunnel facility are described in Chapter 3. A model of a supercavitating vehicle is developed in Chapter 4, and the hydrodynamic model which underlies the modeling effort is experimentally validated in Chapter 5. Chapter 6 describes the experimental work that was performed on the CoSCIS test bed. Chapter 6 has has three main parts: Section 6.1 describes a methodology for testing control algorithms on the CoSCIS test bed, Section 6.2 describes the development of a candidate control architecture, and Sections 6.3-6.5 describe the evaluation of the control design in simulations and water tunnel experiments, and provide a description of the conclusions. A summary of this work is provided in Chapter 7, along with recommendations for future work.

Chapter 2

Development of an Active Control Test Bed

2.1 Design Objectives

The Control Surface-Cavity Interaction Simulator (CoSCIS) was developed to address the need for a test bed for supercavitating vehicle research that enables visualization of the cavity dynamics and testing of candidate control algorithms and associated technologies on a real, physical, supercavitating system inside a water tunnel.

Previous efforts at the St. Anthony Falls Laboratory have successfully demonstrated closed-loop control of a supercavitating fin in a water tunnel experiment, with the ability to measure the torques that the fin generates [10]. This work builds on that result to create a test bed that encompasses a model supercavitating vehicle, with controllable cavitator and fin control surfaces, and the ability to measure both the forces and moments that act on the supercavitating vehicle. The test bed is meant to aid in numerous areas of research related to supercavitating control. The research objectives for the design of the test bed include:

1. Measure the forces and moments generated on a dynamic test body. Compare dynamic and static water tunnel data.

2. Visualize the effects of active control on the cavity - use the results to guide

the modeling effort. Investigate supercavity stability when control surfaces are actuated.

3. Study the effects of active control on cavity ventilation requirements.

4. Measure planing forces on vehicle. Current theory works well for steady state, but there is interest in modeling how the damping and added mass effects impact the planing force when immersion is taking place.

5. Study the supercavity response to gusts and disturbances in the flow. Observe cavity response in experiment.

6. Observe and measure the lift and drag due to supercavitating fins.

7. Evaluate candidate fin and cavitator shapes.

8. Evaluate the effectiveness of a variety of control surface combinations.

9. Evaluate feedback controllers inside the water tunnel on an experimental test bed. Reproduce a real supercavitating system as closely as possible. Implement simplified versions of control strategies for supercavitating vehicles. Evaluate control algorithms on a model supercavitating vehicle in a water tunnel.

A test bed that is meant to accomplish all of these research objectives must satisfy the following design requirements:

1. Mount supercavitating vehicle model in the water tunnel test section.

2. Equip the model with actuated fins and an actuated cavitator.

3. Create a ventilated axisymmetric supercavity around an actuated cavitator.

4. Include the ability to vary cavitator size, fin size, and option to remove the fins.

5. Include the ability to measure the forces and moments acting on the vehicle.

6. Include the ability to actuate the cavitator and fins at high rates.

7. Simulate planing of a supercavitating vehicle.

8. Measure the forces and moments on the vehicle body during planing.

A test bed was developed that satisfies all of these design requirements and is described in the rest of this chapter. The CoSCIS vehicle model and actuation assembly was designed and manufactured by Dr. William Hambleton. The test bed experimental system was assembled in the water tunnel at St. Anthony Falls laboratory.

The research objectives for this test bed are very ambitious. Due to several implementation issues that were encountered during the assembly and testing of the test bed design, it was found that it can not be used to achieve all of the desired objectives. These issues are discussed in Section 2.4 and some are studied further in Chapter 3.

The focus of this thesis will be on research objective #9, i.e. validating a proposed control design on a model supercavitating vehicle in the water tunnel, and the scope of this work will be limited to the implementation of an active control system on the test bed. The goal of this work is to enable researchers to test candidate control algorithms and associated technologies on a real supercavitating system, and validate the performance of control strategies for supercavitating vehicles.

2.2 St. Anthony Falls Water Tunnel Facility

2.2.1 High Speed Water Tunnel

The experiments presented in this thesis were conducted in the St. Anthony Falls Laboratory (SAFL) water tunnel in Minneapolis, MN. The water tunnel, shown in Figure 2.1, is a recirculating, closed-jet water tunnel capable of speeds of up to 20 m/s. The water tunnel design allows for the removal of large amounts of excess gas generated during experiments. This allows the supercavitation water tunnel experiments to be run for long periods of time, e.g. During the experiments described in Chapter 5, the water tunnel tests lasted over 30 minutes.

The water tunnel test section, shown in figure 2.2, is rectangular, 0.19 m (width) x 0.19 m (height) x 1.27 m (length). Three of its side walls have Plexiglas windows.

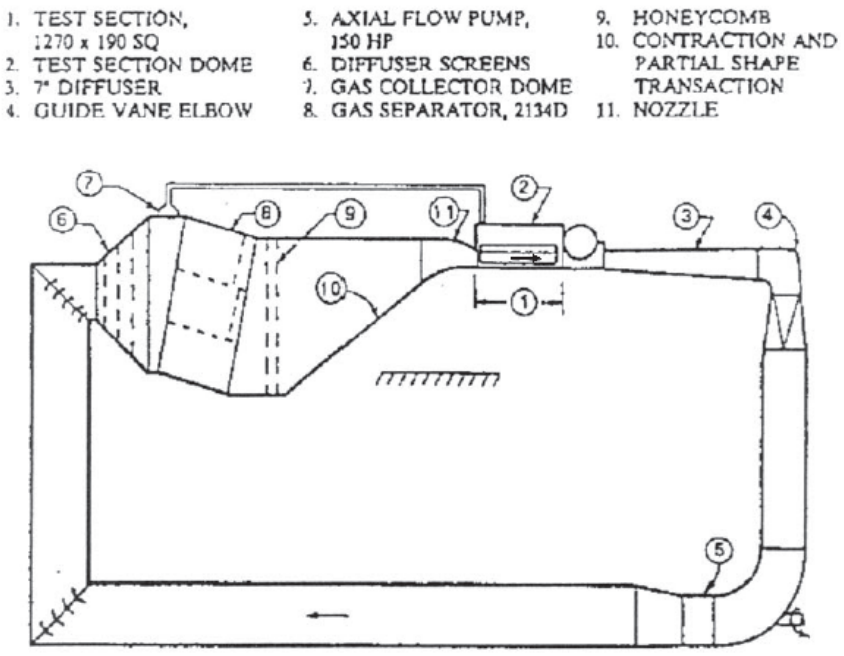

Figure 2.1: Schematic of the St. Anthony Falls water tunnel. All experiments are conducted in the test section.

These Plexiglas windows allow the experiment inside the test section to be observed while it is in progress, and optical measurements to be made. The windows are removable. An experiment can be mounted through any of the three windows as needed. The experimental test bed discussed in this thesis is mounted through the bottom window of the water tunnel test section. The water tunnel facility is equipped with high speed cameras and Laser Doppler Velocimetry apparatus, which is used to estimate the velocity of the flow inside the water tunnel test section.

2.2.2 Gust Generator Capability

The water tunnel can be outfitted with a gust generator, to generate unsteady flows and wavelike motion inside the water tunnel test section. The gust generator was developed and discussed in [18] and adapted to the SAFL water tunnel [19]. The gusts are generated by two NACA-0020 hydrofoils, which lie horizontally, and span the width of the test section as seen in Figure 2.3. The hydrofoils oscillate upstream of the experiment, perturbing the flow as shown in Figure 2.4. The hydrofoils move

Figure 2.2: The water tunnel test section.

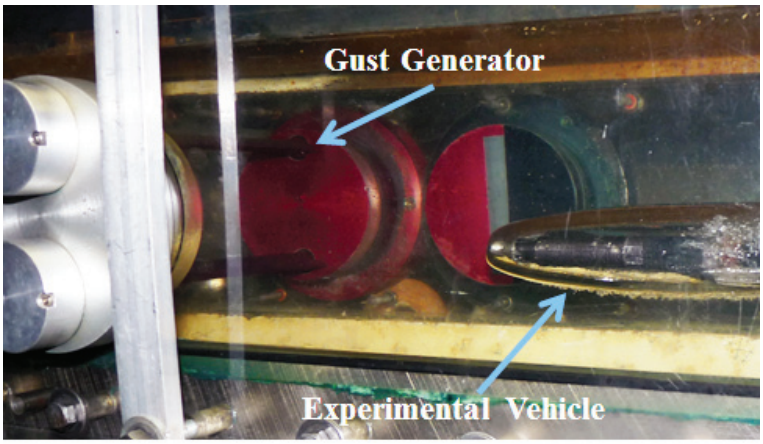

Figure 2.3: The gust generator installed upstream of the model in the water tunnel test section.

together and their oscillations are driven by the rotations of a fly wheel through the mechanism shown in Figure 2.5. The flywheel rotation is driven by a BE-233FJ servo motor. The linkage which connects the hydrofoils to the fly wheel is attached at a point offset from the center of the fly wheel. The magnitude of the offset controls the amplitude of the hydrofoil oscillation. The amplitude can be varied between $2^\circ - 10^\circ$, but only 8° amplitude gust are considered in this work . The gust generator is driven by a BE-233FJ servo motor, and a Parker Automation,

Gemini GV servo drive. The BE-233FJ motor is capable of 4.48 Nm peak torque and includes a built in quadrature encoder with 8000 counts. A detailed description of the gust generator can be found in [19].

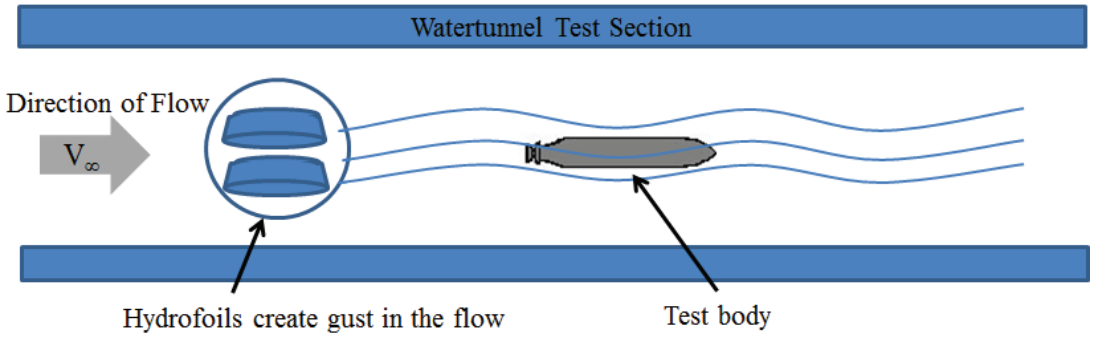

Figure 2.4: Schematic of the setup and function of the gust generator inside the water tunnel test section.

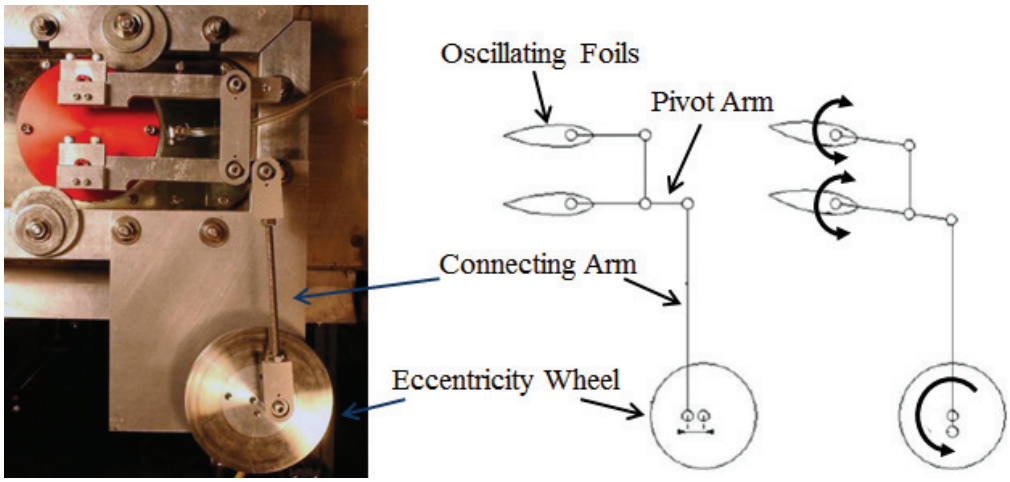

Figure 2.5: Left: The gust generator installed in the SAFL water tunnel Right: Schematic of the oscillating mechanism of the gust generator (figures from [19])

2.3 The CoSCIS Test Bed

The *Control-Surface Cavity Interaction Simulator* (CoSCIS) is an experimental system designed to simulate a supercavitating vehicle in flight, inside a water tunnel test section. The water tunnel component of the CoSCIS consists of a model body, cavitator, fins, six component load-cell and model mount as shown in Figure 2.6. A schematic of the entire CoSCIS experimental system is shown in Figure 2.7. The key components of the system are the following:

1. The CoSCIS vehicle model: A model supercavitating vehicle that sits inside the water tunnel test section.
2. An *AMTI MC1-250* six-component load-cell that measures the forces and moments on the CoSCIS vehicle model.
3. Parker Automation, BE231FJ and BE233FJ actuators that move the model vehicle's control surfaces.
4. A National Instruments CompactRIO (cRIO) embedded controller that controls the experiment.

A short description of each component and a discussion of the system design considerations follows. A discussion of issues encountered during the construction and implementation of the system is found Chapter 3.

2.3.1 The CoSCIS Vehicle Model

The CoSCIS vehicle model is built in the shape of a generic supercavitating vehicle, as it is described in Chapter 1. The CoSCIS vehicle model is shown in Figure 2.6, and a construction drawing with important dimensions is shown in Figure 2.8. The vehicle model is a cylindrical body 110.81 mm in length and 22.23 mm in diameter. A 15 mm diameter disk cavitator is located at the tip of the body, and two horizontal fins are located at the back. A disk shaped cavitator was chosen based on previous work in the SAFL water tunnel using disk cavitators. Their lift and drag coefficients have been published for a range of operating conditions and disk cavitators generate smooth cavities that are clear and easy to see through. The fins are wedge shaped,

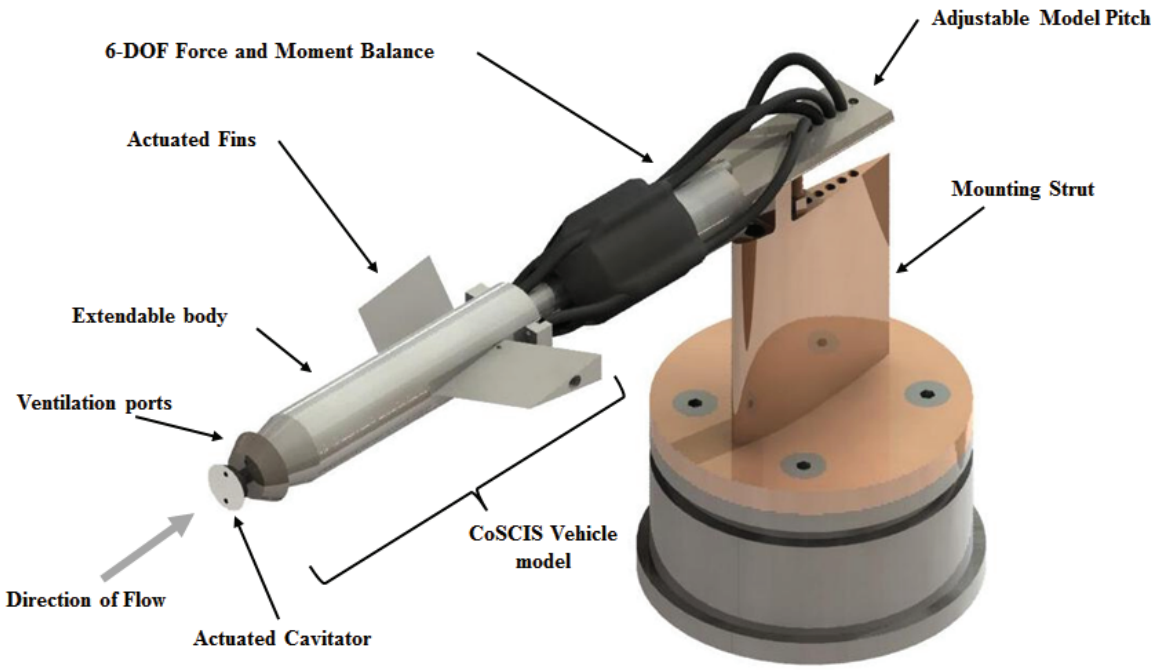

Figure 2.6: The CoSCIS test bed.

25.40 mm in height with a chord and half angle of 29.33 mm and 15° respectively. The fins are swept back 30° and pivot about a point 17.46 mm from the back of the body. Wedge shaped fins are selected because of previous experience with their use at SAFL. The design allows the cavitator and fins to be removed and replaced, if needed, enabling tests with different control surface shapes, as well as tests with the cavitator only when the fins are removed. The CoSCIS vehicle model is mounted on a six component load-cell which measures the forces and moments induced on the model. Detailed construction drawings and further details on the components can be found in the Appendix.

2.3.2 Six Component Load-Cell

The experiment uses an *AMTI MC1-250* six-component load-cell to measure the forces and moments on the model supercavitating vehicle. The dimensions of the MC1-250 are shown in Figure 2.9 along with the axis convention x_{sensor}, y_{sensor} and z_{sensor}. The sensor is mounted on a strut as shown in Figure 2.10 with the

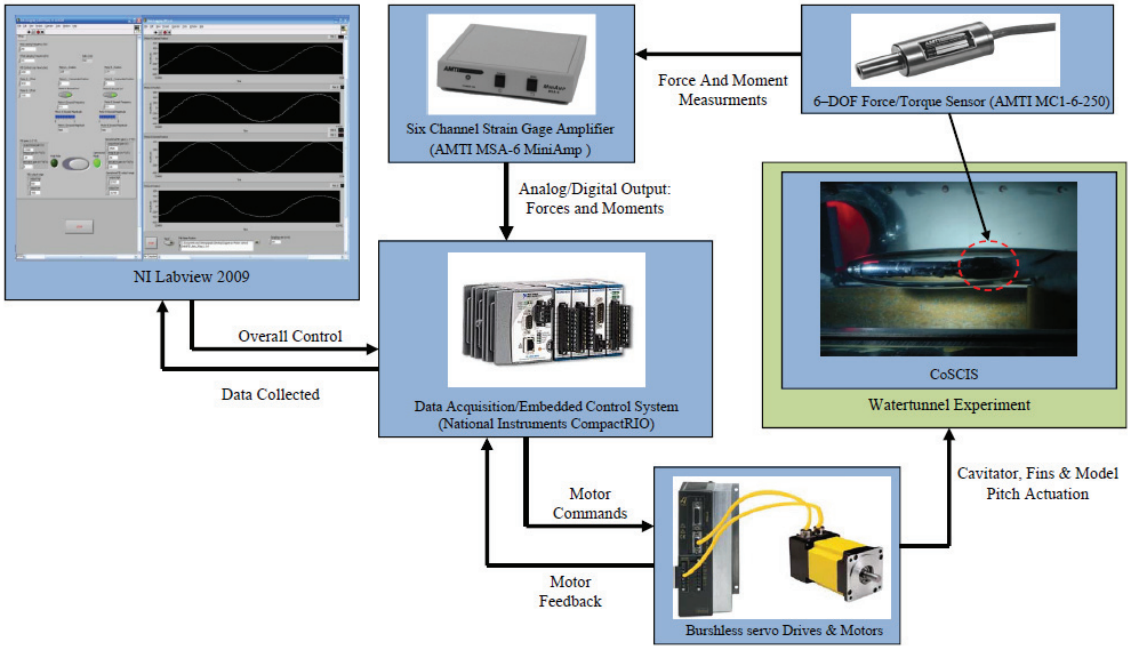

Figure 2.7: A schematic overview of the experimental system. The cRIO handles data acquisition from the load-cell and controls the motors. Higher level control algorithms are also implemented on the cRIO. Supervisory control and data logging is done on a PC.

CoSCIS vehicle model mounted onto the sensor shaft. The MC1-250 is a designed for underwater use and is designed to measure forces of up to 556 N in the x_{sensor} and y_{sensor} axis, and 1112 N in the z_{sensor} axis as well as moments of up to 5.65 Nm about the x_{sensor}, y_{sensor} and z_{sensor} axis [20].

The analog voltage signal from the load-cell is routed to an *MSA-6 MiniAmp* strain gage amplifier, shown in Figure 2.7. The amplifier is designed to work with AMTI load-cells and outputs six ± 10 V analog signals, three for the measured forces and three for the measured moments. Each of the six channels from the load-cell has a two pole low pass filter with a 1000 Hz cutoff and adjustable gains and excitation voltages [21].

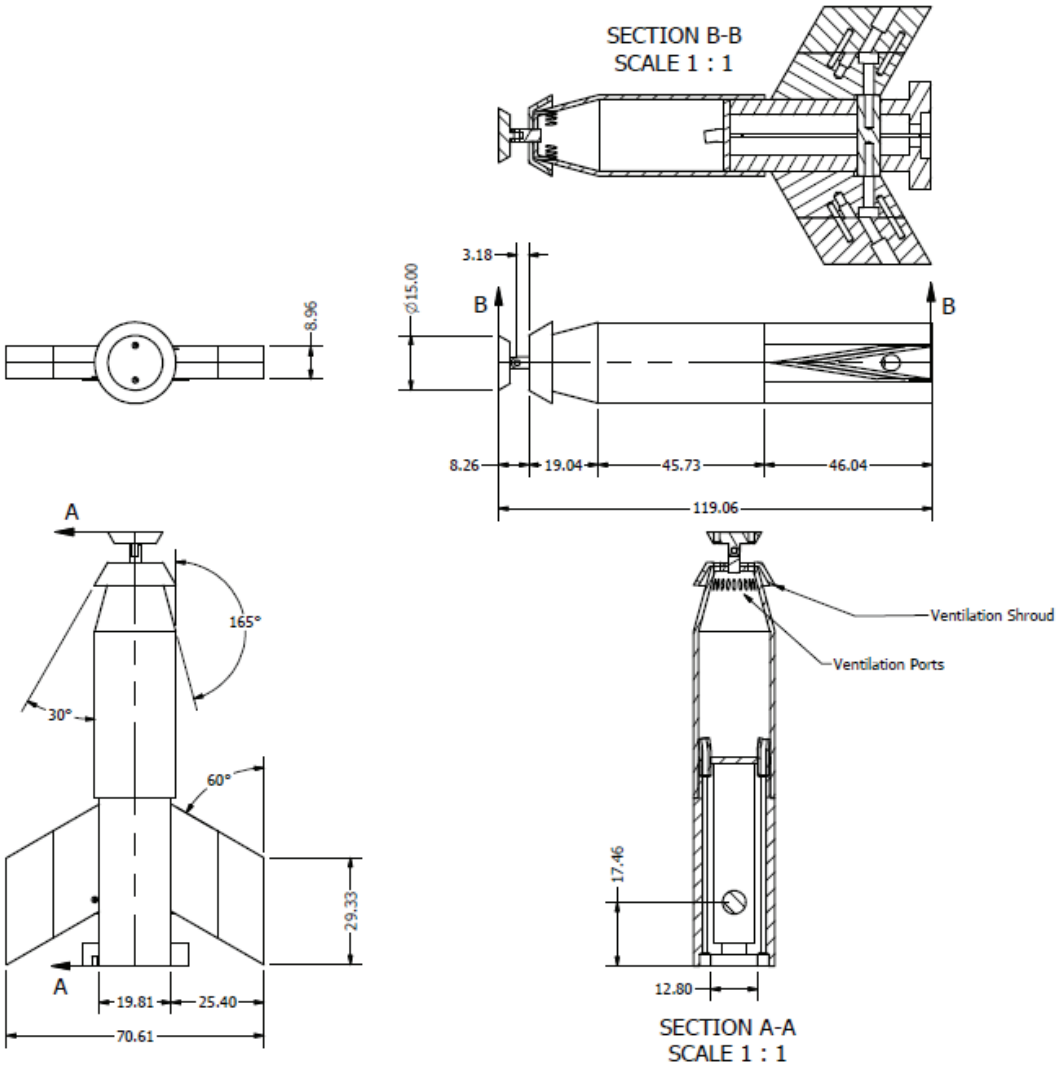

Figure 2.8: A schematic of the CoSCIS vehicle model (all dimension in mm.)

2.3.3 Model Support Structure and Mounting in Water Tunnel

The CoSCIS vehicle model is mounted on the six component load-cell's shaft and the load-cell itself is fixed to a metal strut through a hinged connection, as seen in Figure 2.10. This hinged connection allows the pitch of the vehicle model to be adjusted between experiments by $\pm 10°$ to the horizontal. The strut is fixed to a window plug which fits into the water tunnel's test section window as seen in Figure 2.11. Below the test section, attached to the window plug, is a metal bracket

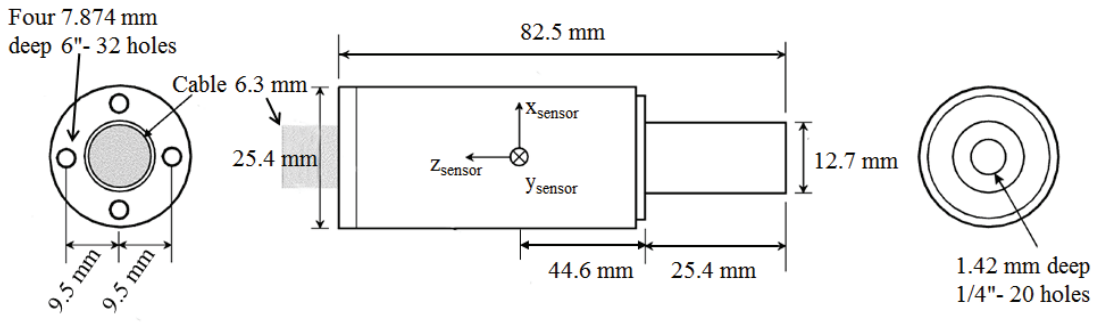

Figure 2.9: Schematic of the AMTI MC1-250 six-component load-cell [20].

where the servos which control the cavitator and fins are mounted. This is the servo mounting bracket seen in Figure 2.11.

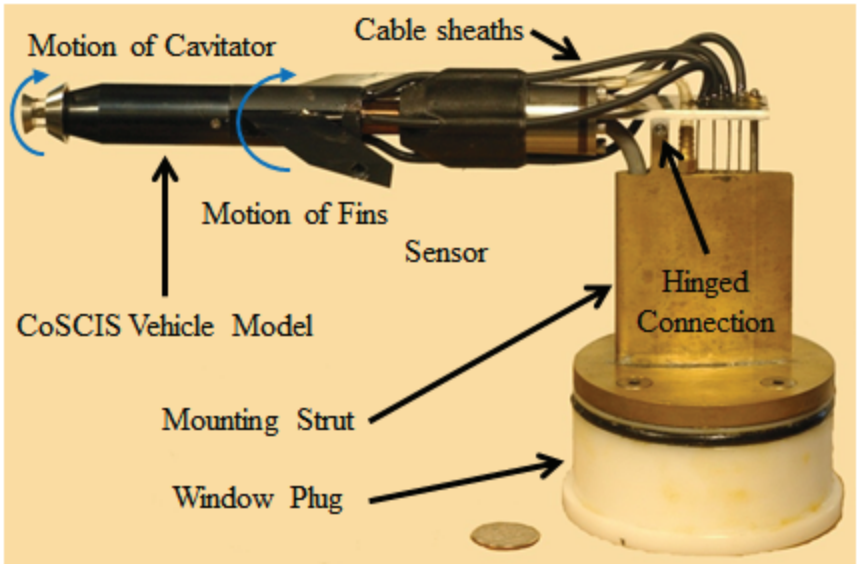

Figure 2.10: A side view of the CoSCIS vehicle model and its mounting structure.

2.3.4 Actuation Scheme

The cavitator and fins are actuated by a pair of Parker Automation brushless servo motors BE-231FJ, which are mounted beneath the water tunnel on the servo mounting bracket, as seen in Figure 2.11. The motors are powered by Parker Automation

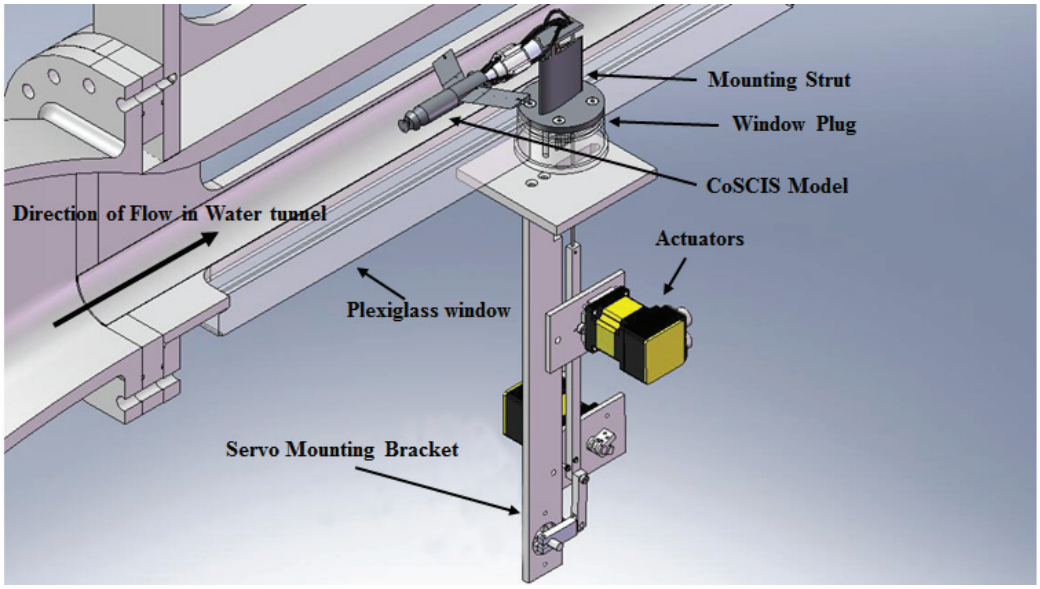

Figure 2.11: The CoSCIS test bed mounted inside the water tunnel test section. The actuators are mounted on a bracket directly beneath the water tunnel test section.

Aries servo drives, AR-08E. These industrial servo motors are capable of 1.98 Nm peak torque, and include a built in quadrature encoder with 8000 counts.

Each servo motor is controlled by an analog voltage signal from the cRIO and a Proportional plus Integral (PI) controller implemented on its FPGA layer. The PI controller receives a measurement of the motor shaft position from the servo's quadrature encoder and controls the motor shaft position by sending a reference rotational velocity command to the servo drive of the respective servo motor.

The cavitator and fins rotate in the longitudinal plane as shown in Figure 2.10, and are actuated independently. The two fins are linked by a metal rod and move together. The range of motion is $\pm 25^{\circ}$ for the cavitator and fins. The cavitator and fins are moved by a cable assembly, as shown in Figure 2.12. The cables are routed from the control surfaces, through the strut and window plug and out of the test section as shown in Figure 2.13. The cables connect to the BE-231FJ servo motors mounted beneath the water tunnel, which control their movement.

A string of wire is attached on the upper and lower side of each control surface as seen in Figure 2.12. In order to pitch the control surface down, the wire on the

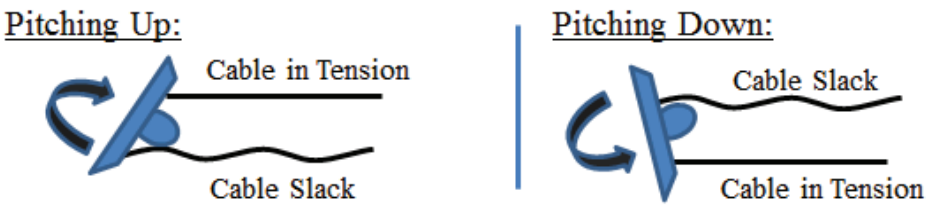

Figure 2.12: The wire cable actuation scheme: Pulling on the wire attached to one side of the control surface and letting out the wire that is attached to the other pitches the control surface in the longitudinal.

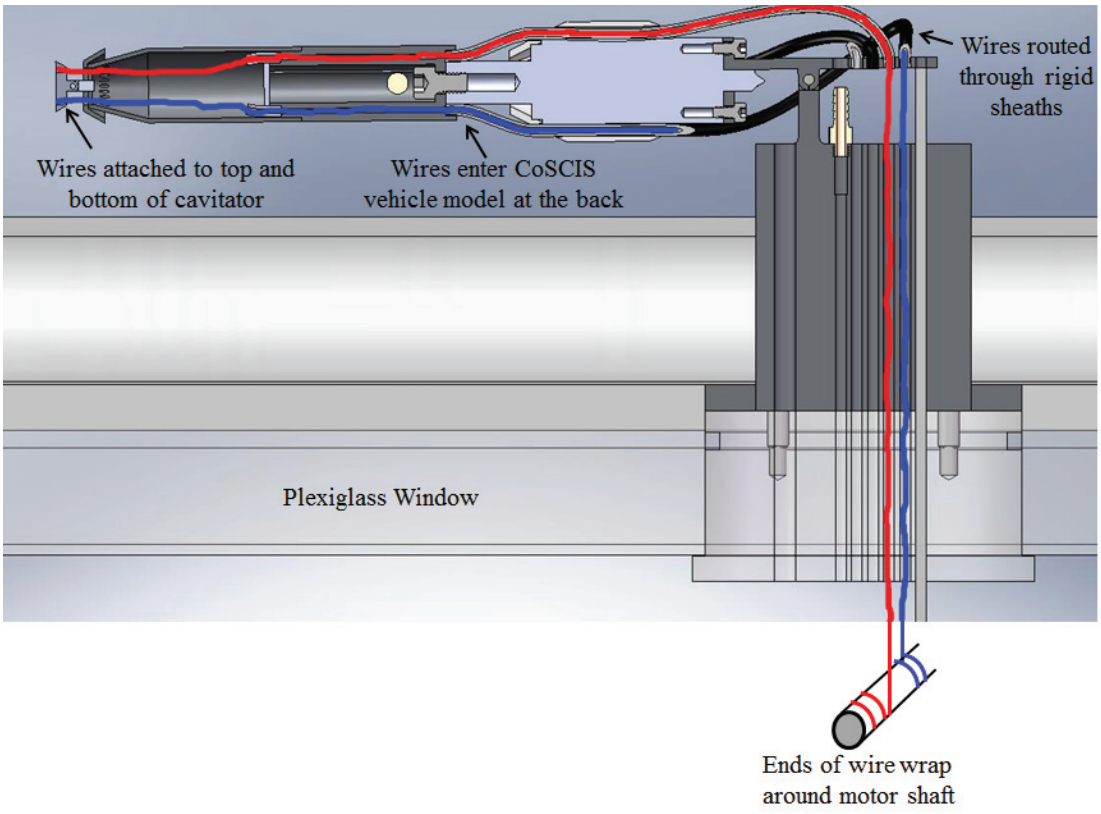

Figure 2.13: Wire cable actuation assembly: Two wires are routed from the servo, through the window plug and strut into the test section, into the CosCIS vehicle model and to their attachment point on the control surface.

lower side is pulled and the wire on the upper side let out, and conversely to pitch the control surface up, the wire attached to the upper side is pulled and the wire

attached to the lower side is eased out. This way the cavitator and fins can be controlled, while inside the water tunnel, by a set of metal wires routed to servo motors mounted outside the water tunnel. The downsides of this actuation scheme are discussed in Chapter 3. These include: backlash and uncertainty in the position of the control surface, and perturbations to the force and moment measurements, due to the pulling motion of the control cables. These are significant issues that severely limit the utility of the CoSCIS test bed.

2.3.5 Ventilation System

The cavity is generated by the cavitator during experiments and is made to envelop the entire CoSCIS vehicle model. A diagram of the ventilation scheme is shown in Figure 2.14. The front of the body is tapered to prevent it from impacting the cavity as it is formed around the cavitator. There is a series of ventilation ports behind the cavitator on the tapered portion of the body, that allow ventilation air into the cavity to augment its formation. Air is fed into the test section up through a pipeline in the mounting strut and window plug. A rubber hose brings the air from the mounting strut, past the sensor and into the CoSCIS vehicle model. The model body is hollow and the ventilation ports are fed by the air which is pumped into the body. Outside the test section the pressurized air is passed through a rotormeter before being pumped into the test section. A rotameter measures the flow rate of the air and regulates the amount being pumped into the cavity. During experiments a flow rate of $Q = 25$ L/min is maintained to ventilate the cavity. A lower ventilation rate results in cavities that are smaller. This ventilation rate yields a cavity that covers the entire CoSCIS vehicle body, and collapses on the load-cell. Increasing the ventilation rate above the chosen level, does not have any discernible effect on the cavity shape.

2.3.6 NI CompactRIO Controller

The National Instrument's Compact Reconfigurable Input/Output (NI cRIO) embedded controller, shown in Figure 2.7, is used to control the experimental test bed and acquire and log experimental data. The NI cRIO-9004 is an embedded controller that combines a microcontroller running Labview Real-Time, with a field-programmable gate array (FPGA) chassis running Labview FPGA. This work uses

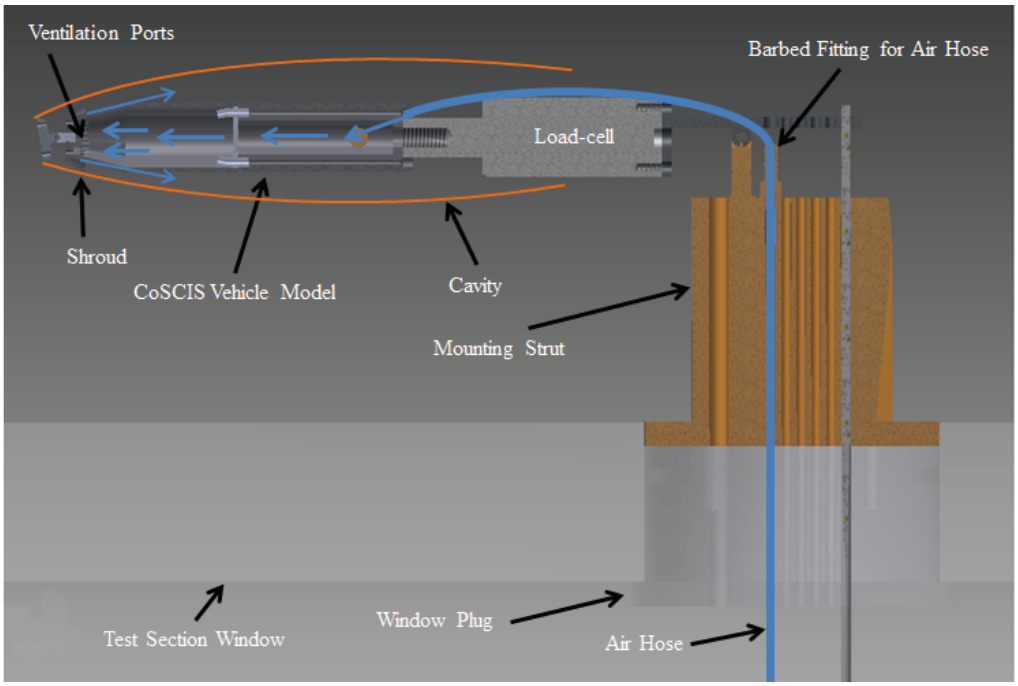

Figure 2.14: Flow of air into the cavity. The air is brought up through the window plug and the strut and pumped into the vehicle model's body. This air is expelled through the ventilation ports at the tip of the vehicle.

the NI 9103 chassis, which has four slots for interchangeable input/output modules.

The line of cRIO controllers from National Instruments use a collection of interchangeable modules which handle input and output (I/O) from the controller. This way, a single controller can be configured with a diverse set of I/O modules according to the needs of the experiment. The NI cRIO-9004 used in this experiment was outfitted with two NI 9239 analog input modules, a NI 9411 digital input module, and a NI 9263 analog output module.

The cRIO accepts six ± 10 V analog inputs from the load-cell's MSA-6 MiniAmp magnifier and two ± 5 V digital inputs from each of the servo motor drives. The analog signals are the force and moment measurements from the force transducer and the digital signals are the outputs of the servo motors quadrature encoder. The cRIO controls the servo drives by outputting a ± 10 V analog signal which commands the servo drive to regulate the servo motor to a specified rotational velocity. A PI controller is implemented on the FPGA layer of the cRIO, for each of

the Servo drives. Each PI controller commands a servo motor's position by reading the position from its quadrature encoder and commanding the servo's rotational velocity.

The cRIO communicates with a PC through Ethernet. The data collected during experiments is conditioned on board the cRIO and sent to the PC for data logging. The cRIO is programmed in NI Labview and all the experimental controllers are implemented on board. During experiments supervisory control is done through the PC, which communicates constantly with the cRIO. The programs which control the cRIO, as well as the PC supervisory programs are written in NI Labview.

2.4 Test Bed Capabilities

The test bed satisfies all of the design requirements outlined in Section 2.1, and models a supercavitating vehicle in flight. The experimental vehicle has controllable cavitator and fin control surfaces, and is mounted on a six degree of freedom force and moment load-cell. The entire body of the experimental vehicle is surrounded by an axisymmetric cavity. The control surfaces are removable, and enable a researcher to study the effects of different cavitator and fins shapes. The entire model can be pitched in the longitudinal plane, allowing the experiment to be run when the CoSCIS model is fixed at a non-zero pitch angle. Pitching in the longitudinal axis also allows planing during the experiment, enabling a study of planing forces.

The CoSCIS test bed was developed to achieve the objectives set out in Section 2.1. The test bed satisfies the design requirements, but several serious implementation issues were encountered when the system was integrated and tested in the water tunnel. These implementation issues limit the capabilities of the test bed, hence some of the desired research objectives can not be accomplished. The implementation and testing of the experimental test bed is described in Chapters 3 and 5.

The test bed enables visual observation of the cavity behavior when the control surfaces are actuated, and when gust are introduced into the flow. The direct observation of the cavity makes it possible to study how cavity stability and ventilation requirements are impacted by the actuation of the control surfaces, and introduction of gusts into the flow.

The initial design had the CoSCIS model pitching dynamically, i.e. there was a motion control system to pitch the CoSCIS model up and down during water tunnel tests. However, this feature was never used, and the pitch of the vehicle is fixed in place throughout the work described in this thesis. The model can be fixed in place at a non-zero pitch angle, such that the cavity impinges on the CoSCIS model body. This enables the study of steady-state planing forces. Note that, all of the water tunnel tests described in this work are done with zero pitch angle, i.e. the CoSCIS model is horizontal.

The actuation system on the CoSCIS test bed made it hard to control the position of the cavitator and fins, since there is no direct measurement of their deflection. The actuation mechanism also had significant backlash. The mechanism was particularly bad in controlling the fins, because of the way the actuation wires connect to the fin surfaces. The objective of measuring the forces and moments on an actuated supercavitating fin is unattainable, but it is possible to gather data on a fin that is fixed in place. The cavitator and fin control surfaces are not permanently fixed in place and can be substituted with different shaped surfaces. This makes it possible to test different control surface shapes in water tunnel experiments.

The cavitator is used as the control surface in closed-loop control experiments. Multiple algorithms are implemented on the motion control system to make it possible to position the cavitator accurately, as described in Section 3.2. The closed-loop control experiments require a measurement of the lift on the cavitator for feedback. The load-cell has a large capacity, and the water tunnel needs to be run very fast to improve the signal-to-noise ratio on the cavitator forces and moments enough to be usable for feedback control.

The fins on the CoSCIS model generate large forces and moments that are disproportionate to the forces and moments generated by the cavitator. High water tunnel velocities are needed to obtain an adequate measurement of the cavitator forces and moments. This results in very large forces on the fins which exceed the structural integrity of the CoSCIS test bed[1]. Hence, the fins had to be taken off for closed-loop control experiments. This makes it impossible to evaluate the effectiveness of different cavitator and fin combinations in experiment.

[1]This was seen in an initial water tunnel test of the CoSCIS test bed, when a component of the test bed suddenly bent out of shape during the test.

The load-cell that is used the in the CoSCIS test bed has a very large capacity compared to the hydrodynamic loads on the cavitator that are seen in the experiments. This results in very poor signal-to-noise ratio, and makes the load-cell measurements susceptible to nonlinearity and hysteresis effects that are inherent to the load-cell hardware, and drift due to temperature and pressure changes. These effects result in large uncertainties to the load-cell measurements, and limit the utility of the test bed for gathering lift and drag data from experiments. Additionally, there are perturbation in the force and moment measurements due to the poor design of the actuation scheme. Actuating the control surfaces induces loads on the CoSCIS model that perturb the force and moment measurements. Due to these *cable induced loads*, it is impossible to gather accurate lift and drag data on dynamic control surfaces for the purpose of updating the hydrodynamic models. However, the effects of the cable induced loads can be mitigated sufficiently in real-time using the data acquisition system, to make the force and moment measurements on the cavitator accurate enough for feedback control. The algorithms that mitigate the effects of the cable induced loads are described in Section 3.3.

The CoSCIS test bed can be used successfully to test feedback control systems. The issues discussed previously limit the utility of the test bed in this regard. The class of feedback control system that can be implemented is restricted to those that use the cavitator as a control surface and the hydrodynamic loads on CoSCIS body as the measurement. The methodology for testing control algorithms on the test bed is discussed in Section 6.1, and a pair of control algorithms is developed and tested on the CoSCIS test bed in Sections 6.2-6.6.

Chapter 3

Test Bed Implementation

Implementation of the experimental test bed described in Chapter 2 proved challenging and required solutions to a set of problems, which are outlined in this chapter. Some of the problems were inherent to the design and placed limitations on the performance of the CoSCIS test bed and the scope of the experiments.

The design of the CoSCIS model was discussed in Chapter 2. Due to size constraints the actuators for the control surfaces could not be placed inside the CoSCIS model and they are needed to be located outside of the water tunnel. The cavitator and fins were designed to be pitched up and down by pulling on a pair of wire cables attached to each of them, as described in Section 2.3.4. There are two main drawbacks to this actuation scheme.

1. The pulling motion induces a load on the control surface which appears in the load-cell measurements. This load is significant compared to the hydrodynamic loads of interest. For example, the lift force due to water impinging on a cavitator is approximately ± 2 N, in the experiments described in Chapter 5, while the cable induced loads are approximately $\pm$ 1.5 N.

2. It is difficult to achieve tight control of the control surface positions, because there is significant backlash in the actuation scheme and there is no direct measurement of their deflections.

The loads induced by the pulling motion of the actuation scheme will be referred to

as "cable induced loads" from now on. A method of controlling the position of the control surfaces, despite the backlash in the actuation scheme, is presented in Section 3.2, and a method of compensating for the cable induced loads is presented in Section 3.3. These methods were successfully applied to the positioning of the cavitator, and to correct for the cable induced loads induced by the cavitator actuation. The fins were removed from the CoSCIS model for the experiments presented in Chapters 5 and 6. The experiments in Chapter 5 only measure the hydrodynamic loads on the cavitator, and only the cavitator is used for control in the closed-loop control experiments of Chapter 6.

The control experiments described in Chapter 6 seek to regulate the lift on the vehicle. Hence, the algorithm in Section 3.3, which corrects for cable induced loads, was only applied to one channel of the load sensor measurement. This channel was the $F_{x,sensor}$ channel, corresponding to the lift on the CoSCIS model when it is aligned with the horizontal, facing straight into the flow.

3.1 Force and Moment Data Acquisition

The force and moment data acquisition scheme is shown in Figure 3.1. The forces and moments are measured by a six-component AMTI MC1-250 load-cell. The load-cell signal is passed to a MSA-6 MiniAmp magnifier that filters the signal with a two pole low-pass filter, with a 1000 Hz cutoff [21]. The output of the MSA-6 magnifier is a ± 10 V analog signal which is read by the NI 9239 analog input module onboard the cRIO. The NI 9239 module is equipped with an anti-aliasing filter with an alias-free bandwidth that is 45% of the sampling frequency [22]. The NI 9239 module is equipped with an internal clock, running at 12.8 MHz, that is used to control the sampling frequency. The possible sampling frequencies are limited to a discrete set between 1612.9 Hz and 50,000 Hz, defined by the equation:

$$f^n_{sampling} = \frac{12.8 \text{ MHz}}{256 \cdot n} \quad \text{where} \quad n \in [1, 2, ...31] \tag{3.1}$$

For any of these sampling frequencies, the alias-free bandwidth (pass-band) is $0.453 \cdot f^n_{sampling}$ and the stop band, i.e. guaranteed 100 dB attenuation, includes all frequencies over $0.547 \cdot f^n_{sampling}$ [22]. The allowable sampling frequencies are all very fast and produce more data than is necessary for the chosen application. A sampling

time of $T_s = 0.0006$ sec $= 1/f^{30}_{sampling}$ is chosen, and the data is reduced to a more manageable size through decimation.

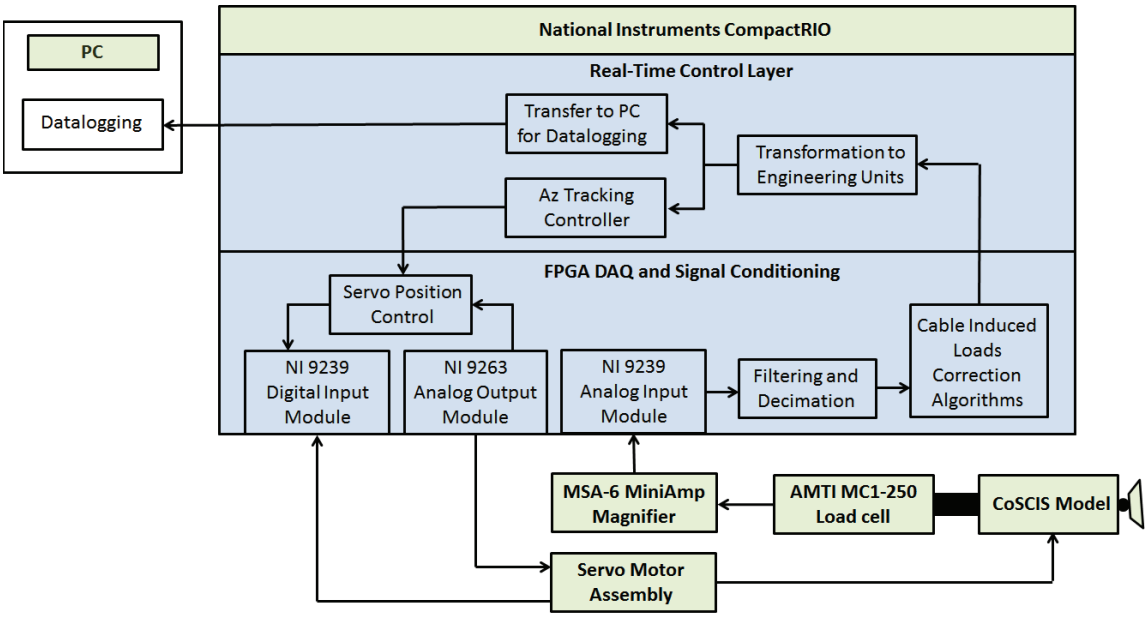

Figure 3.1: The force and moment data acquisition scheme. The path of the load-cell measurement signal is traced from the load-cell to the real-time control layer of the cRIO, and from there to a Personal Computer (PC) where it is saved to a file.

The data from the NI 9239 module is filtered by a fourth order low-pass Butterworth filter, with a breakpoint at 30 Hz, and then decimated by a factor of ten. This brings the sampling frequency down from 1666.7 Hz to 166.7 Hz. The low-pass Butterworth filter prevents aliasing when the data is decimated. This process produces a filtered measurement of the forces and moments every $\tilde{T}_s = 0.006$ sec. The data is transferred from the FPGA layer of the cRIO to the real-time layer, where it is transformed into engineering units and transferred to the PC for data logging. The closed-loop control algorithms presented in Chapter 6 are implemented in the real-time layer and have access to the filtered load-cell measurement.

The NI 9239 module introduces a delay into the load-cell measurements. The time-delay due to the NI 9239 module is dependent on the sampling frequency. It is [22]:

$$\tau_{DAQ,delay} = \frac{38.4}{f^{n}_{sampling}} + 3 \ \mu\text{sec} \tag{3.2}$$

The chosen sampling frequency is $f^{30}_{sampling} = \frac{1}{0.0006 \text{ sec}}$, hence

$$\tau_{DAQ,delay} = \frac{38.4}{f^{30}_{sampling}} + 3 \ \mu\text{sec} = 0.023 \text{ sec} \tag{3.3}$$

The main sources of noise in the force and moment measurements is ambient electric noise from power lines, water tunnel operation, the servo motors, and vibration of both the CoSCIS model and the sensor itself when the test bed is mounted inside the water tunnel and the water tunnel is running. These anti-aliasing filters are adequate to filter this noise, with two exceptions. Power-lines employ alternating current at 60 Hz, and they radiate electromagnetic interference to their surroundings. The interference acts at 60 Hz, and it appears in the load-cell measurements. The low-pass filters which act on the signal, as described above, will attenuate the noise at 60 Hz, but their effect is insufficient. A notch filter is added at 60 Hz to eliminate any trace of noise due to power-lines.

The dominating noise term in the CoSCIS experiment is associated with the water tunnel operation. When the CoSCIS experiment is mounted inside the water tunnel test section, there is a large increase in noise whenever the water tunnel is started. The speed of the water that is circulating in the water tunnel, is controlled by setting the driving frequency of the water tunnel pump. Increased speed is obtained by increasing the driving frequency of the pump. Figure 3.2 illustrates the noise in the $F_{x,sensor}$ signal, before and after the water tunnel is started up, when the CoSCIS model is mounted inside the water tunnel test section. The noise increases when the water tunnel starts up and the pump starts moving the water. The spectrum of the observed noise is shown in Figure 3.3 for three different pump frequencies. Note the roll-off in noise power above 30 Hz, due to the low-pass butterworth filter described above. As can be seen in Figure 3.3, the noise due to the water tunnel operation is a function of the pump frequency. Large amplitude spikes appear in the noise spectrum at frequencies that are integer multiples of twice the pump frequency. For example: Noise spikes appear at 8, 16, 24 and 32 Hz when the pump frequency is set to 4 Hz, and a large noise spike appears at 32 Hz when the pump frequency is set to 16 Hz.

This noise might be due to vibration occurring in the CoSCIS model and the sensor, but it is not electromagnetic interference due to the pump that drives the water

tunnel. Electromagnetic interference due to the pump, can be ruled out because this noise does not appear when the CoSCIS model is placed outside of the water tunnel test section, on a bench next to the water tunnel, and the water tunnel is run.

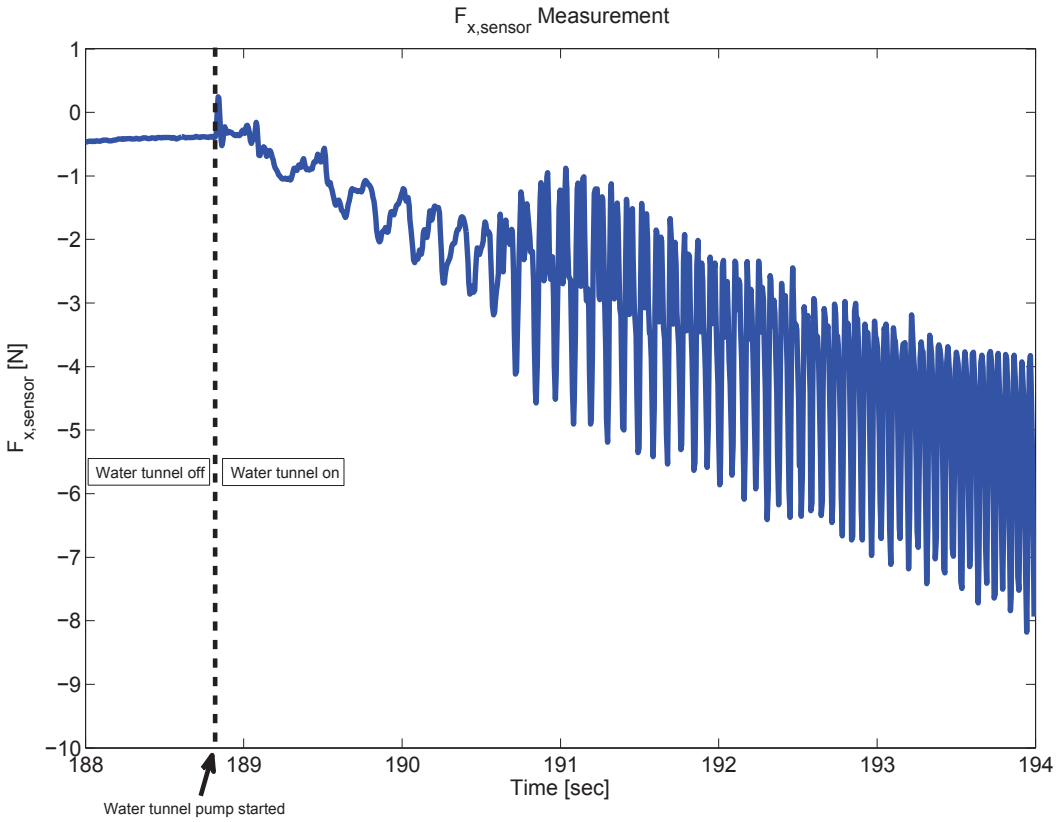

Figure 3.2: Noise in $F_{x,sensor}$ load-cell measurement due to water tunnel operation. The noise in the measurement starts as soon as the water tunnel is started. Water tunnel pump set to 13.5 Hz to generate a velocity of 5 m/s.

The effect of this water tunnel induced noise is reduced at higher velocities, because higher water tunnel velocities require higher pump frequencies and higher pump frequencies cause the noise spikes to be pushed above 30 Hz, where the low-pass filter will attenuate them. An added benefit of running the experiments at high velocities is the increased size of the measured loads. Hence, the experiment should be run as fast as the equipment can safely tolerate to maximize the signal-to-noise ratio in the load-cell measurement.

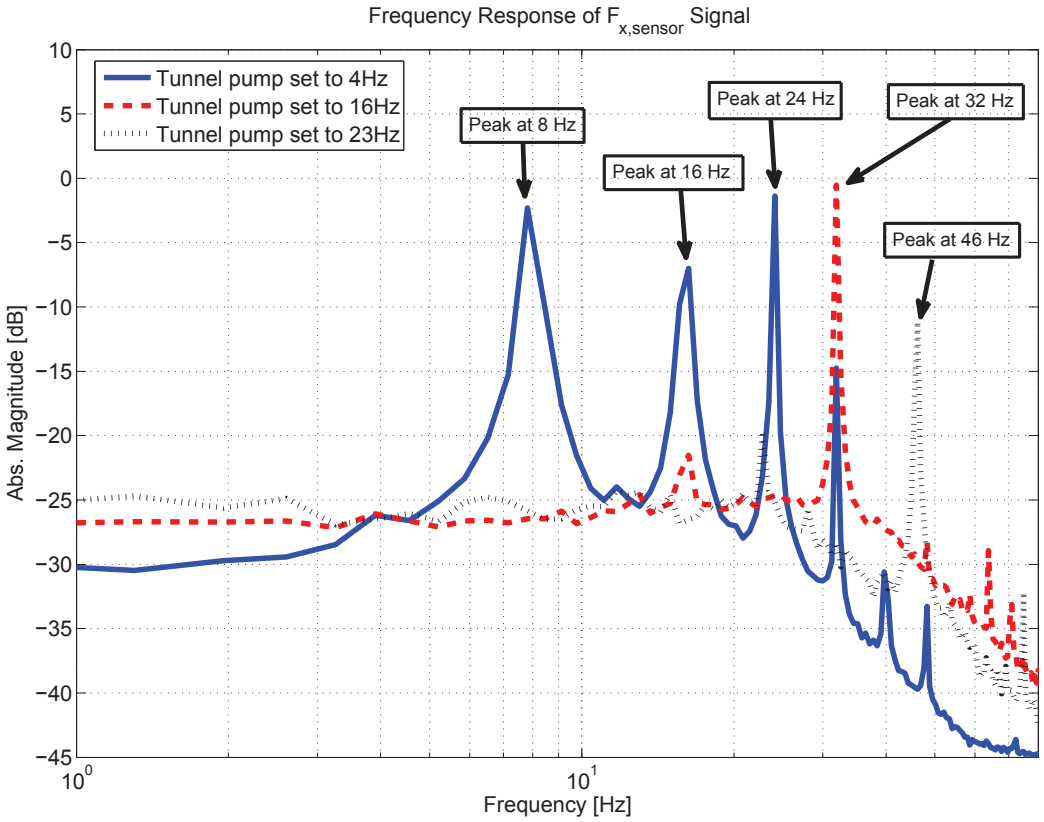

Figure 3.3: Spectrum of $F_{x,sensor}$ load-cell measurement. The noise in the measurement is correlated with the water tunnel pump frequency. Large spikes in noise appear at integer multiples of twice the water tunnel pump frequency.

The target velocity for the CoSCIS experiments is chosen to be 8 m/s. This speed results in stable cavities that envelop the entire CoSCIS model and collapse on the load-cell. This speed is chosen because a component on a prototype version of the CoSCIS model was bent during a trial run at 10 m/s, while the fins were still on the model. Hence, the velocity is limited to 8 m/s to minimize the chance of damaging the CoSCIS test bed. A pump frequency of 23 Hz is associated with this velocity. Hence, noise spikes appear at integer multiples of 46 Hz. The low-pass Butterworth filter, described above, attenuates the noise spikes above 30 Hz. However the noise spike at 46 Hz is not attenuated sufficiently. A notch filter is introduced to remove the noise spike at 46 Hz.

The notch filters for the power-line and water tunnel-induced noise are implemented in Labview FPGA, onboard the FPGA portion of the cRIO. A "Notch Filter" function is provided in Labview FPGA. This function can be used to implement notch filters onboard FPGA boards from National Instruments. Each of the notch filters is designed with a specific notch width w_{notch}. The notch width defines a frequency band, centered at the target notch frequency, where the notch filters achieve a minimum of 3 dB attenuation [23].

The notch filter for the power-line noise at 60 Hz has a notch width of 1.71 Hz, and the notch filter for the water tunnel induced noise at 46 Hz has a notch width of 5.75 Hz. The notch filter at 46 Hz is designed to have a greater notch width because the pump frequency may vary by as much as ± 2 Hz to obtain the desired 8 m/s velocity in the water tunnel.

3.2 Cavitator Positioning

The servo motor moves the cavitator through a pair of wire cables attached to its shaft, as described in Section 2.3.4. There is no direct measurement of the cavitator pitch angle, and its position must be inferred from knowledge of the actuation scheme and measurement of the servo motor's shaft deflection.

The cavitator is driven by a pair of wire cables which connect to the top and bottom of the cavitator. To pitch the cavitator up, the wire on top is pulled, and to pitch the cavitator down, the wire on the bottom is pulled. The other end of the wire cables, are wrapped around the same servo motor shaft as shown in Figure 2.13. Moving the motor shaft in one direction will cause one of the wires to wrap onto the shaft and the other to be unwrapped, causing one cable to be pulled in while the other is let out. Reversing direction of the servo motion reverses the effect.

Tight control over the cavitator position requires an accurate estimate of its position. Unfortunately there is no direct measurement of the cavitator's deflection angle and there is backlash in the actuation scheme. The cavitator's position must be estimated and controlled based on a model of the actuation scheme and a measurement of the driving servo's position. Methods of achieving this are presented in this section. They are only applied to the cavitator movement since the control experiments in Chapter 6 only use the cavitator for control.

3.2.0.1 Summary

A fourth order low-pass Butterworth filter, with a breakpoint at 30 Hz, was implemented on board the CompactRIO to attenuate the noise. Spectral analysis of force and moment data from water tunnel experiments revealed that the water tunnel pump influences the noise level in experiments. The spectral analysis shows that there is a component of measurement noise that is dependent on the operating frequency of the water tunnel pump. There are large amplitude spikes in the spectrum of the noise at integer multiples of twice the tunnel pump frequency, e.g. if the tunnel pump is run at 4 Hz, there are spikes in the spectrum of the noise at 8 Hz, 16 Hz, 32 Hz, etc. The exact mechanism that underlies this phenomenon is unknown, but electromagnetic interference has been ruled out. Notch filters are implemented on board the CompactRIO to remove the noise spikes associated with the desired operating pump frequency.

The load-cell that is used in the CoSCIS test bed has a very large capacity compared to the hydrodynamic loads on the cavitator that are seen in the experiments. This results in poor signal-to-noise ratio, and it makes the measurement sensitive to the nonlinearity and hysteresis effects in the load-cell hardware. The nonlinearity and hysteresis effects in the load-cell hardware are 0.2% of the full scale load. In the lift axis, this results in a 0.56 N uncertainty on the force measurement, compared to expected hydrodynamic loads of $\pm$ 2 N. The effects of the nonlinearity and hysteresis in the load-cell hardware is significant compared to the small hydrodynamic loads that are seen in the water tunnel experiments. This issue is explored further in Section 5.1.3, when the impact of the nonlinearity and hysteresis effects on the lift measurements is quantified.

3.2.1 Motor Shaft to Cavitator Deflection Rate Difference

The cavitator is controlled by a pair of metal wires attached to its upper and lower side as described in section 2.3.4. The other end of these wires are wrapped around a servo motor shaft. The servo shaft rotation is measured in *counts*, which are the discrete states of its quadrature encoder. Hence, 1 count is the smallest unit of servo shaft angular rotation that can be measured or commanded. A full 360^o rotation of the motor shaft is 8000 counts. Rotating the motor shaft by ϕ_s counts will cause the cavitator to pitch up or down by $\delta_c = n\phi_s$ degrees, where the coefficient n

represents how many degrees the cavitator will rotate when the servo shaft rotates by 1 count. There is no direct measurement of the cavitator deflection available for active control, and thus the coefficient n must be estimated and accounted for in the control system to achieve accurate positioning of the cavitator during experiments.

It is possible to obtain a direct steady-state measurement of the cavitator deflection by taking a picture of the cavitator and measuring its deflection angle in photo editing software. The program *ImageJ* is used for this purpose because it allows for easy measurement of angles in digital pictures. This method is used whenever the position of a cavitator must be known with absolute certainty.

An experiment was performed to obtain an estimate of the coefficient n. The cavitator was moved between several deflection angles, in a monotonically increasing pitching up motion (to prevent backlash from occurring). A photo of the cavitator deflection angle, and a reading of the servo shaft position is taken at each position. Plotting the servo shaft position ϕ_s against the measured cavitator deflection angle δ_c allows a line to be fitted to the data points and its slope n to be measured. The results of the experiment are shown in Figure 3.4. The value of n is estimated to be

$$n = -0.054 \ \frac{\text{Degrees of Cavitator Deflection}}{\text{Counts of Servo Shaft Rotation}} \tag{3.4}$$

This n value is used in the closed-loop lift tracking experiments described in Chapter 6. The result indicates that if the servo shaft is rotated by $1^\circ = 22.22$ counts, the cavitator will be deflected by $22.22 \cdot n = -1.2^\circ$.

3.2.2 Estimating Cavitator Position

The wires from the servo to the cavitator have a small amount of slack. This slack causes a backlash in the cavitator positioning. When the servo motor reverses its direction of movement, one of the wire cables is wrapped onto the shaft and is supposed to pull on the cavitator. Because of the slack in the cable, it will not become taut immediately. The motor has to move a short distance before the cable becomes taut and the cavitator starts moving. This effect creates a backlash in the actuation scheme. The backlash in the cavitator movement is approximately $\hat{B} = 60$ counts which is equal to a 2.7° rotation of the servo shaft.

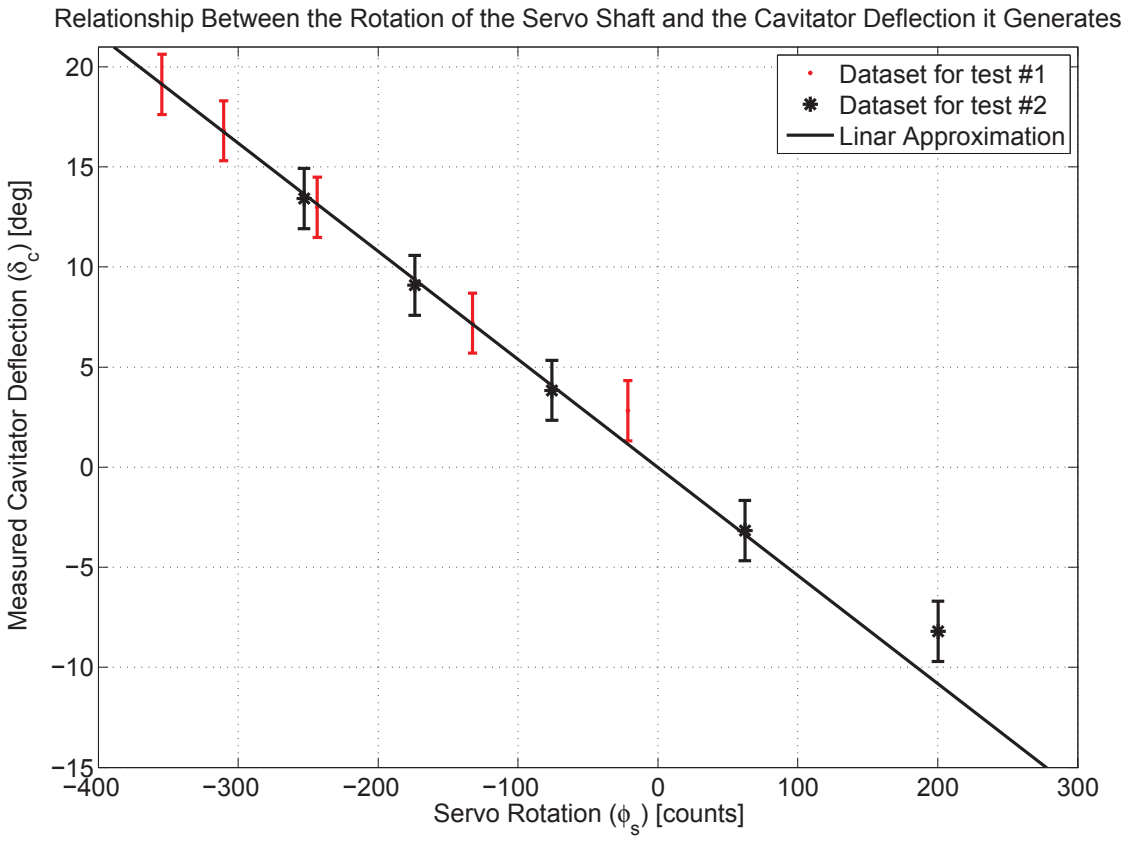

Figure 3.4: The measured cavitator deflection plotted against the servo shaft rotation that generated it. A linear approximation is fit to the data and shown in the figure. The slope of the linear approximation is the coefficient n, the ratio between the cavitator deflection and the servo shaft rotation.

Algorithm 1 estimates the deflection of the cavitator. The cavitator position is estimated by the algorithm by combining the time history of the servo motor position, the $\delta_c = n\phi_s$ relation of section 3.2.1, and knowledge of the backlash. Figure 3.5 illustrates the function of Algorithm 1. The algorithm accepts a single input $\phi_s(i)$, which is the angular position of the servo shaft, and it keeps track of only one state: $y(i)$ which is the intermediary estimate of the position of the cavitator at time step i, uncorrected for the ratio n described in section 3.2.1. Algorithm 1 estimates whether servo movement translates into cavitator movement or is lost in the backlash dead-zone, and keeps track of the cavitator deflection. The system has to be initialized so that the backlash dead-zone, of width $\hat{B}$, all lies in the di-

rection used to pitch up the cavitator, for Algorithm 1 to function correctly. The algorithm tracks the position of the cavitator, denoted by y. Based on the initial configuration, it is possible to locate the backlash dead-zone at each time step. The backlash dead-zone lies between y and $y+B$. The servo movement will not move the cavitator unless the movement goes outside of the dead-zone. When that happens the cavitator position and the location of the dead-zone are updated. Algorithm 1 is implemented in Labview on board the FPGA portion of the cRIO.

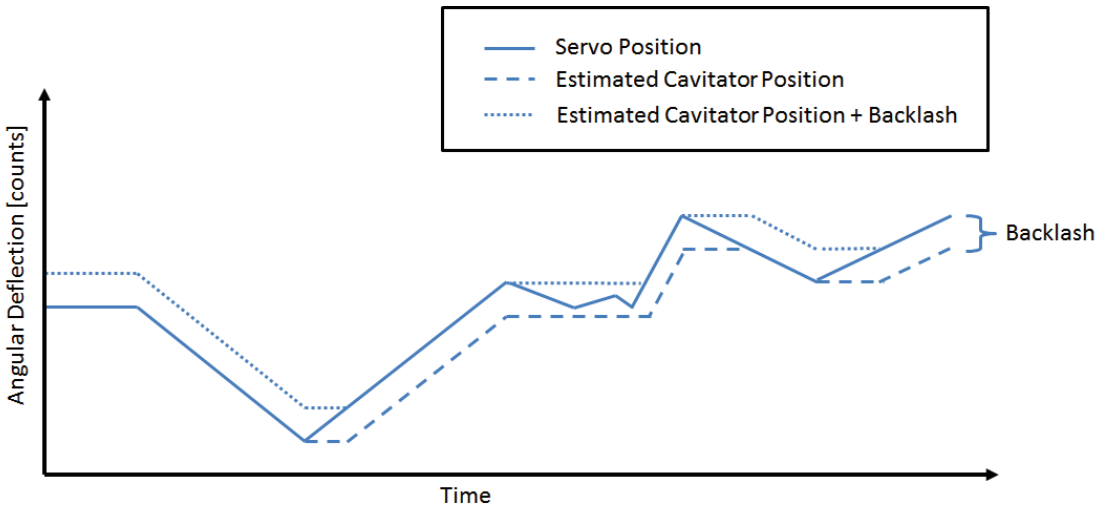

Figure 3.5: An illustration of the function of Algorithm 1. The servo position and the dead zone due to the backlash are shown. The cavitator position is only updated if the servo moves out of the deadzone.

The system is initialized with the cable on the lower side of the cavitator taut, ready to pitch the cavitator down. If a command is given to pitch the cavitator down at the outset there is going to be no slack in the cable and no backlash. The dead-zone due to the backlash is initially all in the direction of the pitching up motion. Hence, the movement of the servo to pitch the cavitator down is completely utilized to move the cavitator and none of it is lost in the backlash. If the servo is moved in the opposite direction, to pitch the cavitator up, up to $\hat{B} = 60$ counts of its movement will be associated with the dead-zone. The servo shaft will rotate and it is only when it has rotated 60 counts that the cable to the upper side of the cavitator will become taut and start to pull on the cavitator. If the servo moves less than 60 counts the cavitator will not move at all. When the system is initialized in this way the

boundaries of the backlash's dead-zone are known. The position of the cavitator is only updated when the servo moves past the estimated dead-zone. When this happens, and the cavitator position is updated, the estimate of the dead-zone is updated to reflect the new cavitator position. Hence, it is possible to keep track of how much of the servo movement has actually contributed to cavitator deflections and the cavitator deflection at any point in time can be estimated based on the time history of the servo movement.

In summary, the initial configuration of the system is well defined, and because it is known, the estimate of the cavitator position, y, can be used to keep track of the boundaries of the dead-zone at each time-step. The cavitator will pitch down when the servo position $\phi_s(i)$ is less than $y(i-1)$ and it will pitch up when it is larger than $y(i-1)+B$. The algorithm keeps track of $y(i)$ at each time-step and updates the value only when $\phi_s(i) < y(i-1)$ or $\phi_s(i) > y(i-1)+B$, because this is when the servo movement translates into cavitator deflections.

3.2.3 Compensating for Backlash

The servo motor positioning is under tight control. The effects of the backlash can be minimized by utilizing the knowledge about the backlash in the actuation scheme, and shaping the servo movement to compensate for the dead zones. The dead zone in the cavitator movement is only a factor when the direction of movement is reversed. The effects of the dead zone can be minimized if the servo motor is commanded to move an extra distance, b, whenever it reverses direction. This extra movement compensates for the servo movement lost crossing the dead-zone. A correction scheme based on this idea is presented in pseudo code in Algorithm 2.

The idea behind Algorithm 2 is illustrated in Figure 3.6. The system is initialized so that the wire on the lower side of the cavitator is taut and ready to pitch the cavitator down. Hence, there is no backlash if the cavitator is initially pitched down, and the dead-zone all lies in the direction that pitches the cavitator up. All servo movement to pitch the cavitator down will be delivered to the cavitator. If the cavitator is pitched up, the first $\hat{B}$ counts of the servo movement will be lost in the dead-zone due to the backlash and the cavitator will be moved $\hat{B}$ counts less.

The algorithm keeps track of which side the dead-zone is on, and adjusts the com-

Algorithm 1 - Cavitator Position Estimation: This algorithm generates an estimate of the cavitator deflection. This is done by keeping track of which side of the cavitator is in tension and whether or not the movement of the servo translates into a cavitator deflection or whether it is lost in the backlash dead-zone. A schematic of the algorithm's function is shown in Figure 3.5.

- $\phi_s(i)$ = Servo position at step i, in units of counts (input)
- $y(i)$ = Intermediary estimate of cavitator position at time step i, in units of counts
- $\delta_c(i)$ = Estimate of cavitator position at time step i, in units of degrees (output)
- $\hat{B}$ = Backlash in cavitator positioning
- n = Ratio between the servo rotation and the cavitator deflection (see section 3.2.1)
- System is initialized with cavitator pitching down

At each time step:

if $\phi_s(i) < y(i-1)$ **then** {Check if servo movement is causing the cavitator to be pitched down}

$y(i) = \phi_s(i)$ {Cavitator is being pitched down}

else if $\phi_s(i) > y(i-1) + B$ **then** {Check if the servo movement is large enough to cross the dead-zone, and cause the cavitator to be pulled up}

$y(i) = \phi_s(i) - B$ {Cavitator is being pitched up - subtract the servo movement lost crossing the dead-zone}

else if $y(i-1) \leq \phi_s(i) \leq y(i-1) + B$ **then** {Check if the entire servo movement is lost in the backlash}

$y(i) = y(i-1)$ {Servo movement lost in dead-zone}

end if

$\delta_c = ny(i)$ {Apply correction factor n to compute the cavitator deflection in degrees.}

manded servo position to compensate for the dead-zone when necessary. Whenever the direction of movement is reversed, an additional b counts of rotation are added to the servo rotation. This makes up for the amount of servo movement that is lost in the dead-zone. This way only $|B - b|$ counts of servo movement are lost in the dead-zone each time the direction of movement is changed. The extra movement, b, is chosen to be slightly smaller than the estimate of the backlash size $\hat{B}$ in practice (Figure 3.6 shows an idealized version of the algorithm's function where $b = B$). The value of b is chosen to be $b = 50$ counts, while the backlash is estimated to be $\hat{B} = 60$ counts. This is done because the servo position control is only accurate to ± 10 counts, and choosing $|b| < |B|$ prevents chatter from appearing in the system. The chosen value of b yields good results.

Algorithm 2 is implemented in Labview on board the FPGA portion of the cRIO. The desired cavitator position $\delta_{c,ref}$ is fed into the algorithm where it is translated into a reference input to the motor, $\phi_{s,ref}$. The algorithm successfully mitigates the effects of the backlash.

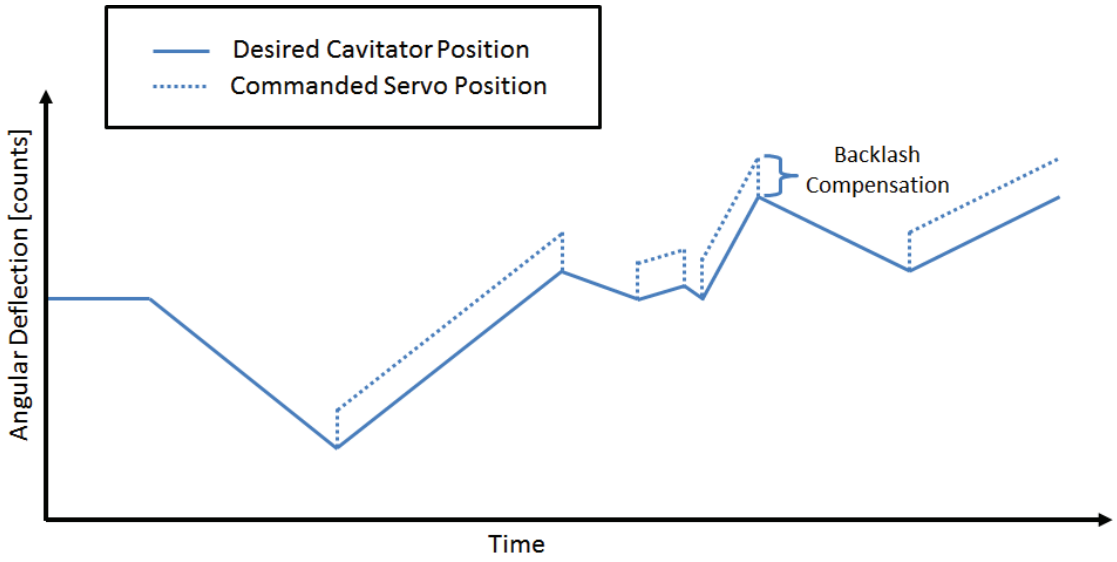

Figure 3.6: An illustration of the function of Algorithm 2. Algorithm 2 compensates for the backlash in the actuation scheme by generating servo commands that deliver the desired cavitator deflection, despite the backlash.

Algorithm 2 - Backlash Compensation: This algorithm accepts a command for a desired cavitator deflection angle, $\delta_{c,ref}$, and outputs a command to the servo motor which generates this desired cavitator deflection, despite the backlash. The output of the algorithm is the command: $\phi_{s,ref}$, the commanded rotation of the servo motor shaft in counts. The idea behind this algorithm is illustrated in Figure 3.6

- $\delta_{c,ref}(i)$ = Desired deflection of the cavitator at step i, in degrees (input)
- $\phi_{s,ref}(i)$ = Commanded rotation of the servo motor shaft at step i, in counts (output)
- n = Ratio between the servo rotation and the cavitator deflection (see section 3.2.1)
- b = Constant value, slightly smaller than the estimate of the backlash $\hat{B}$.
- System is initialized with cavitator pitching down

At each time step:

if $\delta_{c,ref}(i) \leq \delta_{c,ref}(i-1)$ **then**

  if $\delta_{c,ref}(i) < \delta_{c,ref}(i-1)$ **then**
    $\phi_{s,ref}(i) = \frac{1}{n}\delta_{c,ref}(i)$
  else
    $\phi_{s,ref}(i) = \phi_{s,ref}(i-1)$
  end if

else {The command to the servo is augmented with a constant b when a pitch up command is given. This adds b counts to the servo rotation, and compensates for the servo movement being lost in the backlash dead-zone. Similarly these b counts are not added to the servo movement when the direction of movement is reversed and the cavitator is pitched down, in effect adding $-b$ counts to that movement.}

  $\phi_{s,ref}(i) = \frac{1}{n}\delta_{c,ref}(i) + b$

end if

3.3 Correction for Cable Induced Loads

3.3.1 Cable Induced Loads

The control surface actuation scheme, described in section 2.3.4, uses a pair of wire cables to pull on the top and bottom of the cavitator to pitch it up and down, respectively. This pulling motion imparts forces F_{cable} on the cavitator, which the load-cell measures, as shown in Figure 3.7. These "cable induced loads" are significant compared to the hydrodynamic loads of interest.

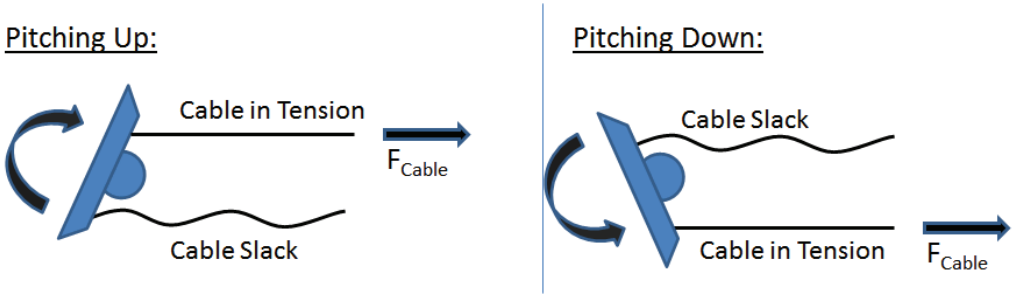

Figure 3.7: An illustration of how the cable induced loads enter the force measurement.

To illustrate how this phenomenon affects the system, the CoSCIS model is placed outside of the water tunnel, and the cavitator is moved back and forth while the load-cell collects data. There are no hydrodynamic loads present, and the only loads that are measured are due to the actuation scheme. Figure 3.8 shows the measured load in the $F_{x,sensor}$ channel when the servo that drives the cavitator is moved back and forth. The change in measured force, imparted on the cavitator when its direction of movement is reversed, is 1.6 N. This change in the $F_{x,sensor}$ channel measurement is due to the actuation scheme, and the cable induced loads it causes. The data presented in Figure 3.8, is from an early test of the CoSCIS system, when the backlash in the system was larger. Superior methods in attaching the cables to to servo motor reduced the size the backlash to $\hat{B} = 60$ counts. Once the cable induced loads starts to appear in Figure 3.8, it takes approximately 85 counts of servo position for the cable induced load to reach its maximum value. This is because the load only reaches its full value once the servo motor has made the control cable completely taut. The cable induced load rises rapidly in the beginning of its onset,

and it only takes approximately 60 counts of servo movement for a majority of the perturbation to enter the system. Once the cable induced load reaches its maximum value it remains approximately constant.

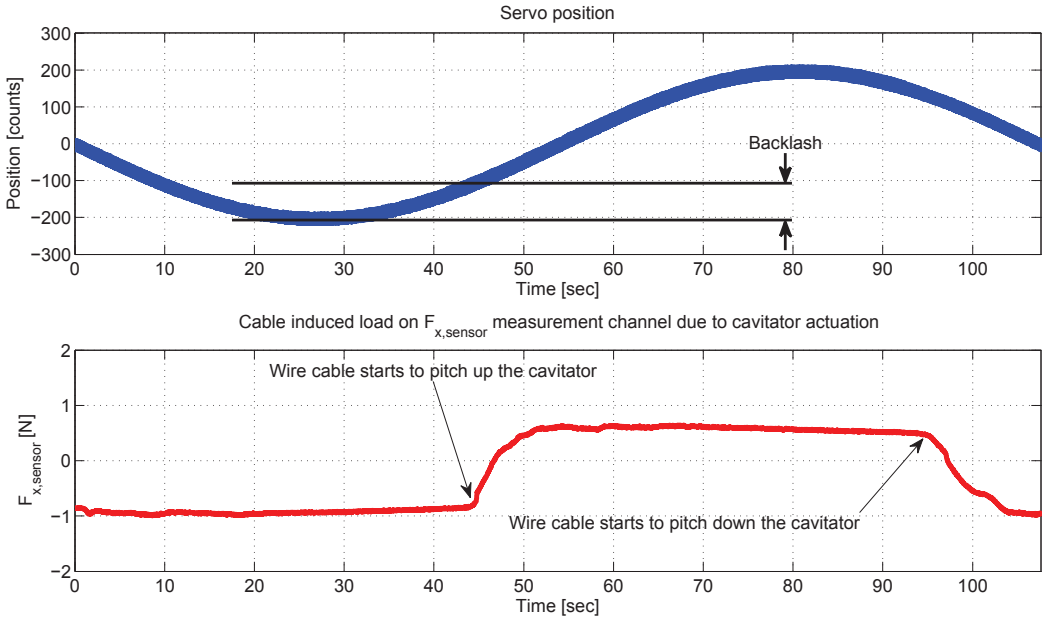

Figure 3.8: Illustration of the cable induced loads as a function of servo movement.

The cable induced loads are significant compared to the hydrodynamic loads observed in the water tunnel tests of Chapter 5. The CoSCIS model is aligned horizontally along the direction of water flow during water tunnel experiments, and the lift force on the CoSCIS vehicle is measured by the $F_{x,sensor}$ channel of the load-cell. As can be seen in Figure 3.8, the $F_{x,sensor}$ channel measurement can be perturbed by as much as 1.6 N, due to cable induced loads. Meanwhile, the lift force due to water impinging on the cavitator is at most approximately ± 2 N at the target operating condition. The cable induced load is a significant perturbation of the lift measurement.

A lift measurement is needed for closed-loop control experiments in Chapter 6. This lift measurement must be reliable, even as the cavitator is actively controlled. Algorithm 3, presented section 3.3.2, uses a model of the actuation scheme to compensate

for the cable induced loads and remove them from the $F_{x,sensor}$ channel measurement of the lift. The corrected $F_{x,sensor}$ signal is used in the control experiments of Chapter 6.

3.3.2 Correcting for Cable Induced Loads

A model of the actuation scheme's function has been introduced in sections 3.2.2 and 3.2.3. The algorithms introduced there provide real-time access to an estimate of the cavitator position, and the state of the control cables. Information about which cable is being pulled in and which is being let out, as well as information on when each cable becomes taut can be extracted from the cavitator position estimation scheme. The cable induced loads can be predicted based on this information, and removed from the measurement data by using a suitable model of the phenomenon. This is done in Algorithm 3. The algorithm is only applied to the cable induced loads in the $F_{x,sensor}$ load-cell measurement channel, associated with the movement of the cavitator.

Algorithm 3 uses the model of the actuation mechanism that was presented in Section 3.2. The algorithm tracks which side of the cavitator has the cable that is in tension, and when the direction of movement changes the algorithm uses a model of the expected cable induced load to correct the force measurement. The goal is to minimize the perturbation due to the cable induced load.

There are two cable induced loads values that the algorithm must know. These are $F_{cable}^{down} < 0$ associated with pitching the cavitator down, and $F_{cable}^{up} > 0$ associated with pitching the cavitator up. F_{cable}^{down} and F_{cable}^{up} are the maximum values of the cable induced load associated with each direction. The F_{cable}^{down} and F_{cable}^{up} variables have units of N, because they represent the perturbation to the force measurement that the algorithm seeks to remove. When the cavitator is pitched down, and the cable induced load associated with the movement has reached its full value, the measurement is perturbed by F_{cable}^{down}. When the cavitator is pitched up, and the cable induced load associated with the movement has reached its full value, the measurement is perturbed by F_{cable}^{up}. When the cavitator direction of movement is changed from pitching down to pitching up, the value of the cable induced load perturbation goes from F_{cable}^{down} to F_{cable}^{up}. This is because the wire that was attached to the bottom of the cavitator and was used to pitch the cavitator down goes slack,

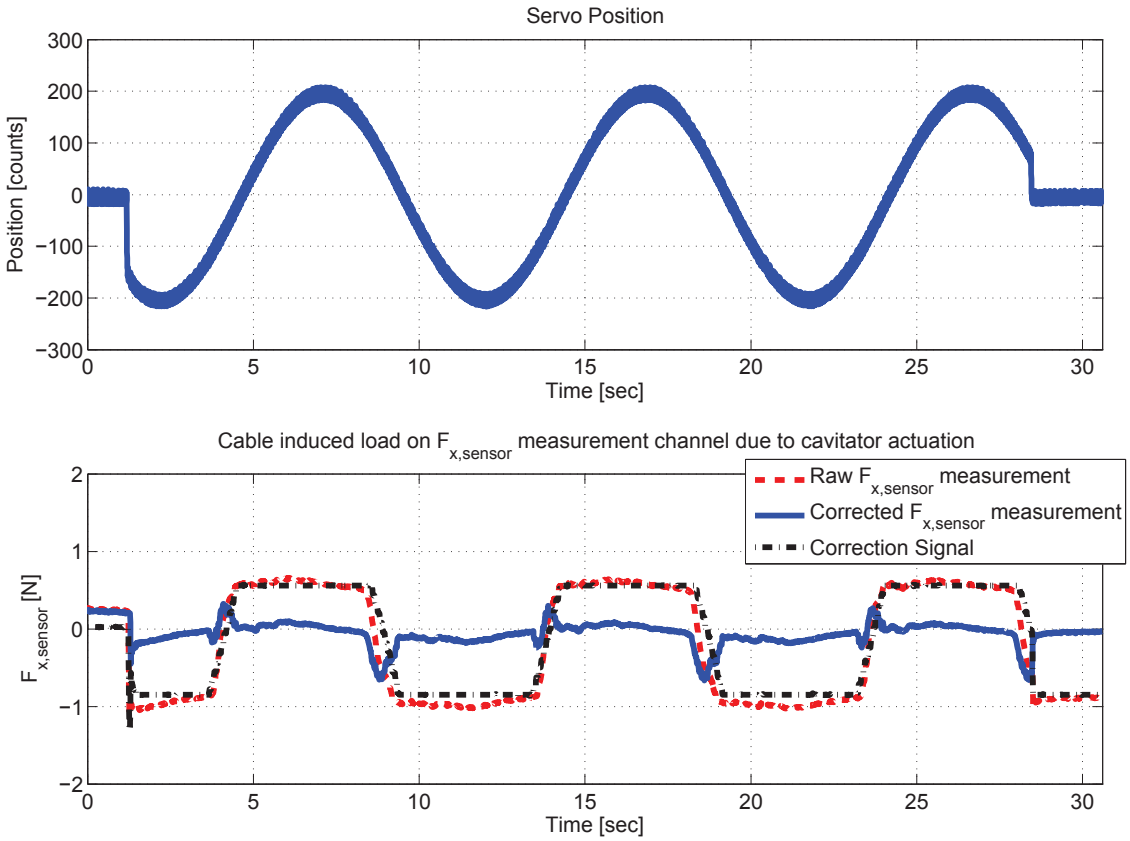

Figure 3.9: Performance of the cable induced loads correction scheme implemented by Algorithm 3.

while the wire that attaches at the top of the cavitator and was used to pitch it up becomes taut. The process is mirrored when the cavitator movement is changed from pitching up to pitching down.

When the cavitator changes direction, the cable induced load does not immediately switch from one maximum value to the other e.g. from F_{cable}^{down} to F_{cable}^{up}. This can be seen in Figure 3.8. The cavitator has to move a certain amount, e, to make the cable completely taut, as explained in Section 3.3.1. The cable induced load has an intermediary value F_{cable} when the cavitator traverses this distance, such that $F_{cable}^{down} < F_{cable} < F_{cable}^{up}$. It is very difficult to derive a model to estimate the value of F_{cable}, because it depends on the initial position of the cavitator, and the deflection rate of the cavitator. The value of F_{cable} is approximated with a linear interpolation

between F_{cable}^{down} and F_{cable}^{up} in Algorithm 3. The variable that is used to interpolate between F_{cable}^{down} and F_{cable}^{up} is the position of the cavitator. When the cavitator changes direction, it is assumed that it takes approximately e degrees of cavitator movement to to make the relevant cable completely taut and switch from one maximum value to the other, e.g from F_{cable}^{down} to F_{cable}^{up}. Pseudo code for the algorithm that accomplishes this is shown in Algorithm Alg:CableInducedLoadsCompensationAlgorithm. The performance of the algorithm is shown in Figure 3.9. The figure shows the perturbation of the $F_{x,sensor}$ load-cell measurement when the servo and cavitator are driven by a sinusoid command. The algorithm performs adequately, as can be seen by the corrected $F_{x,sensor}$ load-cell measurement in Figure 3.9.

The algorithm is successful at mitigating the effects of the cable induced loads. The algorithm is very good at removing the effects of the cable induced loads once they reach their maximum value. The performance of the algorithm is adequate, but not as good when the cavitator movement transitions from one direction to another, and the cable induced load has an intermediary value between its maximum values. This is because of the limitations of the simple cable induced loads model that is used, and the uncertainty associated with the positioning and estimation of the cavitator.

Algorithm 3 extends the cavitator position scheme of section 3.2.2 to include a correction for the cable induced loads. The model of the actuation scheme is used to predict the onset of cable induced loads and apply a correction to the $F_{x,sensor}$ measurement signal. Algorithm 3 was integrated in real-time on board the CoSCIS test bed. It mitigated the effects of cable induced loads sufficiently to make the force measurements accurate enough for feedback control.

Algorithm 3 This algorithm corrects the $F_{x,sensor}$ load-cell measurement, by removing cable induced loads which appear when the cavitator is actuated.

- $\delta_c(i)$ = Cavitator position at time step i (input)
- $D(i)$ = Direction of cavitator motion at time step i
- D_{down} = Cavitator is pitching down, D_{up} = Cavitator is pitching up
- e = Interpolation distance
- $F_{cable}(i)$ = Estimate of cable induced load to $F_{x,sensor}$ measurement at step i
- F_{cable}^{up} = Cable induced load associated with pitching the cavitator up, D_{up}.
- F_{cable}^{down} = Cable induced load associated with pitching the cavitator down, D_{down}.
- $C(i) = -F_{cable}(i)$ Correction added to $F_{x,sensor}$ measurement at step i, in units of N (output)
- System is initialized with $D(0) = D_{down}$, and $C(0) = F_{cable}(0) = F_{cable,0} = F_{cable}^{down}$.

At each time step:

if $\delta_c(i) < \delta_c(i-1)$ **then**
  $D(i) = D_{down}$ {Cavitator is being pitched down}
else if $\delta_c(i) > \delta_c(i-1)$ **then**
  $D(i) = D_{up}$ {Cavitator is being pitched up}
else
  $D(i) = D(i-1)$ {Cavitator stays in place}
end if

if $D(i) \neq D(i-1)$ **then**
  Cavitator direction of movement has changed, save current state for next time step:

  $F_{cable,0} = F_{cable}(i)$ {save current estimate of cable induced load}
  $\delta_{c,0} = \delta_c(i)$ {save current cavitator position}

else if $|\delta_c(i) - \delta_{c,0}| < e$ **then**
  Wire cable that is pulling on cavitator is not fully taut
  and the cable induced load has not reached its full value.
  Interpolate between $F_{cable,0}$, and $F_{x,sensor}^{up}$ or $F_{x,sensor}^{down}$

  if $D(i) = D_{down}$ **then**
    $F_{cable}(i) = F_{cable,0} + \frac{|\delta_c(i) - \delta_{c,0}|}{e} \cdot (F_{cable}^{down} - F_{cable,0})$
  end if
  if $D(i) = D_{up}$ **then**
    $F_{cable}(i) = F_{cable,0} + \frac{|\delta_c(i) - \delta_{c,0}|}{e} \cdot (F_{cable}^{up} - F_{cable,0})$
  end if

else if $|\delta_c(i) - \delta_{c,0}| \geq e$ **then**
  Wire cable that is pulling on cavitator is fully taut.
  The cable induced load has reached its full value.

  if $D(i) = D_{down}$ **then**
    $F_{cable}(i) = F_{cable}^{down}$
  end if
  if $D(i) = D_{up}$ **then**
    $F_{cable}(i) = F_{cable}^{up}$
  end if
end if
Define correction to apply to $F_{x,sensor}$ measurement
$C(i) = F_{cable}(i)$

3.4 Conclusion

The implementation issues that arose during the assembly and integration of the CoSCIS experimental test bed, described in Chapter 2, have been discussed in the previous sections. These issues limited the utility of the CoSCIS test bed, and the scope of possible experiments.

A significant issue is that the load-cell that is used in the CoSCIS test bed has a very large capacity compared to the hydrodynamic loads on the cavitator that are seen in the experiments. This results in a poor signal-to-noise ratio, it makes the measurement sensitive to nonlinearity and hysteresis effects in the load-cell hardware, and it results in sensitivity to drift due to temperature and pressure effects in experiments. Another issue with the load-cell measurements was revealed through spectral analysis of force and moment data from water tunnel experiments. There is a component of measurement noise that is dependent on the operating frequency of the water tunnel pump. The exact mechanism that underlies this phenomenon is unknown, but electromagnetic interference has been ruled out.

The actuation scheme that is used on the test bed resulted in several problems that had to be addressed. It is difficult to achieve tight control of the control surface positions, due to the significant backlash in the actuation scheme, and a lack of direct measurement of their deflections. Accurate control over the position of the cavitator is needed for the closed-loop control experiments, described in Chapter 6. A set of algorithms are designed which model the actuation scheme and the backlash mechanism. These algorithms mitigate the effects and provide accurate positioning and real-time estimation of the deflection of the cavitator.

The actuation mechanism also influences the load-cell measurements. The cavitator and fins are pitched up and down by pulling on a pair of wire cables attached to each of them, as described in Section 2.3.4. This pulling motion induces a load on the control surface which appears in the load-cell measurements. These loads are called "cable induced loads". Algorithms to mitigate the effects of the cable induced loads are presented in Section 3.3. These algorithms are integrated in real-time on board the CoSCIS test bed. They mitigate the effects of cable induced loads sufficiently to make the force measurements accurate enough for feedback control.

The goal of this work was to use the CoSCIS test bed to evaluate the performance

of feedback control systems on a model supercavitating vehicle in a water tunnel. The implementation issues restrict the possible control architectures to those that use the cavitator as a control surface and the lift force on the CoSCIS model as the measurement. The most serious issue that was encountered during the implementation of the system are the cable induced loads. These loads are associated with the movement of the cavitator, and perturb the load-cell measurements significantly. The issue was addressed by implementing algorithms that mitigate the effects of the cable induced loads. This enables the test bed to be used to evaluate the performance of control algorithms in the water tunnel experiments.

Chapter 4

Supercavitating Vehicle Longitudinal Dynamics Model

One goal of the CoSCIS experiment, presented in Chapters 2 and 3, is to use the vehicle's control surfaces to regulate the forces and moments acting on the CoSCIS vehicle model inside the water tunnel test section. An accurate model of the expected forces and moments is needed for this purpose.

Modeling of supercavitating vehicles is an active field of research. The full dynamics of the vehicle, the cavity, and the interaction between them is complex, and it remains a challenge to capture the full dynamics in a model suitable for control design. This section presents a brief overview of the models that have been developed to study the dynamics of supercavitating vehicles and control design. A nonlinear mathematical model is developed following the work of [12]. This mathematical model is adapted to the experimental system and linearized about a trim point at an operating condition equivalent to the CoSCIS experimental environment. The linearized model is used for control design in Section 6.2.

4.1 A Generalized Model of a Supercavitating Vehicle

4.1.1 Rigid-Body Equations of Motion

A diagram of a supercavitating vehicle is shown in Figure 4.1. The diagram illustrates the forces acting on the vehicle, and the body-axis coordinate system

(x_{body},y_{body},z_{body}), centered at the vehicle's *center of gravity* (CG). The vehicle's velocity along each of the x_{body}, y_{body}, and z_{body} axis is denoted by u, v, and w, respectively. The total velocity is $V = \sqrt{u^2 + v^2 + w^2}$. The rate of change of angular motion about each of the x_{body}, y_{body}, and z_{body} axis are p, q, and r respectively. The vehicle has a length, L_{body}, and a radius, R_{body}. The mass of the vehicle is m and the moment of inertia about its y_{body} axis is I_{yy}.

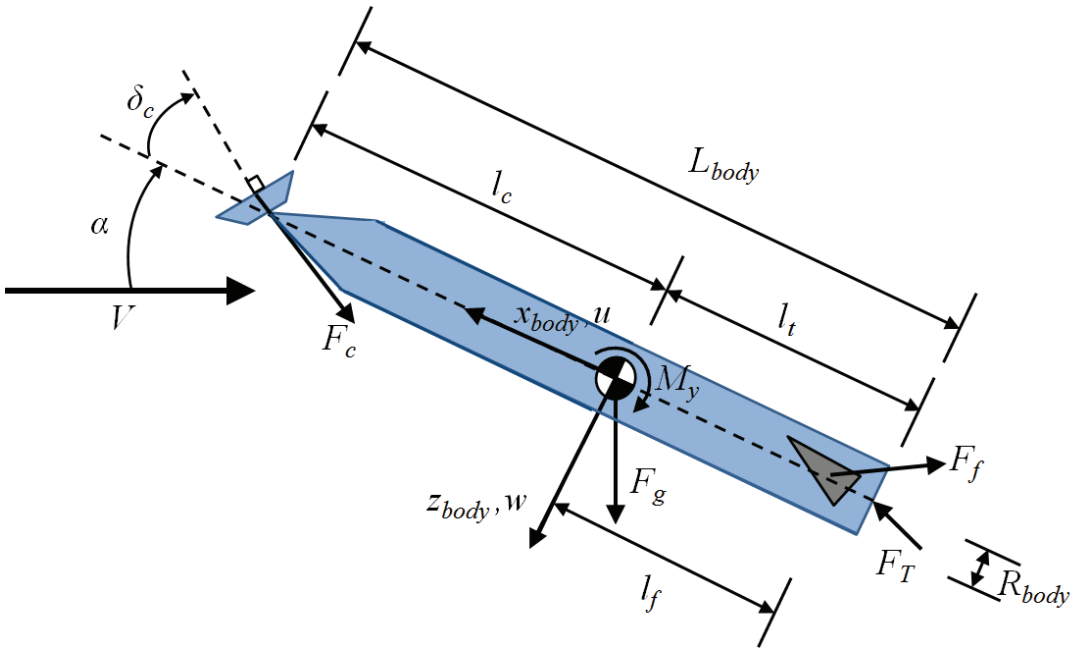

Figure 4.1: Diagram of a supercavitating vehicle in free flight. The forces acting on the vehicle are denoted, along with important distances, and variables that are used to compute the value of the forces and moments that act on the vehicle.

Following the development in [12], the longitudinal dynamics of the vehicle can be described by the three degree of freedom equations summing the forces in the body's x_{body} and z_{body} axis and the moments about the body's y_{body} axis. The forces are denotes as F and the moments by M with subscripts x, y, and z denoting the body-axis upon which the component of force or moment is acting as seen in Figure 4.1. The mass of the vehicle is defined as m. The nonlinear rigid body equations of motion, in the longitudinal plane, can be written as:

$$\begin{aligned}\sum F_x &= m(\dot{u} + wq) \\ \sum F_z &= m(\dot{w} - uq) \\ \sum M_y &= I_{yy}\dot{q}\end{aligned} \tag{4.1}$$

The vehicle has a cavitator at the front, a distance l_c from the vehicle's center of gravity (CG). A pair of horizontal fins and a thrust component are located at the back of the vehicle, a distance l_f and l_t from the CG respectively, as shown in Figure 4.1. The only forces acting on the vehicle are the forces due to the cavitator $\vec{F}_c$, fins $\vec{F}_f$, thrust $\vec{F}_T$, gravity $\vec{F}_g$ and planing $\vec{F}_p$. The moments due to these forces are similarly defined as $\vec{M}_c$, $\vec{M}_f$, $\vec{M}_T$, $\vec{M}_g$ and $\vec{M}_p$. The force due to gravity acts through the CG of the vehicle, and thus $\vec{M}_g = 0$. Equation 4.1 can be rewritten as:

$$\begin{aligned}\dot{u} &= \frac{1}{m}(F_{c_x} + F_{f_x} + F_{T_x} + F_{g_x} + F_{p_x}) - wq \\ \dot{w} &= \frac{1}{m}(F_{c_z} + F_{f_z} + F_{T_z} + F_{g_z} + F_{p_z}) + uq \\ \dot{q} &= \frac{1}{I_{yy}}(M_{c_y} + M_{f_y} + M_{T_y} + M_{p_y})\end{aligned} \tag{4.2}$$

The mathematical model derived in [12], and presented in equation 4.2, models the individual components of force and moment due to the cavitator, fins and planing, using dimensionless hydrodynamic coefficients. The dimensionless hydrodynamic coefficients of lift, drag and pitching moment that are used, are based on static water tunnel tests conducted in the 1950's and 1960's, and published in [24–26]. The hydrodynamic coefficient data is contained in look-up-tables that can be used in nonlinear simulation models.

The full generalized model is presented here for completeness. The CoSCIS vehicle model's fins are not used in this research. Furthermore, the vehicle model will be fixed to the mounting strut horizontally, aligned with the flow in such a way that it is completely contained within the cavity and does not plane. The only forces and moments acting on the CoSCIS vehicle model, whose effects are measured by

the load-cell during experiments, are due to the cavitator at the front and gravity acting through the CG. These forces, along with a thrust component acting at the back of the vehicle, are included in the simulation. The simulation model requires the x_{body} axis component of the thrust to trim the vehicle's forward velocity. The z_{body} axis component of the thrust is used in the control design efforts of Section 6.2.

Expressions for the forces and moments due to the cavitator, gravity and thrust will be introduced in Sections 4.1.3 and 4.1.4. This thesis does not include a description of the forces and moments due to fins and planing. The interested reader can find a study of the forces and moments on wedge fins in [25, 27–29], and a study of the forces and moments due to planing in [26, 27, 30–32]. Examples of previous work on modeling a supercavitating vehicle which incorporates the hydrodynamics of both fins and planing can be found in [1, 11, 12, 29].

4.1.2 Defining Parameters for Supercavitating Flows

The principal parameters that are used to characterize supercavitating flows are the cavitation number:

$$\sigma = \frac{P_\infty - P_c}{\frac{1}{2}\rho V_\infty^2} \tag{4.3}$$

where V_∞ is the velocity of the flow in m/s, ρ is the density of the liquid in kg/m^3, P_∞ is the ambient pressure in the liquid in Pa, and P_c is the pressure inside the supercavity, in Pa.

The Froude number:

$$Fr = \frac{V_\infty}{g d_c} \tag{4.4}$$

where g is the acceleration due to gravity in m/s^2, and d_c is the characteristic length of the supercavitating surface in m, e.g. the diameter of a disk cavitator.

The ventilation coefficient, when the supercavity is ventilated:

$$C_Q = \frac{\tilde{Q}}{V_\infty d_c^2} \tag{4.5}$$

where $\tilde{Q}$ is the ventilation rate of the supercavity, in m^3/s.

4.1.3 The Forces and Moments Due to a Cavitator

Expressions describing the forces and moments on a cavitator were developed in [12]. These expressions will be introduced here and used to model the forces and moments on a disk cavitator.

A disk cavitator is shown in Figure 4.2. The cavitator has a diameter d_c and there is a coordinate system located at the center of the cavitator, aligned along its surface, defined as ($x_{cavitator}$,$y_{cavitator}$,$z_{cavitator}$). For a disk cavitator, the $x_{cavitator}$ axis is normal to the disk and the $y_{cavitator}$ axis is aligned with the y_{body} axis. The angle-of-attack (AoA) of the cavitator is α_c, which is the angle between the incoming flow $\vec{V}_c$, and the normal axis of the cavitator $x_{cavitator}$. The deflection of the cavitator, δ_c, is defined as the angle between the body x_{body} axis and the normal axis of the cavitator, $x_{cavitator}$. The flow past the cavitator has velocity V_c, described in [12] as:

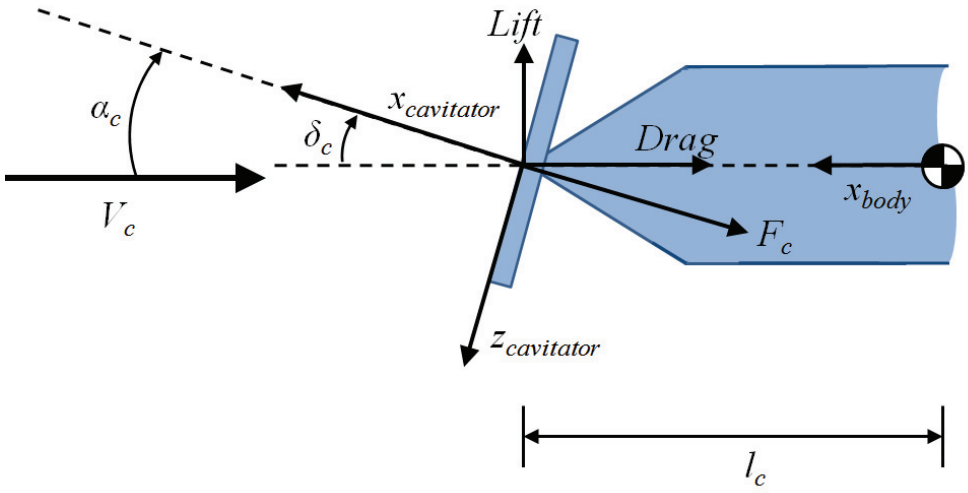

Figure 4.2: A diagram of a cavitator, and the variables that define the attitude and flow conditions around it.

$$V_c = \sqrt{[u\cos(\delta_c) - (w - l_c q)\sin(\delta_c)]^2 + [u\sin(\delta_c) + (w - l_c q)\cos(\delta_c)]^2} \tag{4.6}$$

The direction of the flow past the cavitator is influenced by the AoA of the vehicle, α, the deflection of the cavitator, δ_c, and the pitch rate of the vehicle, q. The AoA

at the cavitator is α_c. An expression for the angle α_c is given by [12] as:

$$\alpha_c = tan^{-1}\left(\frac{u\sin(\delta_c) + (w - l_c q)\cos(\delta_c)}{u\cos(\delta_c) - (w - l_c q)\sin(\delta_c)}\right) \tag{4.7}$$

The force on the cavitator $\vec{F_c}$, can be expressed as [12],

$$\begin{aligned}\vec{F_c} &= \begin{bmatrix} F_{c_x} \\ F_{c_y} \\ F_{c_z} \end{bmatrix} \\ &= \bar{q}_c A_c \begin{bmatrix} \cos\delta_c(-C_{D_c}\cos\alpha_c + C_{L_c}\sin\alpha_c) - \sin\delta_c(C_{D_c}\sin\alpha_c + C_{L_c}\cos\alpha_c) \\ 0 \\ \sin\delta_c(C_{D_c}\cos\alpha_c - C_{L_c}\sin\alpha_c) - \cos\delta_c(C_{D_c}\sin\alpha_c + C_{L_c}\cos\alpha_c) \end{bmatrix}\end{aligned} \tag{4.8}$$

where $\bar{q}_c = \frac{1}{2}\rho V_c^2$ is the dynamic pressure at the cavitator, $A_c = \frac{\pi}{4}d_c^2$ is its reference area and $C_{L_c}(\alpha_c, \sigma)$ and $C_{D_c}(\alpha_c, \sigma)$ are the cavitator's dimensionless coefficients of lift and drag respectively.

The pitching moment about the vehicle's center of gravity, due to the cavitator is [12],

$$M_{c_y} = C_{M_c}\bar{q}_c A_c - l_c F_{c_z} \tag{4.9}$$

where $C_{M_c}(\alpha_c, \sigma)$ is the dimensionless coefficient of pitching moment and l_c is the distance along the x_{body} axis from the cavitator to the vehicle's center of gravity, as shown in Figure 4.1. For a disk cavitator $C_{M_c} \approx 0$, while it can be substantial for other cavitator shapes such as the cone [24].

4.1.4 The Forces and Moments Due to Gravity and Thrust

The forces and moments due to gravity and thrust are included in the mathematical model of equation 4.2. The expressions for these forces and moments will be introduced here, based on the model of [12].

The force of gravity is $\vec{F_g}$, the mass of the vehicle is m and the acceleration due to

gravity is g. Hence,

$$\vec{F}_g = \begin{bmatrix} F_{g_x} \\ F_{g_y} \\ F_{g_z} \end{bmatrix} = \begin{bmatrix} -mg\sin\big(\theta(t)\big) \\ 0 \\ mg\cos\big(\theta(t)\big) \end{bmatrix} \tag{4.10}$$

where

$$\theta(t) = \int_0^t q(t)dt \tag{4.11}$$

is the pitch angle of the vehicle.

The thrust at the back of the vehicle is included in the model for multiple purposes. Its x_{body} axis component is T_x corresponding to the trim thrust at a given forward velocity of the vehicle. In trimmed flight, the T_x component is set to match the drag forces acting on the vehicle, i.e. any other forces acting in the x_{body} axis. The z_{body} component of the thrust is T_z, which is useful to trim the vehicle when studying its dynamics about a certain attitude, as was done in [12]. In Section 6.2 the T_z thrust component will be used in the control design.

The thrust force $\vec{F}_T$ acts on the back of the vehicle as shown in Figure 4.1. The thrust force is applied a distance l_t from the center of gravity. The thrust force is [12],

$$\vec{F}_T = \begin{bmatrix} F_{T_x} \\ F_{T_y} \\ F_{T_z} \end{bmatrix} \begin{bmatrix} T_x \\ 0 \\ T_z \end{bmatrix} \tag{4.12}$$

and the moment due to thrust is

$$\vec{M}_T = \begin{bmatrix} M_{T_x} \\ M_{T_y} \\ M_{T_z} \end{bmatrix} \begin{bmatrix} 0 \\ l_t T_z \\ 0 \end{bmatrix} \tag{4.13}$$

4.2 Mathematical Model for Experimental Control Design

4.2.1 Nonlinear Two-State (α, q) Longitudinal Model

A generalized mathematical model of the longitudinal dynamics of a supercavitating vehicle was given in equation 4.2. This model serves as a basis from which a

simplified linear model will be derived for control design purposes. The generalized model is modified based on the characteristics of the experimental setup.

The experimental vehicle has no fins, and is fixed in place horizontally straight into the flow. In this configuration, the experimental vehicle will not experience planing. Assuming that the simulation vehicle has no fins and is not planing, the fin forces and planing forces can be removed from equation 4.2. The modified equation 4.2 becomes:

$$\begin{aligned} \dot{u} &= \frac{1}{m}(F_{c_x} + F_{T_x} + F_{g_x}) - wq \\ \dot{w} &= \frac{1}{m}(F_{c_z} + F_{T_z} + F_{g_z}) + uq \\ \dot{q} &= \frac{1}{I_{yy}}(M_{c_y} + M_{T_y}) \end{aligned} \tag{4.14}$$

The test body is fixed inside the water tunnel test section, and aligned horizontally straight into the flow. The variations seen in the test vehicle's angle-of-attack will only be due to the gusts induced in the flow by the gust generator. These gusts will be small, on the order of $\pm$ 8°. Furthermore the water tunnel's flow velocity is kept constant during experiments at $V = 8$ m/s.

The flow conditions encountered by the CoSCIS vehicle model can be captured in the mathematical model by assuming that the vehicle has only very small variations in u, its velocity along the x_{body} axis, compared to the magnitude of u itself. The velocity u can be assumed constant for the purposes of modeling[1]. This reduces the equations of motion in equation 4.14 to only the $\dot{w}$ and $\dot{q}$ components.

The vehicle's angle-of-attack is computed as $\alpha = tan^{-1}(\frac{w}{u})$. Assuming that $u \approx$ constant and α is small, this expression can be simplified to $\alpha \approx \frac{w}{u}$, by using the small angle approximation. Then it is possible to express the rate of change of the angle-of-attack as $\dot{\alpha} \approx \frac{\dot{w}}{u}$, and rewrite equation 4.14 in terms of only two states, α

[1]This condition would exist if, for example, an outer loop controller uses the x_{body} axis thrust T_x, to keep the vehicle's velocity constant.

and q [12].

$$\dot{\alpha} = \frac{1}{um}\left(F_{c_z} + F_{T_z} + F_{g_z}\right) + q \tag{4.15}$$

$$\dot{q} = \frac{1}{I_{yy}}\left(M_{c_y} + M_{T_y}\right) \tag{4.16}$$

where the component forces and moments described in Sections 4.1.3 and 4.1.4 are:

$$\begin{aligned}
F_{c_z} &= \bar{q}_c A_c\left[\sin\delta_c(C_{D_c}\cos\alpha_c - C_{L_c}\sin\alpha_c) - \cos\delta_c(C_{D_c}\sin\alpha_c + C_{L_c}\cos\alpha_c)\right] \\
F_{T_z} &= T_z \\
F_{g_z} &= mg\cos\theta \\
M_{c_y} &= -l_c F_{c_z} \\
M_{T_y} &= l_t T_z
\end{aligned} \tag{4.17}$$

where $\bar{q}_c = \frac{1}{2}\rho V_c^2$, $A_c = \frac{\pi}{4}d_c^2$, and α_c and θ are described by equations 4.7 and 4.11 respectively.

The model described by equations 4.15, 4.16 and 4.17, was implemented in MATLAB and Simulink, and will be used to evaluate the controllers synthesized in Chapter 6. This two state model is convenient for control design purposes. The two states α and q describe the important short-period dynamics for the stabilization of a supercavitating vehicle and regulation of α and q allows for a measure of control over the cavity shape.

Regulating the angle-of-attack, α, during maneuvers is useful to minimize cavity deformation, which can lead to the body hitting the cavity wall. The angle between the body and the flow is controlled by regulating α, resulting in steady, predictable cavity shapes. Regulating q allows for controlled turns that combined with a steady cavity shape minimizes the chance of planing. Regulating the combined (α, q) dynamics allows for stable, non-planing flight, and minimizes the effects of cavity shape on the control problem. An added benefit of controlling the (α, q) dynamics is the close connection between this mathematical model of a supercavitating vehicle in free flight and the CoSCIS experiment. This connection is explored further in Section 6.1.

4.2.2 Simulated Vehicle Parameters and Flight Condition

The layout and mass properties of the simulated vehicle are defined to match the CoSCIS vehicle's body. For simplicity, the simulated supercavitating vehicle body is described using simplifying assumptions on its shape, matching those of [33, 34]. The assumed layout is shown in Figure 4.3. The vehicle's body is assumed to consist of a cylinder, of length $L_{cylinder}$ and radius R_{body}, and a cone of height L_{cone} whose base has diameter R_{body}. The cone is at the front of the vehicle, with the tip facing forward and a cavitator with diameter d_c mounted on the tip. The vehicle's total length is $L_{body} = L_{cone} + L_{cylinder}$ and the vehicle body is assumed to have a uniform constant mass density ρ_{body}. The mass density of the water flowing past the vehicle is assumed to be ρ_{water}. For simplicity, the body is assumed to have twice the density of water $\rho_{body} = 2\rho_{water}$, as was assumed in [33]. Hence, the mass of the simulated vehicle is

$$m = \pi \rho_{body} R_{body}^2 (\frac{1}{3} L_{cone} + L_{cylinder}) \tag{4.18}$$

and its moment of inertia about its y_{body} axis is

$$I_{yy} = \frac{\pi \rho_{body} R_{body}^2}{240 L_{cone} + 720 L_{cylinder}} \Big[3L_{cone}^4 + 24 L_{cone}^3 L_{cylinder} + 60 L_{cone}^2 L_{cylinder}^2 \tag{4.19}$$

$$+ 12 L_{cone}^2 R_{body}^2 + 80 L_{cone} L_{cylinder}^3 + 60 L_{cylinder}^4 \tag{4.20}$$

$$+ 96 L_{cone} L_{cylinder} R_{body}^2 + 180 L_{cylinder}^2 R_{body}^2) \Big] \tag{4.21}$$

The distance from the center of gravity and the cavitator at the tip of the vehicle is

$$l_c = \frac{3L_{cone}^2 + 12 L_{cone} L_{cylinder} + 6 L_{cylinder}^2}{4 L_{cone} + 12 L_{cylinder}} \tag{4.22}$$

measured along the x_{body} axis.

The flight condition where the simulated vehicle is assumed to operate is based on the flow conditions in the water tunnel test section during the CoSCIS experiment. Based on Section 5.2, the velocity of the flow in the water tunnel is $V = 8$ m/s, the cavitation number is $\sigma = 0.23$ and the Froude number is $Fr = 20.47$.

The force on the cavitator is formulated using $C_{L_c}(\alpha_c, \sigma)$ and $C_{D_c}(\alpha_c, \sigma)$, the hy-

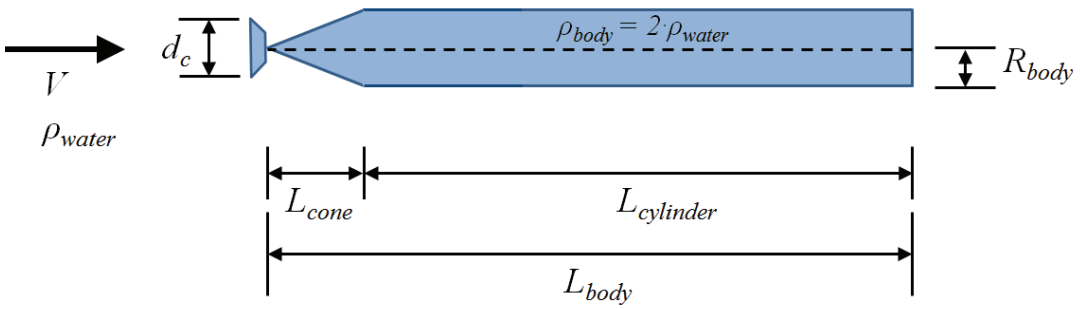

Figure 4.3: The assumed shape of the supercavitating vehicle that is being modeled in this chapter.

drodynamic coefficients of lift and drag respectively. These were published for a number of different cavitators and flow conditions in [24]. The hydrodynamic coefficients depend on the cavitator's angle-of-attack α_c and the cavitation number σ. The cavitation number in the experiments described in this work is $\sigma = 0.23$, while the hydrodynamic data for disk cavitators in [24] is only given for $0.06 \leq \sigma \leq 0.15$. To calculate the hydrodynamic coefficients at a cavitation number $\sigma = 0.23$, the results of [24] need to be extrapolated from $0.06 \leq \sigma \leq 0.15$ to $\sigma = 0.23$. This is done by utilizing the work done in [29], on deriving analytical expressions for the data in [24] and extrapolating it to different cavitation numbers. In [29], the lift and drag coefficients in [24] are modeled as

$$C_{L_c} \approx -C_{D,0}(1+\sigma)\cos\alpha_c \sin\alpha_c \tag{4.23}$$

$$C_{D_c} \approx \quad C_{D,0}(1+\sigma)\cos^2\alpha_c \tag{4.24}$$

where $C_{D,0} = 0.805$ [12, 27]. These analytical expressions were derived from hydrodynamic data in the $0.06 \leq \sigma \leq 0.15$ range, and used to predict the value of C_{L_c} and C_{D_c} at smaller cavitation numbers, $\sigma = 0.015 - 0.030$ [29]. In this research they are used to predict the value of C_{L_c} and C_{D_c} at a larger cavitation number, $\sigma = 0.23$.

The values of C_{L_c} and C_{D_c} at $\sigma = 0.23$, which are predicted by equations 4.23 and 4.24, are fitted with polynomial approximations to yield simplified expressions for C_{L_c} and C_{D_c}. This approach was introduced in [12] which found that simple polynomial expressions could be used to approximate experimental C_{L_c} and C_{D_c} data

Operating Conditions of Experimental System		
Parameter	Value	Description
σ	0.23	Measured ventilated cavitation number
Fr	20.47	Froude number
V	8 m/s	Water tunnel flow velocity
ρ_{water}	1000 kg/m^3	Mass density of water
Q	25 L/min	Ventilation Rate

Table 4.1: Parameters of experimental operating condition

with sufficient accuracy for cavitators experiencing angles of attack between $-20^o \leq \alpha_c \leq 20^o$. The polynomial expressions allow for an easy analytical linearization of the dynamical model.

In this work the C_{L_c} and C_{D_c} coefficient data, that is obtained from equations 4.23 and 4.24 when $\sigma = 0.23$, is used to derive a polynomial expression for the C_{L_c} and C_{D_c} coefficients:

$$C_{L_c} \approx -k_3 \alpha_c \tag{4.25}$$

$$C_{D_c} \approx -k_2 \alpha_c^2 + k_1 \tag{4.26}$$

where the constants k_1, k_2 and k_3 are chosen to minimize the root mean square of the error between the results of equations 4.23 and 4.24 on one hand, and the results of equations 4.25 and 4.26 on the other. It should be noted that while the polynomial approximations in equations 4.25 and 4.26 are sufficiently accurate for $-20^o \leq \alpha_c \leq 20^o$, the dynamical model is derived for small angles of attack. Hence, α and α_c must be kept small.

The values of k_1, k_2, and k_3, at the cavitation number $\sigma = 0.23$, are listed in Table 4.2. This extrapolation of the hydrodynamic data of [24] is compared to experimental results in Chapter 5, where the lift on a cavitator is measured for different flow velocities and angles-of-attack.

The hydrodynamic parameters of the experimental system, which define the flight conditions of the simulated vehicle, are presented in table 4.1. The parameters of the simulated vehicle are presented in Table 4.2.

Parameters of Simulated System		
Parameter	Value	Description
k_1	0.9881	C_{D_c} Approximation constant (α_c is in rad)
k_2	$0.0003(180/\pi)^2$	C_{D_c} Approximation constant (α_c is in rad)
k_3	$0.0150(180/\pi)$	C_{L_c} Approximation constant (α_c is in rad)
d_c	0.015 m	Cavitator diameter
L_{body}	13.90 cm	Length of the simulated vehicle body
$L_{cylinder}$	11.68 cm	Length of cylinder portion of the vehicle body
L_{cone}	2.22 cm	Length of cone portion of the vehicle body
R_{body}	1.11 cm	Radius of the simulated vehicle
l_c	7.68 cm	Distance between the cavitator and CG
l_t	6.22 cm	Distance from the back of the vehicle to CG
g	9.8 $\mathrm{m/s^2}$	Gravitational acceleration
m	0.0963 kg	Vehicle Mass
I_{yy}	$1.2806 \cdot 10^{-4}$ $\mathrm{kg\,m^2}$	Vehicle mass moment of inertia about y_{body} axis

Table 4.2: Parameters of simulated system

4.2.3 Linearization

In Section 4.2.1, the longitudinal dynamics of a supercavitating vehicle were described by equations 4.15 and 4.16 using the forces and moments due to the cavitator, thrust and gravity as described by equation 4.17. This model of the longitudinal dynamics can be simplified, by utilizing the small angle approximation, to a form that can be easily linearized analytically.

First, assume that the vehicle is traveling at a constant forward velocity u, and the cavitator deflections δ_c and the AoA of the cavitator α_c are kept small. Second, assume that the vehicle is operating around the straight and level flight condition, and the pitch angle θ is kept small. Then equation 4.17 can be rewritten as:

$$
\begin{aligned}
F_{c_z} &\approx \bar{q}_c A_c\big[\delta_c(C_{D_c} - C_{L_c}\alpha_c) - (C_{D_c}\alpha_c + C_{L_c})\big] \\
F_{T_z} &= T_z \\
F_{g_z} &\approx mg \\
M_{c_y} &= -l_c F_{c_z} \\
M_{T_y} &= l_t T_z
\end{aligned} \tag{4.27}
$$

The small angle approximation can be used to simplify the expressions for α_c in equation 4.7. Following the development in [12], α_c can be rewritten as follows when α_c and δ_c are small:

$$
\begin{aligned}
\alpha_c &= tan^{-1}\left(\frac{u\sin(\delta_c) + (w - l_c q)\cos(\delta_c)}{u\cos(\delta_c) - (w - l_c q)\sin(\delta_c)}\right) \\
&\approx \frac{u\delta_c}{u - \delta_c(w - l_c q)} + \frac{w - l_c q}{u - \delta_c(w - l_c q)}
\end{aligned} \tag{4.28}
$$

This expression can be further simplified because the u term in the denominator is much larger than the $\delta_c(w - l_c q)$ term, and thus $u - \delta_c(w - l_c q) \approx u$ yielding [12]

$$
\begin{aligned}
\alpha_c &\approx \frac{u\delta_c}{u - \delta_c(w - l_c q)} + \frac{w - l_c q}{u - \delta_c(w - l_c q)} \\
&\approx \frac{u\delta_c}{u} + \frac{w - l_c q}{u} \\
&\approx \delta_c + \alpha - \frac{l_c q}{u}
\end{aligned} \tag{4.29}
$$

The simplified (α, q) dynamical model in 4.15 and 4.16 can be rewritten as:

$$
\dot{\alpha} = \frac{1}{um}\Big(\bar{q}_c A_c\big[\delta_c(C_{D_c} - C_{L_c}\alpha_c) - (C_{D_c}\alpha_c + C_{L_c})\big] + T_z + mg\Big) + q \tag{4.30}
$$

$$
\dot{q} = \frac{1}{I_{yy}}\Big(-l_c\bar{q}_c A_c\big[\delta_c(C_{D_c} - C_{L_c}\alpha_c) - (C_{D_c}\alpha_c + C_{L_c})\big] + l_t T_z\Big) \tag{4.31}
$$

where C_{L_c} and C_{D_c} are described by equations 4.25 and 4.26, and α_c is given by equation 4.29.

The simplified mathematical model of equations 4.30 and 4.31 can be linearized analytically. The linearization is done about a trim point at the operating condition described in Section 4.2.2, by using a first order Taylor series approximation. A trim point is a combination of states and inputs such that $\dot{\alpha} = 0$ and $\dot{q} = 0$ in equations 4.30 and 4.31. Written in state space form, the linearization of equations 4.30 and 4.31 is [12]:

$$\begin{bmatrix} \dot{\alpha} \\ \dot{q} \end{bmatrix} = \begin{bmatrix} \frac{1}{um}\left(\frac{\partial F_{c_z}}{\partial \alpha}\right) & \frac{1}{um}\left(\frac{\partial F_{c_z}}{\partial q}\right) + 1 \\ \frac{1}{I_{yy}}\left(\frac{\partial M_{c_y}}{\partial \alpha}\right) & \frac{1}{I_{yy}}\left(\frac{\partial M_{c_y}}{\partial q}\right) \end{bmatrix} \begin{bmatrix} \alpha \\ q \end{bmatrix} + \begin{bmatrix} \frac{1}{um}\left(\frac{\partial F_{c_z}}{\partial \delta_c}\right) & \frac{1}{um} \\ \frac{1}{I_{yy}}\left(\frac{\partial M_{c_y}}{\partial \delta_c}\right) & \frac{l_t}{I_{yy}} \end{bmatrix} \begin{bmatrix} \delta_c \\ T_z \end{bmatrix} \tag{4.32}$$

where

$$\frac{\partial F_{c_z}}{\partial \alpha} = \bar{q}_c A_c \left(2(k_3 - k_2)\alpha_c \delta_c + 3k_2 \alpha_c^2 + k_3 - k_1\right) \tag{4.33}$$

$$\frac{\partial F_{c_z}}{\partial q} = \frac{-l_c \bar{q}_c A_c}{u} \left(2(k_3 - k_2)\alpha_c \delta_c + 3k_2 \alpha_c^2 + k_3 - k_1\right) \tag{4.34}$$

$$\frac{\partial F_{c_z}}{\partial \delta_c} = \bar{q}_c A_c \left(2(k_3 - k_2)\alpha_c \delta_c + (k_3 + 2k_2)\alpha_c^2 + k_3\right) \tag{4.35}$$

and

$$\frac{\partial M_{c_y}}{\partial \alpha} = -l_c \left(\frac{\partial F_{c_z}}{\partial \alpha}\right) \tag{4.36}$$

$$\frac{\partial M_{c_y}}{\partial q} = -l_c \left(\frac{\partial F_{c_z}}{\partial q}\right) \tag{4.37}$$

$$\frac{\partial M_{c_y}}{\partial \delta_c} = -l_c \left(\frac{\partial F_{c_z}}{\partial \delta_c}\right) \tag{4.38}$$

since $M_{c_y} = -l_c F_{c_y}$.

The simulated vehicle is trimmed around a flight condition that matches the flow conditions around the CoSCIS vehicle model in the water tunnel test section. The CoSCIS vehicle is aligned horizontally, straight into the flow. Its steady-state angle-of-attack is $\alpha_{ss} = 0^o$. Thus the simulated vehicle is trimmed around an angle-of-attack $\alpha_{trim} = \alpha_{ss} = 0^o$, flying straight and level at a velocity $u = 8$ m/s about a pitch angle $\theta_{trim} = 0^o$ and zero pitch rate $q_{trim} = 0$ rad/s. The control inputs needed to trim the vehicle about this flight condition are: Cavitator pitch $\delta_{c,trim} = -4.979°$, x_{body} axis thrust $T_{x,trim} = 5.546$ N and z_{body} axis thrust $T_{z,thrust} = -0.522$ N. These

trim inputs are found by using the "*fminsearch*" function in MATLAB to solve for values of δ_c, T_x, and T_z in equation 4.14, which yield $\dot{\alpha} = \dot{q} = 0$. The cavitator lift and drag coefficients used with equation 4.14 when the trim inputs are found, are those described by equations 4.25 and 4.26.

The linear model obtained by evaluating equation 4.32 at this trim point is:

$$\begin{bmatrix} \dot{\alpha} \\ \dot{q} \end{bmatrix} = \begin{bmatrix} -0.794 & 1.008 \\ 367 & -3.523 \end{bmatrix} \begin{bmatrix} \alpha \\ q \end{bmatrix} + \begin{bmatrix} 6.448 & 1.297 \\ -2981 & 485.7 \end{bmatrix} \begin{bmatrix} \delta_c \\ T_z \end{bmatrix} \tag{4.39}$$

where α and δ_c are in units of rad, q is in units of rad/s, and T_z is in units of N.

The response of the linearized model can be verified qualitatively by comparing the open-loop response of the two state nonlinear model of equations 4.15 and 4.16, against the linear model of equation 4.39, at the specified trim point and operating condition. The result of such a comparison are shown in Figures 4.4 and 4.5 for δ_c and T_z input doublets.

The open-loop response of both models matches qualitatively for short periods. However the two models diverge over time. This is because the force due to gravity depends on the pitch angle, θ, in the nonlinear model of equations 4.15 and 4.16.

4.2.4 State-Space Model for Control Design

The linear state-space model presented in this section will be used to synthesize controllers for a supercavitating vehicle in Chapter 6.2. The linear model of equation 4.32 models the short-period dynamics of a supercavitating vehicle, as it flies straight and level at a constant speed and small angle-of-attack. The longitudinal plane position of the supercavitating vehicle can be controlled by regulating its z_{body} axis acceleration, A_z. The linear model of equation 4.32 is augmented with α, q, and A_z output, enabling a control designer to use the augmented linear model to design controllers which track A_z reference commands while stabilizing the unstable (α, q) dynamics and avoiding planing.

By utilizing Newton's Second Law, the vehicle's acceleration along the z_{body} axis, A_z, can be written as a function of the total z_{body} axis force acting on the simulated

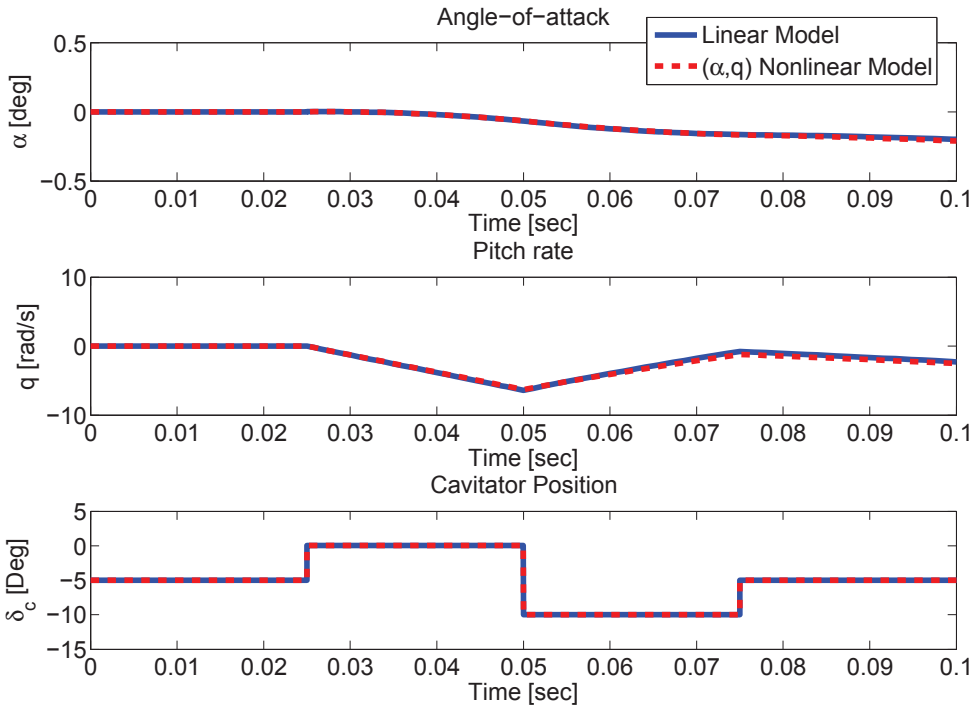

Figure 4.4: A comparison of the response of the the nonlinear model of equations 4.15 and 4.16, and the linear model of equation 4.39, for a cavitator pitch doublet of $\delta_c = \pm 5°$.

vehicle, $\sum F_{z_{body}}$, as:

$$A_z = \frac{1}{m} \sum F_{z_{body}} = \frac{1}{m} \left(F_{z_c} + F_{z_{T_z}} + F_{z_g} \right) \tag{4.40}$$

The acceleration A_z can be related to α and q by using equation 4.15

$$\begin{aligned} \dot{\alpha} &= \frac{1}{u} \left[\frac{1}{m} \left(F_{c_z} + F_{T_z} + F_{g_z} \right) \right] + q \\ &= \frac{1}{u} A_z + q \end{aligned} \tag{4.41}$$

Hence, A_z can be written as a function of α and q by rearranging equation 4.41:

$$A_z = u(\dot{\alpha} - q) \tag{4.42}$$

A linear state-space model for control design is formed using the linear model of

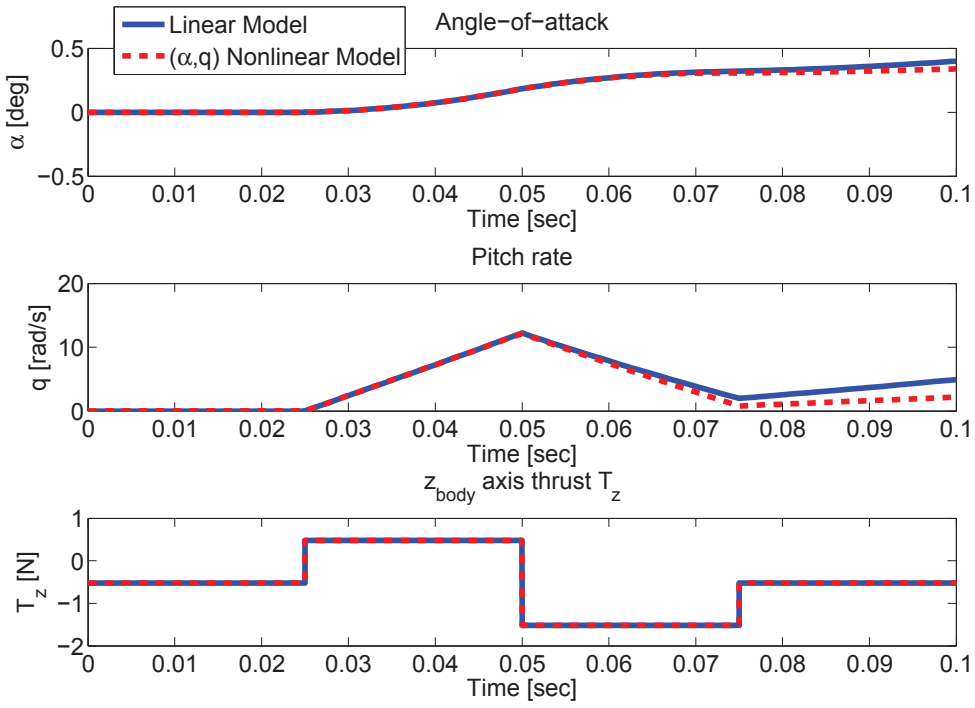

Figure 4.5: A comparison of the response of the nonlinear model of equations 4.15 and 4.16, and the linear model of equation 4.39, for a cavitator pitch doublet of $T_z = \pm 1$ N.

equation 4.32. The state-space model has outputs: α, q, and A_z, where the A_z output of the model is computed from equation 4.42:

$$\begin{bmatrix} \dot{\alpha} \\ \dot{q} \end{bmatrix} = \begin{bmatrix} \frac{1}{um}\left(\frac{\partial F_{c_z}}{\partial \alpha}\right) & \frac{1}{um}\left(\frac{\partial F_{c_z}}{\partial q}\right) + 1 \\ \frac{1}{I_{yy}}\left(\frac{\partial M_{c_y}}{\partial \alpha}\right) & \frac{1}{I_{yy}}\left(\frac{\partial M_{c_y}}{\partial q}\right) \end{bmatrix} \begin{bmatrix} \alpha \\ q \end{bmatrix} + \begin{bmatrix} \frac{1}{um}\left(\frac{\partial F_{c_z}}{\partial \delta_c}\right) & \frac{1}{um} \\ \frac{1}{I_{yy}}\left(\frac{\partial M_{c_y}}{\partial \delta_c}\right) & \frac{l_t}{I_{yy}} \end{bmatrix} \begin{bmatrix} \delta_c \\ T_z \end{bmatrix}$$

$$\begin{bmatrix} A_z \\ \alpha \\ q \end{bmatrix} = \begin{bmatrix} \frac{1}{m}\left(\frac{\partial F_{c_z}}{\partial \alpha}\right) & \frac{1}{m}\left(\frac{\partial F_{c_z}}{\partial q}\right) \\ 1 & 0 \\ 0 & 1 \end{bmatrix} \begin{bmatrix} \alpha \\ q \end{bmatrix} + \begin{bmatrix} \frac{1}{m}\left(\frac{\partial F_{c_z}}{\partial \delta_c}\right) & \frac{1}{m} \\ 0 & 0 \\ 0 & 0 \end{bmatrix} \begin{bmatrix} \delta_c \\ T_z \end{bmatrix} \quad (4.43)$$

The augmented model is evaluated at the trim point described by equation 4.39:

$$\begin{bmatrix} \dot{\alpha} \\ \dot{q} \end{bmatrix} = \begin{bmatrix} -0.794 & 1.008 \\ 367 & -3.523 \end{bmatrix} \begin{bmatrix} \alpha \\ q \end{bmatrix} + \begin{bmatrix} 6.448 & 1.297 \\ -2981 & 485.7 \end{bmatrix} \begin{bmatrix} \delta_c \\ T_z \end{bmatrix}$$
$$\begin{bmatrix} A_z \\ \alpha \\ q \end{bmatrix} = \begin{bmatrix} -6.352 & 0.06097 \\ 1 & 0 \\ 0 & 1 \end{bmatrix} \begin{bmatrix} \alpha \\ q \end{bmatrix} + \begin{bmatrix} 51.59 & 10.38 \\ 0 & 0 \\ 0 & 0 \end{bmatrix} \begin{bmatrix} \delta_c \\ T_z \end{bmatrix} \tag{4.44}$$

where α and δ_c are in units of rad, q is in units of rad/s, T_z is in units of N, and A_z is in units of m/s^2.

The linear system in equation 4.44 is unstable. The system has a right half-plane pole at 17.12 rad/s and is open-loop unstable. The ability of the thrust T_z and cavitator δ_c to affect the simulated vehicle's angle-of-attack α and pitch rate q is illustrated in the Bode plots of Figures 4.6 and 4.7.

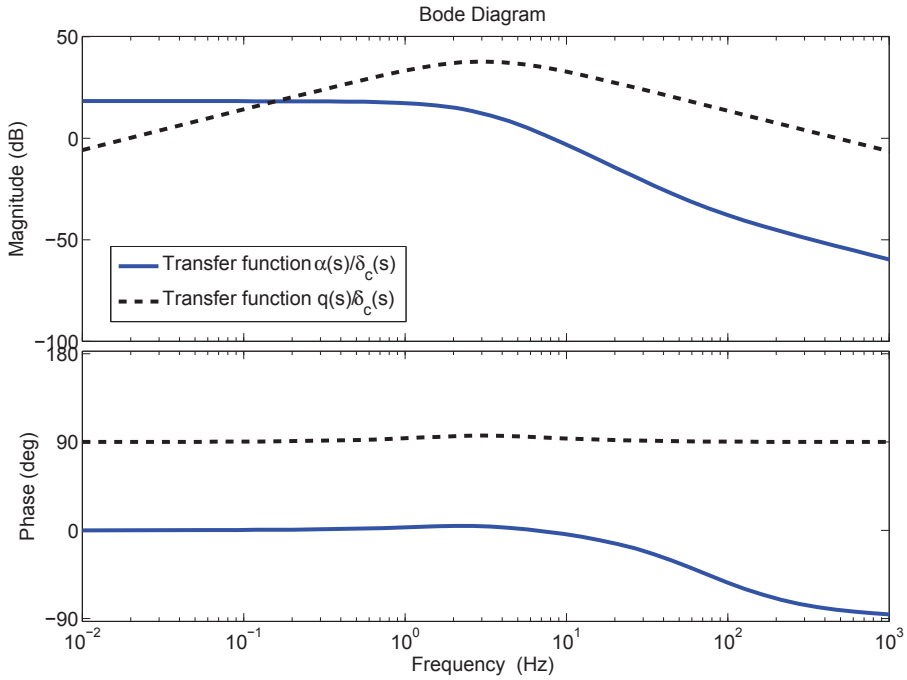

Figure 4.6: Bode Plot: Cavitator input δ_c to α and q.

The cavitator can be used to track α as shown in Figure 4.6, but due to a zero at the origin, it can not be used to affect the pitch rate q at steady-state. Figure 4.7

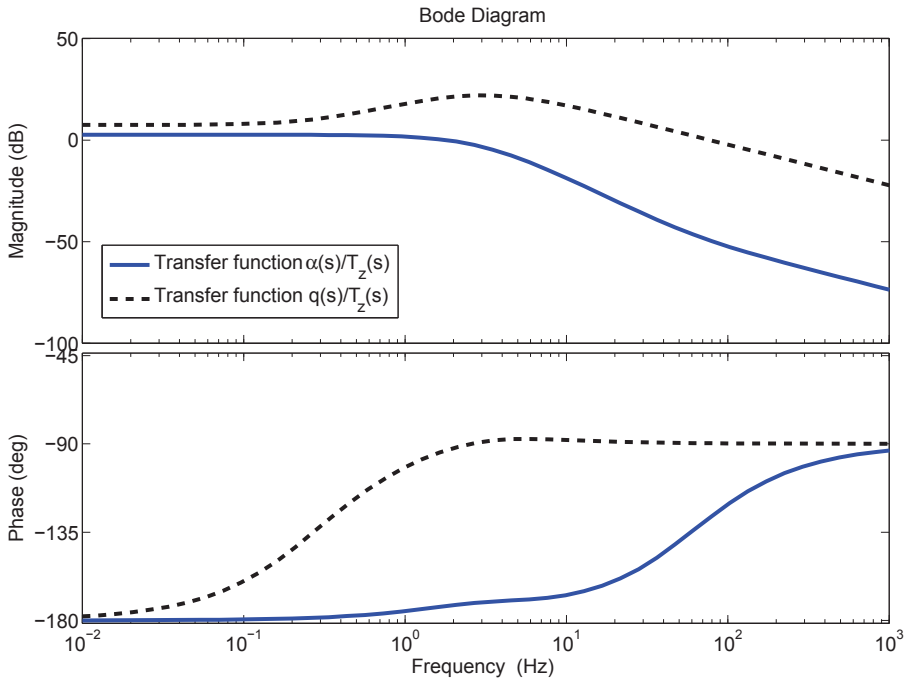

Figure 4.7: Bode Plot: Thrust input T_z to α and q.

shows that the thrust T_z can be used to effect control over both α and q.

A Bode plot, illustrating the effect that the thrust and cavitator have on the acceleration A_z is shown in Figure 4.8. The thrust is effective at all frequencies, while the cavitator has no effect on A_z at steady-state. This result is to be expected because the cavitator can't be used to control the pitch rate at stead-state, and a steady turn will experience constant centripetal acceleration, due to the centripetal force required to keep the vehicle turning.

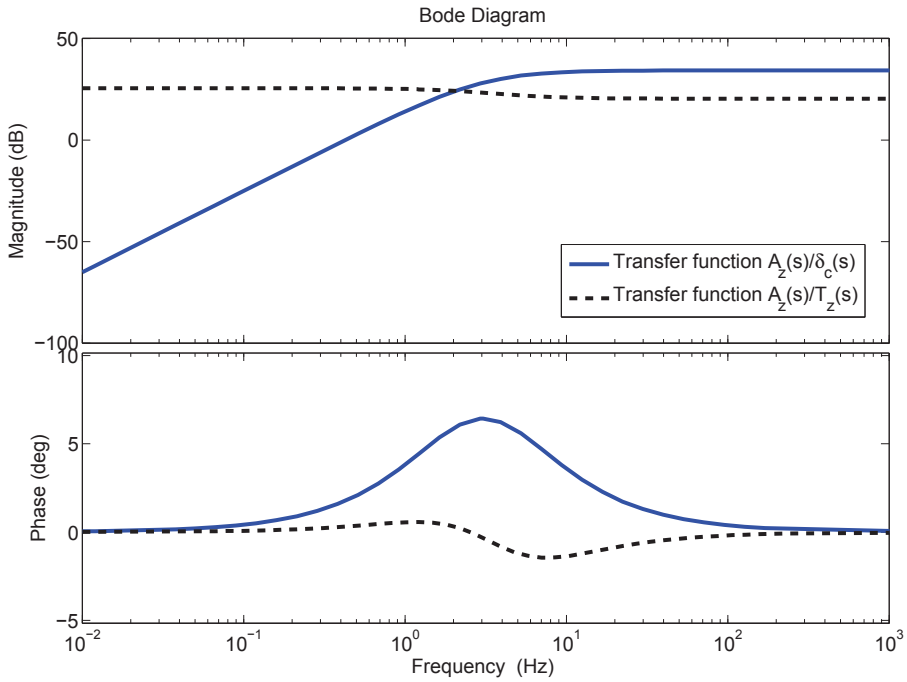

Figure 4.8: Bode Plot: Normalized acceleration response to cavitator deflections δ_c (solid line) and thrust input T_z (dashed line).

Chapter 5

Open-Loop Water Tunnel Testing

The CoSCIS test bed was placed in the water tunnel and the component of lift force on the cavitator was measured. The results are compared against the hydrodynamic model presented in Chapter 4, in order to verify the models validity.

5.1 Experimental Setup

The CoSCIS test bed is installed inside the water tunnel, as discussed in Section 2.3.3. The test bed is oriented so that the the cavitator is oriented directly into the direction of flow such that the z_{sensor}-axis of the load-cell is aligned with the direction of flow, and the drag on the cavitator is confined to the z_{sensor}-axis of the load-cell. The x_{sensor}-axis of the load-cell is aligned with the pitch axis of the cavitator such that the lift on the cavitator is confined to the x_{sensor}-axis of the load-cell during experiments.

A picture of the experiment is shown in Figure 5.1. The cavity forms around the cavitator at the front and completely envelops the CoSCIS model, collapsing behind the model on the load-cell's outer shell during experiments. The load-cell measures the forces and moments on the CoSCIS model. The only part of the CoSCIS model in contact with the water is the cavitator. Hence, the load-cell measures the forces and moments on the cavitator, as well as the downward force on the CoSCIS model due to gravity. The force due to gravity is constant and can be compensated for

when the sensor is tared[1] (i.e. zeroed with load) at the start of the experiment, leaving only the lift and drag forces on the cavitator. As long as the CoSCIS model is not planing, the lift force on the cavitator is equal to the force measured in the x_{sensor}-axis of the sensor, $F_{x,sensor}$, while the drag force on the cavitator is equal to the force measured in the z_{sensor}-axis of the sensor, $F_{z,sensor}$. The measurement of the lift force, based on the $F_{x,sensor}$ measurements, is denoted as $L_{F_{x,sensor}}$:

$$L_{F_{x,sensor}} = F_{x,sensor} \tag{5.1}$$

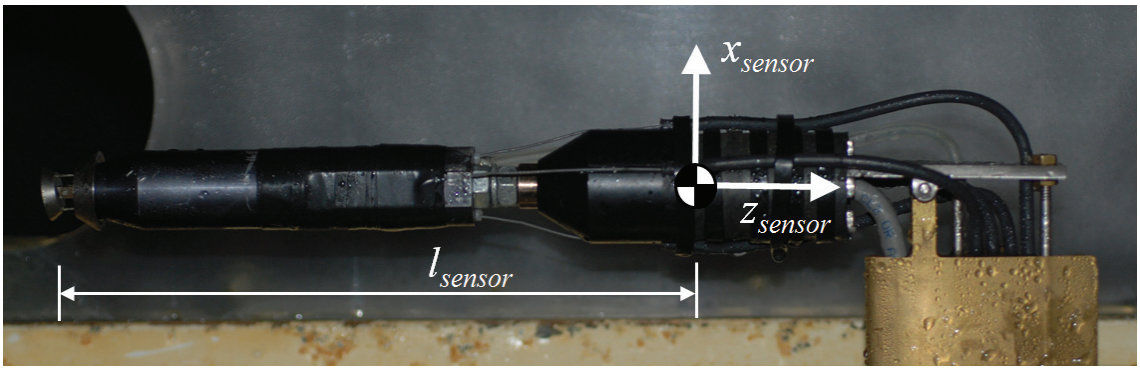

Figure 5.1: A side view of the CoSCIS test bed mounted inside the water tunnel. The axis of the load-cell, x_{sensor} and z_{sensor}, are denoted in the figure. The distance between the cavitator and the load-cell's center of measurement is defined as l_{sensor}.

The lift on the cavitator generates a pitching moment which the load-cell measures as the moment $-M_{y,sensor}$ (the negative sign is due to the orientation of the sensor's y_{sensor}-axis.) This moment can be used to obtain a second measurement of the lift on the cavitator, when the CoSCIS model is not planing. The pitching moment experienced by the body, is exclusively due to the lift force on the cavitator, and acts at $l_{sensor} = 0.195$ m away from the center of measurement of the load-cell as seen in Figure 5.1. The lift on the cavitator can be estimated by dividing the $M_{y,sensor}$

[1]In force and moment measurement applications there is often a component of force or moment that will remain constant throughout an experiment. When a load-cell is "tared" or "zeroed with load", it refers to the process of offsetting the force and moment measurements by the value of the constant forces and moments so that the load-cell reads zero when no other force or moment acts on the load-cell. This process is commonly used in practice to remove steady-state offsets in load-cell measurement data, e.g. forces and moments due to gravity

measurement by l_{sensor}. Hence, the measurement of the lift force which is based on $M_{y,sensor}$, is denoted as $L_{M_{y,sensor}}$:

$$L_{M_{y,sensor}} = -\frac{M_{y,sensor}}{l_{sensor}} \tag{5.2}$$

The active control experiments described in Chapter 6 rely exclusively on the load-cell's x_{sensor}-axis $F_{x,sensor}$ measurements, and seek to regulate the lift force on the body by regulating the $F_{x,sensor}$ forces. The lift measurements derived from the pitching moment can be used to validate the hydrodynamic model. However, the lift measurements derived from the pitching moment were not used for the active control experiments, because of the possibility of planing during those experiments. The pitching moment can only be used to estimate the lift on the body, when the distance between the lift force and the load-cell's center of measurement is known. In the experiments described in this chapter, the only force on the body which causes a pitching moment is the lift on the cavitator, which acts at a distance l_{sensor}. If the CoSCIS model planes, there will be a planing force, whose direction and point of application is unknown, invalidating the relationship described in equation 5.2. The active control experiments include a gust generator, capable of introducing disturbances into the flow about the CoSCIS model. These flow disturbances may cause the backside of the CoSCIS model to come into contact with the water, causing the model to plane. It would be impossible to obtain an accurate estimate of the lift from the pitching moment, if the CoSCIS model were to plane during a control experiment, without knowing exactly when and the amount the model is planing.

The experiments described in this chapter sought to determine the validity of the cavitator hydrodynamic model. Unfortunately the $F_{z,sensor}$ measurement of the load-cell is unreliable due to drift, as is explained in Section 5.1.4. Hence, the drag on the cavitator can not be reliably measured, and only the validity of the cavitator lift model will be examined in the experiments described here.

The $F_{x,sensor}$, $F_{z,sensor}$, and $M_{y,sensor}$ measurements experience a zero shift when the water tunnel is started. The lift force on the cavitator should be zero when the cavitator's angle-of-attack is zero, according to the hydrodynamic model. Hence, the lift measurement when the cavitator is at zero angle-of-attack, $\delta_c = \alpha_c = 0°$, is used as an estimate of the zero shift for each test, and subtracted from those

measurements where $\delta_c = \alpha_c \neq 0°$. This yields the change in lift coefficient as a function of cavitator angle-of-attack.

Several tests are conducted to ascertain the validity of the hydrodynamic model presented in Chapter 4. The hydrodynamic lift, generated by the cavitator, is measured for various cavitator angles of attack and water tunnel velocities. The lift measured in these experiments is compared against the values predicted by the hydrodynamic model. The CoSCIS model does not plane in any of the experiments described here, enabling the inclusion of the pitching moment based estimate of the lift, described above, when verifying the hydrodynamic model.

5.1.1 Hydrodynamic Model of Loads on a Cavitator

The expected lift coefficient of a cavitator, predicted by the hydrodynamic model introduced in Chapter 4, is described by equation 4.23:

$$C_{L_c} \approx C_{D,0}(1+\sigma)\cos\alpha_c \sin\alpha_c \tag{4.23}$$

where α_c is the angle-of-attack of the cavitator, as described by equation 4.7,

$$\alpha_c = \tan^{-1}\left(\frac{u\sin(\delta_c) + (w - l_c q)\cos(\delta_c)}{u\cos(\delta_c) - (w - l_c q)\sin(\delta_c)}\right) \tag{4.7}$$

In the water tunnel experiment, the pitch rate of the test bed is zero, $q = 0$ rad/s, and the test bed is aligned with the direction of the flow, such that $w = 0$ m/s. The angle-of-attack of the cavitator becomes the same as the deflection angle of the cavitator, δ_c:

$$\alpha_c = \tan^{-1}\left(\frac{u \cdot \sin(\delta_c) + 0}{u \cdot \cos(\delta_c) + 0}\right) = \delta_c \tag{5.3}$$

Hence, equation 4.23 can be updated to yield a model of lift on the cavitator in this experiment:

$$C_{L_c} \approx C_{D,0}(1+\sigma)\cos\delta_c \sin\delta_c \tag{5.4}$$

5.1.2 Computing the Dimensionless Lift Coefficient from Experimental Data

The measured lift, $L_{F_{x,sensor}}$ or $L_{M_{y,sensor}}$, is used to compute the dimensionless lift coefficient, C_L, using the following relationship:

$$C_{L_i} = \frac{L_i}{\frac{1}{2}\rho_{water}(\frac{\pi}{4}d_c^2)V_c^2} \tag{5.5}$$

where i stands for either $F_{x,sensor}$ or $M_{y,sensor}$, and $\rho_{water} = 1000$ kg/m^3 is the density of water, $d_c = 0.015$ m is the diameter of the cavitator, and V_c m is the velocity of the water flowing about the cavitator as was explained in Chapter 4.

5.1.3 Accounting for Uncertainty in Lift Coefficient Estimates

The systematic uncertainty in the lift coefficient estimate is determined by propagating the uncertainty in the lift measurements, $\Delta_{L_{F_{x,sensor}}}$ and $\Delta_{L_{M_{y,sensor}}}$, uncertainty in the velocity measurement, Δ_V, uncertainty in the cavitator diameter, Δ_{d_c} and uncertainty in the estimate of the density of the water $\Delta_{\rho_{water}}$, through equation 5.5. The velocity, density, and cavitator diameter are estimated once for each test condition while lift is measured continuously at a sampling rate of 166.67 Hz. Hence, the uncertainty in the velocity, cavitator diameter and water density are treated as fixed systematic uncertainties. This systematic uncertainty is combined with the systematic and random uncertainty associated with the lift measurements, to establish bounds on the total uncertainty of the lift coefficient estimates.

The density of the water which is used by the water tunnel is assumed to be $\rho_{water} = 1000$ kg/m^3, the density of water at 4° C and 1 atm. The uncertainty in ρ_{water} is due to the discrepancy in temperature and air pressure between the ideal conditions, and the actual operating conditions on the day that each experiment was performed. The temperature of the water was not recorded during each test, and a worst case estimate of its effects on the density is used. The temperature of the water used by the water tunnel, is assumed to fluctuate at most between 0° C and 30° C. The density of water at 1 atm and 30° C is 995.7 kg/m^3, while the density of water at 1 atm and 0° C is 999.8 kg/m^3 [35]. Hence, the uncertainty in ρ_{water} is estimated to

be

$$\Delta_{\rho_{water}} = \pm 5 \text{ kg/m}^3 \tag{5.6}$$

The velocity of the water in the water tunnel was measured by a Laser Doppler Velocimetry (LDV) system. The LDV system generates an estimate of the mean velocity by measuring the velocity of the water multiple times. The number of individual measurements varies, but an estimate of the mean velocity was not deemed valid unless there were at least 1000 individual measurements used to generate it. The LDV system yields a measurement of the mean velocity, accompanied by the standard deviation of the velocity measurements which were used to compute the mean velocity. The standard deviation of the velocity measurements is on the order of $\Omega_V = 0.1$ m/s, when at least 1000 individual measurements are taken. The uncertainty associated with the estimate of the mean velocity is [36]

$$\Delta_V = \pm t_s \frac{\Omega_V}{\sqrt{N}} \tag{5.7}$$

where N is the number of individual velocity measurements, and t_s is the value of the "Student's t" for $N-1$ degrees of freedom and the appropriate level of confidence. The uncertainty in the estimate of the velocity is greatest if only 1000 individual measurements are used to compute the mean of the velocity measurements. This worst-case uncertainty of the mean velocity estimate, with a 95% confidence level, is:

$$\Delta_V = \pm 1.960 \frac{0.1 \text{ m/s}}{\sqrt{1000}} = \pm 0.006 \text{ m/s} \tag{5.8}$$

The uncertainty in the diameter of the cavitator is assumed to be on the order of 3%.

$$\Delta_{d_c} = \pm 0.5 \text{ mm} \tag{5.9}$$

The systematic uncertainty associated with the lift measurements is due to hysteresis, nonlinearities and drift in the load-cell measurements, as well as errors due the transmission of measurements from the load-cell to the cRIO, and the Analog-to-Digital (A/D) conversion in the NI 9239 analog input module of the cRIO.

The uncertainty due to the load-cell hysteresis is $\pm 0.2\%$ of full-scale [20], where the range of the load-cell's $F_{x,sensor}$ measurment is ± 278.01 N and the range of the

load-cell's $M_{y,sensor}$ measurment is ± 2.8245 Nm. The uncertainty in the $F_{x,sensor}$ measurements due to the load-cell's hysteresis is:

$$\Delta_{F_{x,sensor}}^{hysteresis} = \pm 278.01 \cdot \frac{0.2}{100} = \pm 0.56 \text{ N} \tag{5.10}$$

The uncertainty in the $M_{y,sensor}$ measurements due to the load-cell's hysteresis is:

$$\Delta_{M_{y,sensor}}^{hysteresis} = \pm 2.8245 \cdot \frac{0.2}{100} = \pm 0.0056 \text{ Nm} \tag{5.11}$$

The uncertainty due to the nonlinearity of the load-cell's measurements is also $\pm 0.2\%$ of full-scale [20]. Hence, the uncertainty in the $F_{x,sensor}$ measurements due to the load-cell's nonlinearity is:

$$\Delta_{F_{x,sensor}}^{nonlinearity} = \pm 0.56 \text{ N} \tag{5.12}$$

The uncertainty in the $M_{y,sensor}$ measurements due to the load-cell's nonlinearity is:

$$\Delta_{M_{y,sensor}}^{nonlinearity} = \pm 0.0056 \text{ Nm} \tag{5.13}$$

The drift in the load-cell measurements is determined by measuring the measurement drifts during the experiments described in Section 5.3.1. The drift is measured by noting the difference in measured lift between step 3 and step 6f in the experimental procedure described in Section 5.3.1. This represents the drift in $F_{x,sensor}$ and $M_{y,sensor}$ over a span of approximately 20 min. The drift in each of the five experimental runs described in Section 5.3.1 is computed. The largest of the five drift measurements is used to represent the uncertainty due to measurement drift. The worst-case drift in the $F_{x,sensor}$ measurement is:

$$\Delta_{F_{x,sensor}}^{drift} = \pm 0.29 \text{ N} \tag{5.14}$$

and the worst-case drift in the $M_{y,sensor}$ measurement is

$$\Delta_{M_{y,sensor}}^{drift} = \pm 0.0245 \text{ Nm} \tag{5.15}$$

The load-cell measurements are transmitted from the MSA-6 MiniAmp magnifier

to the NI9239 module of the cRIO in the form of an analog ±10 V signal. The uncertainty due to a offset in the A/D conversion inside the NI9239 module is 0.008% [22]. A full-scale 10 V signal represents 269.99 N in the $F_{x,sensor}$ channel. Hence, the uncertainty in the $F_{x,sensor}$ measurement, due to the A/D conversion, will at most be:

$$\Delta^{A/D}_{F_{x,sensor}} = \pm\, 269.99 \text{ N} \cdot \frac{0.008}{100} = \pm\, 0.02 \text{ N} \tag{5.16}$$

Similarly a full-scale 10 V signal represents 3.6707 Nm in the $M_{y,sensor}$ channel, and the uncertainty in the $M_{y,sensor}$ measurements, due to the A/D conversion, is at most:

$$\Delta^{A/D}_{M_{y,sensor}} = \pm\, 3.6707 \text{ N} \cdot \frac{0.008}{100} = \pm\, 0.0003 \text{ Nm} \tag{5.17}$$

Noise in the $F_{x,sensor}$ and $M_{y,sensor}$ measurements contributes random uncertainty to the estimate of the lift coefficient of the cavitator at each test condition. A test condition is a specific combination of water tunnel velocity, cavitator angle-of-attack, and cavitation number. The $F_{x,sensor}$ and $M_{y,sensor}$ data is collected for approximately 5 min at each test condition in the experiments described in this chapter. The noise in the lift measurements is greatest when the water tunnel velocity is 5.5 m/s in the experiment of Section 5.3.1, for the reasons described in Section 3.1. The noise at this test condition is used to determine the worst-case noise level for the lift measurements. The standard deviation of the unfiltered $F_{x,sensor}$ measurement is $\Omega_{F_{x,sensor}} = 0.74$ N, and the standard deviation of the unfiltered $M_{y,sensor}$ measurement is $\Omega_{F_{x,sensor}} = 0.0199$ Nm. Both $\Omega_{F_{x,sensor}}$ and $\Omega_{M_{y,sensor}}$ are based on a minimum of 30,000 measurements at each test condition. The random uncertainty in the mean of the $F_{x,sensor}$ and $M_{y,sensor}$ measurements is computed using the method presented in equation 5.7. The worst-case random uncertainty of the mean $F_{x,sensor}$ measurement, with a 95% confidence level, is:

$$\Delta^{noise}_{F_{x,sensor}} = \pm\, t_s \frac{\Omega_{F_{x,sensor}}}{\sqrt{30000}} = \pm\, 1.960 \frac{0.74}{\sqrt{30000}} = \pm\, 0.01 \text{ N} \tag{5.18}$$

The worst-case uncertainty of the mean $M_{y,sensor}$ measurement, with a 95% confidence level, is:

$$\Delta^{noise}_{M_{y,sensor}} = \pm\, t_s \frac{\Omega_{M_{y,sensor}}}{\sqrt{30000}} = \pm\, 1.960 \frac{0.0199}{\sqrt{30000}} = \pm\, 0.0002 \text{ Nm} \tag{5.19}$$

The total uncertainty in the $F_{x,sensor}$ measurement is computed as

$$\begin{aligned}\left(\Delta_{F_{x,sensor}}\right)^2 = & \left(\Delta_{F_{x,sensor}}^{hysteresis}\right)^2 + \left(\Delta_{F_{x,sensor}}^{nonlinearity}\right)^2 + \left(\Delta_{F_{x,sensor}}^{drift}\right)^2 \\ & + \left(\Delta_{F_{x,sensor}}^{A/D}\right)^2 + \left(\Delta_{F_{x,sensor}}^{noise}\right)^2\end{aligned} \tag{5.20}$$

such that

$$\Delta_{F_{x,sensor}} = \pm 0.84 \text{ N} \tag{5.21}$$

This is a large uncertainty, compared to the expected size of the cavitator lift at the chosen experimental condition (approximately ±2 N.) It should be noted that the largest elements of uncertainty are contributed by the the load-cell's nonlinearity and hysteresis. Both elements are systematic uncertainties inherent to the hardware, and their value is derived from the manufacturers specifications of their worst-case value. The total uncertainty in the $M_{y,sensor}$ measurement is computed as

$$\begin{aligned}\left(\Delta_{M_{y,sensor}}\right)^2 = & \left(\Delta_{M_{y,sensor}}^{hysteresis}\right)^2 + \left(\Delta_{M_{y,sensor}}^{nonlinearity}\right)^2 + \left(\Delta_{M_{y,sensor}}^{drift}\right)^2 \\ & + \left(\Delta_{M_{y,sensor}}^{A/D}\right)^2 + \left(\Delta_{M_{y,sensor}}^{noise}\right)^2\end{aligned} \tag{5.22}$$

such that

$$\Delta_{M_{y,sensor}} = \pm 0.0258 \text{ Nm} \tag{5.23}$$

When the lift coefficient is computed from the $F_{x,sensor}$ measurements, no computation is necessary because the lift equals the $F_{x,sensor}$ measurement: $L_{F_{x,sensor}} = F_{x,sensor}$. Hence, the uncertainty in the lift measurement is equal to the uncertainty in the $F_{x,sensor}$ measurement:

$$\Delta_{L_{F_{x,sensor}}} = \Delta_{F_{x,sensor}} \tag{5.24}$$

Equation 5.2 is used to compute $L_{M_{y,sensor}}$, when the $M_{y,sensor}$ measurement is used to estimate the lift on the cavitator:

$$L_{M_{y,sensor}} = -\frac{M_{y,sensor}}{l_{sensor}} \tag{5.2}$$

The uncertainty in l_{sensor} is:

$$\Delta_{l_{sensor}} = \pm 10 \text{ mm} \tag{5.25}$$

and the systematic uncertainty in $L_{M_{y,sensor}}$ is computed as:

$$\Delta_{L_{M_{y,sensor}}} = \pm \left\{ \left(\Delta_{M_{y,sensor}} \frac{\partial L_{M_{y,sensor}}}{\partial M_{y,sensor}} \right)^2 + \left(\Delta_{l_{sensor}} \frac{\partial L_{M_{y,sensor}}}{\partial l_{sensor}} \right)^2 \right\}^{1/2} \tag{5.26}$$

The lift coefficient is computed using equation 5.5. The total uncertainty in the $C_{L_{F_{x,sensor}}}$ and $C_{L_{M_{y,sensor}}}$ estimates at each test condition is determined by propagating the uncertainty in the measured lift, velocity, density, and cavitator diameter through equation 5.5. The uncertainty in the estimate of the lift coefficient at each test condition is computed as follows [36]

$$\Delta_{C_{L_i}} = \pm \left\{ \left(\Delta_{L_i} \frac{\partial C_{L_i}}{\partial L_i} \right)^2 + \left(\Delta_{\rho_{water}} \frac{\partial C_{L_i}}{\partial \rho_{water}} \right)^2 + \left(\Delta_V \frac{\partial C_{L_i}}{\partial V} \right)^2 + \left(\Delta_{d_c} \frac{\partial C_{L_i}}{\partial d_c} \right)^2 \right\}^{1/2} \tag{5.27}$$

where i stands for either $F_{x,sensor}$ or $M_{y,sensor}$. In practice the uncertainty in C_{L_i} becomes smaller when the water tunnel velocity is increased. When the water tunnel is run at 8 m/s $\Delta_{C_{L_{F_{x,sensor}}}} \approx \pm 0.10$ and $\Delta_{C_{L_{M_{y,sensor}}}} \approx \pm 0.006$, while $\Delta_{C_{L_{F_{x,sensor}}}} \approx 0.21$ and $\Delta_{C_{L_{M_{y,sensor}}}} \approx \pm 0.025$ when the water tunnel is run at 5.5 m/s.

The angle-of-attack of the cavitator is measured by taking pictures of the cavitator and measuring the angle in *ImageJ*, as described in Section 3.2.1. Multiple pictures are taken at each test condition to yield multiple measurements for each angle-of-attack. The estimate of the angle-of-attack is the mean of these measurements. The random uncertainty $\Delta_{\Omega_{\alpha_c}}$, associated with the variation of the individual estimates that are used to compute the mean angle-of-attack, is computed using the method presented in equation 5.7 for each test condition. The systematic uncertainty associated with this method is assumed to be no larger than $\Delta_{\bar{\alpha}_c} = \pm 1°$. The total uncertainty in the angle-of-attack measurements is

$$\Delta_{\alpha_c} = \sqrt{\left(\Delta_{\bar{\alpha}_c}\right)^2 + \left(\Delta_{\Omega_{\alpha_c}}\right)^2} \tag{5.28}$$

In practice $1.0^\circ < |\Delta_{\alpha_c}| < 1.5^\circ$.

5.1.4 Uncertainty in $F_{z,sensor}$ Measurements

The systematic uncertainty associated with the $F_{z,sensor}$ measurements is dominated by the uncertainty due to the hysteresis, nonlinearities and drift in the load-cell's z_{sensor}-axis. The uncertainty due to the load-cell hysteresis is $\pm 0.2\%$ of full-scale [20], where the range of the load-cell's $F_{z,sensor}$ measurment is $\pm\, 556.03$ N. The uncertainty in the $F_{z,sensor}$ measurements due to the load-cell's hysteresis is:

$$\Delta_{F_{z,sensor}}^{hysteresis} = \pm 556.03 \cdot \frac{0.2}{100} = \pm\, 1.11 \text{ N} \tag{5.29}$$

The uncertainty due to the nonlinearity of the load-cell's measurements is also $\pm 0.2\%$ of full-scale [20]. Hence, the uncertainty in the $F_{z,sensor}$ measurements due to the load-cell's nonlinearity is:

$$\Delta_{F_{z,sensor}}^{nonlinearity} = \pm\, 1.11 \text{ N} \tag{5.30}$$

The drift in the load-cell measurements is determined by measuring how much the measurement drifts during the experiments described in Section 5.3.1. The drift is measured by noting the difference in measured lift between phase 3 of the experimental procedure and phase 6f. This represents the drift in $F_{z,sensor}$ over a span of approximately 20 min. The drift in each of the five experimental runs described in Section 5.3.1 is computed. The largest of the five drift measurements is used to represent the uncertainty due to measurement drift. The worst-case drift in the $F_{z,sensor}$ measurement is:

$$\Delta_{F_{z,sensor}}^{drift} = \pm\, 2.54 \text{ N} \tag{5.31}$$

The uncertainties due to the drift, nonlinearity and hysteresis contribute the most to the uncertainty in the $F_{z,sensor}$ measurement. Together they contribute an uncer-

tainty $\Delta_{F_{z,sensor}}$, defined as:

$$\begin{aligned}\Delta_{F_{z,sensor}} &= \pm\sqrt{\left(\Delta_{F_{z,sensor}}^{hysteresis}\right)^2+\left(\Delta_{F_{z,sensor}}^{nonlinearity}\right)^2+\left(\Delta_{F_{z,sensor}}^{drift}\right)^2} \\ &= \pm 2.98 \text{ N}\end{aligned} \tag{5.32}$$

$\Delta_{F_{z,sensor}}$ is very large compared to the expected drag forces in all of the experiments described in this work. Equation 4.24 can be used to predict the expected coefficient of drag when the water tunnel is run at V=8 m/s and a cavitation number of $\sigma = 0.23$. When the cavitator is at zero angle-of-attack, the coefficient of drag is:

$$C_D^{\alpha_c=0^\circ} = 0.805 \cdot (1+\sigma)\,\cos^2(0) = 0.99 \tag{5.33}$$

and the drag force is:

$$D_{\alpha_c=0^\circ} = C_D^{\alpha_c=0^\circ}\left[\frac{1}{2}\rho_{water}V^2\left(\frac{\pi}{4}d_c^2\right)\right] = 5.60 \text{ N} \tag{5.34}$$

When the cavitator is at $\alpha_c = \pm 25^\circ$, the coefficient of drag is:

$$C_D^{\alpha_c=25^\circ} = 0.805 \cdot (1+\sigma)\,\cos^2(25^\circ) = 0.81 \tag{5.35}$$

and the drag force is:

$$D_{\alpha_c=0^\circ} = C_D^{\alpha_c=25^\circ}\left[\frac{1}{2}\rho_{water}V^2\left(\frac{\pi}{4}d_c^2\right)\right] = 4.60 \text{ N} \tag{5.36}$$

The difference in drag force that the experiment needs to measure is

$$|D_{\alpha_c=0^\circ} - D_{\alpha_c=25^\circ}| = 1.00 \text{ N} \tag{5.37}$$

The uncertainty due to the drift, nonlinearity and hysteresis of the $F_{z,sensor}$ measurement is $\Delta_{F_{z,sensor}} = \pm 2.98$ N, almost three times the size of the difference in drag force that the experiment is trying to measure. This accuracy is insufficient. Hence, this measurement can not be used to ascertain the validity of the hydrodynamic model of equation 4.24, which describes how the coefficient of drag changes with the cavitator angle-of-attack, due to the large uncertainty in the measurement.

5.2 Estimation of the Cavitation Number

The modeling effort in Chapter 4, requires an estimate of the cavitation number at the target operating conditions that the closed-loop experiments will be conduced in. The target operating conditions are a flow velocity of $V = 8$ m/s, and a ventilation rate of $Q = 25$ L/min.

The cavitation number was defined in Section 4.1.2:

$$\sigma = \frac{P_\infty - P_c}{\frac{1}{2}\rho V_\infty^2} \tag{5.38}$$

where V_∞ is the velocity of the flow in m/s, ρ is the density of the liquid in kg/m^3, P_∞ is the ambient pressure in the liquid in Pa, and P_c is the pressure inside the supercavity, in Pa.

This section describes an experiment to determine what the cavitation number is at the target operating conditions. The setup for the experiment was described in Section 5.1. The cavitation number is computed from a measurement of the water tunnel velocity, the ambient pressure in the test section, and the pressure inside the supercavity. The water tunnel velocity is measured using Laser Doppler Velocimetry (LDV). The ambient pressure in the test section is measured using a pressure transducer. The CoSCIS model is not equipped with a pressure transducer to measure the pressure inside the cavity. Hence, the pressure inside the cavity is derived using the Bernoulli Principle, with the aforementioned velocity and pressure measurements.

Bernoulli's Principle for an incompressible flow states that the total pressure in the fluid is constant at all points along a streamline in the flow. This yields Bernoulli's equation:

$$\frac{1}{2}\rho V_\infty^2 + \rho g h + P = \text{constant} \tag{5.39}$$

where ρ is the density of the fluid, V_∞ is the velocity of the fluid, g is the acceleration due to gravity, h is the height of the point measured in the direction of $-g$, and P is the pressure at the point. Equation 5.39 can be used to relate the velocity, pressure, and height of two points in an incompressible fluid.

Figure 5.2 illustrates the experimental setup in the water tunnel when the cavitation

number is estimated. The points $\hat{p}_1$ and $\hat{p}_2$ are shown in Figure 5.2. Point $\hat{p}_1$ represents the center of the test section, upstream of the CoSCIS model, where there is a pressure port in the test section window. The pressure port enables a direct measurement of the pressure P_1, at point $\hat{p}_1$. The pressure is $P_1 = 3.16$ kPa. The height of the $\hat{p}_1$ point, measured from the test section bottom, is $h_1 = 96$ mm. The velocity of the flow at $\hat{p}_1$, denoted by $V_1 = 7.851$ m/s, is measured using the LDV system. Point $\hat{p}_2$ is on the boundary of the cavity. The height of $\hat{p}_2$ is $h_2 = 72$ mm, and the velocity of the flow at $\hat{p}_2$, denoted by $V_2 = 8.686$ m/s, is measured using the LDV system. The pressure at $\hat{p}_2$, denoted by P_2, can not be measured directly and is determined by using Bernoulli's equation.

$$\frac{1}{2}\rho V_1^2 + \rho g h_1 + P_1 = \frac{1}{2}\rho V_2^2 + \rho g h_2 + P_2 \tag{5.40}$$

Point $\hat{p}_2$ is on the boundary of the cavity, and the pressure at $\hat{p}_2$ must equal the pressure of the cavity, P_c, since the cavity would expand if it did not. Hence, equation 5.40 and the measurements of P_1, h_1, h_2, V_1, and V_2, can be used to estimate the pressure inside the cavity:

$$P_c = P_2 = \frac{1}{2}\rho\left(V_1^2 - V_2^2\right) + \rho g\left(h_1 - h_2\right) + P_1 \tag{5.41}$$

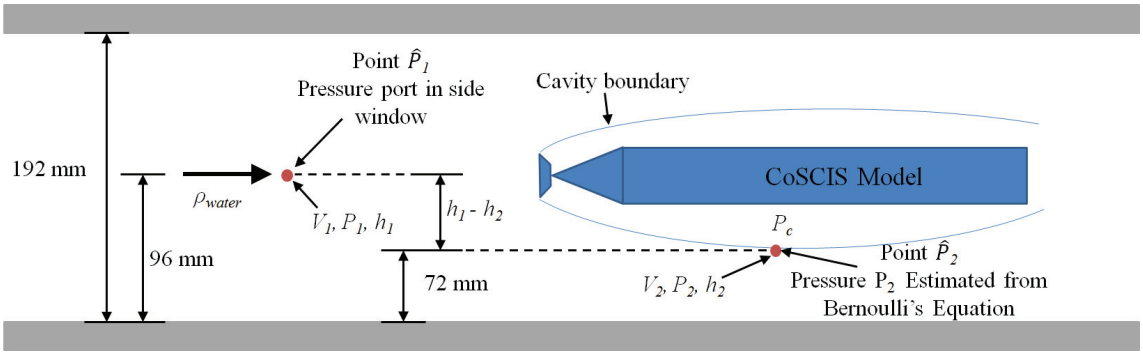

Figure 5.2: A diagram of the experimental setup when the cavitation number is estimated.

The ambient pressure, and velocity in the liquid is approximated by P_1 and V_1, which

are the pressure and velocity that are measured upstream of the model. Hence, the cavitation number of the supercavity that is observed in the experiment is computed as:

$$\sigma = \frac{P_1 - P_c}{\frac{1}{2}\rho V_1^2} \tag{5.42}$$

Inserting equation 5.41 into equation 5.42, and rearranging, yields:

$$\sigma = \frac{V_2^2}{V_1^2} + \frac{2g\left(h_2 - h_1\right)}{V_1^2} - 1 \tag{5.43}$$

Hence, the cavitation number in at the target operating condition for the closed-loop experiments is computed as:

$$\sigma = \frac{V_2^2}{V_1^2} + \frac{2g\left(h_2 - h_1\right)}{V_1^2} - 1 = 0.23 \tag{5.44}$$

The Froude number was defined in Section 4.1.2:

$$Fr = \frac{V_\infty}{g d_c} \tag{5.45}$$

where V is the velocity of the flow, $g = 9.81$ m/s^2 is the acceleration due to gravity and $d_c = 0.015$ m is the diameter of a disk cavitator. The Froude number in this experiment is:

$$Fr = \frac{V_1}{g d_c} = 20.47 \tag{5.46}$$

The ventilation coefficient was defined in Section 4.1.2:

$$C_Q = \frac{\tilde{Q}}{V d_c^2} \tag{5.47}$$

where $\tilde{Q}$ is the ventilation rate of the supercavity, in m^3/s. The ventilation rate in the experiment was $Q = 25$ L/min, hence $\tilde{Q} = 4.1667 \cdot 10^{-4}$ m^3/s and the ventilation coefficient in this experiment is:

$$C_Q = \frac{\tilde{Q}}{V_1 d_c^2} = 0.2315 \tag{5.48}$$

The cavitation number can not be measured directly by the CoSCIS test bed during experiments. A separate test was necessary to determine the cavitation number of the supercavity around the CoSCIS model at the desired test condition. The cavitation number was $\sigma = 0.23$, when the test was performed at a velocity of $V = 7.851$ m/s and a ventilation rate of $Q = 25$ L/min.

5.3 Measured Lift on a Static Cavitator

5.3.1 Experiment #1

5.3.1.1 Description of Experiment

The initial experiment investigates how the lift coefficient of the cavitator changes as a function of the cavitator's angle-of-attack, at different water tunnel velocities. The procedure for this test is as follows:

1. The cavitator is moved to the desired angle-of-attack. The angle-of-attack of the cavitator is measured by taking pictures of the cavitator and measuring the angle in *ImageJ*, as described in Section 3.2.1.
2. The load-cell is tared while the water tunnel is turned off.
3. The water tunnel is started and the water tunnel velocity is set to 5.5 m/s.
4. The cavity ventilation system is turned on and the supercavity is formed. The ventilation rate is set to 25 L/min.
5. The water tunnel's flow velocity is cycled between six different test velocities in a prearranged order. At each velocity the following is done:
   (a) The water tunnel velocity is verified by measuring it with the LDV system.
   (b) The water tunnel is run for several minutes at the new velocity while load-cell data is collected.
6. The water tunnel velocity, V, is cycled between the following six velocities in order:

(a) $V = 6.6$ m/s

(b) $V = 7.7$ m/s

(c) $V = 5.9$ m/s

(d) $V = 7.0$ m/s

(e) $V = 8.0$ m/s

(f) $V = 5.5$ m/s

5.3.1.2 Results

The results of Experiment 1 are presented in Figures 5.3-5.10 which plot the estimated coefficient of lift, based on the $F_{x,sensor}$, and $M_{y,sensor}$ measurements. Figures 5.3-5.8 each plot the result from single test condition. Figure 5.9 shows the estimate of the lift coefficient based on the $F_{x,sensor}$ measurement, from all the test conditions together on a single plot. Figure 5.10 shows the estimate of the lift coefficient based on the $M_{y,sensor}$ measurement, from all the test conditions together on a single plot.

The results of experiment 1 indicate that as the angle-of-attack of the cavitator varies, the lift coefficient based on the $F_{x,sensor}$ measurement changes less than expected, see Figures 5.8 for example. In contrast, the agreement between the hydrodynamic model and the experimental results that are based on the $M_{y,sensor}$ measurement is better, see Figure 5.8 for example. The response is qualitatively the same across all the different velocities that were tested in experiment 1. The velocity, V, has no discernible effect on the lift coefficient at each angle-of-attack. The lift coefficient based on the $F_{x,sensor}$ measurement appears to fit the hydrodynamic model better at negative angles-of-attack than at positive angles-of-attack in Figures 5.3-5.8. The slope of the data appears to change at $\alpha_c = 0°$. This is could be due to the nonlinearity in the load-cell, discussed in Section 5.1.3. The nonlinearity is factored into the uncertainty in the data points. The results based on the $M_{y,sensor}$ measurement have less uncertainty because the moment on the cavitator is sufficiently large, compared to the capacity of the y_{sensor}-axis of the load-cell, to mitigate the effects of the nonlinearity, drift and hysteresis effects in the load-cell. The results based on the $M_{y,sensor}$ measurement overlap the uncertainty range around the results based on the $F_{x,sensor}$ measurement in most cases in Figures 5.3-5.8, i.e. the uncertainty in the data point based on the $F_{x,sensor}$ measurement is large enough

to reach the value of the data point based on the $M_{y,sensor}$ measurement. Hence, the agreement between the results based on the $F_{x,sensor}$ measurement, and the results based on the $M_{y,sensor}$ measurement may actually be much better (or much worse). It is impossible to determine which case holds true, without reducing the level of uncertainty in the $F_{x,sensor}$ measurement.

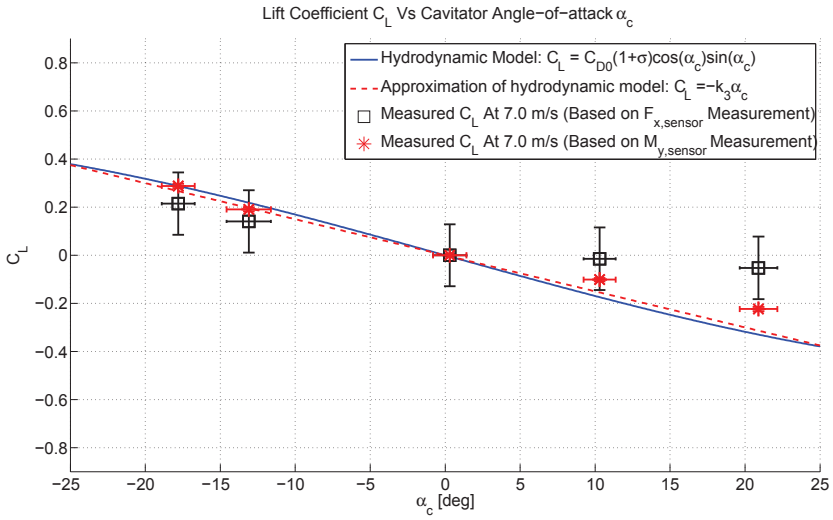

Figure 5.3: Cavitator lift coefficient as a function of cavitator angle-of-attack. This plot shows the measured lift coefficient at $V = 7.0$ m/s in experiment 1, and the hydrodynamic model described by equations 4.23 and 4.25.

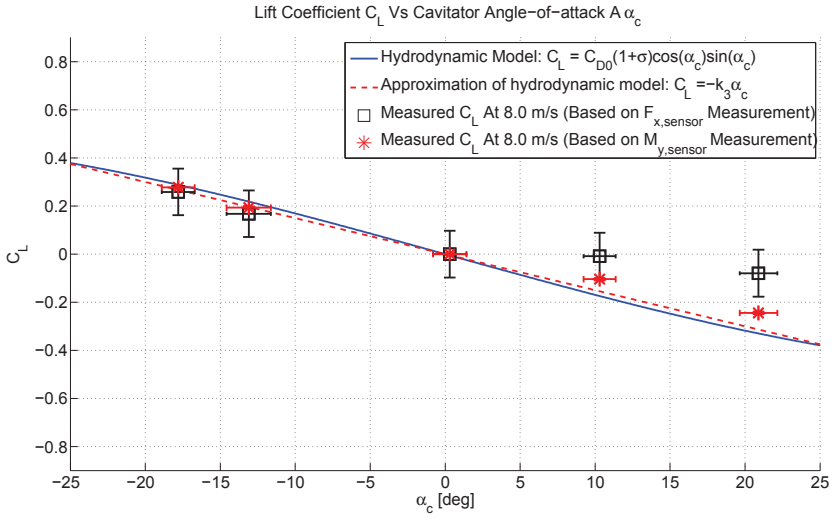

Figure 5.4: Cavitator lift coefficient as a function of cavitator angle-of-attack. This plot shows the measured lift coefficient at $V = 8.0$ m/s in experiment 1, and the hydrodynamic model described by equations 4.23 and 4.25.

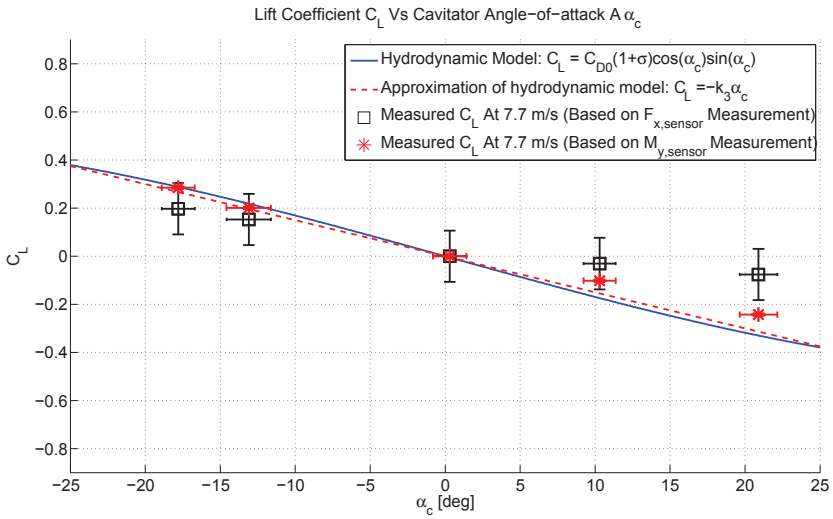

Figure 5.5: Cavitator lift coefficient as a function of cavitator angle-of-attack. This plot shows the measured lift coefficient at $V = 7.7$ m/s in experiment 1, and the hydrodynamic model described by equations 4.23 and 4.25.

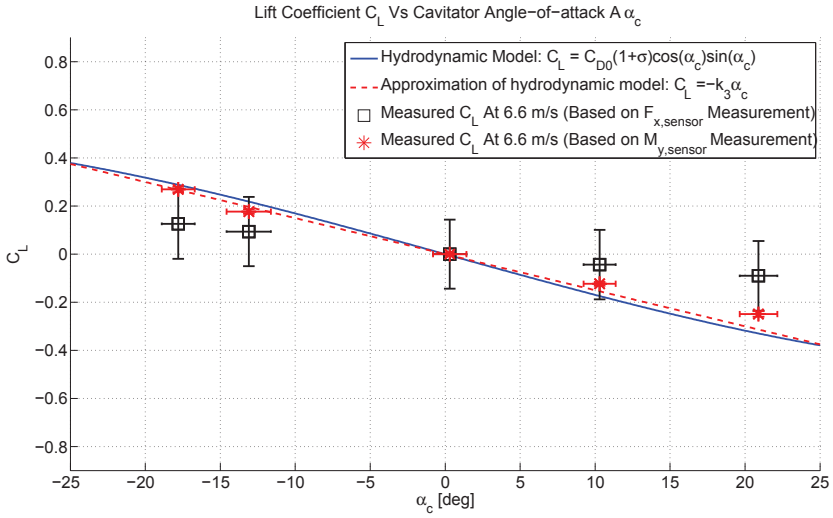

Figure 5.6: Cavitator lift coefficient as a function of cavitator angle-of-attack. This plot shows the measured lift coefficient at $V = 6.6$ m/s in experiment 1, and the hydrodynamic model described by equations 4.23 and 4.25.

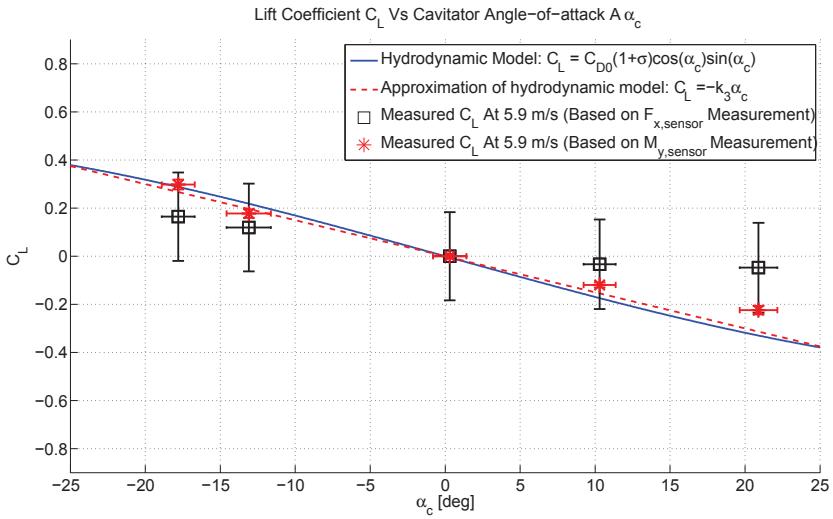

Figure 5.7: Cavitator lift coefficient as a function of cavitator angle-of-attack. This plot shows the measured lift coefficient at $V = 5.9$ m/s in experiment 1, and the hydrodynamic model described by equations 4.23 and 4.25.

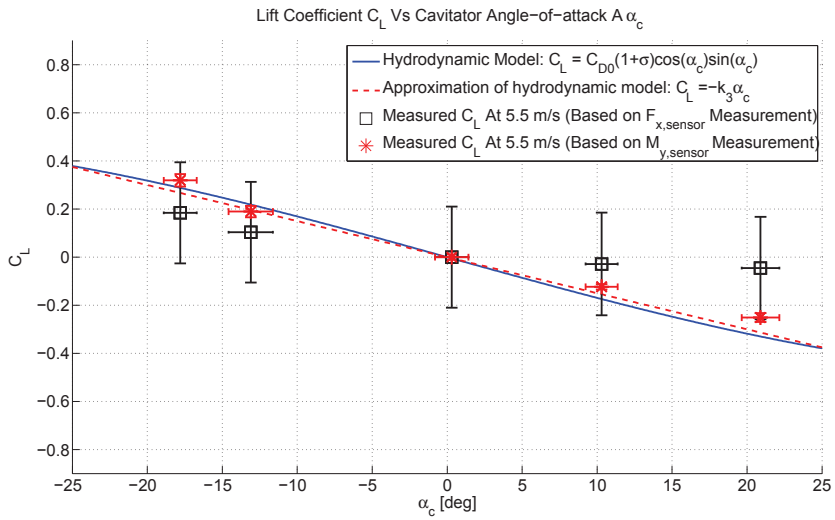

Figure 5.8: Cavitator lift coefficient as a function of cavitator angle-of-attack. This plot shows the measured lift coefficient at $V = 5.5$ m/s in experiment 1, and the hydrodynamic model described by equations 4.23 and 4.25.

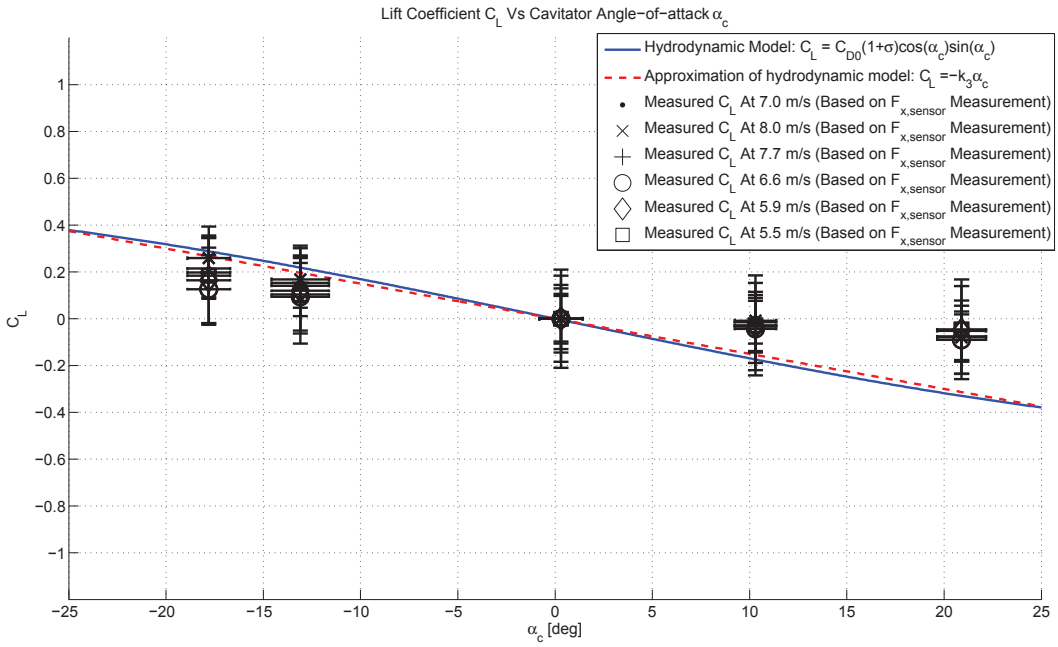

Figure 5.9: Cavitator lift coefficient as a function of cavitator angle-of-attack. This plot shows the measured lift coefficient (based on $F_{x,sensor}$ load-cell measurement) from experiment 1, and the hydrodynamic model described by equations 4.23 and 4.25.

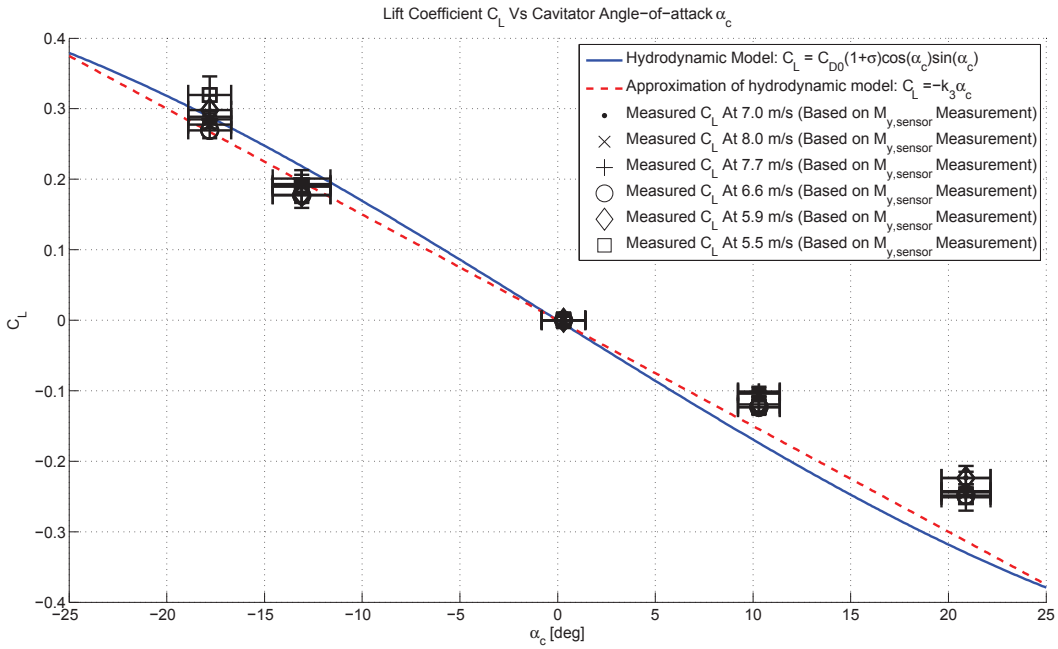

Figure 5.10: Cavitator lift coefficient as a function of cavitator angle-of-attack. This plot shows the measured lift coefficient (based on $M_{y,sensor}$ load-cell measurement), and the hydrodynamic model described by equations 4.23 and 4.25.

5.3.2 Experiment #2

5.3.2.1 Description of Experiment

Experiment 2 investigates how the lift coefficient of the cavitator changes as a function of the cavitator's angle-of-attack, at a single water tunnel flow velocity. The procedure for this test is as follows:

1. The cavitator is moved to the desired initial angle-of-attack of $\alpha_c = \delta_c = -3.7°$. Care is taken to make sure that the cable induced load on the cavitator has reached its maximum value. Hence, the cavitator is deflected to $\delta_c = -20°$ and then pulled back up to $\delta_c = -3.7°$. This ensures that the cable induced load, due to the pitching up of the cavitator, has reached its maximum value. When the cavitator is moved to different deflection angles in this experiment, it is exclusively pitched up, i.e. its direction of movement is never reversed and it is never pitched back down during the experiment. Constraining the direction of the cavitator movement ensures that the cable induced load, associated with the pitching up motion, remains at its maximum value.

2. The load-cell is tared while the water tunnel is turned off.

3. The water tunnel is started and the water tunnel velocity is set to $V = 7.6$ m/s.

4. The cavity ventilation system is turned on and the supercavity is formed. The ventilation rate is set to $Q = 25$ L/min.

5. The water tunnel velocity is verified using the Laser Doppler Velocimetry (LDV) system.

6. The cavitator is moved between four angles-of-attack, in a prearranged sequence. At each angle-of-attack, the water tunnel is run for several minutes while load-cell data is collected.

7. The cavitator angle-of-attack, α_c, is cycled between the following values in order:

   (a) $\alpha_c = -3.7°$

   (b) $\alpha_c = 3.7°$

(c) $\alpha_c = 9.1^\circ$

(d) $\alpha_c = 13.1^\circ$

In each case, the angle-of-attack of the cavitator is measured by taking pictures of the cavitator and measuring the angle in *ImageJ*, as described in Section 3.2.1. The cable induced loads should not effect the measurement of the lift in these experiments. This is because the cable induced load due to the pitching up motion of the cavitator was made to reach its maximum value before the experiment was begun (see 1.), and this value was tared out. The cavitator is restricted to move in a single direction, pitching up, as it follows the sequence of angles-of-attack. The cable induced load only changes when the cavitator direction of movement is changed. Hence, the cable induced load will be constant when the cavitator movement is restricted to a pitching up motion in this experiment.

5.3.2.2 Results

The results of Experiment 2 are presented in Figure 5.11, which plots the estimated coefficient of lift based on the $F_{x,sensor}$ and $M_{y,sensor}$ measurements. The agreement between the hydrodynamic model and the experimental results is relatively good for the lift coefficient based on the $F_{x,sensor}$ measurements, although the lift coefficient appears to be a weaker function of the angle-of-attack than expected. The agreement between the hydrodynamic model and the experimental results is excellent for the lift coefficient based on the $M_{y,sensor}$ measurements. There is very little uncertainty in this estimate of the lift coefficient and this result implies that that the hydrodynamic model is accurate.

5.3.3 Conclusion

Experiments 1 and 2 measured the lift on a static cavitator. The results of these experiments are presented together in Figure 5.12, which plot the estimated coefficient of lift based on the $F_{x,sensor}$ and $M_{y,sensor}$ measurements for both experiments. The agreement between the hydrodynamic model and the experimental results is excellent for the lift coefficient based on the $M_{y,sensor}$ measurements, while the lift coefficient based on the $F_{x,sensor}$ measurements appears to be a weaker function of the angle-of-attack than expected.

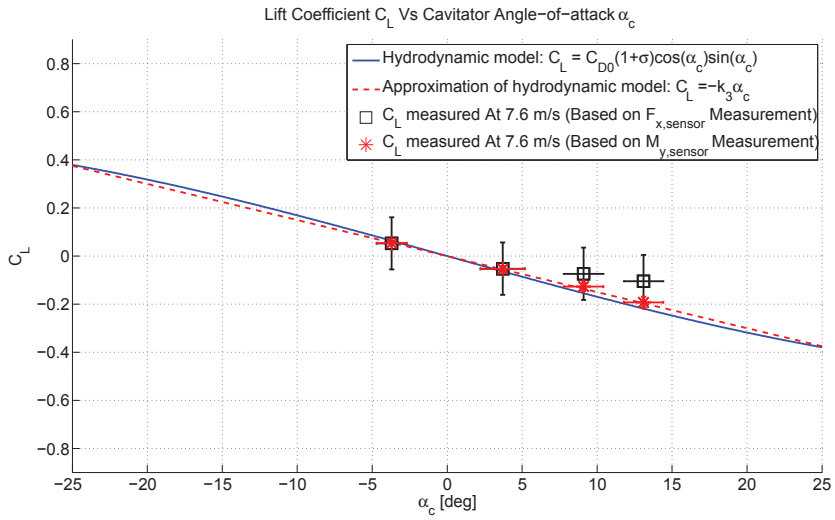

Figure 5.11: Cavitator lift coefficient as a function of cavitator angle-of-attack. This plot shows the measured lift coefficient from experiment 2, and the hydrodynamic model described by equations 4.23 and 4.25.

The lift coefficient that is computed from the $F_{x,sensor}$ measurement is a very poor match to the hydrodynamic model. The uncertainty in the $F_{x,sensor}$ measurement is far larger than in the $M_{y,sensor}$ measurements because the hydrodynamic loads being measured in the $F_{x,sensor}$ channel represent less than 1% of the Full Scale (FS) load of the load-cell's $F_{x,sensor}$ channel, while the hydrodynamic load observed in the $M_{y,sensor}$ channel is on the order of 10% of the FS load in the load-cell's $M_{y,sensor}$ channel. The accuracy of the $F_{x,sensor}$ measurement is heavily influenced by limitations in the hardware when such small loads are being measured, as was discussed in Section 5.1.3. This fact explains why the lift coefficient that is computed from the $M_{y,sensor}$ measurement matches the hydrodynamic model far better than the lift coefficient that is computed from the $F_{x,sensor}$ measurement. The poor quality of the $F_{x,sensor}$ measurement will be detrimental to the control experiments described in Chapter 6, because they are the sole measurement of the lift on the CoSCIS vehicle, that is fed back to the controllers that are being tested.

The lift coefficients that are computed from the $M_{y,sensor}$ measurement are a good fit to the hydrodynamic model. However, there is still a slight, unaccounted for, discrepancy between the hydrodynamic model and these experimentally measured lift coefficients. This discrepancy is larger than the estimated error bounds of the

lift coefficient measurements. Either, the measurement contains an error that is unaccounted for, and missing in the estimated uncertainty, or the hydrodynamic model contains a small error.

Lift and drag coefficient data for a disk cavitator has been published for various cavitation numbers [37]. A dataset from the $0.06 \leq \sigma \leq 0.15$ range is used to derive the hydrodynamic model that is used in this work. The lift coefficient of a cavitator, and a model of how it changes with angle-of-attack, was obtained from these data. This model was extrapolated to $\sigma = 0.23$ using equation 4.23, as was explained in Section 4.2.2. This hydrodynamic model may contain errors if the assumption that the results from $0.06 \leq \sigma \leq 0.15$ can be extrapolated exactly to $\sigma = 0.23$ is erroneous. The experimental results indicate that the hydrodynamic model is a good fit to the experimental data. Hence, the errors associated with this method of obtaining an expression for the coefficient of lift, at higher cavitation numbers, are very small.

The experiments described in this section have shown that the hydrodynamic model is sufficiently accurate to predict how the lift coefficient changes with angle-of-attack. There is a minor discrepancy between the hydrodynamic model and the experimental results in some cases. All the known sources of uncertainty and error were included in the uncertainty bounds on the experimental data. Hence, the source of the remaining discrepancy between the hydrodynamic model and the experimental results is unknown. The size of the error between the hydrodynamic model and the experimental results is smaller than the uncertainty and noise encountered in the real-time measurements of lift that are used in the feedback control experiments described in Chapter 6. Hence, the hydrodynamic model is deemed sufficiently accurate.

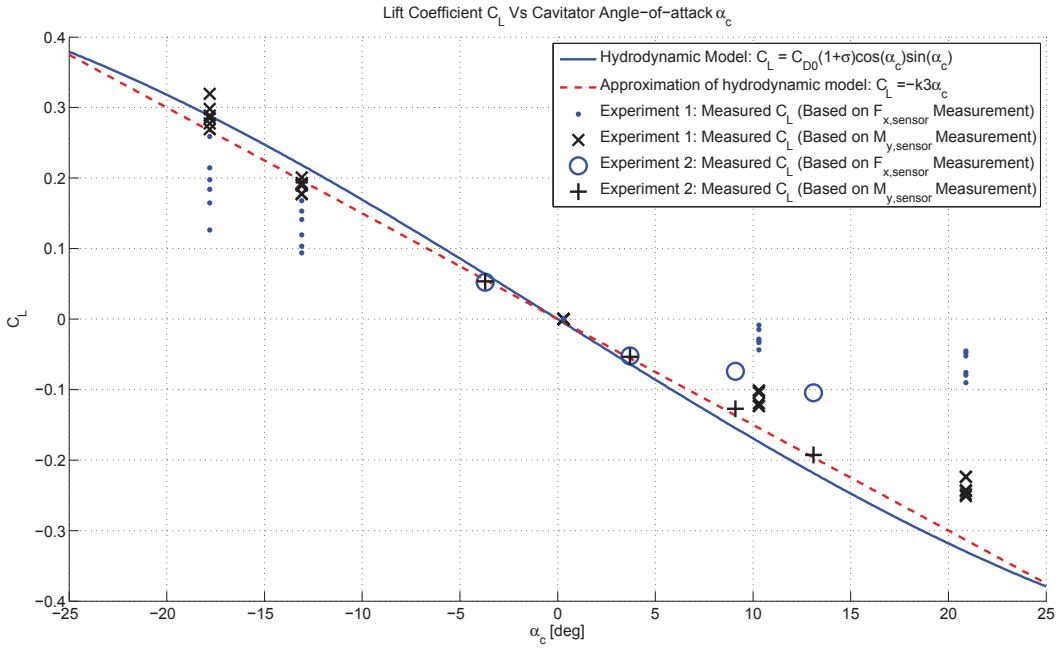

Figure 5.12: Cavitator lift coefficient as a function of cavitator angle-of-attack. This plot shows the measured lift coefficient from experiments 1 and 2, and the hydrodynamic model described by equations 4.23 and 4.25. Experimental results are shown without error bars to avoid clutter. (See Figures 5.3-5.11 for error estimates)

5.4 Measured Lift on a Moving Cavitator

5.4.1 Experimental Description

The lift generated by an oscillating cavitator is measured for several different cavitator actuation rates, at a single water tunnel flow velocity, in this experiment. The procedure for this test is as follows:

1. The cavitator is moved to the desired initial angle-of-attack of $\alpha_c = \delta_c = 0°$.
2. The water tunnel is started and the water tunnel velocity is set to $V = 7.8$ m/s.
3. The cavity ventilation system is turned on and the supercavity is formed. The ventilation rate is set to $Q = 25$ L/min.
4. The water tunnel velocity is verified using the LDV system.
5. The load-cell is tared, while the water tunnel velocity is $V = 7.8$ m/s and the cavitator angle-of-attack is $\alpha_c = 0°$.
6. The cavitator deflection, and hence its angle-of-attack α_c, is driven by a fixed magnitude sinusoidal signal of varying frequency ω_{cav}:

$$\delta_{c,sinusoid} = 14° \cdot \sin(2\pi\omega_{cav}t) - 2.7° \tag{5.49}$$

   The $-2.7°$ offset in the sinusoid is due to the backlash in the cavitator positioning system. This experiment was performed before the backlash inversion algorithm described in Section 3.2.3 was implemented on the test bed. The size of the backlash is $-2.7°$, and a portion of the δ_c command is lost in the backlash dead-zone when the backlash is not accounted for in the cavitator positioning system. This causes the $\delta_{c,sinusoid}$ sinusoid to be offset from $0°$.

   The cavitator oscillation is cycled between four different frequencies, chosen to cover the range of expected control experiment operating frequencies. The cavitator is oscillated between the following frequencies in order:

   (a) $\omega_{cav} = 0.2$ Hz

   (b) $\omega_{cav} = 1.0$ Hz

   (c) $\omega_{cav} = 3.0$ Hz

(d) $\omega_{cav} = 5.0$ Hz

Load-cell data is collected while the cavitator oscillates at each frequency. The cavitator oscillates at each frequency for a short period of time, sufficient to obtain at least 10 full periods of the sinusoid.

5.4.2 Results

The results of the experiment are shown in Figures 5.13-5.20. The lift coefficients computed from the $F_{x,sensor}$, and $M_{y,sensor}$ measurements are shown in Figures 5.13-5.16. The lift coefficient computed from the $F_{x,sensor}$ measurement and the lift coefficient computed from the corrected $F_{x,sensor}$ measurement, i.e. the $F_{x,sensor}$ measurement corrected for cable induced loads as was explained in Section 3.3, are shown in Figure 5.17-5.20.

The oscillation of the cavitator causes a cable-induced load which results in a large deviation from the lift coefficients that the hydrodynamic model predicts. This point can be illustrated by tracking how the lift coefficient changes as a function of cavitator angle-of-attack during a back and forth oscillation of the cavitator, when it is driven by a 0.2 Hz sinusoid.

Figure 5.13 shows the lift coefficient, C_L, as a function of cavitator angle-of-attack, α_c, when the cavitator is driven by a 0.2 Hz sinusoid. The trajectory of the (α_c, C_L) data in Figure 5.13 is in a clockwise direction. The load-cell was tared when the cavitator deflection was $\delta_c = \alpha_c = 0°$, and the cable induced load was entirely associated with pitching the cavitator up (i.e. the cable which pulls on the top of the cavitator, to pitch it up, was completely taut when the sensor was tared.) Starting at $\alpha_c = 0°$ the cavitator is pitched up and the lift coefficient of the cavitator decreases in value as the hydrodynamic model predicts. When the cavitator is pitched up to $\alpha_c = 11°$, it's direction of movement changes and it starts to pitch down. The cable induced load, associated with the pulling of the cable on the bottom of the cavitator, which is required to pitch down the cavitator, effects the C_L measurements as the cavitator starts to pitch down. In this case, the cable induced load appears as negative lift, and the C_L measurement becomes more negative when the angle-of-attack decreases, instead of becoming more positive like the hydrodynamic model predicts. The lift coefficient decreases in value until the cable induced load has

reached its full value, at which point the cable induced load is constant and the value of the lift coefficient increases, just as the hydrodynamic model predicts. When the cavitator is pitched down to $\alpha_c = -17°$, the direction of movement changes and the cavitator starts to be pitched back up. This change of direction causes the cable induced load associated with the pitching down motion of the cavitator, to be replaced with the cable induced load associated with the pitching up motion of the cavitator. The results is that the lift coefficient increases in value as the cavitator is pitched down, instead of decreasing in value like the hydrodynamic model predicts. The lift coefficient increases in value until the cable induced load, associated with the pitching up motion, has reached its full value. When this cable induced load has reached its full value, it becomes constant, and the lift coefficient starts to decrease in value as a function of α_c, just as the hydrodynamic model predicts. The lift coefficient is approximately zero again, when the cavitator returns to $\alpha_c = 0°$.

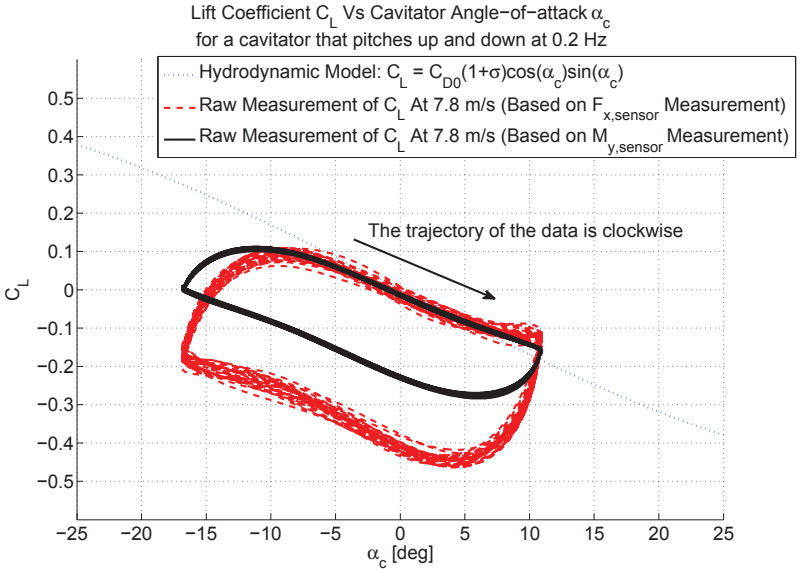

Figure 5.13: Cavitator lift coefficient as a function of cavitator angle-of-attack when the cavitator tracks the sinusoid: $\delta_{c,sinusoid} = 14° \cdot sin(2\pi\omega_{cav}t) - 2.7°$, for $\omega_{cav} = 0.2$ Hz. This plot shows the measured lift coefficient from experiment, and the hydrodynamic model described by equation 4.23.

The distortion of the lift measurement, due to the cable induced loads, is significant for slow sinusoidal cavitator oscillations, as seen in Figure 5.13. The lift coefficient measurement should lie on the dotted line indicated by the hydrodynamic model in

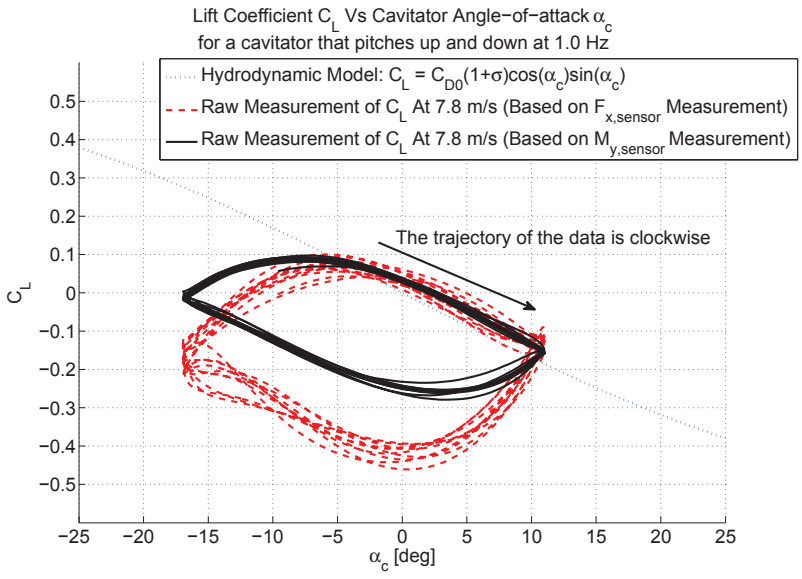

Figure 5.14: Cavitator lift coefficient as a function of cavitator angle-of-attack when the cavitator tracks the sinusoid: $\delta_{c,sinusoid} = 14^\circ \cdot sin(2\pi\omega_{cav}t) - 2.7^\circ$, for $\omega_{cav} =$ 1.0 Hz. This plot shows the measured lift coefficient from experiment, and the hydrodynamic model described by equation 4.23.

Figure 5.13, but instead follows a circular trajectory because of the cable induced loads. The lift coefficient measurement lies on the dotted line when the cavitator is pitched up, but is offset by -0.4 when the cavitator is pitched down. This effects become even more pronounced for faster cavitator deflection rates, as is observed in Figures 5.15 and 5.16. The slope of the lift coefficient vs cavitator angle-of-attack data changes when the cavitator tracks faster sinusoids. At 5.0 Hz the response of the lift coefficient data is the opposite of what the hydrodynamic model predicts.

The frequency dependent distortion of the measured cavitator lift coefficient as a function of cavitator angle-of-attack is caused by the cable induced loads, not unmodeled dependence of the lift coefficient upon the cavitator deflection rate. The results of the experiments presented here are insufficient to determine if this is the case, but later experiments [38], have determined that the lift coefficient of a cavitator does not depend on the actuation rate in any significant way, for the range of actuation rates examined in this work.

The results presented in Figures 5.13-5.16 illustrate a significant deviation from the

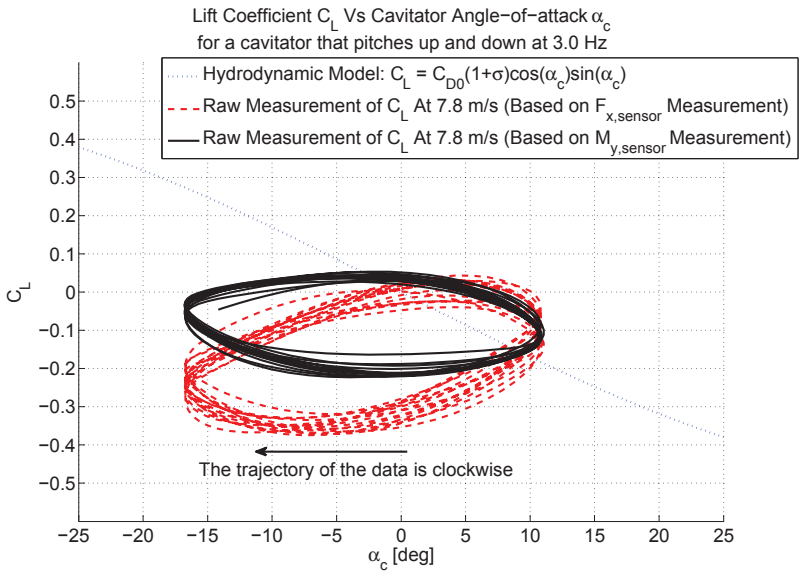

Figure 5.15: Cavitator lift coefficient as a function of cavitator angle-of-attack when the cavitator tracks the sinusoid: $\delta_{c,sinusoid} = 14° \cdot sin(2\pi\omega_{cav}t) - 2.7°$, for $\omega_{cav} = 3.0$ Hz. This plot shows the measured lift coefficient from experiment, and the hydrodynamic model described by equation 4.23.

predicted model due to the cable induced loads. A simple model of the cable induced loads was developed in Section 3.3. This model was used to develop an algorithm to mitigate the effects of the cable induced loads on the $F_{x,sensor}$ measurement. The algorithm is implemented in real-time on board the cRIO. It estimates what the cable induced load is at each time-step and subtracts it from the $F_{x,sensor}$ measurement. This algorithm was used on the experimental system during the tests described here, to obtain a corrected $F_{x,sensor}$ measurement, and consequently a corrected C_L estimate, as is shown in Figures 5.17-5.20. Figures 5.17-5.20 show the lift coefficient computed from the $F_{x,sensor}$ measurement, and the lift coefficient computed from the corrected $F_{x,sensor}$ measurement, as a function of the cavitator angle-of-attack.

Figures 5.17-5.20 illustrates that the correction algorithm reduces the influence of the cable induced loads, but due to the simple model used to represent the nonlinear cable induced loads, the correction algorithm is insufficient to completely remove the effects of the cable induced loads in practice. In practice, the cavitator actuation rate should be kept lower than 1 Hz to ensure the best fit between the lift coefficient vs cavitator angle-of-attack data and the hydrodynamic model. At higher frequencies

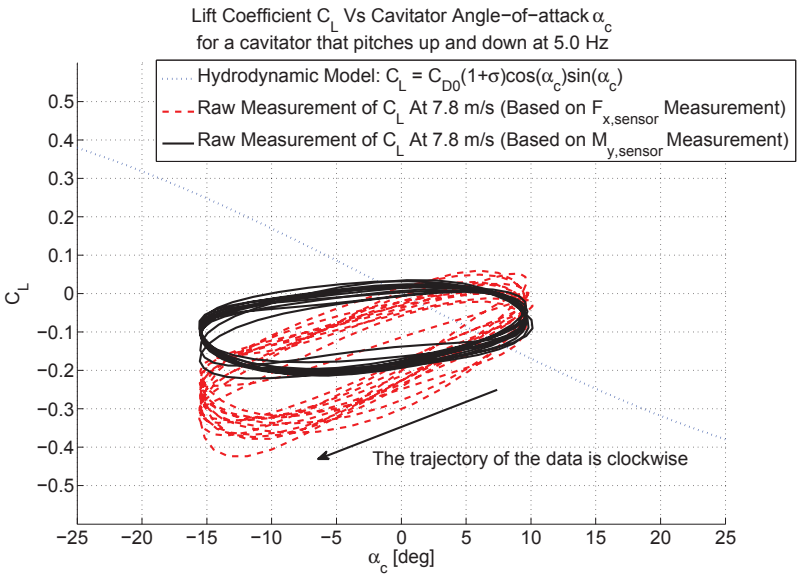

Figure 5.16: Cavitator lift coefficient as a function of cavitator angle-of-attack when the cavitator tracks the sinusoid: $\delta_{c,sinusoid} = 14^\circ \cdot sin(2\pi\omega_{cav}t) - 2.7^\circ$, for $\omega_{cav} =$ 5.0 Hz. This plot shows the measured lift coefficient from experiment, and the hydrodynamic model described by equation 4.23.

the cable induced loads have such a large effect on the response that it becomes qualitatively the opposite of what it should be. The cavity remained stable when the cavitator was oscillated at 0.2 Hz, 1 Hz, 3 Hz, and 5 Hz.

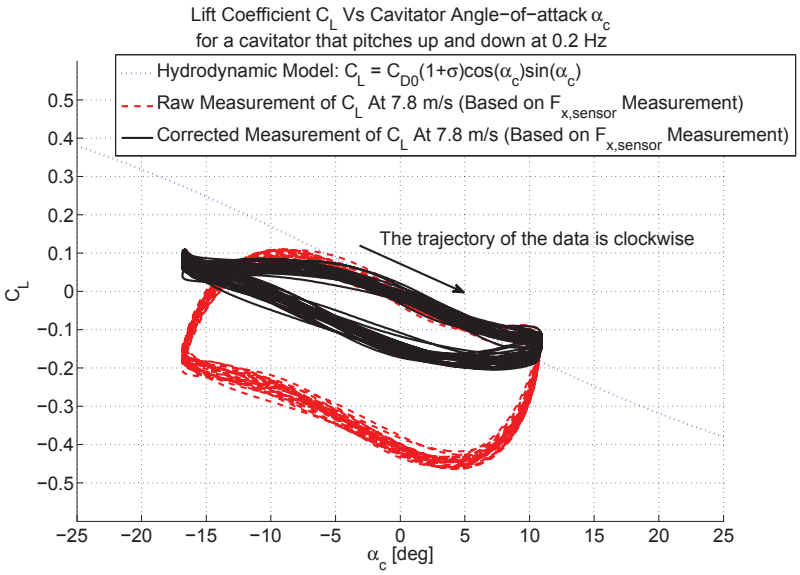

Figure 5.17: Cavitator lift coefficient as a function of cavitator angle-of-attack when the cavitator tracks the sinusoid: $\delta_{c,sinusoid} = 14° \cdot sin(2\pi\omega_{cav}t) - 2.7°$, for $\omega_{cav} =$ 0.2 Hz.. Comparison of the measured lift coefficient from experiment, and the hydrodynamic model described by equations 4.23 and 4.25.

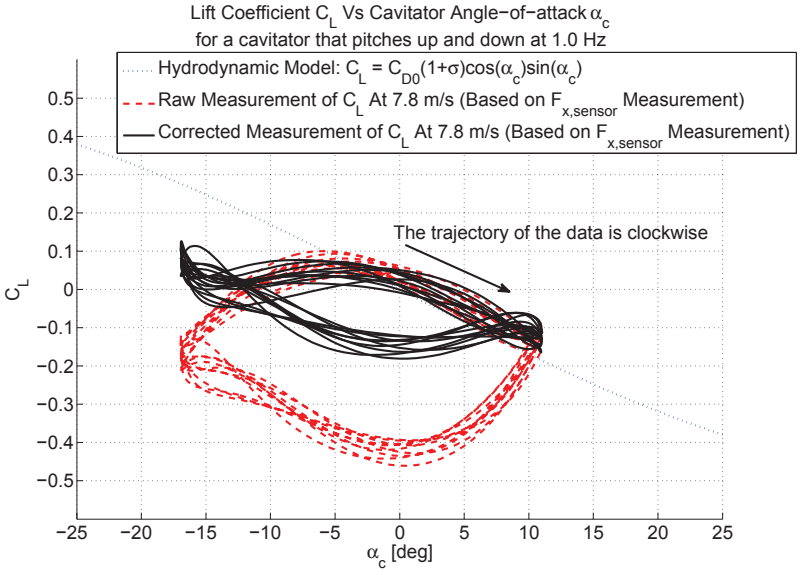

Figure 5.18: Cavitator lift coefficient as a function of cavitator angle-of-attack when the cavitator tracks the sinusoid: $\delta_{c,sinusoid} = 14° \cdot sin(2\pi\omega_{cav}t) - 2.7°$, for $\omega_{cav} =$ 1.0 Hz.. Comparison of the measured lift coefficient from experiment, and the hydrodynamic model described by equations 4.23 and 4.25.

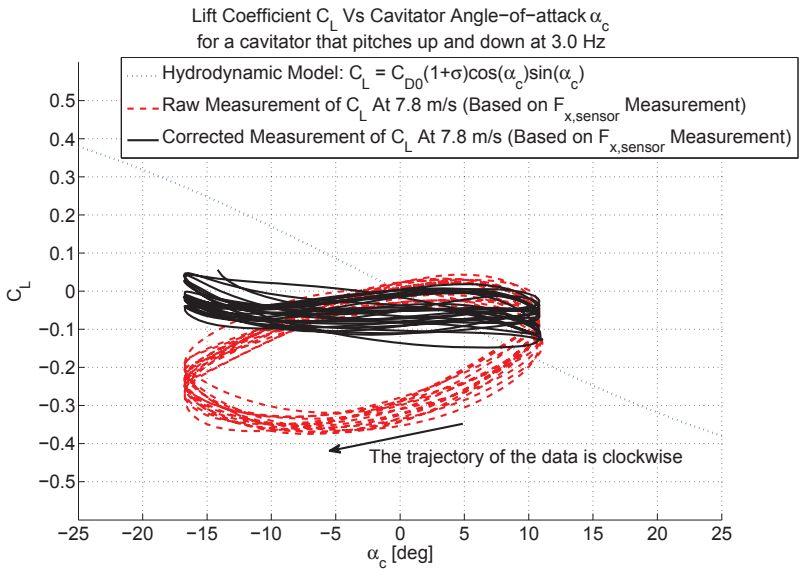

Figure 5.19: Cavitator lift coefficient as a function of cavitator angle-of-attack when the cavitator tracks the sinusoid: $\delta_{c,sinusoid} = 14° \cdot sin(2\pi\omega_{cav}t) - 2.7°$, for $\omega_{cav} =$ 3.0 Hz.. Comparison of the measured lift coefficient from experiment, and the hydrodynamic model described by equations 4.23 and 4.25.

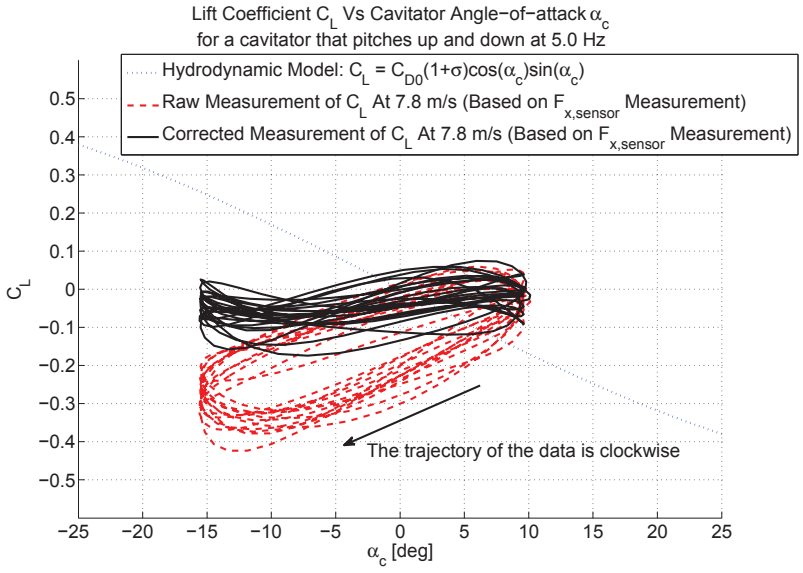

Figure 5.20: Cavitator lift coefficient as a function of cavitator angle-of-attack when the cavitator tracks the sinusoid: $\delta_{c,sinusoid} = 14° \cdot sin(2\pi\omega_{cav}t) - 2.7°$, for $\omega_{cav} =$ 5.0 Hz.. Comparison of the measured lift coefficient from experiment, and the hydrodynamic model described by equations 4.23 and 4.25.

5.5 Conclusion

The cavitation number can not be measured directly by the CoSCIS test bed during experiments. A separate test was necessary to determine the cavitation number of the supercavity around the CoSCIS model at the desired test condition. The cavitation number was $\sigma = 0.23$, when the experiment was performed at a velocity of $V =$ 7.85 m/s and a ventilation rate of $Q = 25$ L/min.

Several experiments were run to determine the validity of using the hydrodynamic model of Chapter 4 to model the lift on the test bed's cavitator in the active control experiments of Chapter 6.

The lift coefficient was measured experimentally, using two channels of the AMTI MC-1 load-cell to obtain two separate measurements the lift in the experiments. The moment about the y_{sensor}-axis of the load-cell, $M_{y,sensor}$, yielded accurate measurements of the lift, while the force in the x_{sensor}-axis of the load-cell, $F_{x,sensor}$, yielded poor quality measurements of the lift. The primary components of uncertainty in the $F_{x,sensor}$ measurements are due to the nonlinearity and hysteresis of the AMTI MC-1 load-cell. These effects are inherent to the hardware, but they have a large effect in this channel because the range of loads that are being measured in these experiments are very small compared to the full scale range of the load-cell's x_{sensor}-axis force measurement channel.

The lift coefficient of a static (i.e. constant angle-of-attack) cavitator was estimated based on $F_{x,sensor}$ and $M_{y,sensor}$ measurements. The lift coefficients which are computed from the $M_{y,sensor}$ measurements of the load-cell are a good match to the hydrodynamic model, while the lift coefficients which are based on the $F_{x,sensor}$ measurements of the load-cell are a poor fit. The $M_{y,sensor}$ measurements are more reliable and they indicate that the error in the hydrodynamic model is small.

The lift coefficient of a moving cavitator was also estimated experimentally. When the cavitator is dynamically pitched up and down, the response of the test bed was qualitatively the same as the hydrodynamic model, though heavily distorted by cable induced loads. The cable induced loads correction algorithm, presented in Section 3.3, attenuated their effects in the $F_{x,sensor}$ measurements, but proved insufficient to completely correct for the cable induced loads. The cable induced loads cause a further deterioration in the quality of the $F_{x,sensor}$ measurements.

The cable induced loads are inherent to the experimental system and effect both the $F_{x,sensor}$ and $M_{y,sensor}$ measurements. The effects of the cable induced loads are well defined. Fast cavitator actuation rates increase the mismatch between the hydrodynamic model and the measured response. Hence, the bandwidth of any controller which uses the cavitator and is implemented on the test bed, should be limited to be less than 1 Hz. At these slow actuation rates the effects of the cable induced loads are minimized. The dynamic tests determined that the supercavity is robust to fast cavitator actuation rates. The cavity remained stable when the cavitator was oscillated at 0.2 Hz, 1 Hz, 3 Hz, and 5 Hz. This is an important result from a control's standpoint, because previous work [10] had established that the fin control surface can destabilize the supercavity at fast actuation rates. The cavitator movement is not destabilizing at $\sigma = 0.23$ and $Q = 25$ L/min.

The active control experiments described in Chapter 6, employ the $F_{x,sensor}$ measurements to obtain a measurement of the lift on the CoSCIS model. The results presented in this chapter indicate that the accuracy of the $F_{x,sensor}$ measurements is poor for the range of loads that are expected in the control experiments of Chapter 6, and that the measurement is perturbed by dynamic cable induced loads which accompanies the actuation of the cavitator. No attempt is made to incorporate the nonlinear effects of the cable induced loads into the model that is used for control synthesis in Section 6.2. Hence, the cable induced loads are likely to have a detrimental effect on the control experiments of Chapter 6.

Chapter 6

Closed-Loop Feedback Control Experiments

6.1 Methodology for Experimental Validation of Control Laws

The design and implementation of the CoSCIS experimental system was reviewed in Chapters 2 and 3. The primary goal of the CoSCIS experimental system is experimental validation of control algorithms for supercavitating vehicles. There are numerous works that have studied the control of supercavitating vehicles in the literature [11, 29, 33]. However, none of the published control architectures have had their performance evaluated on a real physical system. This chapter introduces a methodology for experimental validation of control laws for supercavitating vehicles. This methodology uses the CoSCIS experimental system desccribed in Chapter 2 and 3, and the simulation model developed in Chapter 4. A candidate control architecture is developed for a simulated supercavitating vehicle and tested in simulation. Performance is evaluated experimentally in the water tunnel, under real flow conditions, and compared against its performance in simulation. The predicted performance of the control law, based on simulation results and linear analysis, is validated experimentally.

6.1.1 Concept

A mathematical model of a supercavitating vehicle moving in the longitudinal plane was developed in Chapter 4. The model was adapted to the CoSCIS experimental system, by matching its operating point to the conditions in the water tunnel test section, and matching the simulated vehicle's configuration to the CoSCIS system. This development was described in Section 4.2.2.

The CoSCIS experiment is designed to evaluate control algorithms which are synthesized for the mathematical model of the vehicle. However, the CoSCIS vehicle model is fixed in place, while the simulated vehicle moves freely in the longitudinal plane. To reconcile this difference, candidate controllers to be evaluated must be able to tightly regulate the simulated vehicle about trim points and state trajectories to match the conditions that the CoSCIS experiment can emulate. By regulating the vehicle's flight to these trajectories, the flow around the simulated vehicle and the forces it experiences in simulation will correspond to the flow around the CoSCIS vehicle model in the water tunnel and the forces it experiences. The predicted performance of a controller for a given state trajectory can then be experimentally validated in the water tunnel by comparing the simulated and experimental response for matching flight conditions.

6.1.2 Scope of the CoSCIS Experiments

To maintain parity between simulations and the results of the CoSCIS experiments, the simulated vehicle performance can only be evaluated as it flies along trajectories which produce flow conditions which match those in the water tunnel. These trajectories represent a subset of the maneuvers which a supercavitating vehicle may be able and required to perform. Evaluating the performance of a controller at these flight conditions can yield valuable insights.

The CoSCIS vehicle model is fixed in place inside the water tunnel test section, and experiences an angle-of-attack $\alpha = \alpha_{ss} + \alpha_{gust}$ which consists of the nominal angle-of-attack $\alpha_{ss} = 0^\circ$ and a component induced by flow disturbances $\alpha_{gust} \in [-8^\circ, 8^\circ]$, as explained in Section 2.2.2. This experimental flight condition is described by the two state mathematical model of Section 4.2.1. The two state model uses the states α and q, which capture the short period longitudinal dynamics of a supercavitating

vehicle. The model is developed for small angles-of-attack and constant forward velocity. The flow conditions in the CoSCIS experiment match those around the simulated vehicle when it is flying at a steady angle-of-attack α_{ss} in the presence of flow disturbances α_{gust}. The control algorithm that is to be tested must have the ability to tightly regulate the simulated vehicle's angle-of-attack about α_{ss} in order for this two-state longitudinal model to be valid, and a parity between the simulation and CoSCIS experiments to be maintained.

6.1.3 Control Effectors and Measurements

The range of control architectures which can be tested on the CoSCIS test bed are limited by the fact that only a single control effector, and a single measurement are available during experiments. The CoSCIS vehicle model is used with the fins removed, and the single control surface available to a controller is the cavitator at the front. The measurement available from the CoSCIS test bed is the lift on the cavitator, measured as the force in the x_{sensor}-axis of the load-cell, $F_{x_{sensor}}$.

The "*body*" coordinate system of the CoSCIS model, and the "*sensor*" coordinate system of the load-cell are shown in Figure 6.1. The force measured in the x_{sensor}-axis of the load-cell is equivalent to the negative of the force that would be perceived in the z_{body}-axis at the center of gravity of the CoSCIS model, were it not fixed in place.

The z_{body}-axis forces that a body experiences can be related to the body's z_{body}-axis acceleration A_z, by using Newton's Second Law $F_{z,body} = mA_z$. Hence, the $F_{x_{sensor}}$ measurement from the CoSCIS test bed can be used to determine the z_{body}-axis acceleration that the CoSCIS model would experience at any given moment, if it were not fixed in place. A control system that is implemented on board the CoSCIS test bed has access to this estimate of the z_{body}-axis acceleration. Acceleration measurements are commonly available in vehicle control systems, and it is reasonable to assume that a control system would have access to A_z in practice.

6.1.4 Control Architecture for Experimental Validation

The controllers that can be implemented on board the CoSCIS test bed will need to be designed to only have control over the vehicles cavitator deflections δ_c, and

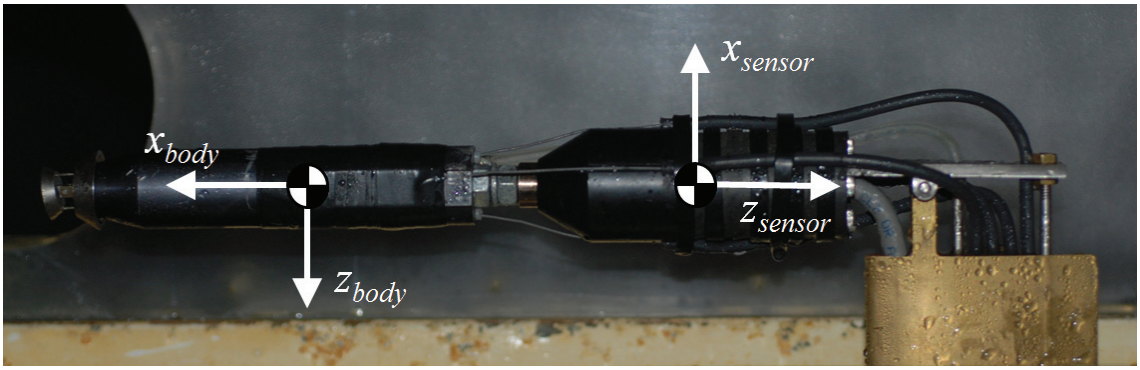

Figure 6.1: A side view of the CoSCIS test bed mounted inside the water tunnel. The figure depicts the "*body*" coordinate system of the CoSCIS model, and the "*sensor*" coordinate system of the load-cell.

access to the vehicle's z_{body}-axis acceleration measurement A_z, due to the limitations of the experiment.

A two-loop control architecture is proposed. The two-loop architecture is designed to control a simulated supercavitating vehicle that is flying along at the flight condition that the CoSCIS experiments is simulating in the water tunnel, as described in Section 6.1.2. The inner-loop control law in this architecture is designed to stabilize the vehicle and regulate flight about this chosen flight condition. The inner-loop control law has access to measurements of the simulated vehicle's angle-of-attack and pitch rate, and effects control by using a thrust vectoring system at the tail of the vehicle, as described in Section 4.1.4. An outer-loop control law is wrapped around this stabilized, thrust controlled system. The outer-loop control has access to a measurement of the simulated vehicle's z_{body}-axis acceleration A_z, and uses the cavitator to maneuver the vehicle and track z_{body}-axis acceleration reference commands $A_{z,ref}$. The outer-loop control law can be tested on the CoSCIS test bed, because it only requires access to A_z measurements and control over the cavitator. Hence, the performance of the outer-loop control law can be validated in experiment. The experiments described in Chapter 6 are focused on validating the tracking and disturbance rejection performance of the outer-loop control law.

6.1.5 Objectives of Experiments

The CoSCIS test bed is meant to validate the function and performance of control laws for a supercavitating vehicle, as described is Section 6.1.1. The test bed is capable of replicating real flight conditions about a model supercavitating vehicle inside the water tunnel test section. The candidate control laws are designed to achieve a set of performance objectives. They are initially evaluated in simulation, where it is verified that they perform as expected and satisfy their design specifications. Experimental validation of a candidate control law is the process of implementing the control law on board the CoSCIS test bed, and testing its function and performance inside the water tunnel in an experimental replica of the desired flight condition. The goal of the validation process it to illustrate that the control law performs as expected on a real system at the target flight condition. This process has the potential to yield valuable insight into the practicality of proposed control strategies, and identify deficiencies in the modeling effort.

The CoSCIS test bed has several implementation issues, as described in Chapters 2 and 3. These issues limit the scope of the experiments that can be performed on the test bed, and reduce their quality. The complete process of controller synthesis, evaluation in simulation, and validation in experiment, is performed in this chapter. The objective is to show that the CoSCIS test bed can be used to validate the performance of control algorithms, despite the implementation issues.

The significant implementation issues that will affect the experiments are the low signal to noise ratio in the force measurements, and a poorly implemented cavitator deflection mechanism which causes backlash, uncertainty in the cavitator position, and nonlinear perturbations to the force measurements. The low signal to noise ratio causes high levels of noise in the force measurement. This results in these measurements being sensitive to drift due to temperature and pressure effects. The measurements are also sensitive to nonlinearities and hysteresis in the load-cell hardware, as seen in the water tunnel tests that are presented in Chapter 5. The cable induced loads are associated with the movement of the cavitator, and perturb the load-cell measurements significantly. This effect creates an unwanted non-linear dynamic between the cavitator movement and the force measurements, which masks the hydrodynamics of interest. The effect is mitigated by algorithms on board the CoSCIS test bed, but the effect could not be removed completely.

The CoSCIS test bed is used to evaluate the basic performance of the proposed controllers in this chapter, i.e. step response, sinusoid tracking response, and sinusoid disturbance rejection. The response from the test bed during water tunnel experiments should match the simulation response for these simple maneuvers. The limitations of the test bed are expected to perturb the experimental response. The water tunnel experiments will be used to evaluate the performance of each controller, study how much the implementation issues affect the CoSCIS test bed, and determine whether the test bed can be used to validate the performance of control algorithms.

6.2 Control Design

6.2.1 Control Architecture

The simulated vehicle is controlled using a two loop topology, shown in Figure 6.2. An inner-loop controller K_{T_z} uses thrust T_z to stabilize the simulated vehicle's (α, q) dynamics and regulate flight about the flight condition which matches the flow conditions about the CoSCIS model in experiment. Once the plant is stabilized, an outer-loop controller K_{δ_c} uses the cavitator deflection δ_c to control the vehicle's z_{body}-axis acceleration A_z. The K_{δ_c} controller tracks A_z reference trajectories and maneuvers the vehicle. K_{δ_c} is the controller which will be implemented in experiment.

The supercavitating vehicle, modeled by equation 4.44, is open-loop unstable. The inner-loop thrust controller K_{T_z} is used to stabilize the vehicle. The two-loop topology is necessary, because A_z is the only available measurement, and the cavitator is the only available control surface in the CoSCIS experiment. Hence, the controller which can be implemented on the CoSCIS test bed must regulate A_z using the cavitator, and be partitioned from the control which stabilizes the (α, q) dynamics.

A model-based approach is used to synthesize controllers for the CoSCIS experiment, based on the linear model in equation 4.44. Both the inner-loop K_{T_z} controller, and the outer-loop K_{δ_c} controller are synthesized using H_∞ synthesis techniques.

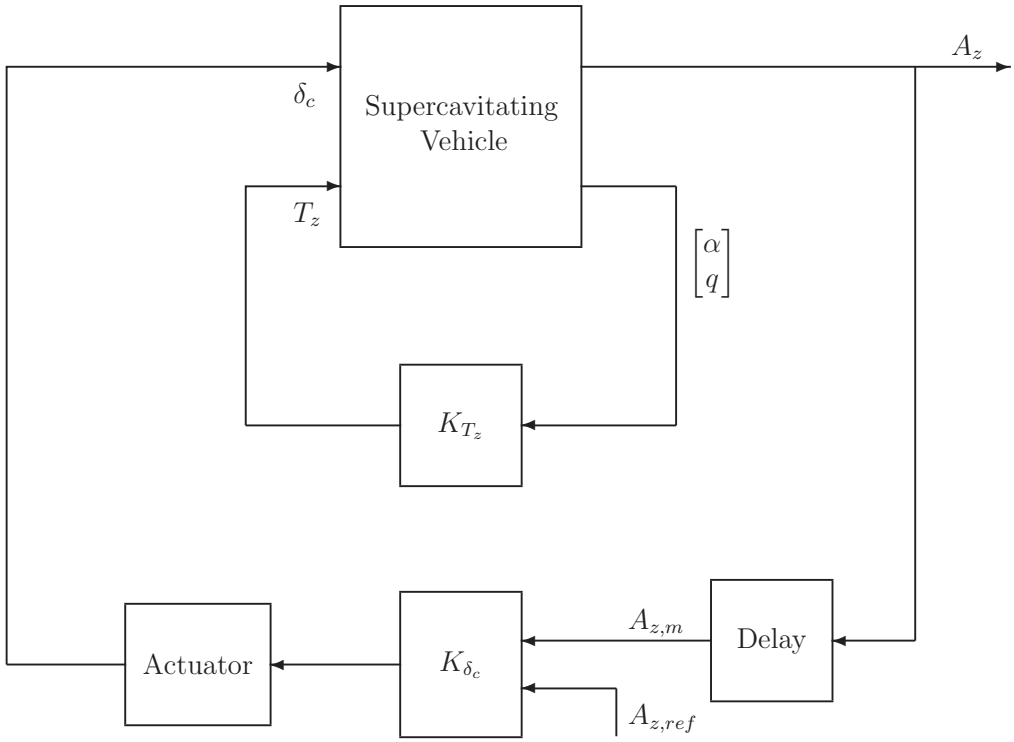

Figure 6.2: Two-loop topology for control design, denoting the inner-loop controller K_{T_z} and outer-loop controller K_{δ_c}.

6.2.2 H_∞ Control Design and Synthesis

A general feedback interconnection for H_∞ control design is shown in Figure 6.3. The signals denoted in the figure represent: u is a vector of commands output from the controller K and input to the Linear-Time Invariant (LTI) plant G, v is a vector of measurements or commands that the controller K has access to, w is a vector of exogenous inputs to the system, such as reference commands, disturbances, noise etc., and z is a vector of outputs from the system, such as regulated variables and error signals.

The H_∞ control problem concerns the synthesis of a controller K, which minimizes the H_∞ norm of the closed-loop transfer function from w to z. This transfer function is defined by the transfer function:

$$z = F_l(G, K)w \tag{6.1}$$

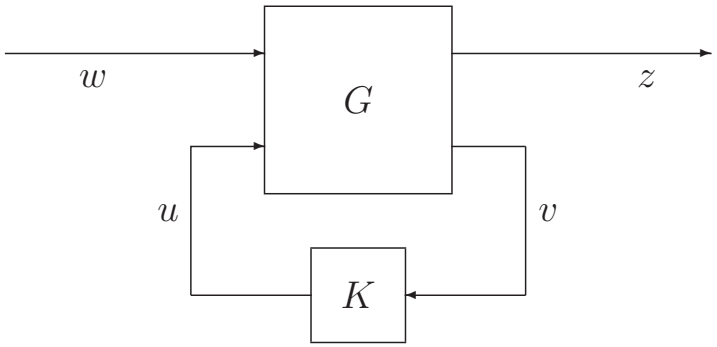

Figure 6.3: General feedback interconnection for H_∞ control design.

The H_∞ control problem is formulated as a search for a stabilizing controller K which minimizes the H_∞ norm of $F_l(G, K)$:

$$\inf_K \|F_l(G,K)\|_\infty = \inf_K \max_\omega \bar{\sigma}\left(F_l(P,K)(j\omega)\right) \tag{6.2}$$

The solution to this problem is a controller K_{opt}, which achieves an H_∞ norm

$$\|F_l(G,K_{opt})\| = \gamma_{min} \tag{6.3}$$

In practice, the H_∞ control problem can be solved using algorithms which yield sub-optimal controllers [39–41]. The algorithms generate controllers K, which are guaranteed to achieve a H_∞ norm less than some $\gamma > \gamma_{min}$, such that:

$$\|F_l(G,K)\| < \gamma \tag{6.4}$$

where γ approaches γ_{min} to within some tolerance. The H_∞ controllers presented in this work are generated by the *hinfsyn* function from the *Robust Control Toolbox* in MATLAB [41].

6.2.3 Inner-Loop H_∞ Control Design for Stability and α Regulating

The z_{body}-axis component of the thrust, denoted as T_z, is used to stabilize the super-cavitating vehicle and regulate its flight about the desired flight condition. The K_{T_z} controller is synthesized using H_∞ synthesis techniques. This controller stabilizes the simulated vehicle's (α, q) dynamics, and maintains the stability of the vehicle

when the outer-loop controller, which uses the cavitator for control, is added to the system and the vehicle is guided along trajectories. The controller K_{T_z} is only implemented in simulation. Hence, the goal in designing the controller K_{T_z}, is to stabilize the vehicle in such a manner that from the perspective of the outer-loop controller K_{δ_c}, the flight conditions in the simulation match the experimental conditions that the CoSCIS test bed is operating in, inside the water tunnel.

6.2.3.1 Problem Formulation

A dynamical model of a supercavitating vehicle was presented in Chapter 4. A linearized model was derived for the supercavitating vehicle and presented in equation 4.44. This model can be rewritten as a partitioned state-space model:

$$\begin{bmatrix} \dot{\alpha} \\ \dot{q} \end{bmatrix} = A_I \begin{bmatrix} \alpha \\ q \end{bmatrix} + B_I \begin{bmatrix} \delta_c \\ T_z \end{bmatrix} \tag{6.5}$$

$$\begin{bmatrix} A_z \\ \alpha \\ q \end{bmatrix} = \begin{bmatrix} C_{A_z} \\ I_{2\times 2} \end{bmatrix} \begin{bmatrix} \alpha \\ q \end{bmatrix} + \begin{bmatrix} D_{A_z} \\ 0_{2\times 2} \end{bmatrix} \begin{bmatrix} \delta_c \\ T_z \end{bmatrix}$$

where

$$A_I = \begin{bmatrix} -0.794 & 1.008 \\ 367 & -3.523 \end{bmatrix}, \quad B_I = \begin{bmatrix} 6.448 & 1.297 \\ -2981 & 485.7 \end{bmatrix} \tag{6.6}$$

$$C_{A_z} = \begin{bmatrix} -6.352 & 0.06097 \end{bmatrix} \quad D_{A_z} = \begin{bmatrix} 51.59 & 10.38 \end{bmatrix}$$

and α, and δ_c are in rad, q is in rad/s, A_z is in m/s^2, and T_z is in N.

The state-space model of the open-loop supercavitating vehicle linearized plant is defined as G_{OL}:

$$G_{OL} \triangleq \left[\begin{array}{c|c} A_I & B_I \\ \hline C_{A_z} & D_{A_z} \\ I_{2\times 2} & 0_{2\times 2} \end{array}\right] \tag{6.7}$$

The A_z output is not required for the synthesis of the inner-loop control law, and the state-space model that is used in the synthesis of K_{T_z} is the plant G_I:

$$G_I \triangleq \left[\begin{array}{c|c} A_I & B_I \\ \hline I_{2\times 2} & 0_{2\times 2} \end{array}\right] \tag{6.8}$$

The open-loop linearized system, described by G_{OL} and G_I, is unstable and has an unstable pole at 17.12 rad/s = 2.72 Hz. The frequency response of the supercavitating vehicle linearized plant was described in Section 4.2.4. The Bode plots of the α and q frequency response to T_z and δ_c inputs are shown in Figures 6.4 and 6.5, respectively. The δ_c input is a disturbance from the perspective of the inner-loop control law which must regulate the angle-of-attack when the outer-loop controller uses the cavitator to maneuver the vehicle. The open-loop frequency response due to δ_c inputs, shown in Figure 6.5, indicates how the system responds to unit δ_c sinusoid disturbances at different frequencies. The K_{T_z} control law must compensate for the effects of these δ_c disturbances when it regulates the vehicle's angle-of-attack.

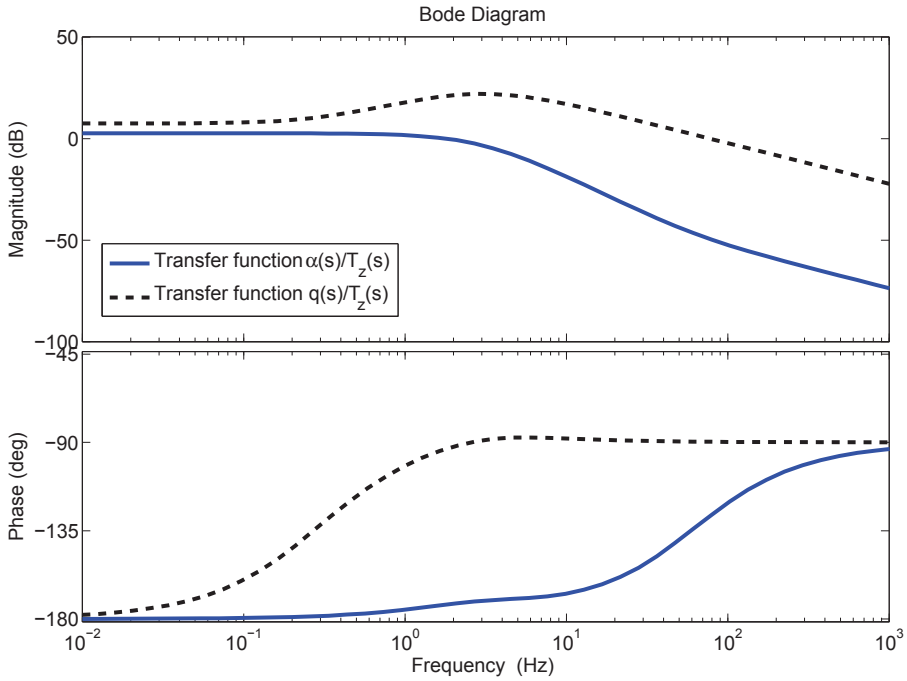

Figure 6.4: Bode Plot of $G_I(s)$: Thrust input T_z to α and q.

The system interconnection for the signal based H_∞ control synthesis of the controller K_{T_z} is shown in Figure 6.6. The K_{T_z} controller must stabilize the vehicle, and maintain tight tracking of α in the presence of both flow disturbances α_{gust}, and the action of an outer loop controller which uses the cavitator δ_c to maneuver the vehicle. A signal based approach to H_∞ control allows multiple design objectives to be accounted for simultaneously in the control synthesis. Hence, the expected

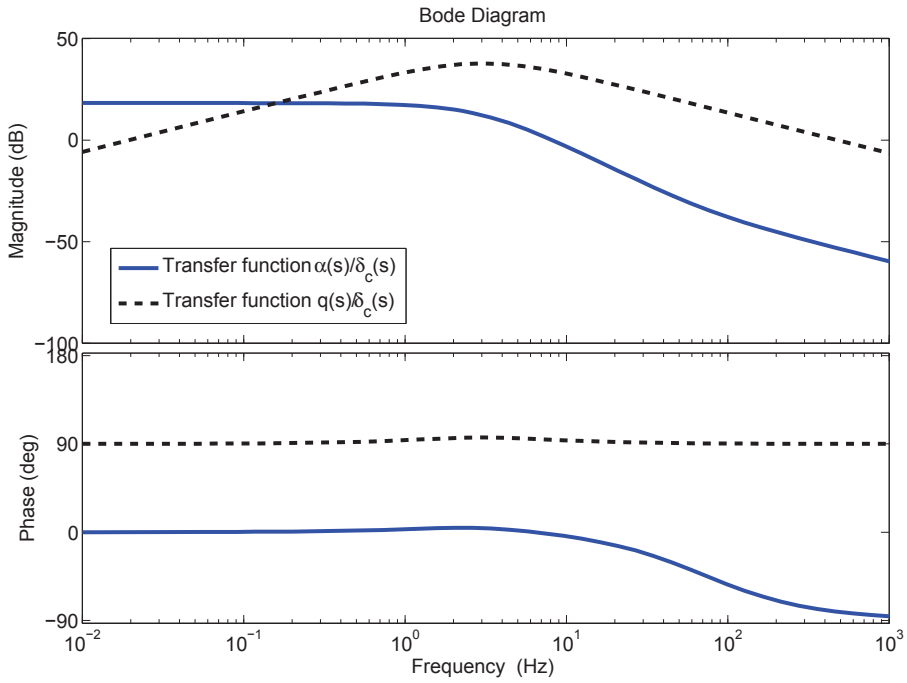

Figure 6.5: Bode Plot of $G_I(s)$: Cavitator input δ_c to α and q. The δ_c input is a disturbance from the perspective the inner-loop control law.

disturbances due to δ_c and α_{gust} can be modeled explicitly and included in the design along with a specification of the desired α tracking performance. The weights shown in Figure 6.6, are defined in the following sections, along with a description of their purpose.

6.2.3.2 Performance Weight

A pair of weighting functions penalize the magnitude of the vehicle's angle-of-attack and pitch rate. The performance weight $W_{\alpha,perf}$ penalizes the amplitude of the perturbed α output, as shown in Figure 6.6. Excellent regulation of angle-of-attack is desired in the 0 - 2 Hz frequency range, since flow disturbances and maneuvers are expected in that frequency range. The $W_{\alpha,perf}$ weighting function is defined as:

$$W_{\alpha,perf} = \frac{1}{1^\circ \left(\frac{\pi}{180}\right)} \frac{2 \cdot 2\pi}{s + 2 \cdot 2\pi} \tag{6.9}$$

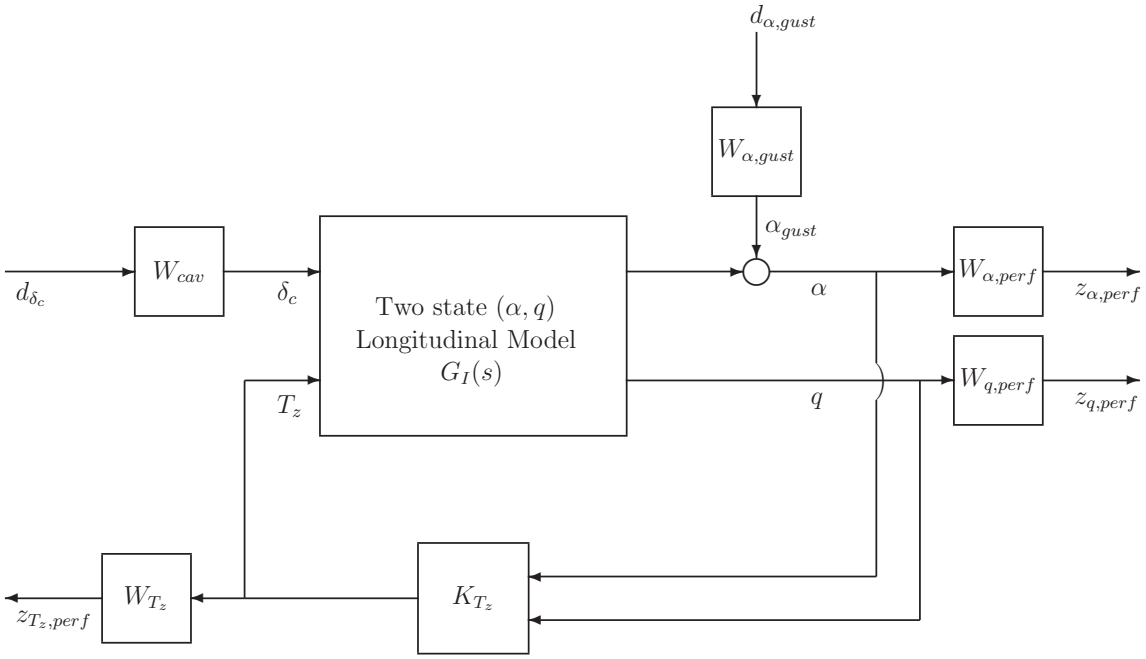

Figure 6.6: Diagram of the weighted interconnection used for the signal based H_∞ control synthesis of the K_{T_z} controller.

This weighting function is used to limit the magnitude of the angle-of-attack to be less than $\pm 1^o$ up to 2 Hz.

The performance weight $W_{q,perf}$ penalizes the pitch rate of the vehicle. The $W_{q,perf}$ weight is used to limit the size of transients in the system response. The $W_{q,perf}$ weight is defined as:

$$W_{q,perf} = \frac{1}{30} \cdot \frac{s}{s + 1.5 \cdot 2\pi} \cdot \frac{2.5 \cdot 2\pi}{s + 2.5 \cdot 2\pi} \tag{6.10}$$

$W_{q,perf}$ is a combination of a washout filter and a first order system. The weight penalizes the magnitude of q between 1 - 4 Hz to be less than 60 rad/s.

6.2.3.3 Disturbance Model for Flow Disturbances α_{gust}

Flow disturbances are represented by α_{gust}, and the weight $W_{\alpha,gust}$ in Figure 6.6. The K_{T_z} controller must tightly regulate the vehicle angle-of-attack in the presence of flow disturbances. Hence, the effects of flow disturbances α_{gust} are modeled as $\pm 10^\circ$ variations in the angle-of-attack, up to 2 Hz, and the weight $W_{\alpha,gust}$ is defined

as:

$$W_{\alpha,gust} = 10^\circ \left(\frac{\pi}{180^\circ}\right) \frac{2 \cdot 2\pi}{s + 2 \cdot 2\pi} \tag{6.11}$$

The $W_{\alpha,gust}$ models the magnitude of α_{gust} disturbances as being $\pm 10^\circ$ up to 2 Hz.

6.2.3.4 Cavitator Disturbance Model

The inner-loop controller must contend with disturbances due to the maneuvering of the outer-loop controller. The weight W_{cav} models the effects of cavitator deflections that are made as the outer-loop controller maneuvers the vehicle. The W_{cav} weight is included in the synthesis to make the α regulation of the inner-loop controller robust to the outer-loop controllers maneuvering. The cavitator actuator is modeled as a first order system with a pole at 10 Hz. The W_{cav} weight is defined like the actuator model and models aggressive maneuvering by the outer-loop controller as $\pm 15^\circ$ cavitator deflections up to 10 Hz:

$$W_{cav} = 15^\circ \left(\frac{\pi}{180^\circ}\right) \frac{10 \cdot 2\pi}{s + 10 \cdot 2\pi} \tag{6.12}$$

6.2.3.5 Thrust Magnitude Weight

A weight W_{T_z} is placed on the output of the K_{T_z} controller and limits the magnitude of its output to be less than 50 N:

$$W_{T_z} = \frac{1}{50} \tag{6.13}$$

The W_{T_z} weight is included in the synthesis to limit the gain of the K_{T_z} controller.

6.2.3.6 Synthesis and Result

The inner-loop thrust controller K_{T_z} is synthesized using the *hinfsyn* command in MATLAB, and a design is obtained that achieves a $\gamma = 0.09$. The K_{T_z} controller has seven states, and a numerical state-space representation can be found in the Appendix. The thrust controller K_{T_z} stabilizes the vehicle and regulates the angle-of-attack about the desired trim condition. A diagram of the closed-loop system is shown in Figure 6.7. This diagram shows the *thrust stabilized system*, i.e. the vehicle model in feedback with the inner-loop control law K_{T_z}. This figure shows

how the α_{gust} and δ_c disturbances are modeled when the frequency response of the closed-loop thrust stabilized system is analyzed, and is used in the discussion that follows.

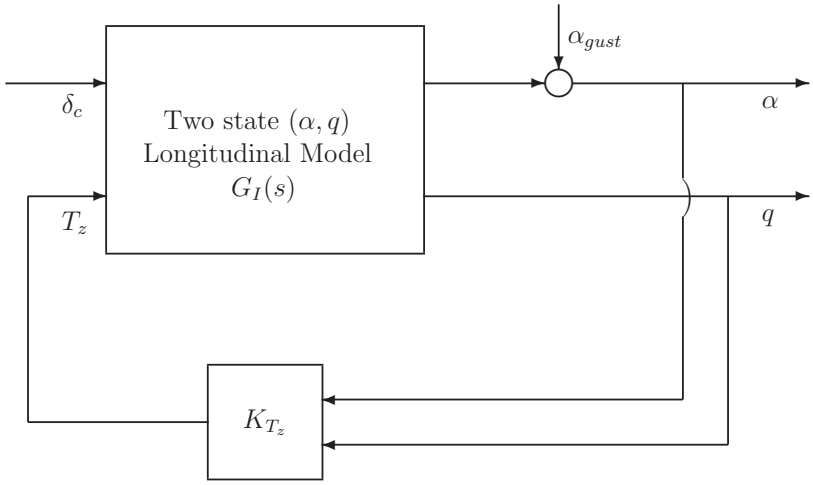

Figure 6.7: Diagram of the closed-loop system representing a supercavitating vehicle stabilized by the thrust controller K_{T_z}.

The singular values of the closed-loop system input and output sensitivity functions, and complementary sensitivity functions are shown in Figure 6.8. The peaks of the input sensitivity and complementary sensitive functions are both less than 1.8 (5 dB), indicating good robustness to input multiplicative uncertainty. The singular values of the output sensitivity and complimentary sensitivity functions have a peak of approximately 290 (50 dB). The peak indicates very poor robustness to output multiplicative uncertainty. This result is acceptable because the K_{T_z} controller is only required to perform in simulations, and won't be used in experiments. The inner-loop control law is designed to tightly regulate α in simulations, in order to mimic the flight conditions in the water tunnel. It acts on the simulated plant, which can be assumed to be a completely known quantity, with perfect state-feedback for simulation purposes. Hence, the poor robustness of the inner-loop is acceptable. This is not the case for the K_{δ_c} outer-loop controller which is designed in the next section. It is designed for the mathematical model of the vehicle, but is required to perform in both simulation and experiment. Hence, K_{δ_c} must have the ability to tolerate the mismatch between the mathematical model of the vehicle and the experimental system.

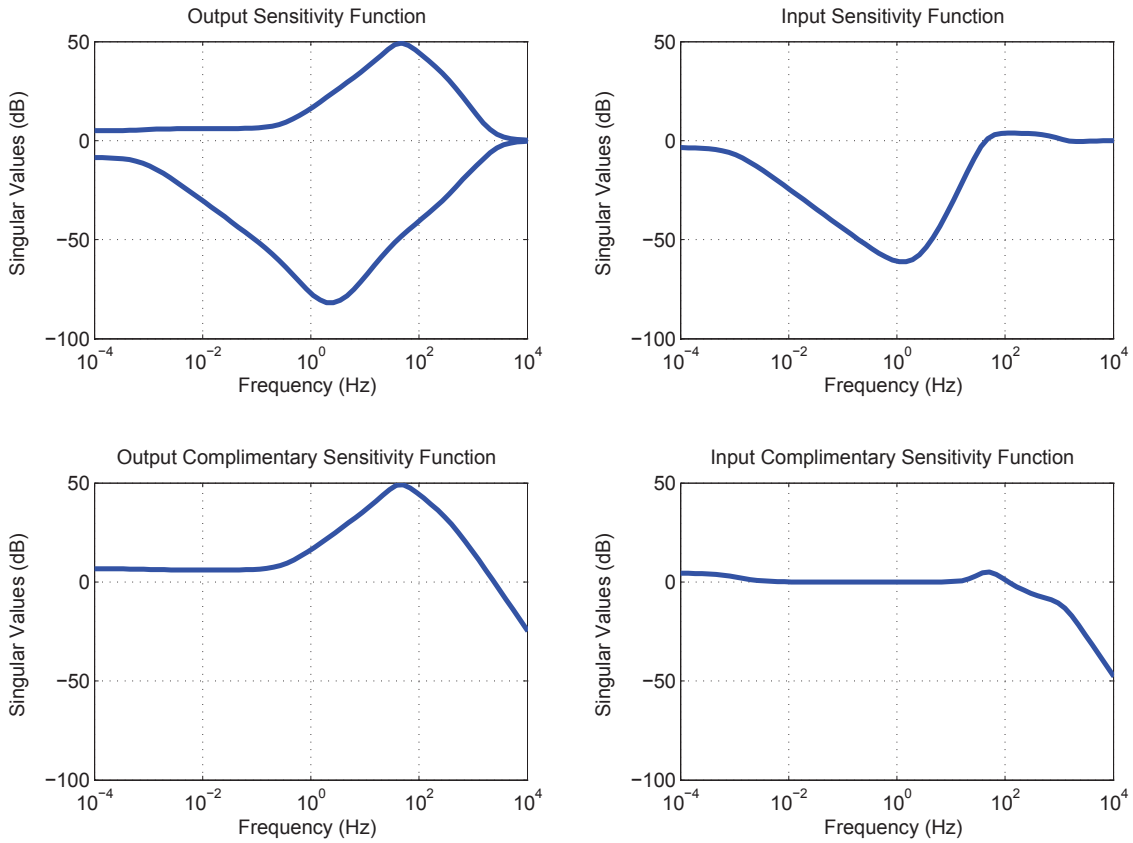

Figure 6.8: Frequency response of the closed-loop output sensitivity function, output complimentary sensitivity function, input sensitivity function and input complimentary sensitivity function (input/output refers to the T_z input and the $[\alpha, q]$ outputs of the $G_I(s)$ plant in the positive feedback closed-loop system shown in Figure 6.7).

A Bode magnitude plot of the α and q response of the closed-loop thrust stabilized system is shown in Figure 6.9 for δ_c and α_{gust} disturbances. The Bode magnitude plot of the closed-loop $\frac{\alpha(s)}{\alpha_{gust}(s)}$ transfer function in Figure 6.9, shows that the K_{T_z} controller is excellent at rejecting flow disturbances α_{gust} in the 0 - 2 Hz frequency range specified by the $W_{\alpha,perf}$ performance weight. A flow disturbance α_{gust} will have negligible effects on the angle-of-attack in this frequency range, and its effects are attenuated by at least two orders of magnitude up to 2 Hz. This performance satisfies the design requirement of regulating the angle-of-attack to have less than 1° error when the vehicle experiences flow disturbances $\alpha_{gust} = \pm 10^\circ$ at frequencies

up to 2 Hz.

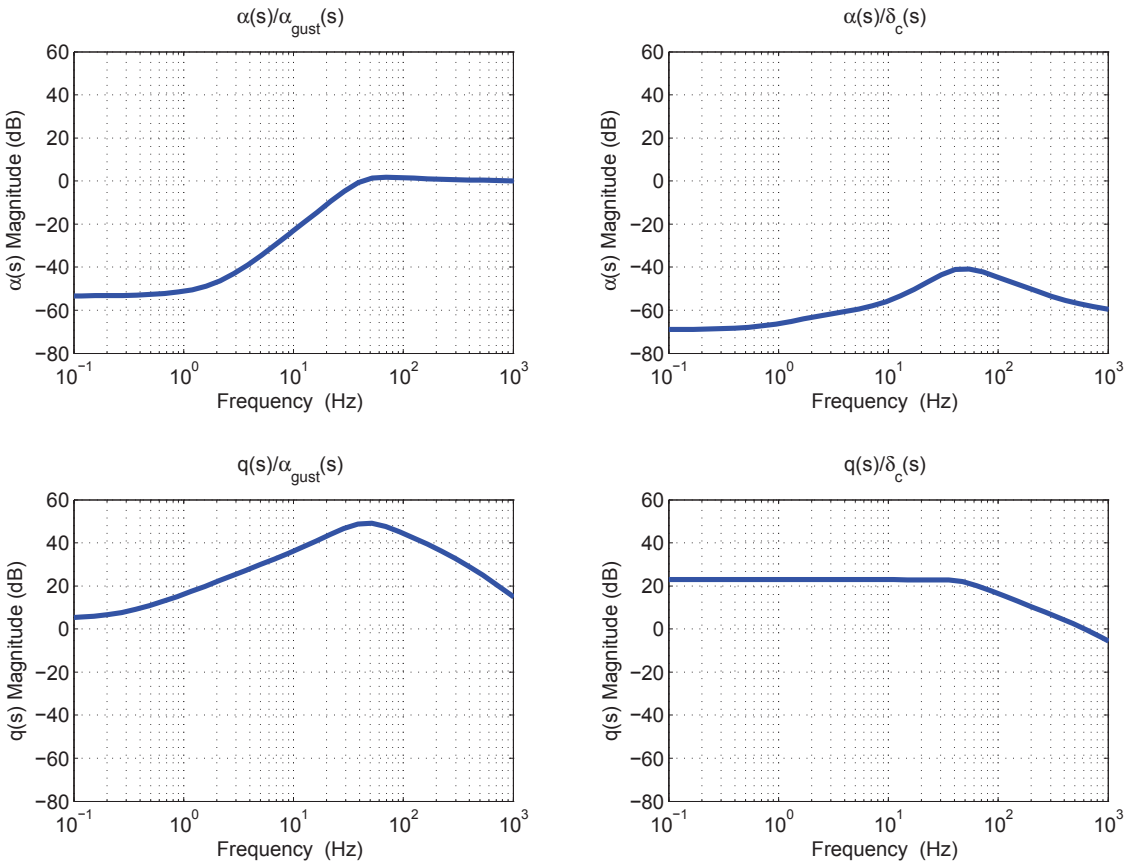

Figure 6.9: Frequency response of the closed-loop system shown in Figure 6.7. The closed-loop system represents the supercavitating vehicle stabilized by the thrust controller K_{T_z}. The effect of flow disturbances and cavitator deflections is shown.

The Bode magnitude plot of the closed-loop $\frac{q(s)}{\alpha_{gust}(s)}$ transfer function in Figure 6.9, shows that α_{gust} flow disturbances have a significant effect on the pitch rate of the vehicle. The pitch rate is affected by flow disturbances because the K_{T_z} controller is regulating the angle-of-attack, and maneuvering the vehicle so that it is aligned with the oncoming flow. When the flow is disturbed, the K_{T_z} controller pitches the vehicle up or down to face the oncoming flow. These maneuvers cause a non-zero pitch rate, and require faster pitching motions (larger pitch rates) when the gusts are oscillating at a higher frequency. Hence, the magnitude of the $\frac{q(s)}{\alpha_{gust}(s)}$ transfer function grows with frequency up to 49 Hz, where it starts to roll off as the K_{T_z}

controller becomes less effective at maneuvering the vehicle. The K_{T_z} controller has a high bandwidth because it is tasked with replicating the effects of the strut that is holding the CoSCIS model in place in experiments. The high variability in the pitch rate is satisfactory, because the K_{T_z} controller is not designed to regulate or control the pitch rate of the vehicle. Note that the pitch rate can change the angle-of-attack of the cavitator, see equation 4.7. This is an effect that can not be replicated on the CoSCIS test bed. The CoSCIS model is fixed in place in the water tunnel experiments, and can not pitch up or down. Hence, it is not capable of replicating the pitching motion of the simulated vehicle. For a short vehicle, like the one modeled in Chapter 4, the effects of the pitch rate upon angle-of-attack of the cavitator, and consequently the forces on the cavitator, are minimal. Nonetheless, the dynamics associated with the pitching motion are missing from the experiments, and this fact will contribute to the difference between simulation and experiment.

The Bode magnitude plot of the closed-loop $\frac{\alpha(s)}{\delta_c(s)}$ transfer function in Figure 6.9, shows that cavitator deflections have a negligible effect on the angle-of-attack of the stabilized vehicle. The $\frac{q(s)}{\delta_c(s)}$ transfer function in Figure 6.9, shows that the cavitator has a large impact on the pitch rate of the vehicle in the frequency range of interest. These results are satisfactory, because the K_{T_z} controller is not designed to regulate or control the pitch rate of the vehicle, it is only meant to stabilize the vehicle and regulate the angle-of-attack about trim. The outer-loop controller K_{δ_c} would have trouble maneuvering the vehicle if the K_{T_z} controller were to strongly attenuate the effects of the cavitator deflection on the pitch rate.

The frequency response of the K_{T_z} controller indicates that it satisfies the design specifications that were used. This controller is used to stabilize the supercavitating vehicle and regulate angle-of-attack about trim. A pair of K_{δ_c} outer-loop controllers are designed in Section 6.2.4. These controllers are designed for the thrust stabilized system, which is defined as the stable closed-loop system which has the K_{T_z} controller in feedback with the open-loop linearized plant of the supercavitating vehicle.

6.2.4 Outer-Loop Control Design: H_∞ Design for A_z Tracking

The inner-loop controller K_{T_z}, which was designed in Section 6.2.3, uses the thrust to stabilize the vehicle and tightly regulate its angle-of-attack. This section describes

the design and synthesis of an outer-loop controller K_{δ_c} which will be added to this thrust stabilized system.

The outer-loop controller K_{δ_c} uses the cavitator to maneuver the stabilized vehicle and track a z_{body}-axis acceleration reference $A_{z,ref}$. Two different versions of the controller K_{δ_c} are synthesized using signal based H_∞ control synthesis methods. The K_{δ_c} designs vary in the selection of weights used in their synthesis. The weights specify the performance goals for each controller. Both K_{δ_c} controllers are designed to track $A_{z,ref}$ reference commands and reject z_{body}-axis acceleration disturbances $A_{z,gust}$.

The K_{δ_c} controllers are tested in simulation, and experimentally validated on the CoSCIS test bed inside the water tunnel. The purpose of the experiments is to validate that when each controller is tested in an experimental replica of the real system, it achieves the performance that it is designed for, and the simulations predict it will achieve. The description of the simulations and experiments is found in Section 6.3.

6.2.4.1 Problem Formulation

The system interconnection for the signal based H_∞ control synthesis of the K_{δ_c} controllers is shown in Figure 6.10. The objective of the K_{δ_c} controllers is to track a z_{body}-axis acceleration reference $A_{z,ref}$. During the control synthesis, a signal based H_∞ control design approach allows for direct incorporation of the desired performance specifications and design constraints imposed by the experimental platform. Weighting functions are defined to model the expected noise, time-delays, cavitator actuator deflection and rate limits, acceleration disturbances, reference commands, and desired performance specifications. The K_{δ_c} controllers are synthesized as two-degree-of-freedom controllers.

The weights used in the synthesis of K_{δ_c} are shown in Figure 6.10. A model matching approach is taken in the definition of the tracking performance specification. The difference between the vehicle's acceleration and the output of a reference system W_{ref} is penalized by the weight $W_{A_z,perf}$. Hence, the acceleration of the vehicle is made to match the output of W_{ref} in a manner specified by the weight $W_{A_z,perf}$.

The inner-loop controller, K_{T_z}, which was designed in the previous section, uses the

thrust to stabilize the vehicle and regulate its angle-of-attack. The definition of the *thrust stabilized system* will now be extended to mean the system defined by the G_{OL} plant in feedback with the K_{T_z} controller, and includes the cavitator actuator G_{act}. The input to the system is the command u_{δ_c}, being passed to the cavitator actuator $G_{cav,act}$, and the output is the vehicle's z_{body}-axis acceleration A_z. This system is shown in Figure 6.10 and is referred to as the thrust stabilized system G_T.

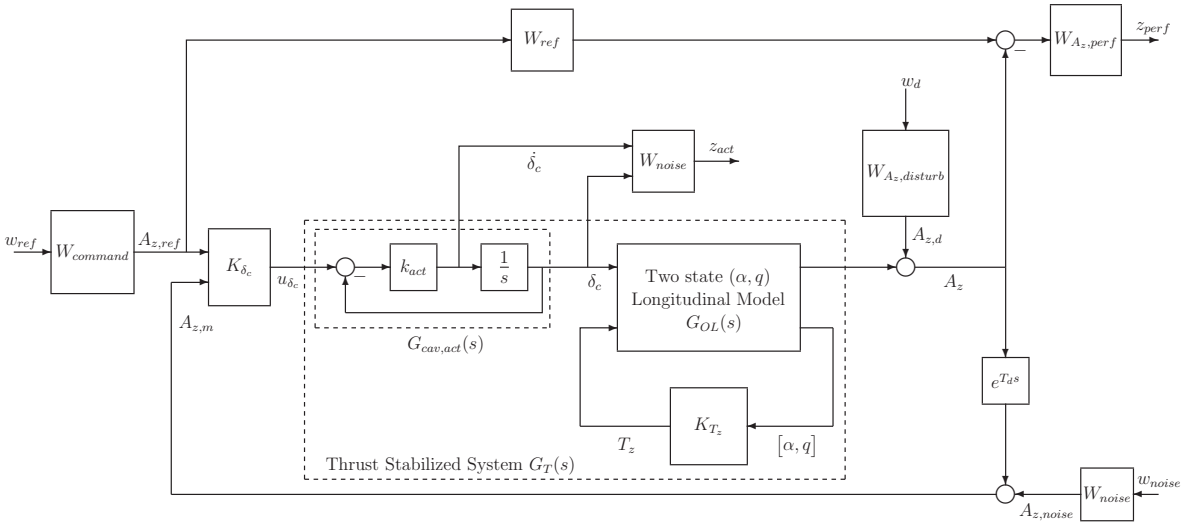

Figure 6.10: Diagram of the weighted interconnection used for the signal based H_∞ control synthesis of the $K^1_{\delta_c}$ and $K^2_{\delta_c}$ controllers.

The Bode plot of $G_T(s) = \frac{A_z(s)}{u_{\delta_c(s)}}$, shown in Figure 6.11, indicates that the cavitator has excellent control authority over A_z, especially at low frequencies. Note that according to equation 4.42, a non-zero A_z will cause a change in the angle-of-attack of the vehicle, unless the rate of change in the vehicle's angle-of-attack is matched by a pitch rate of equal size. The frequency response of the $\frac{\alpha(s)}{\delta_c(s)}$ transfer function, shown in Figure 6.9, demonstrated that the cavitator deflections will not cause a change in the angle-of-attack. Hence, $\dot{\alpha} \approx 0$ in equation 4.42, and the A_z acceleration of the vehicle corresponds to a pitching motion of the vehicle: $A_z \approx -uq$. This result aligns with the frequency response of the $\frac{q(s)}{\delta_c(s)}$ transfer function shown in Figure 6.9, which shows that the cavitator deflections have a large impact on the pitch rate of the vehicle. In practice the outer-loop controller, K_{δ_c}, uses the cavitator to control the vehicle's z_{body}-axis acceleration A_z, and the inner-loop controller, K_{T_z}, maneuvers the vehicle to minimize the vehicle's angle-of-attack. The result is that the closed-

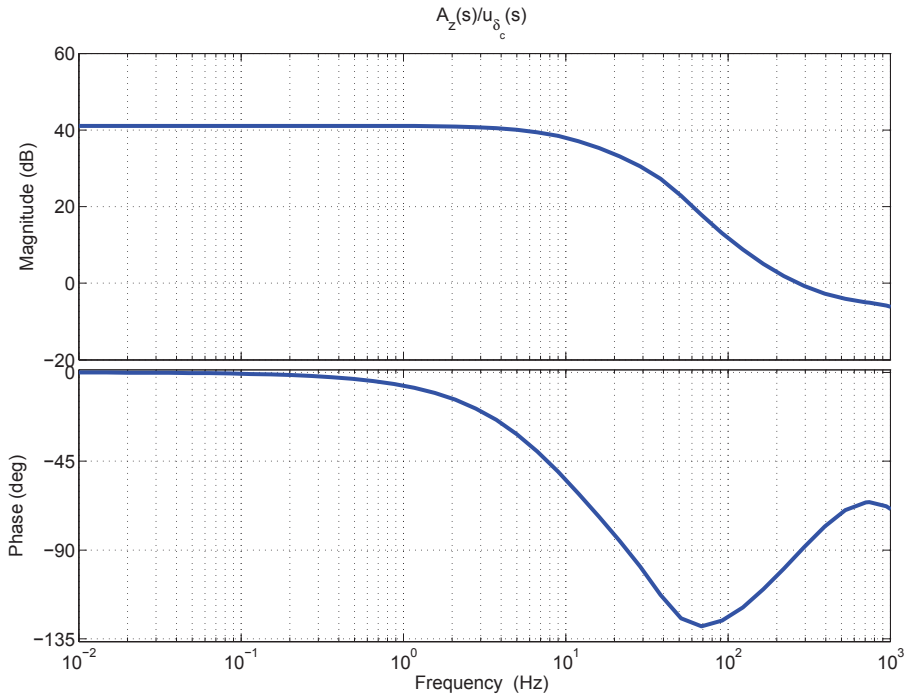

Figure 6.11: Frequency response of $G_T(s)$. The effect of cavitator deflections on the vehicle's z_{body}-axis acceleration A_z is shown.

loop system, which includes both K_{δ_c} and K_{T_z}, tracks A_z reference commands by executing turns in the pitch plane. The controlled vehicle will not accelerate in the z_{body}-axis direction while holding a constant attitude, i.e. it will not perform a skid maneuver in the pitch plane.

6.2.4.2 Performance Objectives

The primary goal of the K_{δ_c} controller design is to track $A_{z,ref}$ reference commands in simulation and experiment. The K_{δ_c} controllers are implemented on board the CoSCIS test bed and the limitations of the experimental platform, described in Chapter 3, restrict the performance goals which the control design can pursue. The $A_{z,m}$ measurement in the experiment is perturbed by noise, has a time-delay, and is subject to cable induced loads which are associated with the movement of the cavitator control surface. The noise in the $A_{z,m}$ measurement is due to the noise in the $F_{x,sensor}$ measurement on the test bed. The noise in the $F_{x,sensor}$ measurement has a standard deviation of 0.2 N which is approximately 10% of the expected range

of hydrodynamic loads ($\approx \pm 2$ N). Hence, the standard deviation of the noise in the $A_{z,m}$ measurement is approximatly 2 m/s^2. There is a time-delay in the $A_{z,m}$ measurement, and a substantial phase lag which is contributed by the filtering on board the CoSCIS test bed. The combined effect of the delay and filtering is modeled as a single measurement time-delay of $T_d = 0.04$ sec. This delay constitutes an upper bound on the achievable bandwidth of the system if good closed-loop performance is required at low frequencies [42]. As the bandwidth of the system approaches 8 Hz, performance becomes progressively worse. The bandwidth should be limited to below 3 Hz for good closed-loop performance. The cable induced loads are associated with changes in the direction of the cavitator movement, as explained in Section 3.3. Hence, a good closed-loop system tracking response will avoid overshoot and other transients, in order to minimize cable load inducing transients in the cavitator usage.

The K_{δ_c} controllers are designed as two-degree-of-freedom controllers, hence their tracking performance is decoupled from their disturbance rejection performance. The $K^1_{\delta_c}$ and $K^2_{\delta_c}$ controllers are designed to achieve different disturbance rejection characteristics, but they share the same desired tracking performance objective. The H_∞ control design is setup as a model matching problem. The target tracking response is that of a first-order system with a 0.5 Hz bandwidth. The $K^1_{\delta_c}$ controller is designed to have a low bandwidth in its disturbance rejection, while the $K^2_{\delta_c}$ controller is designed to push the bandwidth to the limit imposed by the time-delay.

6.2.4.3 $K^1_{\delta_c}$ Controller Performance Weights

The synthesis of $K^1_{\delta_c}$ and $K^2_{\delta_c}$ uses the performance weights shown in Figure 6.10. The controllers are synthesized using the same W_{ref}, W_{act}, $G_{cav,act}$, $e^{-T_d s}$ and $W_{command}$ weights, but differ in the choice of $W_{A_z,perf}$, $W_{A_z,disturb}$ and W_{noise} performance weights. Two different versions of the $W_{A_z,perf}$, $W_{A_z,disturb}$ and W_{noise} performance weights are defined. Each version of $W_{A_z,perf}$, $W_{A_z,disturb}$ and W_{noise} is identified by a superscript which denotes which controller it is used to synthesize. Hence, the $W_{A_z,perf}$, $W_{A_z,disturb}$ and W_{noise} performance weights that are used to synthesize $K^1_{\delta_c}$ are defined as $W^1_{A_z,perf}$, $W^1_{A_z,disturb}$ and $W^{1,variable}_{noise}$, respectively.

The $K^1_{\delta_c}$ controller is designed with a focus on low frequency tracking performance. This controller is expected to achieve good tracking of the $A_{z,ref}$ command, with no overshoot and a rise-time of 0.7 sec. Disturbance rejection is a secondary objective,

and is included in the design to enable the controller to reject very low frequency and steady-state disturbances. This enables the controller to reject steady-state offsets due to cable induced loads, and steady-state flow disturbances. This controller is expected to suffer sever degradation in its tracking performance when it is subjected to gusts in simulation and experiment.

The value of expected $A_{z,ref}$ reference commands is modeled with the weight $W_{command}$:

$$W_{command} = 10 \tag{6.14}$$

The $W_{command}$ weight scales the $A_{z,ref}$ reference commands to be ± 10 m/s^2, which corresponds to approximately ± 1 N of $F_{z,body}$ force for a vehicle with a mass of $m = 0.0963$ kg.

A model reference weight W_{ref}, is included in the synthesis. The W_{ref} weight defines the desired characteristics of the closed-loop system A_z tracking performance. The H_∞ control synthesis problem is set up in such a way that the tracking performance of the K_{δ_c} controller is quantified by how closely the frequency response of the closed-loop system matches the frequency response of the W_{ref} weight. The W_{ref} weight is used to shape the desired closed-loop system tracking performance bandwidth. The tracking performance bandwidth is limited to avoid the problems related to cable induced forces when the cavitator is deflected at high rates, as explained in Section 5.4. The experiments described in Section 5.4 concluded that when the cavitator is actuated at high rates the cable induced loads dominate the measured lift response. Their effect is to invert the cavitator lift vs angle-of-attack response compared to what the hydrodynamic model predicts. This is purely due to the limitations of the experimental platform and is not included in the model of the supercavitating vehicle. The cavitator actuation rates should be kept below 1 Hz to avoid this phenomenon. Hence, the W_{ref} weight is chosen to be a first-order system with a bandwidth of 0.5 Hz:

$$W_{ref} = \frac{0.5 \cdot 2\pi}{s + 0.5 \cdot 2\pi} \tag{6.15}$$

The $K^1_{\delta_c}$ controller is expected to achieve a rise-time of 0.7 sec with no overshoot in its tracking performance.

The actuator used to drive the cavitator on the CoSCIS model is included in the

synthesis and modeled as a first-order system $G_{cav,act}$, with a time constant $\frac{1}{k_{act}}$:

$$G_{cav,act} = \frac{k_{act}}{s + k_{act}};\ k_{act} = 10 \cdot 2\pi \tag{6.16}$$

The actuator is defined using k_{act} and a feedback loop, in the interconnection used for the synthesis of $K^1_{\delta_c}$ and shown in Figure 6.10. The deflection rate of the cavitator can be penalized when the actuator is modeled like this in the synthesis. The rate of the cavitator deflections is limited by the maximum rotation speed of the physical actuator. The rate and deflection limits of the CoSCIS test bed cavitator actuator are represented in the H_∞ control synthesis by the constant matrix W_{act}

$$W_{act} = \begin{bmatrix} \frac{1}{523.4} & 0 \\ 0 & \frac{1}{15^\circ\left(\frac{\pi}{180^\circ}\right)} \end{bmatrix} \tag{6.17}$$

The rate of the cavitator deflections is limited to $\pm\,523.4$ rad/s $= 83.3$ rotations/sec, while the cavitator deflections are limited to $\pm\,15^\circ$.

There is a time-delay in the CoSCIS test bed due to the data acquisition process on board the CompactRIO, as described in Section 3.1. Additional phase lag is contributed by the filtering of the real-time signal to mitigate the noise in the measurement. The effect of the time-delay and filtering is modeled as a $T_d = 0.04$ sec time-delay in the $A_{z,m}$ measurement that is being fed back to the K_{δ_c} controller. A (1,1) Padé approximation of this time-delay is included in the H_∞ control synthesis:

$$\begin{aligned} e^{-T_d s} &\approx \frac{1 - T_d s/2}{1 + T_d s/2} \\ &\approx \frac{50 - s}{50 + s} \end{aligned} \tag{6.18}$$

The $W_{A_z,disturb}$ weight models disturbances in the vehicle's z_{body}-axis acceleration A_z. It is used to define the desired disturbance rejection characteristics of the controller. The $K^1_{delta_c}$ controller is synthesize using the weight $W^1_{A_z,disturb}$, which is modeled as a first-order system:

$$W^1_{A_z,disturb} = 7.5\,\frac{0.01 \cdot 2\pi}{s + 0.01 \cdot 2\pi} \tag{6.19}$$

The $W^1_{A_z,disturb}$ weight indicates that the $K^1_{delta_c}$ controller must be able to handle

7.5 m/s^2 disturbances, entering at up to 0.01 Hz. The $W^1_{A_z,disturb}$ weight limits the disturbance rejection efforts of $K^1_{delta_c}$ to very low frequencies.

The noise in the $A_{z,m}$ measurement is accounted for in the H_∞ control synthesis. The $K^1_{\delta_c}$ controller is synthesized using a frequency dependent model of the noise. The weight $W^{1,variable}_{noise}$ is used to synthesize the $K^1_{\delta_c}$ controller. The $W^{1,variable}_{noise}$ weight is defined as:

$$W^{1,variable}_{noise} = 18\,\frac{s + 0.0404}{s + 14.55} \tag{6.20}$$

The $W^{1,variable}_{noise}$ weight represents a A_z measurement noise level of 0.05 m/s^2 at steady-state and growing from 0.1 m/s^2 at 0.01 Hz to 18 m/s^2 at 3 Hz. The high level of noise at higher frequencies limits the bandwidth of the $K^1_{\delta_c}$ controller, and forces it to roll off.

The performance weight $W_{A_z,perf}$ determines the frequency response of the closed-loop system A_z tracking error. The tracking error is defined as the difference between the output of the reference system W_{ref}, and the acceleration of the actual vehicle. The $K^1_{delta_c}$ controller is synthesized using the $W^1_{A_z,perf}$ performance weight, which is defined as:

$$W^1_{A_z,perf} = \frac{10 \cdot 2\pi}{s + 10 \cdot 2\pi} \tag{6.21}$$

The $W^1_{A_z,perf}$ weight denotes a desire for less than 1 m/s^2 tracking error up to 10 Hz. The allowable tracking error is small and the bandwidth of this weight is high. This requirement, coupled with the noise, disturbance, and reference models described by $W^{1,variable}_{noise}$, $W^1_{A_z,disturb}$ and W_{ref}, places a premium on close tracking of $A_{z,ref}$ commands at low frequencies and rejection of steady-state offsets, while limiting controller action at higher frequencies. The high bandwidth of this performance weight forces the closed-loop transfer function from measurement noise to acceleration to roll off as the level of noise increases. Hence, the tracking response should be largely unaffected by measurement noise, which should prevent unnecessary cavitator usage which can excite the cable induced loads in the experiment.

6.2.4.4 $K^2_{\delta_c}$ Controller Performance Weights

The $K^2_{\delta_c}$ is designed to achieve the same tracking performance as $K^1_{\delta_c}$, while improving its disturbance rejection characteristics. This controller is expected to achieve

good tracking of the $A_{z,ref}$ command, with no overshoot and a rise-time of 0.7 sec. The level of acceptable error in the tracking response is increased compared to controller $K^1_{\delta_c}$, to accommodate the fact that the more aggressive disturbance rejection performance is itself likely to cause an increase in offsets due to the cable induced loads. The controller is expected to maintain its good tracking performance when it is subjected to gusts in simulation and experiment.

The W_{ref}, W_{act}, $G_{cav,act}$, $e^{-T_d s}$, and $W_{command}$ weights are kept unchanged in the $K^2_{\delta_c}$, while the $W_{A_z,perf}$, $W_{A_z,disturb}$ and W_{noise} performance weights are changed to obtain different disturbance rejection characteristics. The $W_{A_z,perf}$, $W_{A_z,disturb}$ and W_{noise} performance weights that are used to synthesize $K^2_{\delta_c}$ are defined as $W^2_{A_z,perf}$, $W^2_{A_z,disturb}$ and $W^{2,constant}_{noise}$, respectively. These weights are used to formulate the desired disturbance rejection performance.

The $W_{A_z,disturb}$ weight models disturbances in the vehicle's z_{body}-axis acceleration A_z. The weight $W^2_{A_z,disturb}$ is used to synthesize controller $K^2_{\delta_c}$. It is defined as the first-order system:

$$W^2_{A_z,disturb} = 5\,\frac{2 \cdot 2\pi}{s + 2 \cdot 2\pi} \tag{6.22}$$

The $W^2_{A_z,disturb}$ weight indicates that the $K^2_{\delta_c}$ controller must be able to handle 5 m/s^2 disturbances, entering at up to 2 Hz. The $W^2_{A_z,disturb}$ weight has two orders of magnitude larger bandwidth than $W^1_{A_z,disturb}$, which was used to synthesize $K^1_{\delta_c}$. This reflects the emphasis on good disturbance rejection performance in the design of $K^2_{\delta_c}$.

The noise in the A_z measurement is included in the H_∞ control synthesis by using the W_{noise} weight. The weight $W^{2,constant}_{noise}$ is used to synthesize the $K^2_{\delta_c}$ controller. The $W^{2,constant}_{noise}$ weight is used to represent a constant 2 m/s^2 noise level in the $A_{z,m}$ measurement at all frequencies:

$$W^{constant}_{noise} = 2 \tag{6.23}$$

The performance weight $W_{A_z,perf}$ determines the frequency response of the closed-loop system A_z tracking error. The tracking error is defined as the difference between the output of the reference system W_{ref}, and the acceleration of the actual vehicle.

Performance weight $W^2_{A_z,perf}$ is used to synthesize $K^2_{\delta_c}$. It is defined as:

$$W^2_{A_z,perf} = \frac{1}{2}\,\frac{1 \cdot 2\pi}{s + 1 \cdot 2\pi} \tag{6.24}$$

The $W^2_{A_z,perf}$ weight denotes a desire for less than 2 m/s^2 tracking error up to 1 Hz. The $W^2_{A_z,perf}$ allows for larger acceptable steady-state tracking error than the $W^1_{A_z,perf}$ weight, which was used to synthesize $K^1_{\delta_c}$. The $W^2_{A_z,perf}$ weight enables the $K^2_{\delta_c}$ control design to be more tolerant of steady-state offsets due to the cable induced loads in the experiment. The bandwidth of the $W^2_{A_z,perf}$ weight is higher than that of the W_{ref} reference system, because the design emphasizes disturbance rejection in addition to tracking performance. The extra allowable tracking error, and the roll off in the $W^2_{A_z,perf}$ weight is required because the measurement noise is modeled as a 2 m/s^2 magnitude perturbation of $A_{z,m}$ and the design would be infeasible without the extra latitude in the tracking error.

6.2.4.5 Synthesis

The outer-loop H_∞ controllers $K^1_{\delta_c}$ and $K^2_{\delta_c}$ are synthesized using the *hinfsyn* command in MATLAB. The controllers are synthesized using the weighted interconnection shown in Figure 6.10. Both controllers are synthesized using the same W_{ref}, W_{act}, $G_{cav,act}$, $e^{-T_d s}$, and $W_{command}$ weights, while the $W_{A_z,perf}$, $W_{A_z,disturb}$ and W_{noise} weights are uniquely defined for each control design. The $K^1_{\delta_c}$ and $K^2_{\delta_c}$ controllers both have 14 states. The state-order of both controllers is reduced to 2 states prior to implementation on board the CoSCIS test bed, as is explained in Section 6.2.4.6.

When the full order $K^1_{\delta_c}$ and $K^2_{\delta_c}$ controllers are integrated into the weighted interconnection shown in Figure 6.10, they achieve a H_∞ norm of $\gamma = 0.72$ and $\gamma = 0.93$, respectively. The reduced order $K^1_{\delta_c}$ and $K^2_{\delta_c}$ controllers, derived in Section 6.2.4.6, achieve a H_∞ norm of $\gamma = 0.88$ and $\gamma = 0.93$, respectively. The order reduction has no effect on the H_∞ norm achieved by $K^2_{\delta_c}$, but increases the H_∞ norm achieved by $K^1_{\delta_c}$ by 0.16.

6.2.4.6 Controller Order Reduction

Both $K^1_{\delta_c}$ and $K^2_{\delta_c}$ are stable and have 14 states. The *slowfast*, *modreal* and *reduce* functions in the *Robust Control Toolbox* in MATLAB are used to reduce their order.

The *slowfast* and *modreal* functions are used to remove fast modes in each controller, then *reduce* is used remove additional modes by balanced truncation. The reduced $K^1_{\delta_c}$ and $K^2_{\delta_c}$ controllers have 2 states.

The *slowfast* and *modreal* functions are used to remove fast modes in each K_{δ_c} controller while maintaining the controller's steady-state gain. These fast modes, on the order of 30 - 4,000 Hz, are outside of the frequency range in which the controller is required to achieve the desired performance objectives.

The *slowfast* function is used to compute the slow and fast modes decompositions of each K_{δ_c} controller model [41]. This decomposition splits the state-space model representation of the controller into two, creating $K_{\delta_c,fast}$ containing the fast modes of the controller and $K_{\delta_c,slow}$ containing the slow modes:

$$K_{\delta_c} = K_{\delta_c,slow} + K_{\delta_c,fast} \tag{6.25}$$

The slow modes of the controller are retained, while the fast modes of the controller are truncated using the *modreal* function which reduces $K_{\delta_c,fast}$ to a constant matrix.

The *modreal* function computes a modal form realization of a state-space system. A modal form realization of a state-space system is one in which the state matrix (i.e. the "A" matrix) of the system is in block diagonal form, with the real and complex eigenvalues of the matrix arranged in 1x1 and 2x2 blocks, respectively, on the diagonal [41]. The *modreal* function can remove unwanted modes from the state-space system while retaining the steady-state system gain. The *modreal* function is used to remove every mode from $K_{\delta_c,fast}$, reducing it to a constant matrix which has a gain equal to the steady-state gain of the original $K_{\delta_c,fast}$ system. This reduced modal form realization of $K_{\delta_c,fast}$ is defined as $K^{constant}_{\delta_c,fast}$.

The $K^{constant}_{\delta_c,fast}$ system is added to the $K_{\delta_c,slow}$ system to define a reduced order version of each K_{δ_c} controller:

$$K_{\delta_c,slowed} = K_{delta_c,slow} + K^{constant}_{delta_c,fast} \tag{6.26}$$

$K_{\delta_c,slowed}$ is a reduced order model of K_{δ_c}, which is missing all of the fast dynamics that were in $K_{\delta_c,fast}$. This process is applied to the $K^1_{\delta_c}$ and $K^2_{\delta_c}$ controllers to obtain a reduced order version of each controller, defined as $K^1_{\delta_c,slowed}$ and $K^2_{\delta_c,slowed}$,

respectively.

The *reduce* function is used to further reduce the state order of the $K^1_{\delta_c,slowed}$ and $K^2_{\delta_c,slowed}$ controllers using balanced truncation. The *reduce* function starts by computing a balanced realization of the $K_{\delta_c,slowed}$ state-space model. A balanced realization of a system is one in which the controllability and observability Gramians of the system are identical, and each state is therefore equally controllable and observable. In this realization, each state is associated with a Hankel singular value which measures the relative energy of that state, i.e. its contribution to the input/output behavior of the system. The states with the lowest Hankel singular values contribute the least to the input/output behavior of the system [42]. Hence, it is reasonable to assume that their removal will affect the system's behavior the least. These states were removed from the balanced realization by truncation, i.e. they were eliminated from the balanced state-space model. Similar results were obtained for both controllers, as compared with the high order controllers, as seen in Figure 6.12.

In practice, multiple reduced order models of each $K_{\delta_c,slowed}$ controller are generated to ascertain how many states can be removed from the controller model using the balanced truncation approach while maintaining acceptable performance. Each of these candidate reduced order controller models is evaluated via frequency responses, and by computing the H_∞ norm that it achieves when it is placed in the weighted interconnection shown in Figure 6.10. The lowest order controller which achieves acceptable performance is desired. Both $K^1_{\delta_c,slowed}$ and $K^2_{\delta_c,slowed}$ are reduced to two states systems: $K^1_{\delta_c,red}$ and $K^2_{\delta_c,red}$, respectively. The singular values of the $K^1_{\delta_c,red}$ and $K^2_{\delta_c,red}$ controllers match the singular values of the original full order controllers at low frequencies, as seen in Figure 6.12. They achieve a H_∞ norm of $\gamma = 0.88$ and $\gamma = 0.93$, respectively, when they are integrated into the weighted interconnection shown in Figure 6.10. Hence, they achieve all of the performance objectives that the original full order controllers were designed for. A numerical state-space representation of $K^1_{\delta_c,red}$ and $K^2_{\delta_c,red}$ can be found in the Appendix. The $K^1_{\delta_c,red}$ and $K^2_{\delta_c,red}$ controllers are implemented on the CoSCIS test bed and it is their performance that will be studied in the work that follows. Hence, references to $K^1_{\delta_c}$ and $K^2_{\delta_c}$ in consequent sections refers to the reduced order controllers $K^1_{\delta_c,red}$ and $K^2_{\delta_c,red}$.

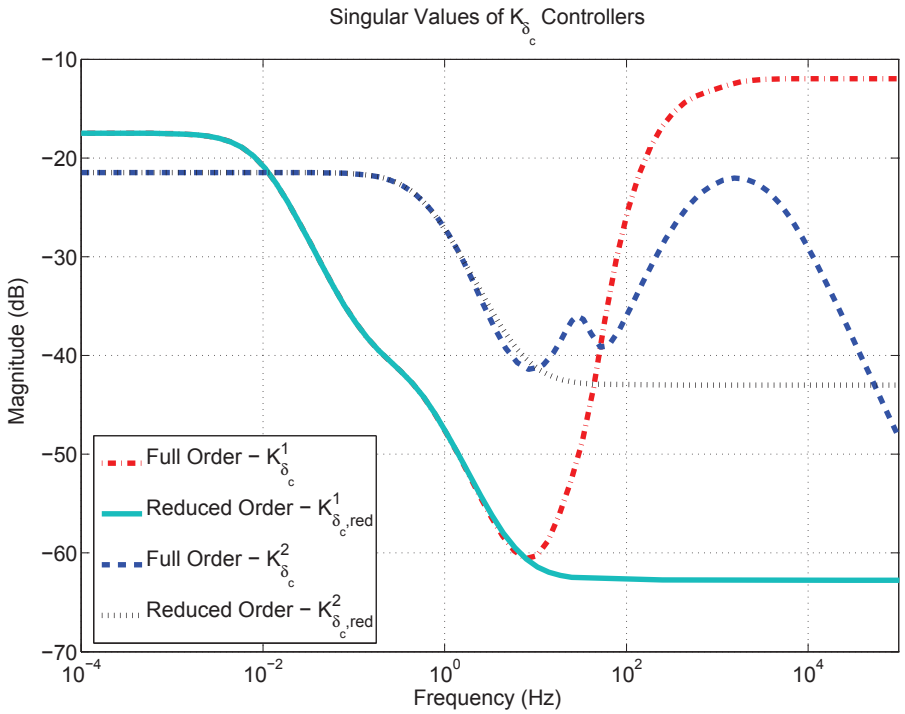

Figure 6.12: Frequency response of the full order and reduced order versions of the outer-loop controllers $K^1_{\delta_c}$ and $K^2_{\delta_c}$.

6.2.4.7 Results for the $K^1_{\delta_c}$ Design

The performance of the $K^1_{\delta_c}$ controller is initially evaluated via the frequency response of the closed-loop system depicted in Figure 6.13, when the $K^1_{\delta_c}$ controller is in the loop. The $K^1_{\delta_c}$ controller is a two degree of freedom controller, with two inputs and one output. It can be separated into a feedforward part $K^1_{\delta_c,(1,1)}$ which shapes the controllers response to $A_{z,ref}$ commands, and a feedback part $K^1_{\delta_c,(2,1)}$ which determines the disturbance rejection, and stability properties of the controller [43]. The magnitude of the loop transfer function $L(s) = K_{\delta_c,(2,1)}(s) \cdot e^{-T_d s} \cdot G_T(s)$ is shown in Figure 6.14. The crossover frequency of the loop transfer function is 0.09 Hz, and the system has a gain margin of 26.3 and a phase margin of 97.0°. The system has excellent stability margins.

The sensitivity and complimentary sensitivity functions of the closed-loop system

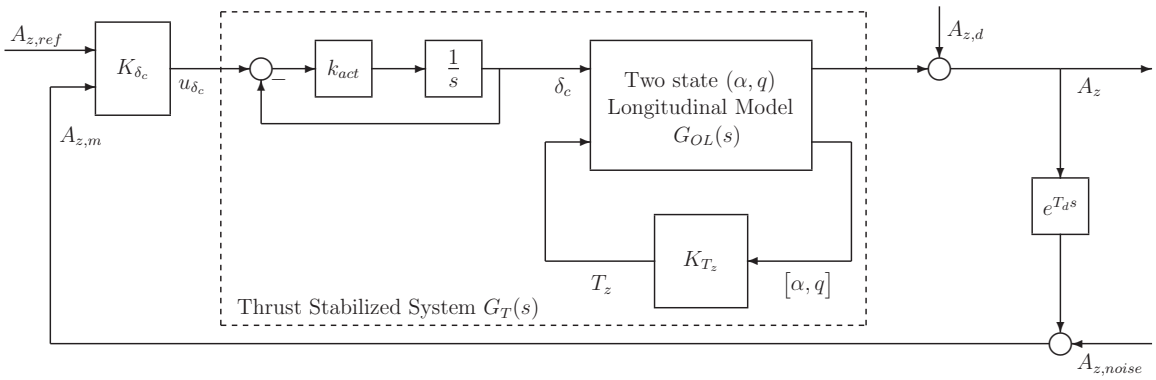

Figure 6.13: Diagram of the closed-loop system representing a supercavitating vehicle stabilized by the thrust controller K_{T_z} and cavitator controller K_{δ_c}.

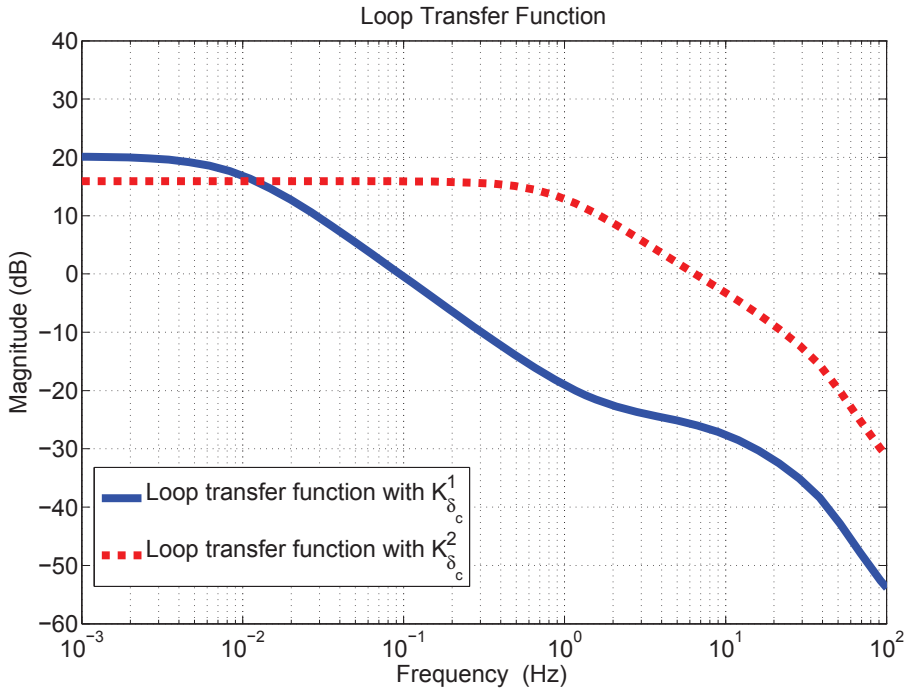

Figure 6.14: Magnitude of the loop transfer function $L(s) = K_{\delta_c,(2,1)}(s) \cdot e^{-T_d s} \cdot G_T(s)$ for the closed-loop system shown in Figure 6.13.

are shown in Figure 6.15. The peak of the sensitivity function has a magnitude of 1.04, while the peak of the complimentary sensitivity function has a peak magnitude of 0.91. The closed-loop system is very robust to input, and output multiplicative uncertainty. The bandwidth of the closed-loop system is defined as the frequency where the magnitude of the sensitivity function crosses -3 dB from below. The bandwidth of the closed-loop system, when the $K^1_{\delta_c}$ controller is in the loop, is

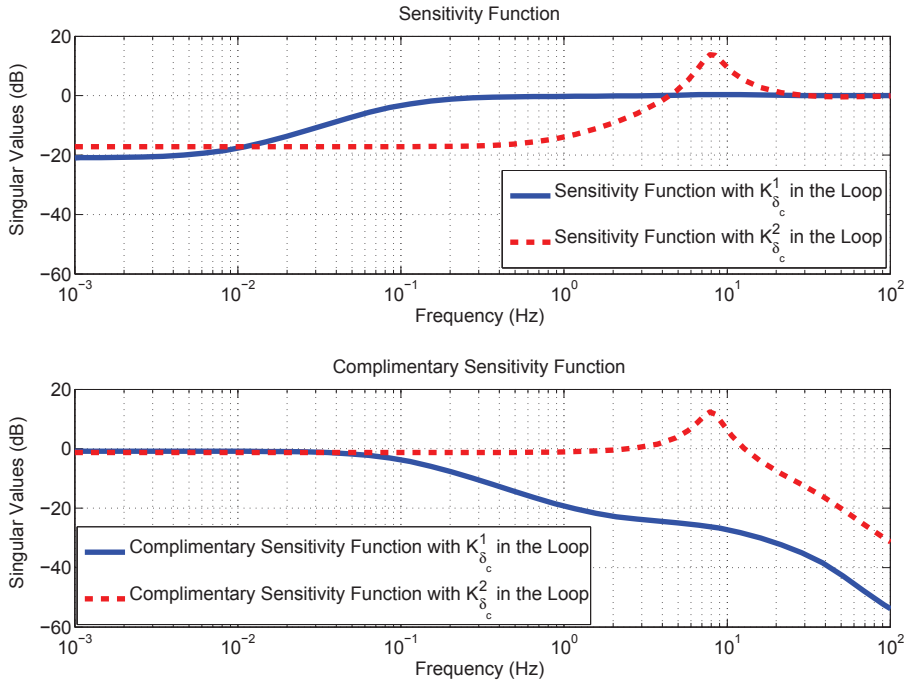

Figure 6.15: Frequency response of the sensitivity function, and complimentary sensitivity function for the closed-loop system shown in Figure 6.13.

0.11 Hz. This bandwidth is very low, and lies far below the upper bound imposed by the time-delay in the $A_{z,m}$ measurement. Hence, the $A_{z,m}$ measurement time-delay will have little effect on the performance of $K^1_{\delta_c}$.

A diagram of the closed-loop system is shown in Figure 6.13. It illustrates how z_{body}-axis acceleration disturbances $A_{z,d}$, measurement noise $A_{z,noise}$, and reference commands $A_{z,ref}$ enter the system. The effects of $A_{z,d}$, $A_{z,noise}$, and $A_{z,ref}$ inputs on the z_{body}-axis acceleration A_z, angle-of-attack α, and cavitator deflections δ_c, are illustrated in the Bode magnitude plots of the closed-loop system shown in Figure 6.16. The solid line in the Bode plots in Figure 6.16, show the response of the closed-loop system when the $K^1_{\delta_c}$ controller is in the loop.

The closed-loop system achieves the desired tracking performance, as can be seen in the Bode magnitude plot of the closed-loop $\frac{A_z(s)}{A_{z,ref}(s)}$ transfer function in Figure 6.16. The shape of the frequency response matches the desired reference system W_{ref}, and the controller achieves the desired tracking bandwidth of 0.5 Hz. Tracking performance is achieved with minimal effects on the angle-of-attack of the vehicle, as can

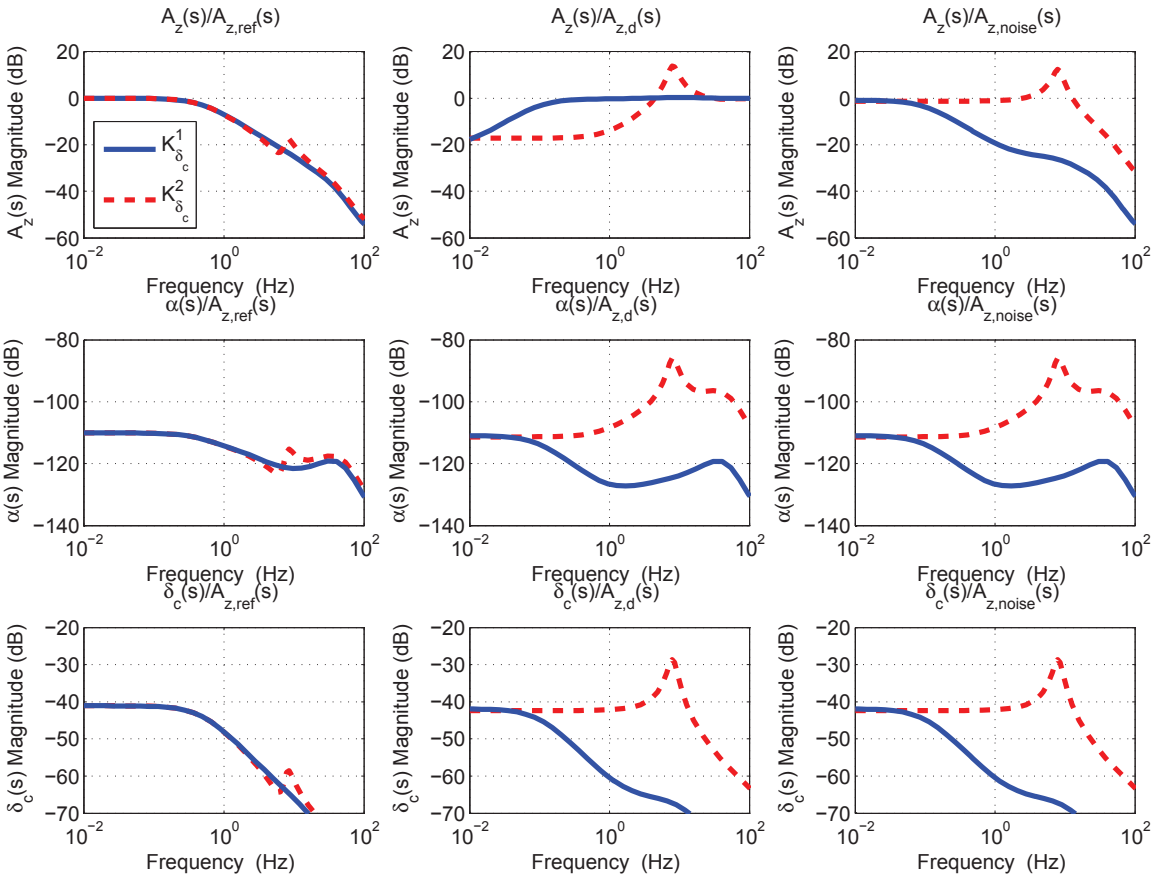

Figure 6.16: Closed-loop frequency response of the supercavitating vehicle stabilized by the inner-loop thrust controller K_{T_z}, and guided by the outer-loop controller K_{δ_c} (a diagram of the closed-loop system is shown in Figure 6.13.)

be seen in the Bode plots of the $\frac{\alpha(s)}{A_{z,ref}(s)}$ and $\frac{\alpha(s)}{A_{z,d}(s)}$ transfer functions. This is due to the aggressive α regulating performance of the inner-loop controller K_{T_z}. The Bode magnitude plot of the $\frac{\delta_c(s)}{A_{z,ref}(s)}$ transfer function shows that only approximately $\pm 6°$ of cavitator deflections are required to track ± 10 m/s^2 $A_{z,ref}$ reference commands in the 0 - 0.5 Hz frequency range. It should be noted that deflecting the cavitator 6° from trim is not sufficient to produce the $F_{z,body}$ forces that are necessary to generate a 10 m/s^2 change in A_z. The 10 m/s^2 change in A_z will be due to the combined effect of the cavitator and the inner-loop thrust controller K_{T_z}, as K_{T_z} strives to maintain the vehicle's angle-of-attack using the thrust T_z. The interplay between the outer-loop controller and the inner-loop controller will become apparent when

the closed-loop system is evaluated in simulation in Section 6.4.1.

The Bode magnitude plot of the closed-loop $\frac{A_z(s)}{A_{z,d}(s)}$ transfer function is shown in Figure 6.16. It has the desired frequency response. The $K^1_{\delta_c}$ controller was designed to attenuate 7.5 m/s^2 $A_{z,d}$ disturbances to cause less than 1 m/s^2 variation in A_z at frequencies below 0.01 Hz. This requirement is satisfied, because the gain of the $\frac{A_z(s)}{A_{z,d}(s)}$ transfer function is no greater than $\frac{1}{7.5} = -17.5$ dB up to 0.01 Hz. Just as in the case of $A_{z,ref}$ commands, the $A_{z,d}$ acceleration disturbances have very little effect on the vehicle's angle-of-attack. The $K^1_{\delta_c}$ controller achieves the desired disturbance rejection performance.

The closed-loop transfer functions $\frac{A_z(s)}{A_{z,noise}(s)}$, $\frac{\delta_c(s)}{A_{z,d}(s)}$ and $\frac{\delta_c(s)}{A_{z,noise}(s)}$ are shown in Figure 6.16. They roll off at 0.1 Hz as desired. This response implies the system is unaffected by noise at these higher frequencies and the $K^1_{\delta_c}$ controller ceases to move the cavitator in response to disturbances and noise inputs entering the system above 0.1 Hz. The Bode magnitude plot of the $\frac{\alpha(s)}{A_{z,noise}(s)}$ transfer function in Figure 6.16 shows that measurement noise $A_{z,noise}$ has almost no effect on the angle-of-attack of the vehicle.

The simulated step response of the $\frac{A_z(s)}{A_{z,ref}(s)}$ transfer function is shown in Figure 6.17. The $K^1_{\delta_c}$ controller achieves the expected tracking response. The system has zero overshoot, a rise time of 0.7 sec and a settling time of 0.95 sec. This response matches the response of W_{ref}, a first order system with a bandwidth of 0.5 Hz, which was used as a reference plant in the synthesis. The step response of the $\frac{A_z(s)}{A_{z,d}(s)}$ transfer function is shown in Figure 6.18. The plot shows how the closed-loop system responds to a unit disturbance $A_{z,d} = 1$ m/s^2 at a time $t = 0$. The system has a well damped response and rejects 90% of the disturbance in 6.9 sec. The steady-state error after this disturbance input is 9% of the disturbance magnitude. This steady-state error satisfies the design requirement of achieving less than 1 m/s^2 steady-state error for 7.5 m/s^2 $A_{z,d}$ disturbances.

The time-domain performance of the $K^1_{\delta_c}$ controller is evaluated further in a simulation in Section 6.4.1. The results of that initial evaluation is tested in experiment in Section 6.4.3, with the goal of verifying that the controller actually performs as expected on a replica of the real system.

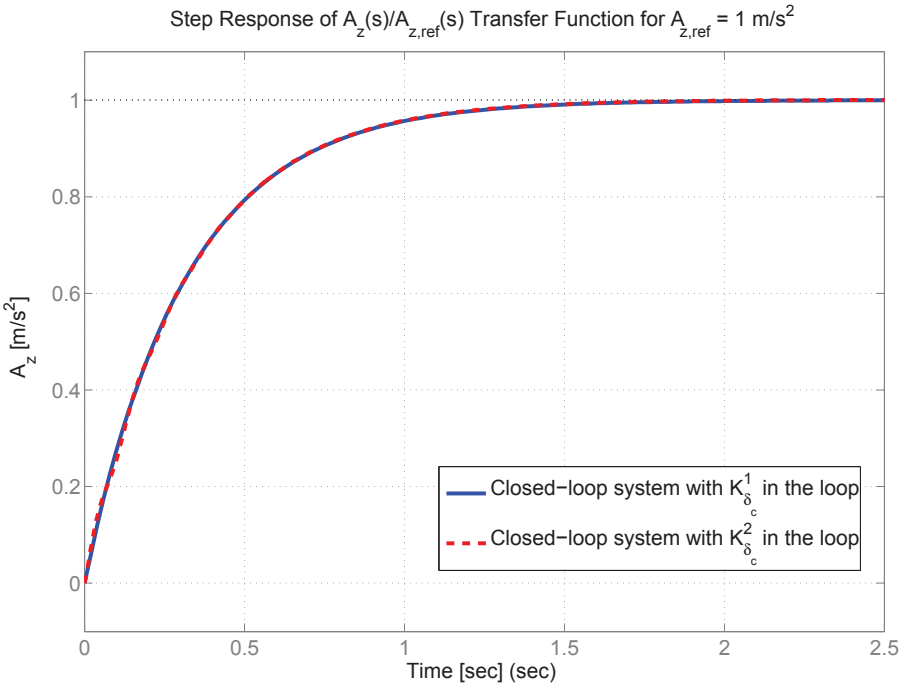

Figure 6.17: Step response of the $\frac{A_z(s)}{A_{z,ref}(s)}$ transfer function for controllers $K^1_{\delta_c}$ and $K^2_{\delta_c}$. The plot shows the $A_{z,ref}$ tracking performance of each controller.

6.2.4.8 Results for the $K^2_{\delta_c}$ Design

The performance of the $K^2_{\delta_c}$ controller is initially evaluated via the frequency response of the closed-loop system depicted in Figure 6.13, when the $K^2_{\delta_c}$ controller is in the loop. The loop transfer function of the closed-loop system is shown in Figure 6.14. The crossover frequency of the loop transfer function is 6.49 Hz, and the system has a gain margin of 1.3 and a phase margin of 21.8°.

The sensitivity and complimentary sensitivity functions of the closed-loop system are shown in Figure 6.15. The bandwidth of the closed-loop system is defined as the frequency where the magnitude of the sensitivity function crosses -3 dB from below. The bandwidth of the closed-loop system, when the $K^2_{\delta_c}$ controller is in the loop, is 3.6 Hz. The sensitivity function has a peak magnitude of 5.0 (14.0 dB) at 8.08 Hz, and the complimentary sensitivity function has a peak magnitude of 4.2 (12.4 dB) at 7.85 Hz. These large peaks indicate poor robustness to multiplicative uncertainty. The large peaks in the magnitude of the sensitivity and complimentary

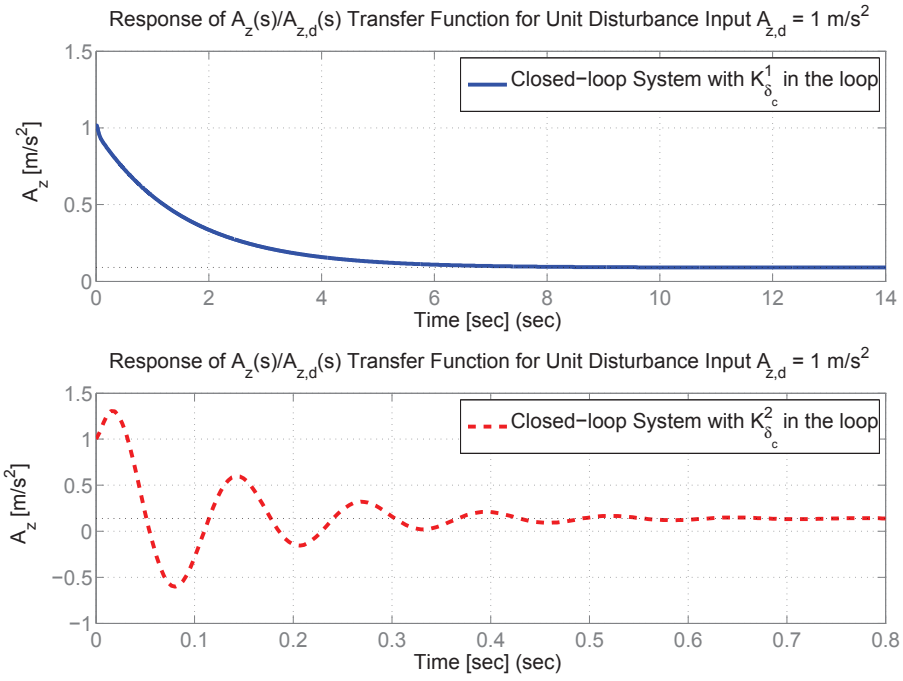

Figure 6.18: Step response of $\frac{A_z(s)}{A_{z,d}(s)}$ transfer function for controllers $K^1_{\delta_c}$ and $K^2_{\delta_c}$.

sensitivity functions appear because the $K^2_{\delta_c}$ controller is designed with ambitious disturbance rejection performance goals which push out the bandwidth of the closed-loop system. The open-loop system has a Right Half Plane (RHP) zero at 7.96 Hz that is associated with the time-delay in the A_z measurement. The RHP zero places a fundamental limitation on the achievable performance of the closed-loop system. When the frequency range of desired performance is increased and pushed out toward the RHP zero, there is a corresponding loss of performance at higher frequencies manifesting itself in a larger peak magnitude of the sensitivity function. This phenomena is the so called "water bed effect" [42]. The required disturbance rejection performance results in a high bandwidth, which leads to poor stability and robustness margins due to the time-delay in the feedback measurement.

The effects $A_{z,d}$, $A_{z,noise}$, and $A_{z,ref}$ inputs have on the closed-loop system z_{body}-axis acceleration A_z, angle-of-attack α, and cavitator deflections δ_c, are shown in Figure 6.16. The results associated with the closed-loop system which has $K^2_{\delta_c}$ in the loop are plotted with a dashed line in Figure 6.16.

The closed-loop system achieves the desired tracking performance, as can be seen in the Bode magnitude plot of the closed-loop $\frac{A_z(s)}{A_{z,ref}(s)}$ transfer function in Figure 6.16. The shape of the frequency response matches the desired reference system W_{ref}, and the controller achieves the desired tracking bandwidth of 0.5 Hz. The tracking performance is achieved with negligible effects on the angle-of-attack regulation of the vehicle, as can be seen in the Bode plots of the $\frac{\alpha(s)}{A_{z,ref}(s)}$ and $\frac{\alpha(s)}{A_{z,d}(s)}$ transfer functions. These results closely match the results for $K^1_{\delta_c}$. The $A_{z,ref}$ and $A_{z,d}$ inputs have little effect on the angle-of-attack of the vehicle, because of the aggressive α regulating performance of the inner-loop controller K_{T_z}.

The Bode magnitude plot of the $\frac{\delta_c(s)}{A_{z,ref}(s)}$ transfer function shows that, just as for the $K^1_{\delta_c}$ controller, approximately $\pm 6^\circ$ of cavitator deflections are required to track ± 10 m/s^2 $A_{z,ref}$ reference commands in the 0 - 0.5 Hz frequency range. Note that a 6° cavitator deflections is insufficient by itself to produce the $F_{z,body}$ forces that will cause a 10 m/s^2 change in A_z. The combined effect of the cavitator and the inner-loop thrust controller K_{T_z}, as K_{T_z} strives to maintain the vehicle's angle-of-attack using the thrust T_z, generates the desired 10 m/s^2 change in A_z. The interplay between the inner, and outer-loop controllers is observed in the simulations described in Section 6.5.1.

The Bode magnitude plot of the closed-loop $\frac{A_z(s)}{A_{z,d}(s)}$ transfer function is shown in Figure 6.16. Disturbances are attenuated by an order of magnitude up to 2 Hz, which satisfies the design specifications described in Section 6.2.4.4. The system is effective at rejecting disturbances up to 3.6 Hz, where the $\frac{A_z(s)}{A_{z,d}(s)}$ transfer function crosses -3 dB magnitude from below. Good performance in the 0 - 3.6 Hz frequency range is paid for by very poor performance at higher frequencies, as illustrated by the 5.0 (14.0 dB) magnitude peak in the $\frac{A_z(s)}{A_{z,d}(s)}$ transfer function at 8.08 Hz. The impact of this peak is that the effects of $A_{z,d}$ disturbances will be amplified by the action of the control system instead of attenuated, in the 4.4 - 30 Hz frequency range.

The closed-loop system with the $K^2_{\delta_c}$ controller in the loop is susceptible to noise due to its high bandwidth. The $\frac{A_z(s)}{A_{z,noise}(s)}$ transfer function in Figure 6.16 has 0.86 (-1.29 dB) gain at low frequencies, but experience a peak magnitude of 4.17 (12.4 dB) at 7.85 Hz before it rolls off. The closed-loop system is very sensitive to noise in the 3 - 13 Hz frequency range, where the effects of the noise are amplified rather than attenuated. This has the potential to cause problems in experiments on the

CoSCIS test bed, since the filtering of the A_z measurement only attenuates noise above 30 Hz as described in Section 3.1. The noise has negligible impact on the vehicle's angle-of-attack, as can be seen in the $\frac{\alpha(s)}{A_{z,noise}(s)}$ transfer function in Figure 6.16. This is due to effective α regulating by the inner-loop K_{T_z} control law.

The disturbances and measurement noise affect the cavitator usage, as can be seen in the $\frac{\delta_c(s)}{A_{z,d}(s)}$ and $\frac{\delta_c(s)}{A_{z,noise}(s)}$ transfer functions in Figure 6.16. The cavitator usage due to disturbances and noise hits its peak at 7.85 Hz, where the $\frac{\delta_c(s)}{A_{z,d}(s)}$ and $\frac{\delta_c(s)}{A_{z,noise}(s)}$ transfer functions have their peak magnitude.

The step response of the $\frac{A_z(s)}{A_{z,ref}(s)}$ transfer function is shown in Figure 6.17. The $K^2_{\delta_c}$ controller achieves the expected tracking response. As in the case of $K^1_{\delta_c}$, the system has zero overshoot, a rise time of 0.7 sec and a settling time of 0.95 sec. This response matches the response of the reference system W_{ref}. The step response of the $\frac{A_z(s)}{A_{z,d}(s)}$ transfer function is shown in Figure 6.18. The plot shows how the system responds to a unit disturbance $A_{z,d} = 1$ m/s^2 at a time $t = 0$. The response of the closed-loop system is poorly damped but the system reaches a steady-state after approximately 0.6 sec. The system has a pair of lightly damped poles which cause this poor damping, but the response is expected from the large peaks in the sensitivity and complimentary sensitive functions. The reference tracking response is not afflicted by this lack of damping because it is driven by the feedforward part of the controller. The steady-state error after the disturbance input is 0.14% of the disturbance magnitude. This steady-state error satisfies the design requirement of achieving less than 2 m/s^2 steady-state error for 5 m/s^2 $A_{z,d}$ disturbances. Note that the response has undereshoot. This is because of a RHP zero in the $\frac{A_z(s)}{A_{z,d}(s)}$ transfer function, that is associated with the time-delay in the measurement.

The time-domain performance of the $K^2_{\delta_c}$ controller is evaluated further in simulation in Section 6.5.1. The results of that initial evaluation are tested in experiment in Section 6.5.3, with the goal of verifying that the controller actually performs as expected on a replica of the real system. The performance of the $K^2_{\delta_c}$ controller is likely to suffer due to the high level of noise in the experiment. The detrimental effects of the noise on the experimental performance of $K^2_{\delta_c}$ are likely to be exacerbated by the cable induced loads that are associated with cavitator deflections on the CoSCIS test bed. The noise may cause excessive cavitator usage, and this cavitator usage can then cause cable induced loads which will negatively effect the

controllers tracking performance.

6.2.4.9 Summary of K_{δ_c} Control Design Effort

The frequency responses of $K^1_{\delta_c}$ and $K^2_{\delta_c}$ controllers were analyzed in detail Sections 6.2.4.7 and 6.2.4.8. Both controllers have two degrees of freedom, and share the same A_z tracking performance, with very different disturbance rejection characteristics. Both controllers are expected to achieve excellent tracking performance, with no overshoot, a rise time of 0.7 sec and a settling time of 0.95 sec. The disturbance rejection bandwidth of the $K^1_{\delta_c}$ controllers is 0.11 Hz, and it is expected to attenuate 90% of a disturbance in 6.9 sec. The controller is only effective at rejecting low frequency and steady-state disturbances. The low bandwidth of the $K^1_{\delta_c}$ controller makes it very robust to A_z measurement noise. The $K^2_{\delta_c}$ controller has a disturbance rejection bandwidth of 3.6 Hz. It is expected to attenuate 86% of a disturbance in 0.6 sec. The high bandwidth of the $K^2_{\delta_c}$ controller makes it succeptable to A_z measurement noise during experiments which may cause noise and disturbances to be amplified, rather than attenuated, in the frequency range around 7.85 Hz.

6.2.5 Controller Implementation

6.2.5.1 Controller Discretization

The $K^1_{\delta_c}$ and $K^2_{\delta_c}$ controllers are synthesized as continuous-time state-space systems in MATLAB. These continuous-time controllers are discretized using the *c2d* function in MATLAB. The *c2d* function is used to implement a bilinear transformation from continuous-time to discrete time. The discretized $K^1_{\delta_c}$ and $K^2_{\delta_c}$ controllers have a sample time of $T_c = 1/40$ sec.

6.2.5.2 Implementation in LabVIEW Real-Time

The $K^1_{\delta_c}$ and $K^2_{\delta_c}$ controllers are tested in the experiments described in Chapter 6. They are implemented in LabVIEW Real-Time on board the CompactRIO. The $K^1_{\delta_c}$ and $K^1_{\delta_c}$ controllers have two inputs and one output. The controllers accept a reference command $A_{z,ref}$, and a measurement of the z_{body}-axis acceleration of the vehicle, $A_{z,m}$. The K_{δ_c} controllers output a command u_{δ_c} to the cavitator actuator. The controllers are implemented at 40 Hz on board the CompactRIO. The "*Discrete*

State-Space Function" block from the LabVIEW *Control Design and Simulation Module* is used to implement the controllers in LabVIEW Real-Time. The function only requires the numeric values of the A, B, C and D matrices in the discrete reduced order state-space representation of the controllers [44].

6.3 Experimental Evaluation of Control Laws

An experimental test bed was presented in Chapters 2 and 3. This test bed enables the experimental validation of control laws for supercavitating vehicles. A methodology for experimentally evaluating a control law was presented in Section 6.1, and a candidate control architecture was presented in Section 6.2. The control architecture yields a pair of candidate controllers, denoted as $K^1_{\delta_c}$ and $K^2_{\delta_c}$, that can be evaluated in on the CoSCIS test bed. The controllers are designed to achieve different performance objectives. Each controller will be studied in simulation, hardware-in-the-loop tests on board the CoSCIS test bed, and the actual water tunnel experiment on board the CoSCIS test bed. A description of the simulation, the hardware-in-the-loop tests, and the water tunnel experiment is provided in Sections 6.3.1, 6.3.2 and 6.3.3, respectively. Each controller is tested in all three, and the results are described in Sections 6.4 and 6.5.

6.3.1 Controller Simulations

The performance of the $K^1_{\delta_c}$ and $K^2_{\delta_c}$ controllers is initially evaluated in simulation. The simulation is based on the supercavitating vehicle linearized plant model, described by equation 4.44, and implemented in Simulink. The diagram of the closed-loop system that is shown in Figure 6.13, illustrates the interconnection of the signals and systems in the simulation. The simulation incorporates actuator dynamics for the cavitator positioning system, and measurement noise and time-delay in the $A_{z,m}$ measurements being fed to the $K^1_{\delta_c}$ and $K^2_{\delta_c}$controllers. The noise in the simulation has a standard deviation of 2 m/s^2, which is similar to the experimental $A_{z,m}$ data. The cavitator actuator is modeled as a first order system with a breakpoint at 10 Hz. The deflection of the cavitator is limited to be less than $\pm 25°$, and its rate of deflection is limited to be less than ± 523.4 rad/s. The $A_{z,m}$ measurement in the simulation has a time-delay of 0.04 sec. The tracking and disturbance rejection performance of the $K^1_{\delta_c}$ and $K^2_{\delta_c}$ controllers is investigated in the simulation and

compared against the design objectives of each controller to verify their function.

6.3.2 Hardware-in-the-Loop CoSCIS Test Bed

A Hardware-In-the-Loop (HIL) tests was performed to test the function of each controller on board the CoSCIS test bed before the final experiments in the water tunnel were performed. The HIL tests are performed on the CoSCIS test bed when it is mounted inside the water tunnel and set up just as it will be in the experiments described in Section 6.3.3. The water tunnel is not running when the HIL tests are performed, and there are no hydrodynamic loads being generated on the CoSCIS model during the HIL tests. A synthetic $A_{z,sim}$ signal is used to simulate the hydrodynamic loads, and test the function of each controller on board the CoSCIS test bed.

The HIL tests are used to study the performance of each controller on board the test bed in a "best case scenario". The $A_{z,m}$ signal that is being fed back to the controller has no noise, and it's hydrodynamic component matches exactly with the theory, because it is being generated artificially. The $A_{z,m}$ signal is only perturbed by whatever cable induced loads the controller's action causes. The HIL tests provide a demonstration of the detrimental effects that the cable induced loads will have on each controller performance, and yield a baseline performance which the actual experimental performance can be compared against.

6.3.2.1 Simulated Hydrodynamic Loads $A_{z,sim}$

The difference between the HIL tests and the actual control experiments, that are described in Section 6.3.3, is that the water tunnel is not run for the duration of the HIL test and a synthetic $A_{z,sim}$ signal is being added to the $A_{z,m}$ measurement being fed back to the K_{δ_c} controller. This synthetic $A_{z,sim}$ signal is used to simulate the hydrodynamic loads on the cavitator. A diagram of the HIL test framework is shown in Figure 6.19. The synthetic $A_{z,sim}$ signal is derived from the hydrodynamic model described in Chapter 4. The cavitator deflection at each time-step is used to compute the expected hydrodynamic forces on the cavitator, and derive the corresponding $A_{z,sim}$ value. This synthetic $A_{z,sim}$ signal is added to the $A_{z,m}$ measurement from the load-cell in real-time on board the CompactRIO, before the combined signal is fed back to the controller.

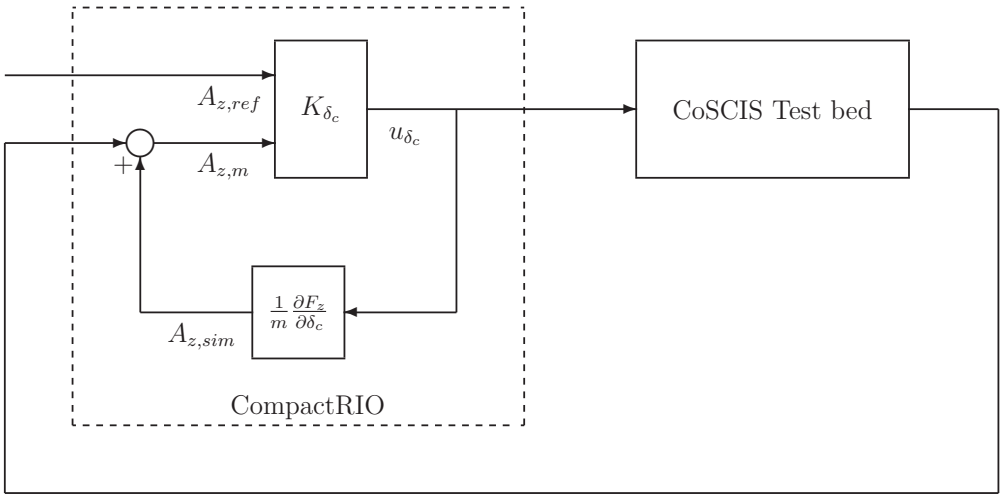

Figure 6.19: A diagram of the HIL test framework.

Equation 4.35, which is repeated below, describes how the z_{body}-axis force F_z changes with cavitator deflection. This equation is a linear approximation that was derived when the mathematical model of the vehicle was linearized analytically in Section 4.2.3:

$$\frac{\partial F_{c_z}}{\partial \delta_c} = \bar{q}_c A_c \left(2(k_3 - k_2)\alpha_c \delta_c + (k_3 + 2k_2)\alpha_c^2 + k_3\right) \tag{4.35}$$

The synthetic A_z signal is computed using equation 4.35, and Newton's Second Law:

$$A_{z,sim} = \frac{1}{m}\frac{\partial F_{c_z}}{\partial \delta_c}\,\delta_c \tag{6.27}$$

where m is the mass of the vehicle

6.3.2.2 Experimental Procedure

The HIL tests will demonstrate the tracking performance of each K_{δ_c} controller on the CoSCIS test bed. There is no difference between the HIL test and the final experiments described in Section 6.3.3, except that in the HIL test the water tunnel is not being run and a synthetic $A_{z,sim}$ signal is used to augment the $A_{z,m}$ measurements. Each HIL test follows the following experimental procedure:

1. The CoSCIS test bed is mounted in the water tunnel test section. There is no water in the test section and the water tunnel is turned off.

2. The experimental system is initialized with the cavitator at zero angle-of-attack. The angle-of-attack of the cavitator is measured by taking pictures of the cavitator and measuring the angle in *ImageJ*, as described in Section 3.2.1.

3. The load-cell is tared, so that $A_{z,m} = 0$ m/s^2.

4. The synthetic $A_{z,sim}$ signal is turned on. It starts off as $A_{z,sim} = 0$ m/s^2, because the cavitator is deflected zero degrees.

5. The $A_{z,ref}$ reference command is set to zero.

6. The K_{δ_c} control system is turned on. The control system will now deflect the cavitator to track the desired $A_{z,ref}$ commands.

7. A set of $A_{z,ref}$ reference commands is fed to the control system. The commands are steps, doublets and sinusoids. The K_{δ_c} control system is tasked with tracking these commands.

8. When the tracking performance of the controller has been evaluated the K_{δ_c} control system is turned off to end the experiment.

6.3.3 Description of Control Experiments on the CoSCIS Test Bed

The CoSCIS test bed is used to evaluate the performance of candidate K_{δ_c} controllers on a real system that replicates the flight of a supercavitating vehicle, described in Section 6.1. The design of a pair of controllers, $K^1_{\delta_c}$ and $K^2_{\delta_c}$, is described in Section 6.2.4. These controllers are initially evaluated in simulation and a hardware-in-the-loop tests, before the experiment that is described here is initiated. This section describes the experimental proceedure for the evaluation of control laws on the CoSCIS test bed in the water tunnel at St. Anthony Falls.

6.3.3.1 Experimental Procedure

The CoSCIS test bed is set up inside the water tunnel test section, as described in Section 2.3.3. The control experiments are all conducted at a single water tunnel flow velocity of $V = 8$ m/s. The procedure for each test is as follows:

1. The CoSCIS test bed is mounted in the water tunnel test section. There is water in the test section, but the water tunnel is turned off.

2. The cavitator is moved to the desired initial angle-of-attack $\alpha_c = \delta_c = 0°$. The angle-of-attack of the cavitator is measured by taking pictures of the cavitator and measuring the angle in *ImageJ*, as described in Section 3.2.1.

3. The water tunnel is started, and the water tunnel pump is set to 23 Hz, which corresponds to a water tunnel velocity of 8.0 m/s.

4. The cavity ventilation system is turned on and the supercavity is formed. The ventilation rate is set to 25 L/min. This ventilated supercavity at $V = 8$ m/s, has a cavitation number of $\sigma = 0.23$.

5. The load-cell is tared[1], while the water tunnel velocity is 8.0 m/s and the cavitator angle-of-attack is 0°. The $A_{z,m}$ measurement reads zero except for noise in the measurement.

6. The $A_{z,ref}$ reference command is set to zero, $A_{z,ref} = 0$.

7. The K_{δ_c} control system is turned on. The control system will now deflect the cavitator to track the desired $A_{z,ref}$ commands.

8. A set of $A_{z,ref}$ reference commands is fed to the control system. The commands are steps, doublets, and sinusoids. The sinusoid is defined as

$$A_{z,ref} = 10 \sin\left(0.5 \cdot 2\pi t\right) \tag{6.28}$$

   The K_{δ_c} control system is tasked with tracking these commands.

9. Once the tracking performance has been evaluated. The control system is sent a reference signal $A_{z,ref} = 0$, in preparation for evaluating the disturbance rejection performance of the controller.

[1]In force and moment measurement applications there is often a component of force or moment that will remain constant throughout an experiment. When a load-cell is "tared" or "zeroed with load", it refers to the process of offsetting the force and moment measurements by the value of the constant forces and moments so that the load-cell reads zero when no other force or moment acts on the load-cell. This process is commonly used in practice to remove steady-state offsets in load-cell measurement data, e.g. forces and moments due to gravity

10. The gust generator is activated, and disturbances are introduced to the flow. The frequency of the gusts is varied from 0.1 - 2 Hz.

11. The K_{δ_c} control system and the water tunnel are turned off to end the experiment when the performance of the controller has been evaluated.

6.3.3.2 Difference Between Simulation and Experiment

The challenges associated with the design and implementation of the CoSCIS test bed were described in Chapters 2 and 3 and 5. The objective of this work is to experimentally evaluate the performance of controllers that are designed for the simulated supercavitating vehicle. The utility of the test bed is limited by the implementation issues discussed in Chapters 3 and 5. Hence, there are important differences between the response of a simulated supercavitating vehicle, and the response observed on the CoSCIS test bed. The major differences between the simulation and the experiments are listed below:

- **Lack of inner-loop thrust controller in experiment**:
  In simulation the supercavitating vehicle is controlled by two controllers, an inner-loop controller K_{T_z} using the thrust T_z to stabilize the vehicle and regulate α, and an outer-loop controller K_{δ_c} using the cavitator to track A_z reference commands. The strut, which holds the CoSCIS model in place during experiments, performs the same function as the thrust controller does in simulation, i.e. it hold the vehicle model at the desired angle-of-attack. Only the K_{δ_c} controller can be implemented and tested on the CoSCIS test bed, as described in Section 6.1. Hence, when the results from simulation and experiment are compared it is important to note that the effects of the thrust T_z are absent from the experimental data. In the experiment, the cavitator is the sole contributor to the measured acceleration of the vehicle. The z_{body}-axis component of the thrust, which is acting to stabilize the vehicle and maintain its angle-of-attack, contributes to the vehicle's z_{body}-axis acceleration which is being fed back to the K_{δ_c} controller in the simulation. Hence, the response of K_{δ_c} to a $A_{z,ref}$ command is not exactly the same in experiment and simulation, because the simulated response of the K_{δ_c} controller will depend on the actions of the inner-loop thrust controller at each time step.

- **Cavitator deflections cause cable induced loads**:
  Actuating the cavitator on the CoSCIS test bed induces a force, $F_{z,cable}$, in the z_{body}-axis force measurement. This force is induced by the pulling of the cables which pitch the cavitator up and down. This phenomena is not modeled in the mathematical model, since it is not an effect which would be observed on a real vehicle. This phenomenon is described in Section 3.3. The effect of this cable induced load is a component of z_{body}-axis acceleration $A_{z,cable} = \frac{F_{z,cable}}{m}$ which perturbs the acceleration measurement that is being fed back to the K_{δ_c} controller in the control experiments that are performed on board the CoSCIS test bed.

- **Backlash in the cavitator movement**:
  The cavitator positioning system is described in Section 3.2. Several important challenges were overcome when this system was implemented on the test bed. Two key issues were addressed during the implementation of the cavitator positioning system. First, there is no real-time measurement of the cavitator deflection. Second, the cavitator movement has backlash. These issues were addressed in Section 3.2. Algorithm 1 is implemented on board the CoSCIS test bed, and provides a real-time estimate of the cavitator position. This enables the control system to command the cavitator deflection, but a small amount of uncertainty is present in the cavitator position estimate. This uncertainty is due to the uncertainty in estimating the initial deflection of the cavitator through pictures, as described in the discussion leading up to equation 5.28 in Section 5.1.3, and the uncertainty due to the potential error in the model of the cavitator movement. The uncertainty is estimated to be on the order of $\pm 2°$. Algorithm 2, minimizes the effects of the backlash by utilizing a model of the actuating system, as described in Section 3.2. This minimizes the effects of the backlash, but a small amount of backlash is still present in the system, on the order of $\pm 0.5°$.

6.4 Evaluation of Control Law $K^1_{\delta_c}$

A description of the $K^1_{\delta_c}$ control law is given in Section 6.2.4. The $K^1_{\delta_c}$ controller is a two degree of freedom controller, with two inputs and one output. It can be separated into a feedforward part $K^1_{\delta_c,(1,1)}$ which shapes the controllers response to

$A_{z,ref}$ commands, and a feedback part $K^1_{\delta_c,(2,1)}$ which determines the disturbance rejection, and stability properties of the controller. The $K^1_{\delta_c}$ controller is designed with a focus on low frequency tracking performance. It is expected to achieve good tracking of the $A_{z,ref}$ command, with no overshoot, a rise-time of 0.7 sec, and a settling time of 0.95 sec. The controller is designed to only reject very low frequency and steady-state disturbances, with a disturbance rejection bandwidth of 0.11 Hz. The performance of the $K^1_{\delta_c}$ control law is evaluated in simulation, hardware-in-the-loop tests and water tunnel experiment in Sections 6.4.1, 6.4.2 and 6.4.3, respectively.

6.4.1 Simulation Performance of the $K^1_{\delta_c}$ Controller

The tracking and disturbance rejection performance of the $K^1_{\delta_c}$ controller is studied in simulation prior to implementation on the experimental platform. The simulated step response of the controller is seen in Figures 6.20 and 6.21. The tracking response is excellent and closely tracks the desired response described by the W_{ref} reference system defined in equation 6.15. The acceleration of the vehicle is not affected by the noise in the $A_{z,m}$ measurement being fed back to the controller. This is consistent with the results of the frequency domain analysis described in Section 6.2.4.7, which indicates that the closed-loop system with the $K^1_{\delta_c}$ controller in the loop is not sensitive to measurement noise.

It is important to note the interplay between the $K^1_{\delta_c}$ controller and the inner-loop thrust controller. As the $K^1_{\delta_c}$ controller deflects the cavitator to track the $A_{z,ref}$ command, the thrust controller changes it's level of thrust to compensate. The thrust controller is regulating the simulated vehicle's angle-of-attack, but the change in thrust impacts the vehicle's acceleration. The thrust controller contributes significant force that the control system needs to generate to track the desired $A_{z,ref}$ reference. When the $K^1_{\delta_c}$ controller is tested on the CoSCIS test bed, its tracking performance suffers because it is not working alongside the thrust controller. The tracking performance of the $K^1_{\delta_c}$ controller is very sensitive to the accuracy of the vehicle model, because it relies heavily on the feedforward part of the controller.

The simulated disturbance rejection performance of the $K^1_{\delta_c}$ controller is seen in Figures 6.22, 6.23, 6.24, and 6.25. The A_z acceleration of the system is perturbed by a step disturbance signal $A_{z,d} = 10$ m/s^2 in Figures 6.22, and 6.23. The $K^1_{\delta_c}$

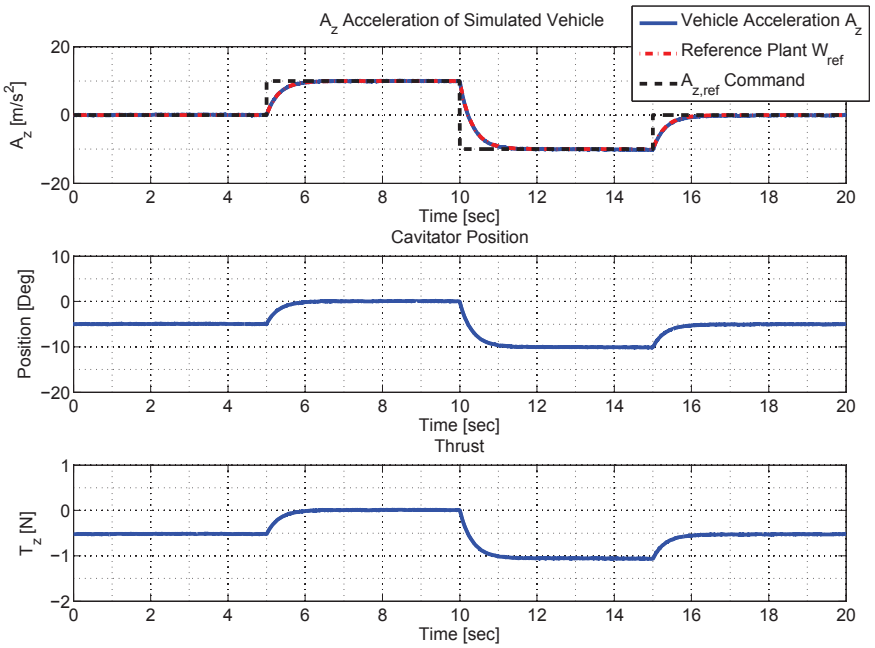

Figure 6.20: Tracking performance with the $K^1_{\delta_c}$ controller: ± 10 m/s^2 $A_{z,ref}$ doublet command in simulation.

controller rejects 90% of the disturbance in approximately 6.5 sec. The disturbance is rejected smoothly, and it does not cause any oscillations or other transient response. This is in line with the expected performance, described in Section 6.2.4.7. The vehicle settles down to a new trim when it has rejected the disturbance. The trim is described by a small constant pitching rate. This occurs because the $K^1_{\delta_c}$ controller is designed to tolerate a small tracking error in A_z, and a non-zero A_z translates into a non-zero pitch rate when the angle-of-attack of the vehicle is regulated to zero by the inner-loop K_{T_z} controller.

The A_z acceleration of the system is perturbed by a 10 m/s^2 chirp disturbance in Figures 6.24, and 6.25. The chirp disturbance is described by a sinusoid with a frequency which grows from 0 Hz to 0.2 Hz in 60 sec. The chirp signal is defined as

$$A^{1,chirp}_{z,d} = 10 \cdot \sin\left(\frac{0.2}{60} 2\pi t\right) \text{ m/s}^2 \tag{6.29}$$

The $K^1_{\delta_c}$ controller is effective at attenuating the chirp disturbance for the first 30 sec of the simulation, which corresponds to sinusoids at frequencies of 0 - 0.1 Hz. The

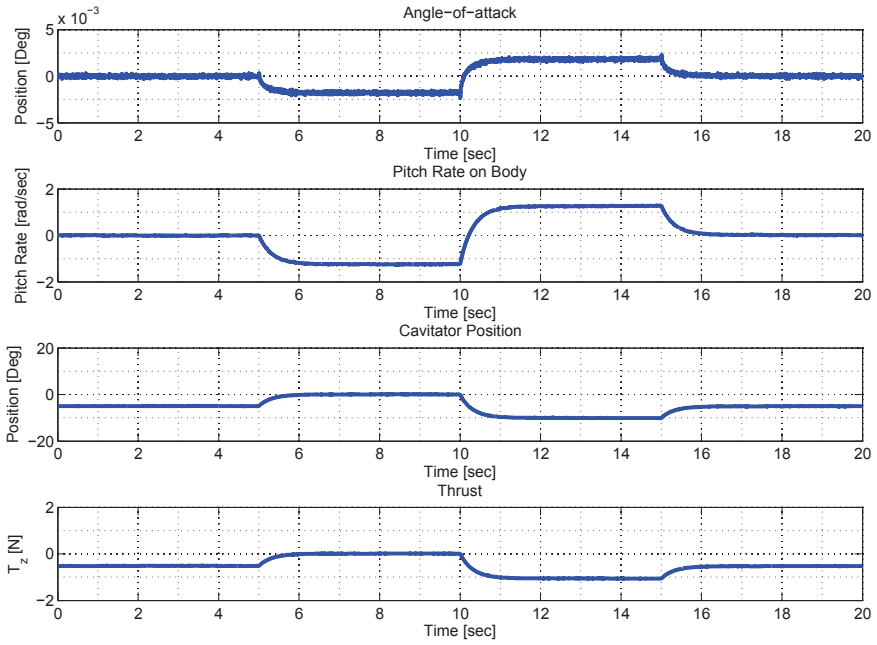

Figure 6.21: Tracking performance with the $K^1_{\delta_c}$ controller: ± 10 m/s^2 $A_{z,ref}$ doublet command in simulation.

attenuation becomes progressively worse as the frequency of the chirp disturbance increases. The A_z response of the vehicle leads the $A_{z,d}$ disturbance in Figure 6.24. This result is consistent with the frequency response of the closed-loop $\frac{A_z(s)}{A_{z,d}(s)}$ transfer function which has a phase lead greater than 30° in the 0.04 - 1 Hz frequency range.

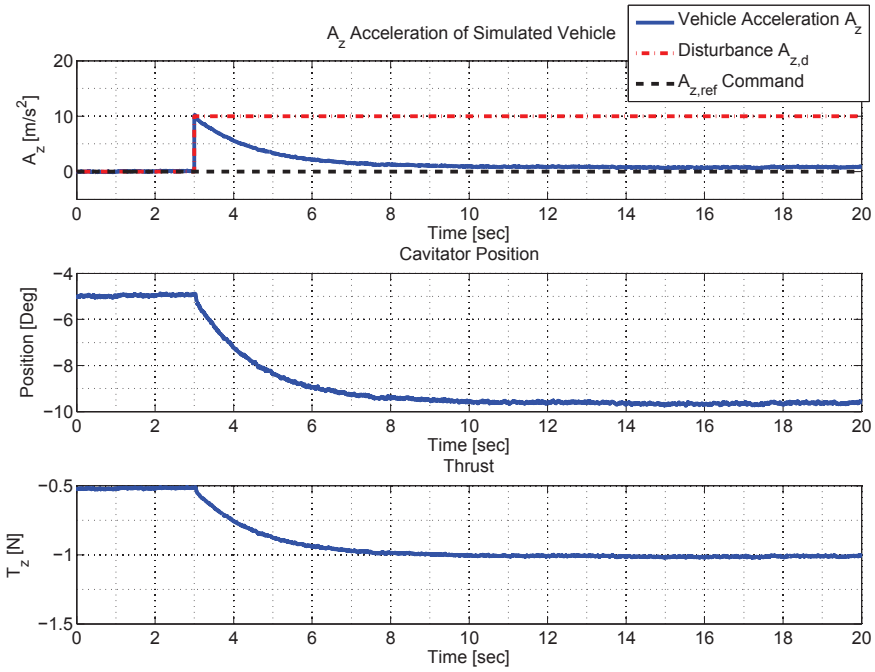

Figure 6.22: Disturbance rejection performance with the $K^1_{\delta_c}$ controller: 10 m/s^2 $A_{z,d}$ step disturbance in simulation.

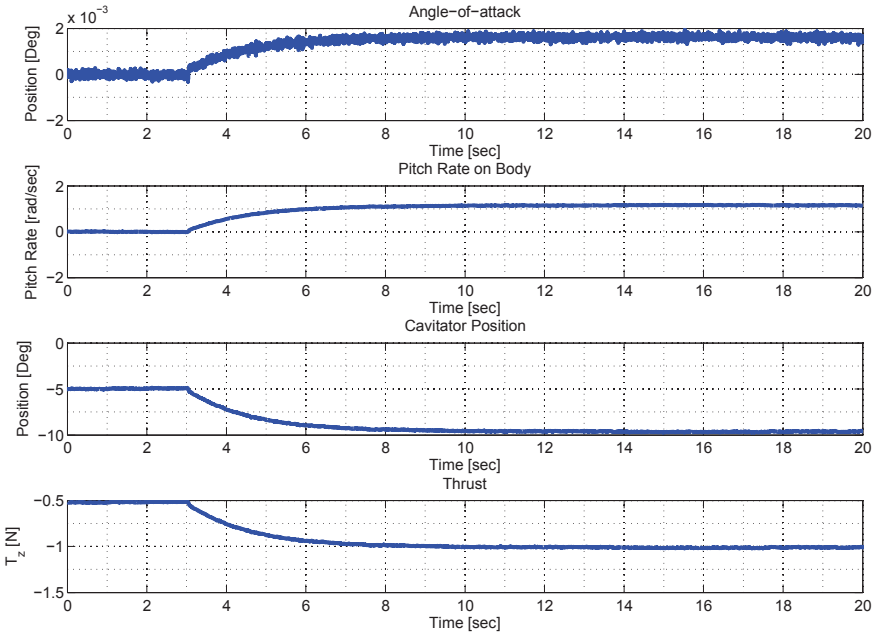

Figure 6.23: Disturbance rejection performance with the $K^1_{\delta_c}$ controller: 10 m/s^2 $A_{z,d}$ step disturbance in simulation.

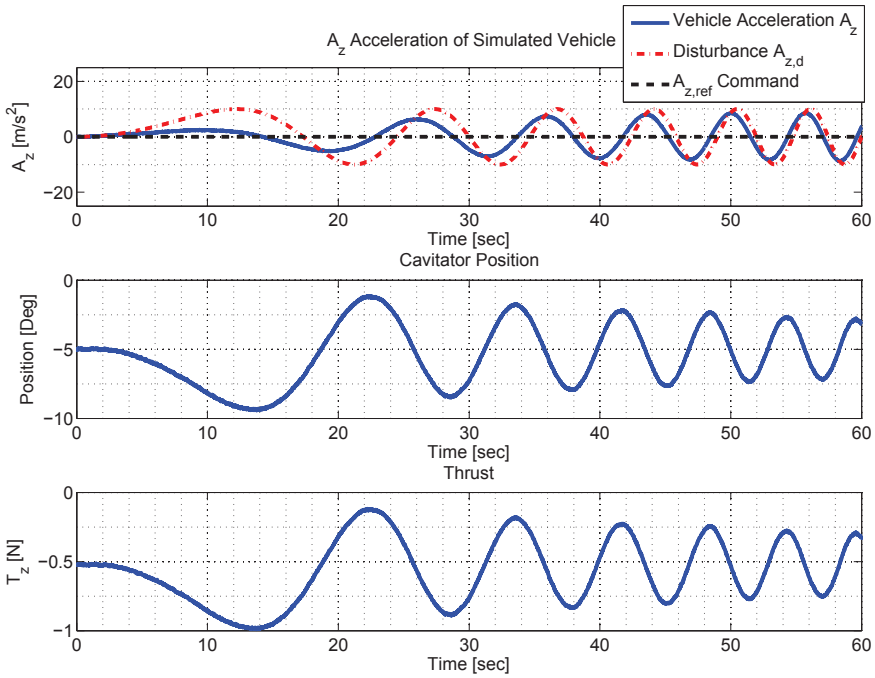

Figure 6.24: Disturbance rejection performance with the $K^1_{\delta_c}$ controller: 10 m/s^2 $A_{z,d}$ chirp disturbance at 0 - 0.2 Hz in simulation.

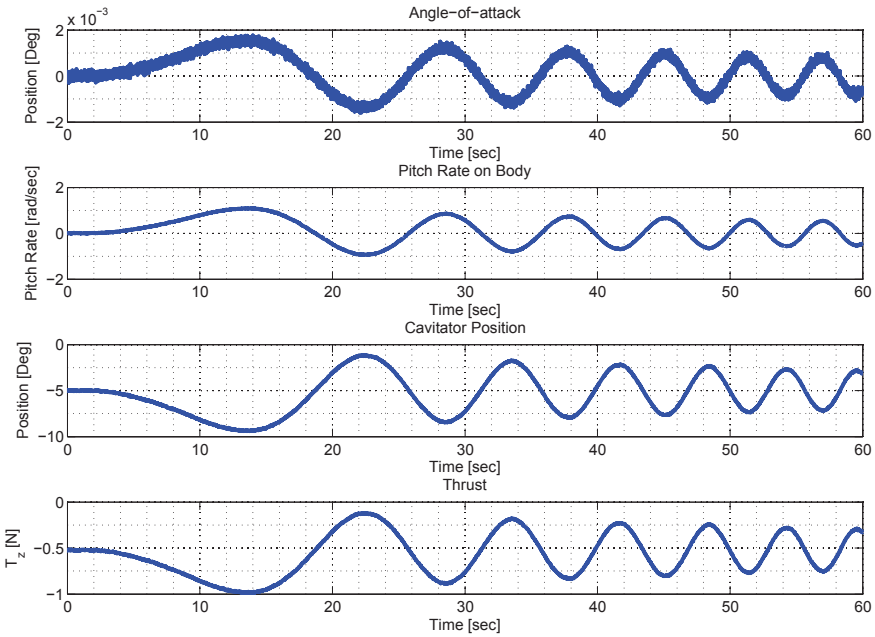

Figure 6.25: Disturbance rejection performance with the $K^1_{\delta_c}$ controller: 10 m/s^2 $A_{z,d}$ chirp disturbance at 0 - 0.2 Hz in simulation.

6.4.2 Hardware-in-the-Loop Performance: $K^1_{\delta_c}$ Controller

The $K^1_{\delta_c}$ controller is tested in a Hardware-in-the-Loop (HIL) test before the water tunnel experiments are performed. The tracking performance of the $K^1_{\delta_c}$ controller in the HIL test is shown in Figures 6.27, 6.26, and 6.28. The step response of the closed-loop system is shown in Figures 6.27 and 6.26. An $A_{z,ref}$ reference command is provided, and it is tasked with tracking $A_{z,ref}$ as it cycles through ± 10 m/s^2 steps. The tracking response is very different from the predicted simulation response. The HIL response is affected by the cable induced loads and the fact that the inner-loop thrust controller that is used in the simulations is not present in the experiments.

The HIL test response at 2 sec in Figure 6.26, illustrates the problem with the controller tracking response when the inner-loop thrust controller is not present. At this point in the experiment, the cable induced load associated with the pitch up motion of the cavitator has reached its maximum value. Hence, the response of the system that is shown in Figure 6.26 is unperturbed by the cable induced loads because the cavitator motion can only pitch up further. The cable induced load associated with increased pitch up won't change if the direction of movement remains the same. At 2 sec the controller receives the command $A_{z,ref} = 10$ m/s^2. The feedforward part of the controller responds by pitching the cavitator up to generate the desired A_z response. However, this movement is not accompanied by a corresponding thrust from the inner-loop thrust controller, as is the case in simulation. Hence, this initial movement is insufficient to generate the desired $A_{z,m}$ response. The results is that the feedforward part of the controller generates insufficient $A_{z,m}$ response, and the feedback part of the controller, which has a low bandwidth of 0.11 Hz, has to take over and move the cavitator further in order have $A_{z,m}$ converge to the desired $A_{z,ref}$ reference. This convergence is slow due to the low bandwidth of the disturbance rejection part of the controller. It takes the controller approximately 10 sec to respond to the step command. This is much slower than the desired 0.95 sec settling time. When the feedforward part of the controller is finished, the system is at $A_{z,m} = 5$ m/s^2 at 3 sec in Figure 6.26 . This is seen by the disturbance rejection part of the controller as a -5 m/s^2 disturbance that must be rejected. The disturbance rejection part of the controller proceeds to reject this disturbance and has brought it down by 90% at 12 sec to a value of $A_{z,m} = 9.5$ m/s^2 in Figure 6.26. The disturbance rejection part of the controller should have accomplished this in

7 sec, but instead does it in approximatly 9 sec.

Figure 6.27 illustrates the step response of the system, when it is perturbed by cable induced loads. The HIL test response at 4.5 sec in Figure 6.27 illustrates the challenges associated with the cable induced loads. The feedforward part of the controller starts to deflect the cavitator to generate the desired $A_{z,m}$ response. This movement causes a cable induced load to appear in the $A_{z,m}$ signal. The cable induced load initially causes a sharp negative spike which then recedes, as seen in the $A_{z,m}$ response at 4.5 - 6 sec in Figure 6.27. This perturbation is due to the cable induced load and the imperfection of the algorithm used to correct this effect, see Section 3.3, which seeks to minimize the effects of these cable induced loads. The cavitator is pitched down at 4.5 sec, and the cable induced load associated with this movement will contribute a positive $A_{z,m}$ component. However, the correction algorithm that is trying to minimize the effect of the cable induced load overshoots it at first, as seen at 4.5 - 5 sec in Figure 6.27. The correction algorithm adds too much correction to the $A_{z,m}$ signal which causes a negative spike in the $A_{z,m}$ response at 4.5 - 5 sec. As the cavitator continues to move the cable induced load approaches its maximum value, and the correction matches the cable induced load better so that the perturbation due to the cable induced load dies down. At 6.5 sec the $A_{z,m}$ signal is rid of the transient effects of the cable induced load, but the system has not reached the desired $A_{z,ref} = 0$ m/s^2 value and remains at $A_{z,m} = 6$ m/s^2. The feedforward part of the controller generates insufficient $A_{z,m}$, because the inner-loop thrust controller designed to operate in tandem with $K^1_{\delta_c}$ is not present in the experiment. The feedback part of the controller acts to move the cavitator further in order to converge to the desired $A_{z,ref}$ reference. The tracking response is qualitatively the same in Figures 6.26 and 6.27. The difference between them is that the cable induced loads perturb the $A_{z,m}$ response in Figure 6.27. The effects of the cable induced loads last approximately 2 sec and the effect is similar to a high frequency disturbance. Hence, it has almost no effect on the response of the disturbance rejection component of the $K^1_{\delta_c}$ controller which has a very low bandwidth of 0.11 Hz.

Figure 6.28 shows the tracking performance of the $K^1_{\delta_c}$ controller when it is fed a sinusoid reference command: $A_{z,ref} = 10 \sin(0.5 \cdot 2\pi t)$. The tracking performance is dominated by the cable induced loads. Whenever the cavitator direction of move-

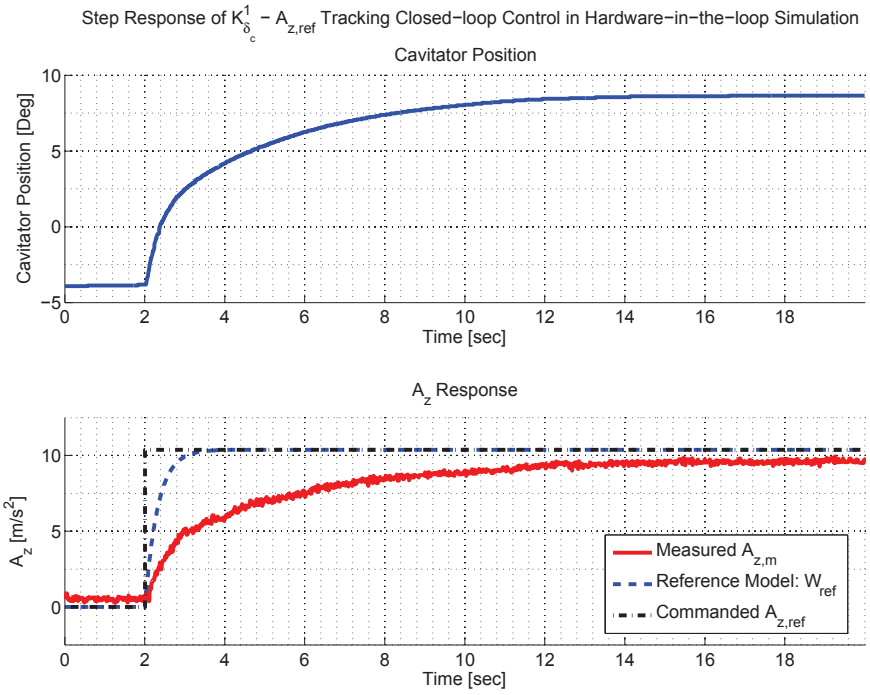

Figure 6.26: Tracking performance with $K^1_{\delta_c}$ controller: $A_{z,ref}$ step command in a hardware-in-the-loop test.

ment changes there is a sharp perturbation in the $A_{z,m}$ response due to the cable induced loads. This effect gives the tracking performance the appearance of leading the reference commands. The reference tracking is accomplished by the feedforward component of the controller. The cavitator position that is plotted in Figure 6.28 shows that the controller delivers insufficient cavitator deflection to generate the desired $A_{z,m}$ response. This is because the movement is not accompanied by a corresponding thrust from the inner-loop thrust controller, as is the case in simulation. The desired $A_{z,m}$ response is plotted as the output of the reference model W_{ref} in Figure 6.28. The controller only delivers approximately 66% of the desired $A_{z,m}$ response, when the transient effects of the cable induced loads are neglected.

The $K^1_{\delta_c}$ controller is a two-degree of freedom design. The feedforward part of the controller contributes little to its A_z tracking performance in experiment, as it relies heavily on the inner-loop controller. In experiments, where the thrust controller is not present, it is the disturbance rejection part of the controller that ends up performing the tracking task. The feedforward part of the controller moves the

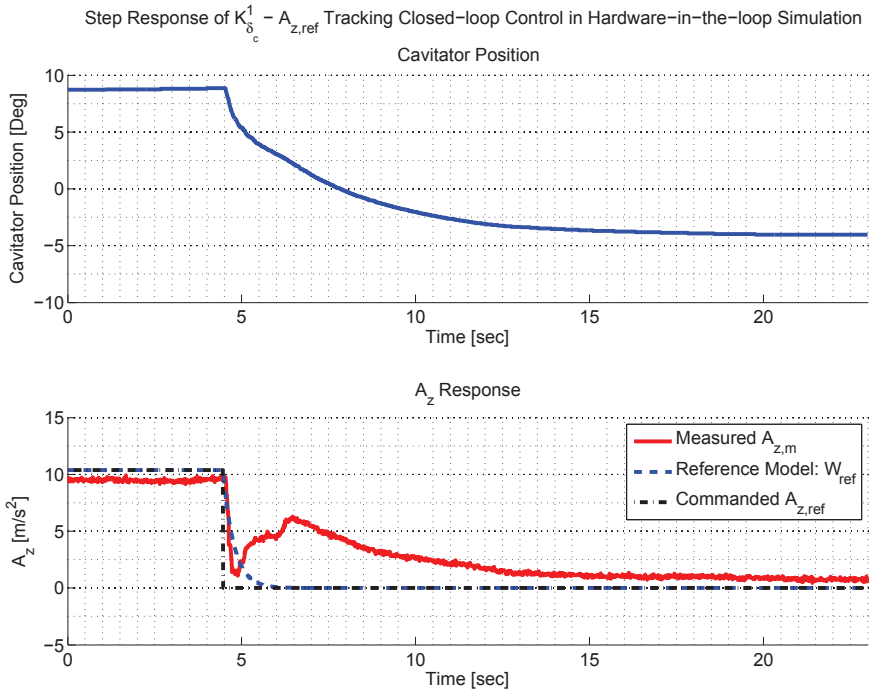

Figure 6.27: Tracking performance with $K^1_{\delta_c}$ controller: $A_{z,ref}$ step command in a hardware-in-the-loop test.

cavitator a small amount which is insufficient to reach the desired A_z value. This initial movement often causes a cable induced load which perturbs the measured acceleration. The feedforward part of the controller has a bandwidth of 0.5 Hz, while the disturbance rejection part of the controller has a bandwidth of 0.11 Hz. Hence, the action of the feedforward part of the controller, and the rapid perturbation of the $A_{z,m}$ signal due to the cable induced loads, occur in such a short span of time that the disturbance rejection part of the controller does not have the opportunity to respond to the cable induced loads. Instead this part of the controller responds to the tracking error it perceives and acts to eliminate it. The disturbance rejection part of the controller eliminates the tracking error by moving the cavitator in a smooth unidirectional motion which enables the system to track the desired $A_{z,ref}$ reference without causing any additional cable induced loads to appear.

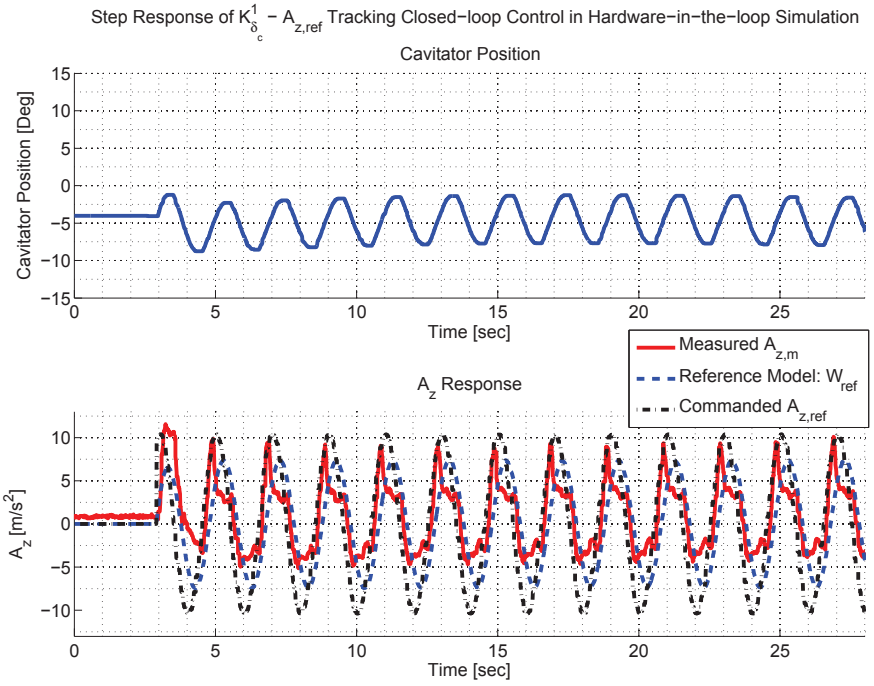

Figure 6.28: Tracking performance with $K^1_{\delta_c}$ controller: $A_{z,ref} = 10\sin(0.5 \cdot 2\pi t)$ m/s^2, in a hardware-in-the-loop test.

6.4.3 Experimental Performance of the $K^1_{\delta_c}$ Controller

The performance of the $K^1_{\delta_c}$ controller is tested on the CoSCIS test bed. The goal of this test is to determine if the controller satisfies its design specifications and achieves the desired performance. The tracking performance of the controller is studied in Section 6.4.3.1 and the disturbance rejection performance of the controller is studied in Section 6.4.3.2.

6.4.3.1 Tracking Performance of the $K^1_{\delta_c}$ Controller

The experimental step response of the $K^1_{\delta_c}$ controller is shown in Figure 6.29. A +10 m/s^2 step reference command $A_{z,ref}$ is input at 2.1 sec in Figure 6.29. The feedforward part of the controller deflects the cavitator to generate the desired $A_{z,m}$ response at 2 - 3 sec. This movement causes a cable induced load to appear in the $A_{z,m}$ signal, causing it to overshoot the target value and then settle back down to a value that undershoots it. The disturbance rejection part of the controller then continues to deflect the cavitator until the system reaches the desired $A_{z,m}$ value.

The step response in Figure 6.29 matches the step response seen in the hardware-in-the-loop tests in Section 6.4.2. The perturbation in the $A_{z,m}$ response is due to the combination of a cable induced load and an imperfect correction algorithm that is used to suppress those loads.

The tracking performance has two distinct phases, as explained in Section 6.4.2. The first phase is when the feedforward part of the controller rapidly moves the cavitator for approximately 1 sec, in an effort to track the desired $A_{z,ref}$ reference. This cavitator movement is not sufficient to generate the desired acceleration, because the feedforward part of the controller is designed to operate alongside an inner-loop thrust controller, as discussed in Sections 6.2.4.8 , 6.3.3.2, and 6.4.1. The inner-loop controller contributes to the acceleration of the vehicle in simulation. In the experiment, the inner-loop controller is not present, and the only forces which contribute to the acceleration are the hydrodynamic loads on the cavitator. The action of the feedforward part of the controller is seen at 2 - 3 sec in Figure 6.29. The cavitator movement by the feedforward part of the controller causes the cable induced loads to perturb the $A_{z,m}$ response. The disturbance rejection part of the controller is acting alongside the feedforward part of the controller, but it is operating at a bandwidth that is 1/5 of the bandwidth of the feedforward part of the controller. The action of the feedforward component of the controller dominates in the beginning, because it's bandwidth is much higher. The second phase of the tracking response is when the feedforward component of the controller is done moving the cavitator, and the disturbance rejection component of the controller takes over and brings the system to the desired $A_{z,m}$ value. The combined response of the controller is one smooth motion of the cavitator, which does not change direction while the controller tracks a step command. This method of tracking ensures that the cable induced loads are not excited unnecessarily. However the response is much slower than the desired 0.95 sec settling time of the original design.

Figure 6.30 shows the filtered tracking response of the $K^1_{\delta_c}$ controller when step and doublet $A_{z,ref}$ commands are input. The data in Figure 6.30 has been filtered to attenuate the measurement noise. The filter that is used is a fourth order low-pass Butterworth filter with a breakpoint at 2 Hz. The controller performs as expected, based on the discussion relating to the tracking performance seen in Figure 6.29. The response of the controller is dominated by the disturbance rejection part of the

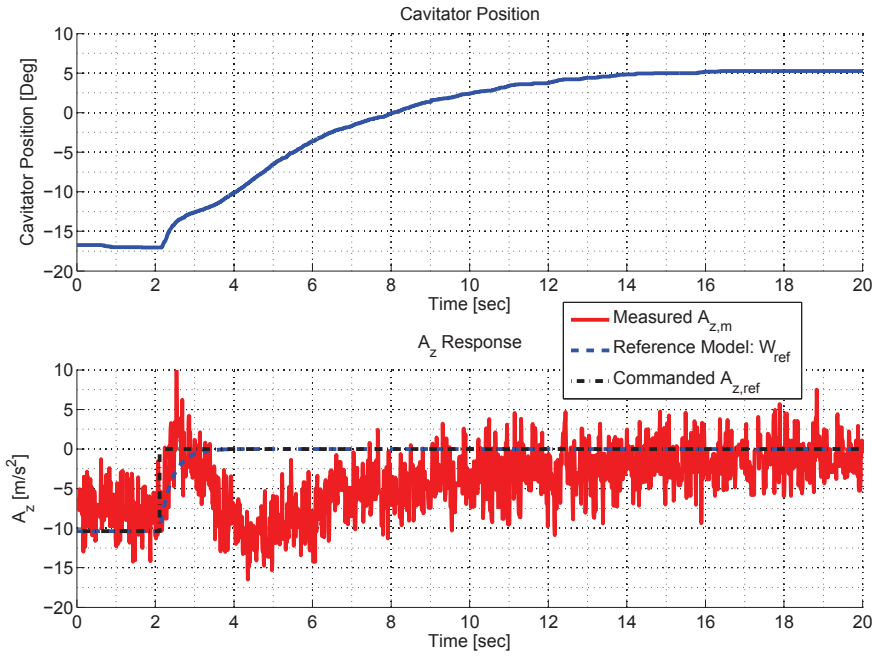

Figure 6.29: Tracking performance with $K^1_{\delta_c}$ controller: $A_{z,ref}$ step command in the water tunnel.

controller, because the feedforward part of the controller generates insufficient $A_{z,m}$.

Figure 6.31 shows the filtered tracking performance of the $K^1_{\delta_c}$ controller when the input is a sinusoid reference command: $A_{z,ref} = 10 \sin(0.5 \cdot 2\pi t)$. The filter that is used is a fourth order low-pass Butterworth filter with a breakpoint at 3 Hz. This response matches the sinusoid tracking performance that is seen in the hardware-in-the-loop tests described in Section 6.4.2. The feedforward part of the $K^1_{\delta_c}$ controller is providing the tracking performance that is seen in Figure 6.31. The $A_{z,ref}$ command is fed to the controller in the experiment, but the desired response is that of the first order reference system W_{ref}, which has a pole at 0.5 Hz. The desired W_{ref} response is plotted in Figure 6.31 with the sinusoid reference command $A_{z,ref}$ and the experimental response $A_{z,m}$. The $A_{z,m}$ response in Figure 6.31 appears to lead the desired W_{ref} response. However, upon close inspection of the cavitator position over time shows that the cavitator movement, which is being driven by the feedforward part of the controller, matches the phase of the W_{ref} response. It is the cable induced loads, which perturb the experimental $A_{z,m}$ response whenever the

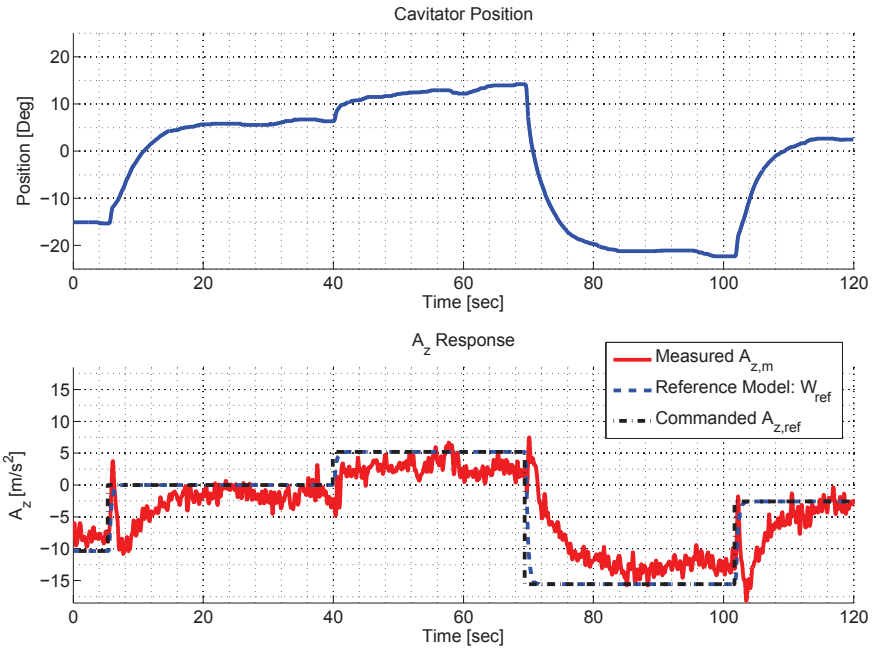

Figure 6.30: Filtered tracking performance with $K^1_{\delta_c}$ controller: $A_{z,ref}$ step and doublet commands in the water tunnel.

cavitator direction of movement is changed, that cause the response to appear to lead the W_{ref} reference. As in the step response described previously, the controller delivers insufficient cavitator deflection to generate the desired $A_{z,m}$ response. This is because the movement is not accompanied by a corresponding thrust from the inner-loop thrust controller, as is the case in simulation.

6.4.3.2 Disturbance Rejection Performance of the $K^1_{\delta_c}$ Controller

The disturbance rejection performance of the $K^1_{\delta_c}$ controller is tested in the water tunnel using the gust generator described in Section 2.2.2. The CoSCIS model is subjected to flow disturbances which the gust generator creates. The gust generator is set to deflect the angle of the flow by $\pm 8°$. The frequency of the gusts is ramped up from 0 - 0.12 Hz over 20 sec. The controller is tasked with rejecting these gust disturbances in the water tunnel. The disturbance frequency is set at 0.12 Hz, which is slightly above the controllers disturbance rejection bandwidth of 0.11 Hz. The controller is not expected to perform well at this frequency. The results of this experiment are shown in Figure 6.32. The results that are plotted in Figure 6.32

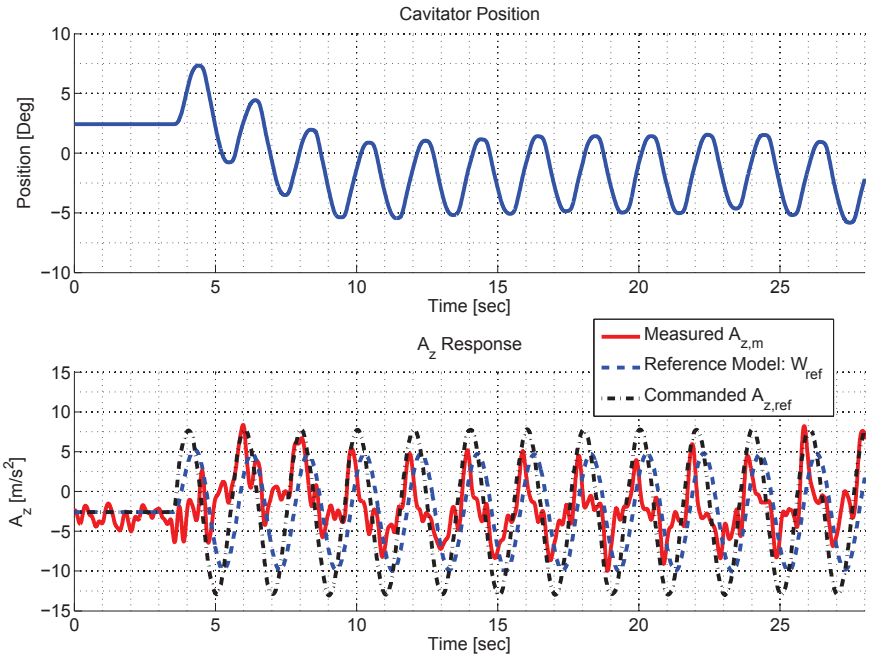

Figure 6.31: Filtered tracking performance with $K^1_{\delta_c}$ controller: $A_{z,ref} = 10\sin(0.5 \cdot 2\pi t)$ sinusoid reference command in the water tunnel.

have been filtered to attenuate the measurement noise. The filter that is used is a fourth order low-pass Butterworth filter with a breakpoint at 3 Hz. The controller is successful at rejecting the disturbances at frequencies up to 0.1 Hz, but loses its effectiveness at higher frequencies. This performance satisfied the design requirements for this controller and corresponds with the expected performance, which is based on the analysis of the controllers frequency response in Section 6.2.4.7 and simulation performance in Section 6.4.1.

6.4.4 Summary of Control Law Evaluation Results for $K^1_{\delta_c}$

The $K^1_{\delta_c}$ controller performs as expected in simulation, and achieves the desired tracking and disturbance rejection performance in the simulations in Section 6.4.1. When the controller is implemented on the CoSCIS test bed in Sections 6.4.2 and 6.4.3. Its tracking performance in experiment is very poor. The $K^1_{\delta_c}$ controller relies heavily on the feedforward part of the controller. It's tracking performance is very sensitive to the accuracy of the vehicle response. The response seen in experiments is different than the simulated response, because the thrust controller

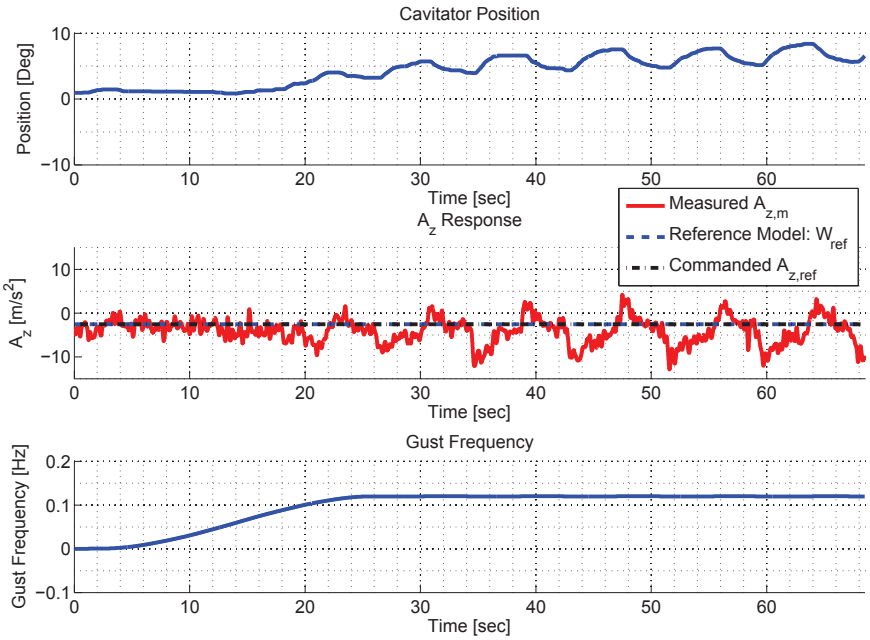

Figure 6.32: Disturbance rejection performance with the $K^1_{\delta_c}$ controller: 0 - 0.12 Hz flow disturbances in the water tunnel.

is not in the loop, and the controller delivers very poor performance as a result. The $K^1_{\delta_c}$ control law relies heavily on the inner-loop thrust controller K_{T_z} to help it track the reference commands in simulation. The K_{T_z} controller is not present in the experiments, and the tracking performance of the controller suffers. The $K^1_{\delta_c}$ controller achieves the desired disturbance rejection performance in simulation and experiments. It successfully rejects steady-state disturbances, and the effects of low frequency flow disturbances. The disturbance rejection part of the controller is not sensitive to the fact that the inner-loop controller is not present in the experiments.

6.5 Evaluation of Control Law $K^2_{\delta_c}$

The $K^2_{\delta_c}$ control law was described in Section 6.2.4. The $K^2_{\delta_c}$ controller is a two degree of freedom controller, with two inputs and one output. It can be separated into a feedforward part $K^2_{\delta_c,(1,1)}$ which shapes the controllers response to $A_{z,ref}$ commands, and a feedback part $K^2_{\delta_c,(2,1)}$ which determines the disturbance rejection, and stability properties of the controller. The $K^2_{\delta_c}$ is designed to achieve the same tracking performance as $K^1_{\delta_c}$, while improving its disturbance rejection characteristics. This controller is expected to achieve good tracking of the $A_{z,ref}$ command, with no overshoot, a rise-time of 0.7 sec, and a settling time of 0.95 sec. It is expected to achieve good disturbance rejection performance up to 3.6 Hz. The performance of the $K^2_{\delta_c}$ control law is evaluated in simulation, hardware-in-the-loop tests and water tunnel experiment in Sections 6.5.1, 6.5.2 and 6.5.3, respectively.

6.5.1 Simulation Performance of $K^2_{\delta_c}$ Controller

The tracking and disturbance rejection performance of the $K^2_{\delta_c}$ controller is studied in simulation prior to implementation on the experimental platform. The simulated step response of the controller is seen in Figures 6.33 and 6.34. The tracking response is excellent and closely tracks the desired response described by the W_{ref} reference system defined in equation 6.15. The acceleration of the vehicle is strongly affected by the noise in the $A_{z,m}$ measurement being fed back to the controller. The noise in the $A_{z,m}$ measurement manifests itself as a persistent 6 - 9 Hz oscillation in A_z. This is consistent with the results of the frequency domain analysis described in Section 6.2.4.8, which indicates that the closed-loop system with the $K^2_{\delta_c}$ controller in the loop is sensitive to measurement noise, and that this noise will perturb the A_z output. The analysis identified a particular sensitivity to noise in the 3 - 13 Hz frequency range. Noise in that frequency range is amplified by the action of the control system. This phenomena is seen in all of the simulation results for the $K^2_{\delta_c}$ controller.

The simulated disturbance rejection performance of the $K^2_{\delta_c}$ controller is shown in Figures 6.35, 6.36, 6.37, and 6.38. The A_z acceleration of the system is perturbed by a step disturbance signal $A_{z,d} = 10$ m/s^2 in Figures 6.35, and 6.36. The $K^2_{\delta_c}$ controller quickly rejects the step disturbance, reducing it to the noise range in approximately 0.5 sec. This is in line with the expected performance, described in

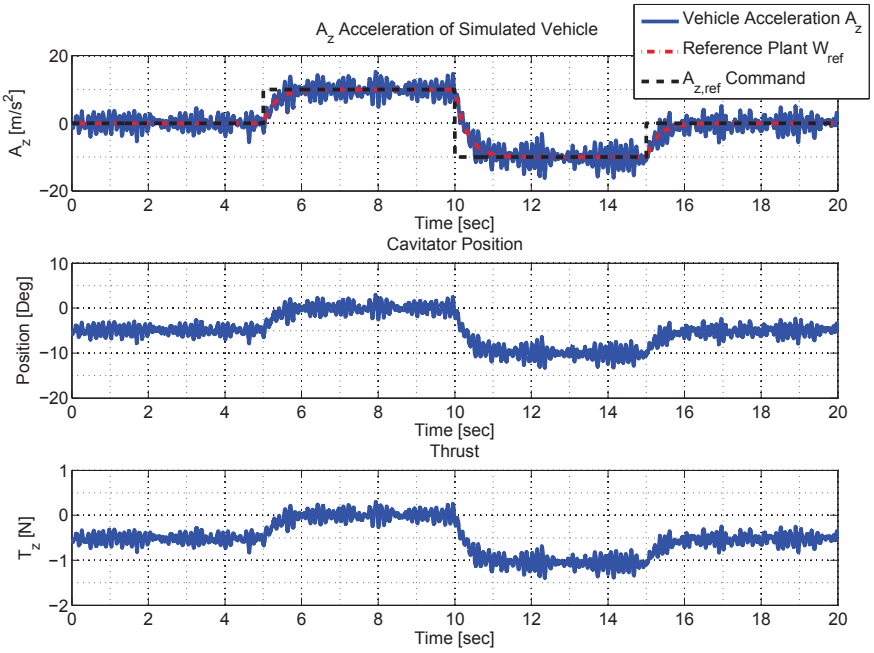

Figure 6.33: z_{body}-axis acceleration tracking performance with the $K^2_{\delta_c}$ controller: ± 10 m/s^2 $A_{z,ref}$ doublet command in simulation.

Section 6.2.4.8. The vehicle settles down to a new trim when it has rejected the disturbance. The trim is described by a small constant pitching rate. This occurs because the $K^2_{\delta_c}$ controller is designed to tolerate a small tracking error in A_z, and a non-zero A_z translates into a non-zero pitch rate when the angle-of-attack of the vehicle is regulated to zero.

The A_z acceleration of the system is perturbed by a 10 m/s^2 chirp disturbance in Figures 6.37 and 6.38. The chirp disturbance is described by a sinusoid with a frequency which grows from 0 Hz to 5 Hz in 15 sec. The chirp signal is defined as

$$A^{2,chirp}_{z,d} = 10 \cdot \sin\left(\frac{5}{15} 2\pi t\right) \text{ m/s}^2 \tag{6.30}$$

The $K^2_{\delta_c}$ controller is very good at attenuating the chirp disturbance for the first 6 sec of the simulation, which corresponds to sinusoids at frequencies of 0 - 2 Hz. The attenuation becomes progressively worse as the frequency of the chirp disturbance increases. At approximately 12 sec, when the frequency of the chirp disturbance is 4 Hz, the acceleration of the vehicle surpasses the size of the disturbance, i.e. the

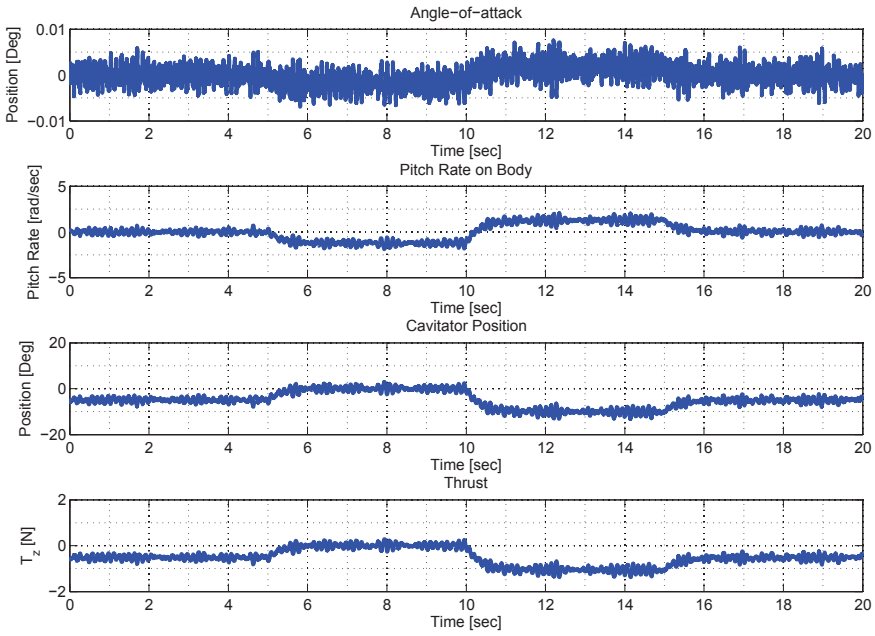

Figure 6.34: Angle-of-attack and pitch rate tracking performance with the $K^2_{\delta_c}$ controller: ± 10 m/s^2 $A_{z,ref}$ doublet command in simulation.

disturbance is magnified, rather than attenuated. This result is expected from the analysis of the frequency response in Section 6.2.4.8. The closed-loop $\frac{A_z(s)}{A_{z,d}(s)}$ transfer function, with the $K^2_{\delta_c}$ controller in the loop, has low gain at low frequencies but crosses unity gain from below at 4.4 Hz and has a peak at 7.85 Hz. Hence, sinusoid $A_{z,d}$ disturbances being input to the system at frequencies above 4.4 Hz are expected to be amplified as seen in the simulation.

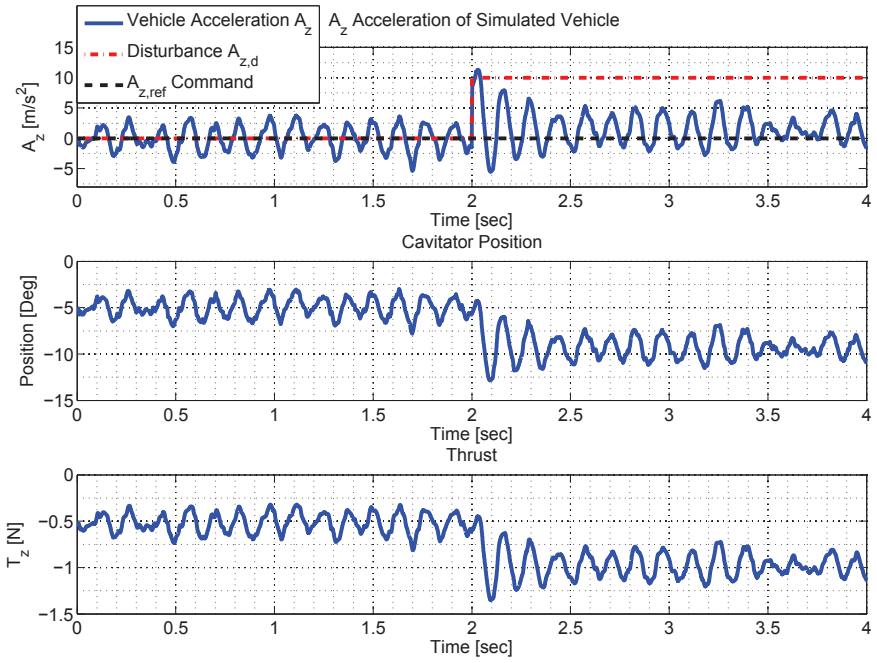

Figure 6.35: z_{body}-axis acceleration disturbance rejection performance with the $K^2_{\delta_c}$ controller: 10 m/s^2 $A_{z,d}$ step disturbance in simulation.

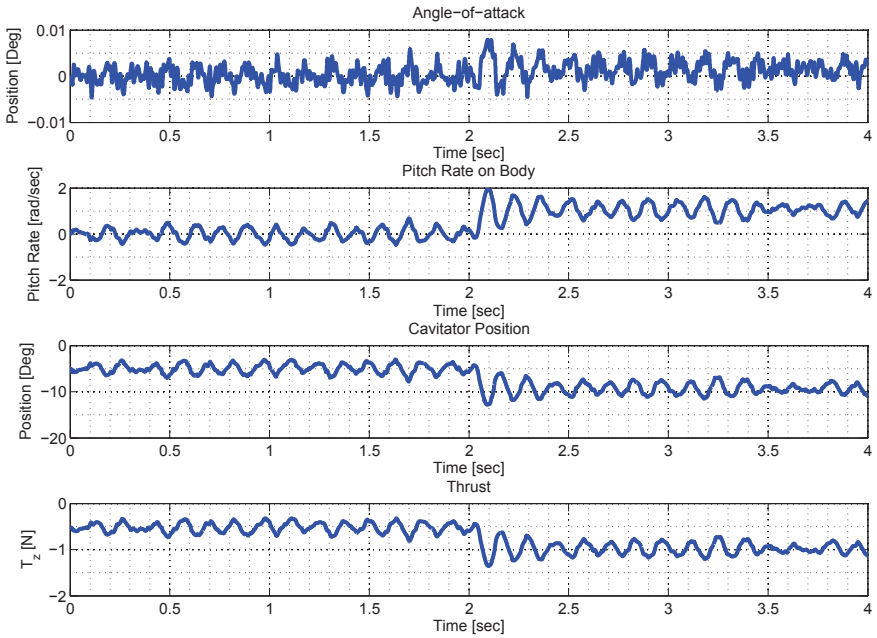

Figure 6.36: Angle-of-attack and pitch rate disturbance rejection performance with the $K^2_{\delta_c}$ controller: 10 m/s^2 $A_{z,d}$ step disturbance in simulation.

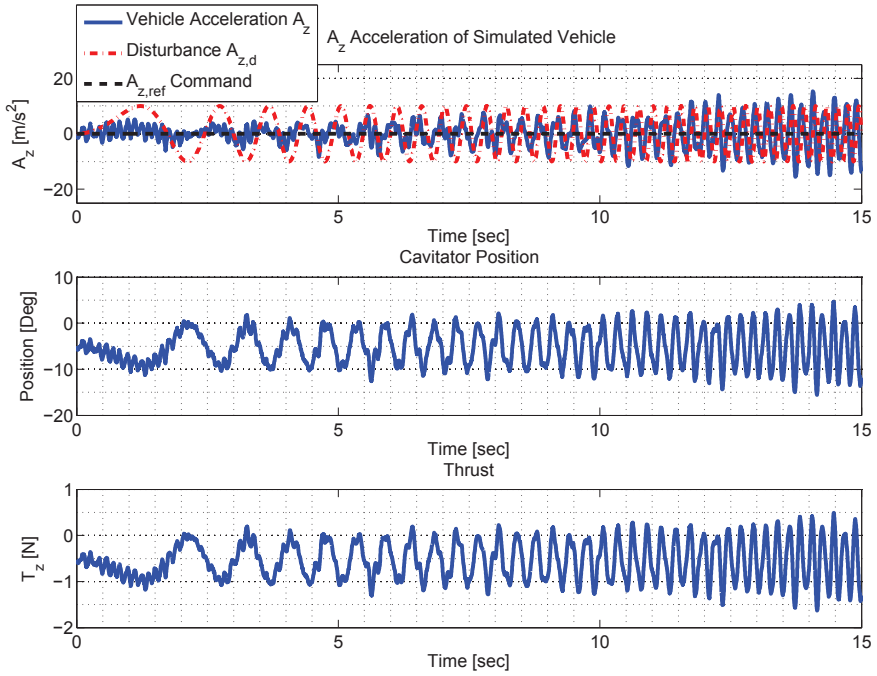

Figure 6.37: z_{body}-axis acceleration disturbance rejection performance with the $K^2_{\delta_c}$ controller: 10 m/s^2 $A_{z,d}$ chirp sinusoidal disturbance at 0 - 5 Hz in simulation.

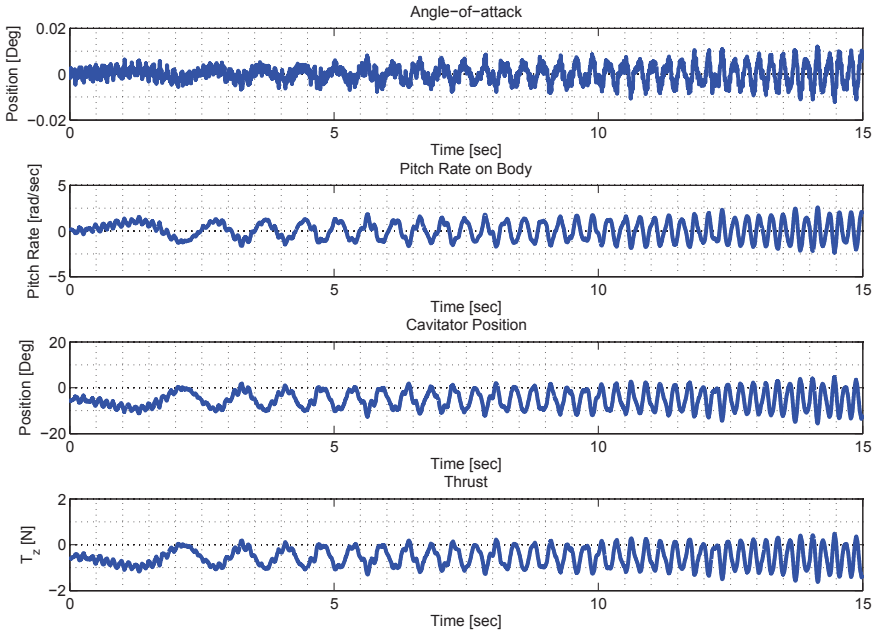

Figure 6.38: Angle-of-attack and pitch rate disturbance rejection performance of the $K^2_{\delta_c}$ controller: 10 m/s^2 $A_{z,d}$ chirp sinusoidal disturbance at 0 - 5 Hz in simulation.

6.5.2 Hardware-in-the-Loop Performance: $K^2_{\delta_c}$ Controller

The $K^2_{\delta_c}$ controller is tested in a Hardware-in-the-Loop (HIL) test before the final experiments are performed. The tracking performance of the $K^2_{\delta_c}$ controller in the HIL test is shown in Figures 6.39 and 6.40. The step response of the closed-loop system is shown in Figure 6.39. An $A_{z,ref}$ reference command is input, and it is tasked with tracking it as $A_{z,ref}$ cycles through ± 10 m/s^2 steps over 35 sec. The system tracks the reference commands with the desired first order response that is described by the W_{ref} reference system, as seen in Figure 6.39. The tracking response is good, but the $A_{z,m}$ response contains unwanted perturbations due to the cable induced loads. The system suffers from oscillation in the cavitator deflection, and consequently in the $A_{z,m}$ signal. This effect is especially pronounced when $A_{z,ref} = -10$ m/s^2 at 3.5 - 10.5 sec. The system suffers from two distinct oscillation modes at 3.5 - 10.5 sec. A fast oscillation at approximately 3.9 Hz, and a slower oscillation at approximately 0.66 Hz. The oscillations in the cavitator cause significant cable induced loads in the $A_{z,m}$ measurement. The oscillation at 3.9 Hz is near the bandwidth of the disturbance rejection part of the controller, which is at 3.6 Hz. This effect is likely to be seen in the actual water tunnel experiment, and to be made worse by the measurement noise which was seen to perturb the system significantly in the simulations described in Section 6.5.1.

The system displays considerable undershoot as it tracks the reference signal. This response can be seen at 2 sec in Figure 6.39. This phenomenon is associated with the feedforward part of the controller. The controller is fed a $A_{z,ref} = -10$ m/s^2 reference signal at 2 sec, and instead of moving the cavitator directly in the negative direction that will generate the desired $A_{z,m}$, it displays undershoot, i.e. an initial movement in the wrong direction, where it first moves approximately $+5^\circ$ before reversing direction and moving in the negative direction. Analysis of the closed-loop $\frac{\delta_c}{A_{z,ref}}$ transfer function indicates that the system should not have any undershoot. Undershoot is characteristic of systems with RHP zeros. The closed-loop $\frac{\delta_c}{A_{z,d}}$ transfer function, which is associated with the disturbance rejection part of the controller, has a RHP zero at approximately 8 Hz because of the time-delay in the $A_{z,m}$ measurement. This results in undershoot, as seen in the simulated disturbance rejection results that are shown in Figures 6.18 and 6.35. The disturbance rejection part of the controller has a higher bandwidth than the feedforward part of the controller,

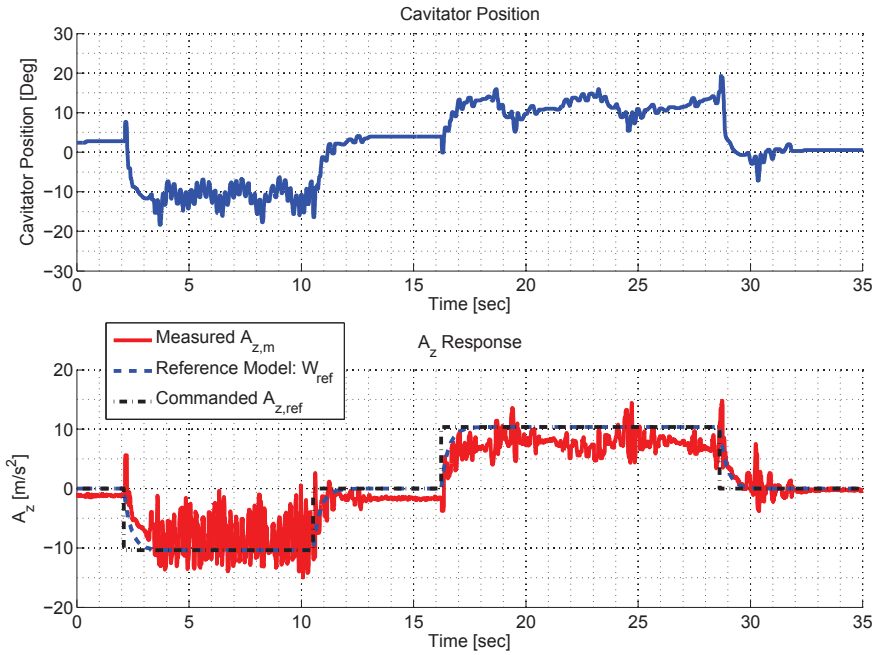

Figure 6.39: Tracking performance with the $K^2_{\delta_c}$ controller: $A_{z,ref}$ doublet command, in a hardware-in-the-loop test.

i.e. 3.6 Hz as compared to the feedforward part's 0.5 Hz. It is possible that the undershoot is caused by the way the control system is implemented on the CompactRIO. If the reference command is treated as a disturbance to be rejected for a few time steps on the controller on board the CompactRIO, that would be sufficient to cause the disturbance rejection part of the controller to send a command to the actuator which would cause the undershoot. It is difficult to determine the validity of this hypothesis.

Figure 6.40 shows the tracking performance of the $K^2_{\delta_c}$ controller subject to a sinusoid reference command: $A_{z,ref} = 10 \sin(0.5 \cdot 2\pi t)$. The tracking performance is satisfactory, but whenever the cavitator direction of movement changes there is a spike in the $A_{z,m}$ response due to the cable induced loads. The controller treats this spike as a disturbance which it then tries to compensate. The cable induced load does not prevent the controller from achieving satisfactory tracking performance. The aforementioned undershoot in the tracking performance is also present in the results presented in Figure 6.40, and can be seen at 1.75 sec.

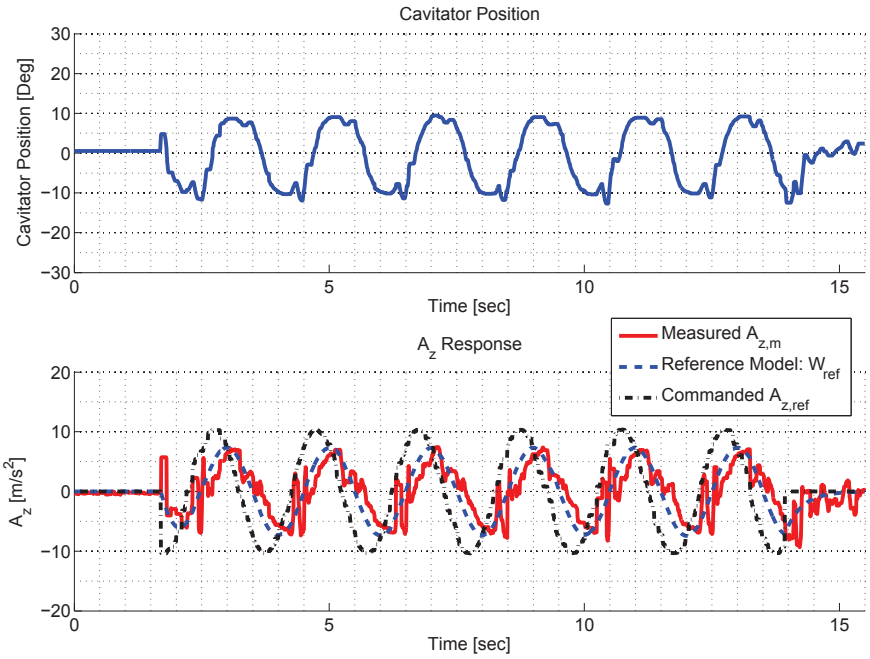

Figure 6.40: Tracking performance with $K^2_{\delta_c}$ controller: $A_{z,ref} = 10\sin(0.5 \cdot 2\pi t)$ m/s^2, in a hardware-in-the-loop test.

6.5.3 Experimental Performance of the $K^2_{\delta_c}$ Controller

The performance of the $K^2_{\delta_c}$ controller is tested on the CoSCIS test bed. The goal of this test is to determine if the controller satisfies its design specifications and achieves the desired performance. The tracking performance of the controller is studied in Section 6.5.3.1 and the disturbance rejection performance of the controller is studied in Section 6.5.3.2.

6.5.3.1 Tracking Performance of $K^2_{\delta_c}$ Controller

The tracking performance of the controller $K^2_{\delta_c}$ is tested on the CoSCIS test bed. The filtered tracking response to step command is shown in Figure 6.41. The results shown in Figure 6.41 have been filtered to attenuate the measurement noise. The filter that is used is a fourth order low-pass Butterworth filter with a breakpoint at 5 Hz. The control system is fed a -10 m/s^2 step in the reference command $A_{z,ref}$ at 4 sec in Figure 6.41. The system has the desired settling time, but it does not achieve the desired smooth first order response or tight tracking desired. It has a

very significant "hunting" behavior in the response. This hunting response is characterized by the slow oscillation about the desired $A_{z,m}$ value. The system has two different oscillations in its response. There is a fast oscillation at 3.9 Hz, and a slow "hunting" oscillation at 0.65 Hz. These same oscillation frequencies were observed in the hardware-in-the-loop tests in Section 6.5.3.1. The results from the hardware-in-the-loop tests demonstrate that neither the fast oscillation nor the "hunting" oscillation are due to hydrodynamic effect in the experiment. The oscillations are due to the limitations of the hardware. Figures 6.42 and 6.43 show the results when the system is tasked with tracking multiple doublets and step commands sequentially. The results shown in Figures 6.42 and 6.43 have been filtered to attenuate the measurement noise. The filter that is used is a fourth order low-pass Butterworth filter with a breakpoint at 5 Hz. The system has the desired tracking response and matches the desired W_{ref} reference system response well, except of the hunting behavior. This is good performance in the face of the challenges associated with the measurement noise, and cable induced loads.

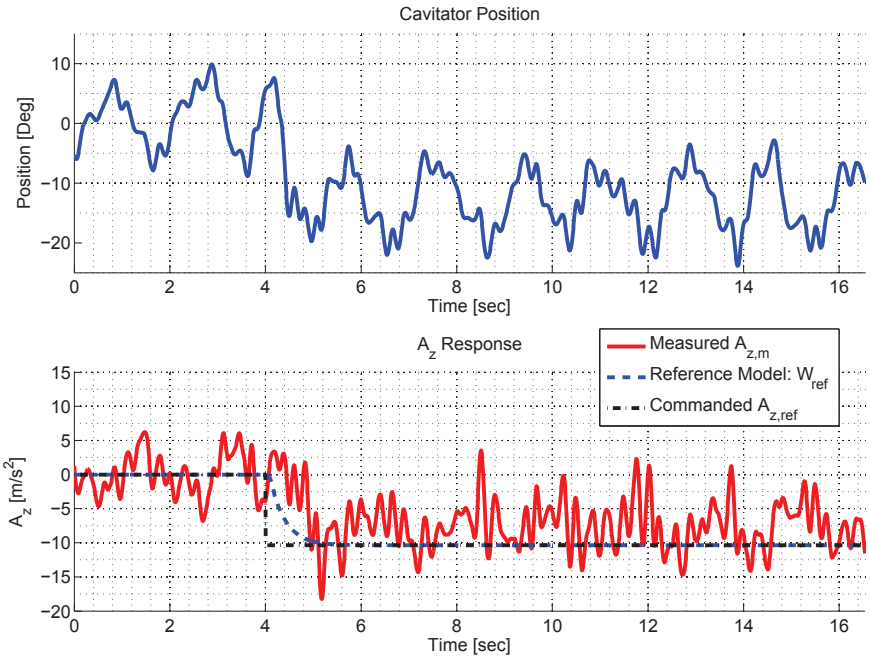

Figure 6.41: Water tunnel tracking performance with the $K^2_{\delta_c}$ controller: $A_{z,ref}$ step command.

Figure 6.44 shows the tracking performance of the $K^2_{\delta_c}$ controller when the reference

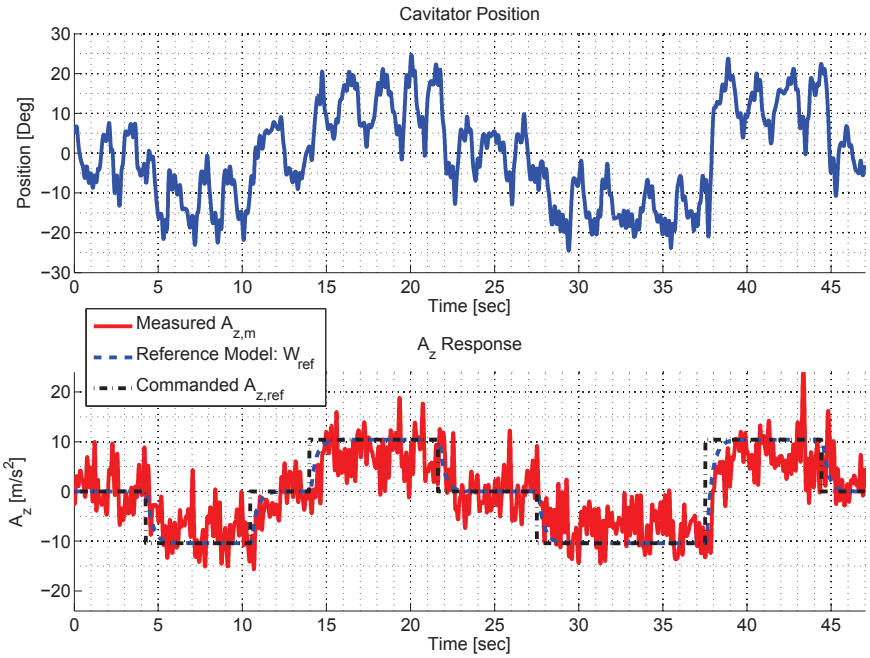

Figure 6.42: Water tunnel tracking performance with $K^2_{\delta_c}$ controller: $A_{z,ref}$ doublet commands.

command is a sinusoid: $A_{z,ref} = 10 \sin(0.5 \cdot 2\pi t)$. The results shown in Figure 6.44 have been filtered to attenuate the measurement noise. The filter that is used is a fourth order low-pass Butterworth filter with a breakpoint at 5 Hz. The controller achieves the desired tracking response, despite the measurement noise and cable induced loads. This response is similar to the sinusoid tracking performance seen in the hardware-in-the-loop tests described in Section 6.4.2, except the tracking performance is slightly degraded due to the noise level in the water tunnel experiment.

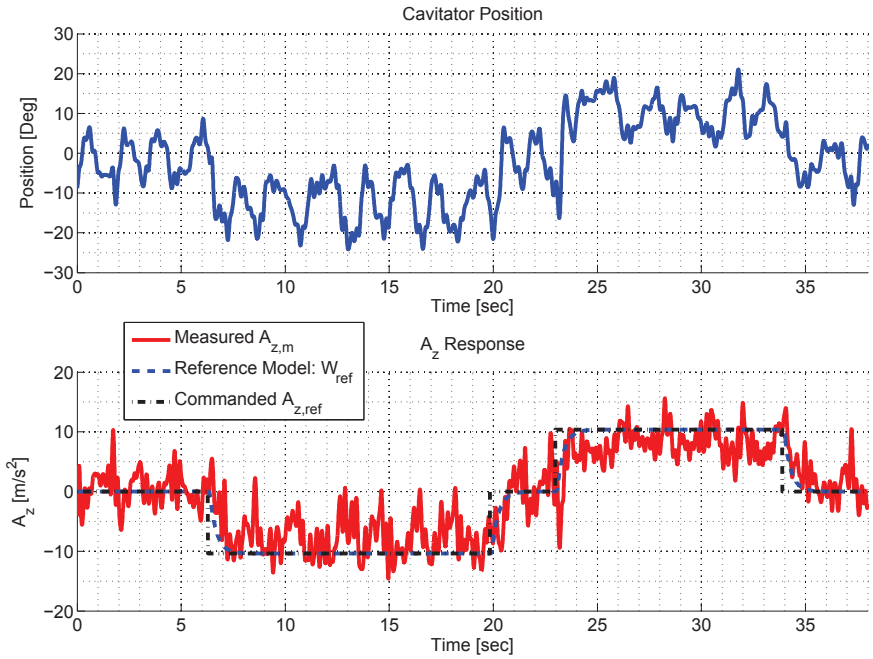

Figure 6.43: Water tunnel tracking performance with $K^2_{\delta_c}$ controller: $A_{z,ref}$ doublet command.

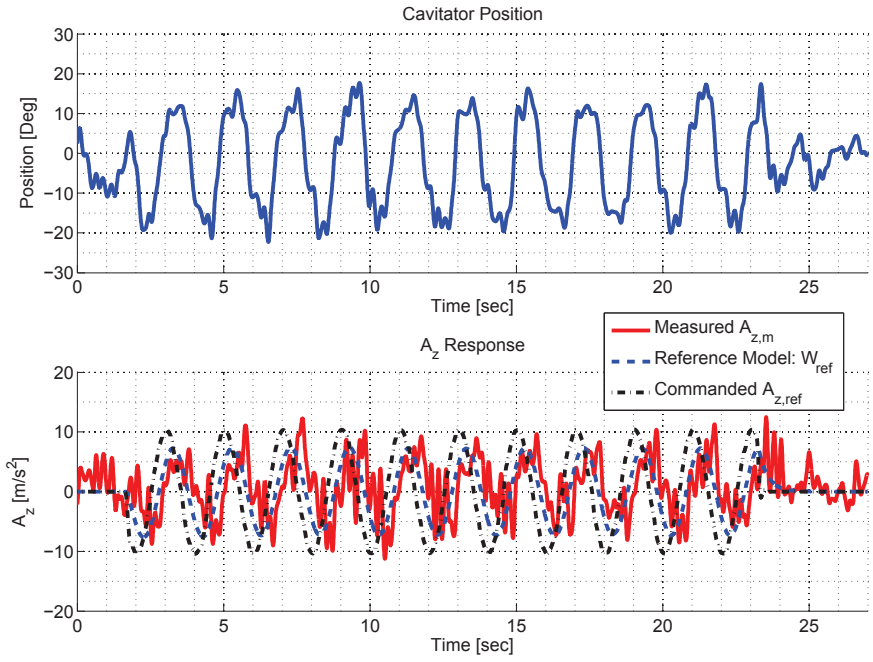

Figure 6.44: Water tunnel tracking performance with $K^2_{\delta_c}$ controller: $A_{z,ref} = 10\sin(0.5 \cdot 2\pi t)$ sinusoid reference command.

6.5.3.2 Disturbance Rejection Performance of $K^2_{\delta_c}$ Controller

The disturbance rejection performance of the $K^2_{\delta_c}$ controller is tested in the water tunnel using the gust generator described in Section 2.2.2. The CoSCIS model is subjected to flow disturbances which the gust generator creates. The gust generator is set to deflect the angle of the flow by $\pm 8°$. The frequency of the gusts is ramped from 0 - 0.1.88 Hz over 25 sec. The controller is tasked with rejecting these gust disturbances in the water tunnel. The final frequency that the disturbances enter at is 1.88 Hz, which is below the controllers disturbance rejection bandwidth of 3.6 Hz. The controller is expected to perform well at this frequency range. The results of the experiment are shown in Figure 6.45. The results shown in Figure 6.45 have been filtered to attenuate the measurement noise. The filter that is used is a fourth order low-pass Butterworth filter with a breakpoint at 5 Hz.

The controller is successful at rejecting the disturbances at frequencies up to 1.88 Hz, in the sense that they do not perturb the $A_{z,m}$ response more than the "hunting" oscillations which persist in the system. This performance satisfied the design requirements for this controller and corresponds with the expected performance, which is based on the analysis of the controllers frequency response in Section 6.2.4.8 and simulation performance in Section 6.5.1. However, the utility of the test is hampered by the constant "hunting" oscillations that degrade the tracking and disturbance rejection performance throughout all of the water tunnel experiments.

6.5.4 Summary of Control Law Evaluation Results for $K^2_{\delta_c}$

The $K^2_{\delta_c}$ controller is tested in simulation in Section 6.5.1. It achieves the desired tracking and disturbance rejection performance, but the quality of the performance is degraded by measurement noise in the simulation. The controller is implemented on the CoSCIS test bed in Sections 6.4.2 and 6.4.3. The tracking performance in water tunnel experiments is adequate, but suffers from a fast oscillation that appears near its bandwidth frequency, and "hunting", i.e. a slow oscillation about the desired $A_{z,m}$ value. These oscillations are a product of the noise in the experiment, and the cable induced loads associated with the cavitator movement. Unlike the $K^1_{\delta_c}$ controller, the performance of the $K^2_{\delta_c}$ controller is unaffected by the absence of the inner-loop thrust controller in the experiments. This is because the $K^2_{\delta_c}$ is more aggressive at rejecting disturbances than $K^1_{\delta_c}$. The disturbance rejection component

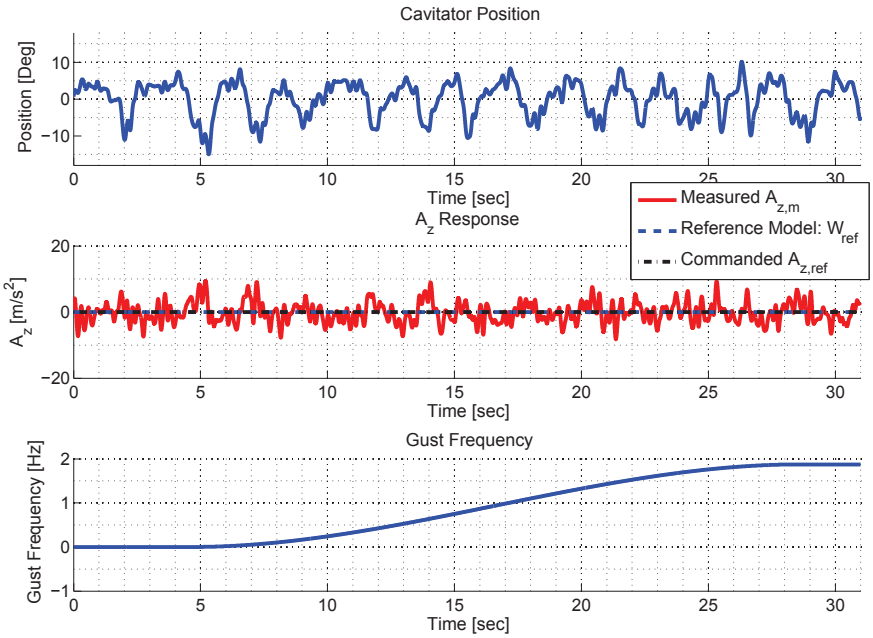

Figure 6.45: Water tunnel disturbance rejection performance of $K^2_{\delta_c}$ controller: 0 - 1.88 Hz flow disturbances.

of $K^2_{\delta_c}$ has a higher bandwidth than the feedforward response, and can compensate for its poor performance. The $K^2_{\delta_c}$ controller achieves the desired disturbance rejection performance in simulation. In the experiments the "hunting" behavior in the tracking response has a large time-varying effect on the response. This phenomenon makes it hard to distinguish between oscillations in the $A_{z,m}$ response due to flow disturbances, and oscillations due to the "hunting". Hence, the controller is either very good at attenuating the effects of the flow disturbances, or the "hunting" behavior in the response completely masks their effects. The $K^2_{\delta_c}$ controller successfully rejects steady-state disturbances associated with the cable induced loads, and the tracking response is unaffected by the gust flow disturbances.

6.6 Summary of Results

The CoSCIS test bed was used to evaluate the basic performance of the two proposed controllers, i.e. step tracking performance, sinusoid tracking performance, and sinusoid disturbance rejection performance. The response from the CoSCIS test bed during water tunnel experiments did not exactly match the simulation response for these simple maneuvers. This is primarily due to the low signal to noise ratio on the load-cell measurements, and the cable induced loads that are associated with the movement of the cavitator. The cable induced loads perturb the load-cell measurements and create an unwanted non-linear dynamic between the cavitator movement and the force measurements.

The controllers are synthesized as two-degree-of-freedom controllers. Their tracking performance is decoupled from their disturbance rejection performance and they both share the same feedforward response. The $K^1_{\delta_c}$ controller is designed to have low bandwidth in its disturbance rejection. The experiments confirm that it is robust to high levels of noise, and has excellent performance at rejecting steady state and low frequency disturbances. The controller has poor reference tracking performance in experiment, because the cable induced loads perturb the measurement and it takes the controller a long time to reject the perturbation due to its low bandwidth disturbance rejection component. The controller tolerates the cable induced loads and the high levels of noise, without sustaining any negative effects beyond the poor tracking performance. This result aligns with the simulations and frequency domain analysis, which indicated excellent robustness to input and output multiplicative uncertainty. The performance of the $K^1_{\delta_c}$ controller stands in stark contrast to the performance of $K^2_{\delta_c}$, which is susceptible to noise and cable induced loads.

The $K^2_{\delta_c}$ controller is designed to push the bandwidth to the limit imposed by the time-delay in the feedback measurement. Frequency domain analysis and simulations indicate that this design has poor stability margins, is susceptibility to noise, and is not robust to input and output multiplicative uncertainty. The design achieves great performance at lower frequencies but is very sensitive to noise and disturbances in a frequency band near the crossover frequency. The system suffers from poor performance in this frequency band, due to the aggressive performance requirements at lower frequencies and the limiting effects of the time-delay. Experiments show that the analysis and simulation are correct that the system is very sensitive to the

noise, and the non-linear dynamic due to the cable induced loads. The $K^2_{\delta_c}$ controller achieves the expected tracking and disturbance rejection performance, but the response is plagued by noise, small amplitude oscillations that appear near the bandwidth of the controller, and low frequency "hunting".

The noise and cable induced loads have a significant effect in the experiments, and limit the utility of the test bed in evaluating the performance of feedback control systems. The test bed is effective at evaluating the basic performance and defining characteristics of control algorithms, as demonstrated in this chapter when two very disparate control laws are compared. However, the response seen in experiments is distorted due to the limitations of the experiment, and is not an exact match to the response of the simulated supercavitating vehicle. Hence, it is not possible to completely validate the performance of control algorithms due to the test bed limitations.

Chapter 7

Conclusions

7.1 Summary

The work presented in this thesis describes the development and testing of an experimental test bed for validating the performance of control strategies for supercavitating vehicles. The test bed addresses the need for an experimental platform to enable researchers to test candidate control algorithms and associated technologies on a real, physical, supercavitating system.

The Control Surface and Cavity Interaction Simulator (CoSCIS) test bed was developed to model a supercavitating vehicle in flight in a water tunnel experiment. The experimental vehicle had a controllable cavitator and fin control surfaces, and was mounted on a six degree of freedom force and moment load-cell. The entire body of the experimental vehicle was surrounded by an axisymmetric cavity.

The test bed was used to evaluate the performance of feedback control systems on a model supercavitating vehicle in a water tunnel. The capabilities of the test bed are limited by several implementation issues that were encountered when the CoSCIS system was integrated. The implementation issues resulted in the fins being removed from the model, and limited the range of potential control architectures that could be tested. Two controllers were developed using H_∞ control design techniques and evaluated on the test bed. A partial validation of their performance was obtained, and tests showed that the cavity is robust to fast cavitator actuation. The validity of the hydrodynamic model that the control designs were based on

was also established. The experiments demonstrated that a test bed of this kind can be used to evaluate control algorithms, and study the effects of active control systems on a supercavitating vehicle. These supercavitating control experiments and results played a central role in the redesign of the experimental test bed by current researchers.

7.2 Recommendations

Several implementation issues were encountered when the test bed was integrated and tested, which should be avoided in any future work. The most significant issues were:

1. Low signal to noise ratio in the force and moment measurements.
2. Poorly implemented cavitator deflection mechanism which causes backlash, uncertainty in the cavitator positioning method, and nonlinear perturbations to the force and moment measurements.
3. Limitations placed on the scope of the control experiments due to the lack of fins, i.e. constraining the control design to use the cavitator only.

The insights gained in this work have already been adapted by current researchers when the experimental test bed was redesigned. The redesigned vehicle was able to address the issues associated with the actuation mechanism, use the fins in experiments, and mitigate the effect of the the small signal to noise ratio in the force and moment measurements.

The primary insight was that the CoSCIS model should be made larger, and the actuators placed inside the model body. This design achieves two things: First, it prevents the actuators from perturbing the load-cell measurements, because they sit inside the model body that is mounted on the load-cell. Second, the linkage between the actuators and the control surfaces can be made rigid by using push rods, which eliminates the excessive backlash that is associated with the actuation scheme presented in this thesis.

The experience from this work has shown that the AMTI MC1-250 load-cell is sensitive to temperature and pressure changes, and it should not be placed in the

flow near the cavity closure. Future designs should attempt to isolate the load-cell from the supercavity and its wake.

An ideal test bed for supercavitating vehicle control research would allow the test body to have additional freedom of motion, i.e. the ability to pitch freely or plunge inside the water tunnel test section. The force and moment measurements could then be replaced or augmented by measurements of the states associated with the degree of freedom, e.g. a vehicle model that is free to pitch can supply pitch rate, pitch angle, and angle-of-attack measurements to the controller.

Bibliography

[1] Dzielski, J. E., "Longitudinal Stability of a Supercavitating Vehicle," *IEEE Journal of Oceanic Engineering*, Vol. 36, No. 4, Oct. 2011, pp. 562–570.

[2] Federation of American Scientists, "VA-111 Shkval underwater rocket," (accessed March 5, 2012), `http://www.fas.org/man/dod-101/sys/missile/row/shkval.htm`.

[3] United States Navy, "United States Navy Fact File: Attack Submarines - SSN," (accessed March 5, 2012), `http://www.navy.mil/navydata/fact_display.asp?cid=4100&tid=100&ct=4`.

[4] Vincent C., T., *The Almanac of Seapower*, Navy League of the United States, 1987.

[5] Federation of American Scientists, "Project 705 Lira Alfa class Attack Submarine (Nuclear Powered)," (accessed March 5, 2012), `http://www.fas.org/man/dod-101/sys/ship/row/rus/705.htm`.

[6] Ng, K. W., "Overview of the ONR Supercavitating High-Speed Bodies Program," *AIAA Guidance, Navigation, and Control Conference*, No. AIAA 2006-6440, Aug. 2006.

[7] Kirschner, I. N., Uhlman, J. S., and Perkins, J. B., "Overview of High-Speed Supercavitating Vehicle Control," *AIAA Guidance, Navigation, and Control Conference*, No. AIAA 2006-6442, Aug. 2006.

[8] Kuklinski, R., Fredette, A., Henoch, C., and Castano, J., "Experimental Studies in the Control of Cavitating Bodies," *AIAA Guidance, Navigation, and Control Conference*, Aug. 2006, AIAA 2006-6443.

[9] Kirschner, I. N., Fine, N. E., Uhlman, J. S., Gieseke, T. A., Kuklinski, R., Kring, D. C., Rosenthal, B. J., Varghese, A. N., Stinebring, D. R., Dzielski, J., Lindau, J. W., and Kunz, R. F., "Supercavitation research and development," *Undersea Defense Technologies*, Waikiki, HI, Oct. 2001.

[10] Syrstad, J. J., *Experimental Investigation of Wedge Shaped Fin and Supercavity Interaction*, Master's thesis, University of Minnesota, 2006.

[11] Vanek, B., *Control methods for High-Speed Supercavitating Vehicles*, Ph.D. dissertation, University of Minnesota, 2008.

[12] Mokhtarzadeh, H., *Supercavitating Vehicle Modeling and Dynamics for Control*, Master's thesis, University of Minnesota, 2010.

[13] Mao, X., *Nonlinear robust control design for a high-speed supercavitating vehicle*, Ph.D. dissertation, The Pennsylvania State University, 2010.

[14] Wired, "Maritime Batmobile Hopes to Combat Pirates, Iran," (accessed March 5, 2012), `http://www.wired.com/dangerroom/2012/01/maritime-batmobile-hopes-to-combat-pirates-iran/`.

[15] Juliet Marine Systems Inc., "GHOST," (accessed March 5, 2012), `http://julietmarine.com/Products.htm`.

[16] Popular Science, "Supercavitating Torpedo," (accessed March 5, 2012), `http://www.popsci.com/scitech/article/2004-06/supercavitating-torpedo`.

[17] Wikipedia, "VA-111 Shkval," (accessed March 5, 2012), `http://en.wikipedia.org/wiki/VA-111_Shkval`.

[18] Delpero, P. M., *Investigation of flows around a two dimensional hydrofoil subject to a high reduced frequency gust loading*, Master's thesis, Massachusetts Institute of Technology, 1992.

[19] Kopriva, J. E., *Experimental Study of a High Performance Partial Cavitating Hydrofoil under Steady and Periodic Flows*, Master's thesis, Univerisity of Minnesota, 2006.

[20] AMTI, "MC1-250 Force/Torque Sensor Fact sheet," (accessed December 23, 2011), `http://www.amti.uk.com/downloads/MC1.pdf`.

[21] AMTI, "MSA-6 MiniAmp Strain Gage Amplifier Fact sheet, Bulletin MSA-6-1004," 2005, http://www.amti.uk.com/downloads/MSA-6.pdf.

[22] National Instruments, "Operating Instructions and Specifications for NI 9239," *National Instruments cRIO Module Documentation*, 2007 (accessed July 28, 2009), http://www.ni.com/pdf/manuals/372409a.pdf.

[23] National Instruments, "Notch Filter Express VI," *National Instruments LabVIEW 2009 FPGA Module Help*, 2009 (accessed January 10, 2010), http://zone.ni.com/reference/en-XX/help/371599E-01/lvfpga/fpga_notch/.

[24] Kiceniuk, T., "An Experimental Study of the Hydrodynamic Forces Acting on a Family of Cavity-Producing Conical Bodies of Revolution Inclined to the Flow," Technical Report No. E-12.17, Bureau of Ordinance, Department of the Navy, 1954.

[25] Kermeen, R. W., "Experimental Investigations of Three-Dimensional Effects on Cavitating Hydrofoils," Technical Report No 47-14, Department of the Navy, Bureau of Ships, 1960.

[26] Waid, R. L. and Kermeen, R. W., "Forces on Cylinders Planing on Flat and Curved Surfaces in Cavitating and Noncavitating Flow," Technical Report No. E-73.5, Department of the Navy, Bureau of Ordnance, 1957.

[27] May, A., "Water Entry and Cavity-Running Behavior of Missiles," Technical Report No. 75-2, Naval Surface Weapons Center, White Oak Laboratory, 1975.

[28] Kirschner, I. N., Fine, N. E., Uhlman, J. S., and Kring, D. C., "Numerical Modeling of Supercavitating Flows," *RTO AVT/VKI special course on supercavitating flows, von Kármán Institute for Fluid Dynamics*, Rhode-Saint-Genese, Belgium, Feb. 2001.

[29] Kirschner, I. N., Kring, D. C., Stokes, A. W., Fine, N. E., and Uhlman, J. S., "Control Strategies For Supercavitating Vehicles," *Journal of Vibration and Control*, Vol. 8, No. 2, Feb. 2002, pp. 219–242.

[30] Logvinovich, G. V., *Hydrodynamics of Free Boundary Flows*, NASA Translation NASA-TT-F-658, U.S. Department of Commerce, Washington, D.C., 1972.

[31] Logvinovich, G. V., "Some Problems in Planing Surfaces (Translated from: Nekotoryye Voprosy Glissirovaniya i Kavitatsii)," *Trudy TsAGI*, Vol. 2, No. 2052, 1980.

[32] Paryshev, E. V., "The Plane problem of Immersion of an Expanding Cylinder Trough a Cylindrical Free Surface of Variable Radius," *The International Summer Scientific School, High Speed Hydrodynamics*, Cheboksary, Russia, June 2002.

[33] Dzielski, J. and Kurdila, A., "A Benchmark Control Problem for Supercavitating Vehicles and an Initial Investigation of Solutions," *Journal of Vibration and Control*, Vol. 9, No. 7, July 2003, pp. 791–804.

[34] Vanek, B., Bokor, J., Balas, G., and Arndt, R. E. A., "Longitudinal Motion Control of a High-Speed Supercavitation Vehicle," *Journal of Vibration and Control*, Vol. 13, No. 2, Feb. 2007, pp. 159–184.

[35] Lide, D. R., editor, *CRC Handbook of Chemistry and Physics*, CRC Press, 70th ed., 1990.

[36] Wheeler, A. J. and Ganji, A. R., *Introduction to Engineering Experimentation*, Prentice Hall, 2nd ed., 2004.

[37] Tulin, M., *Cavitation*, chap. 1211.4, Handbook of Fluid Dynamics, McGraw-Hill, 1961.

[38] Escobar, D. S., "Personal Communication," December 2011.

[39] Doyle, J. C., Glover, K., Khargonekar, P. P., and Francis, B. A., "State-space solutions to standard H_2 and H_∞ control problems," *IEEE Transactions on Automatic Control*, Vol. 34, No. 8, 1989, pp. 831–847.

[40] Gahinet, P. and Apkarian, P., "A linear matrix inequality approach to H_∞ control," *International Journal of Robust and Nonlinear Control*, Vol. 4, No. 4, 1994, pp. 421–448.

[41] Balas, G., Chiang, R., Packard, A., Safonov, M., Gahinet, P., and Nemirovski, A., "Robust Control Toolbox v 3.3.2 User's Guide," 2008.

[42] Skogestad, S. and Postlethwaite, I., *Multivariable Feedback Control: Analysis and Design*, Wiley-Interscience, 2nd ed., 2005.

[43] Bates, D. and Postlethwaite, I., *Robust Multivariable Control of Aerospace Systems*, Delft University Press, 2002.

[44] National Instruments, "Specifications for the "CD Discrete State-Space Function" in LabVIEW," *National Instruments LabVIEW 2009 Control Design and Simulation Module Help*, 2009 (accessed 27 January 2012), `http://zone.ni.com/reference/en-XX/help/371894D-01/lvctrldsgn/cd_discss/`.

Appendix A

Model Drawings

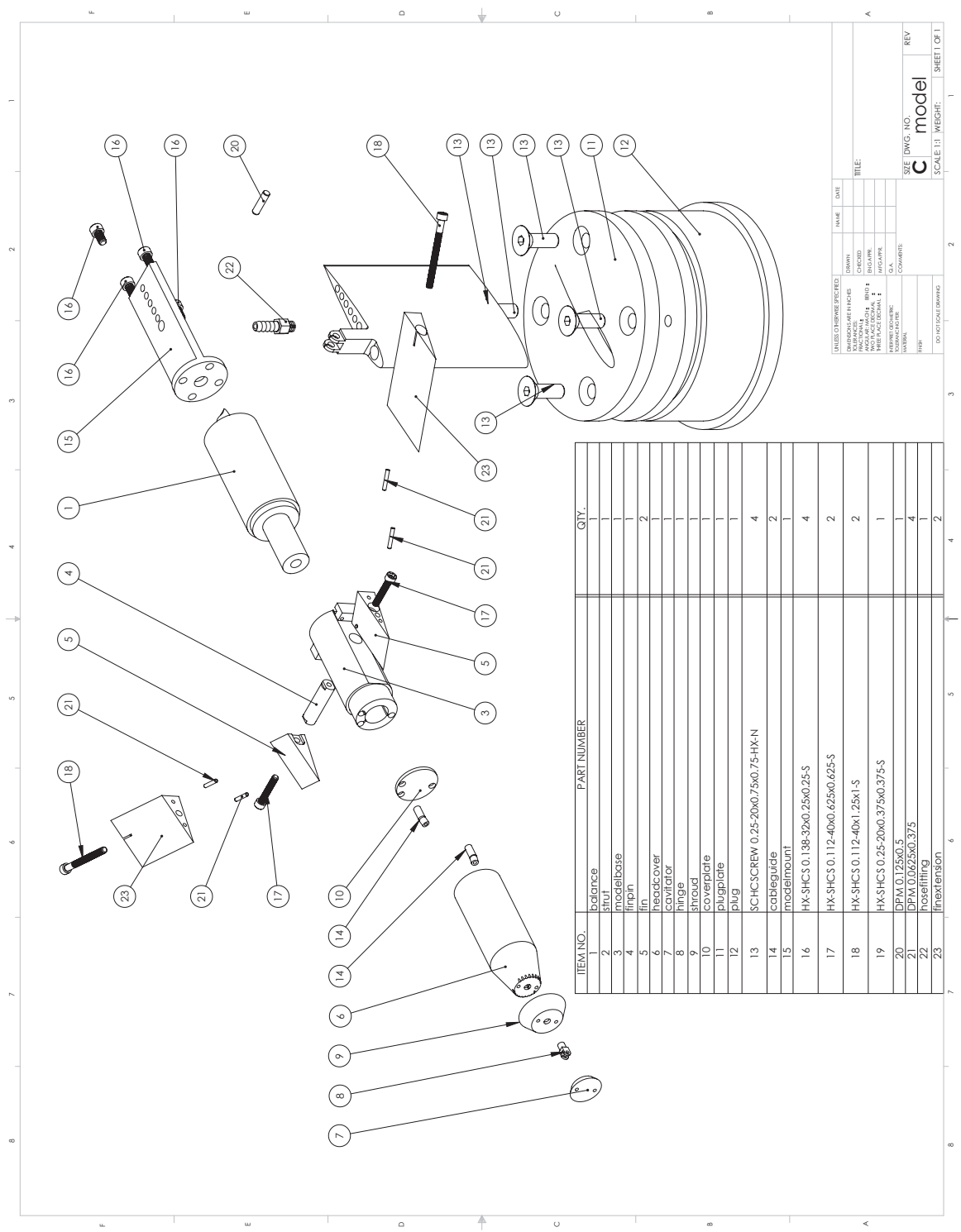

Figure A.1: A schematic of the CoSCIC Model Assembly

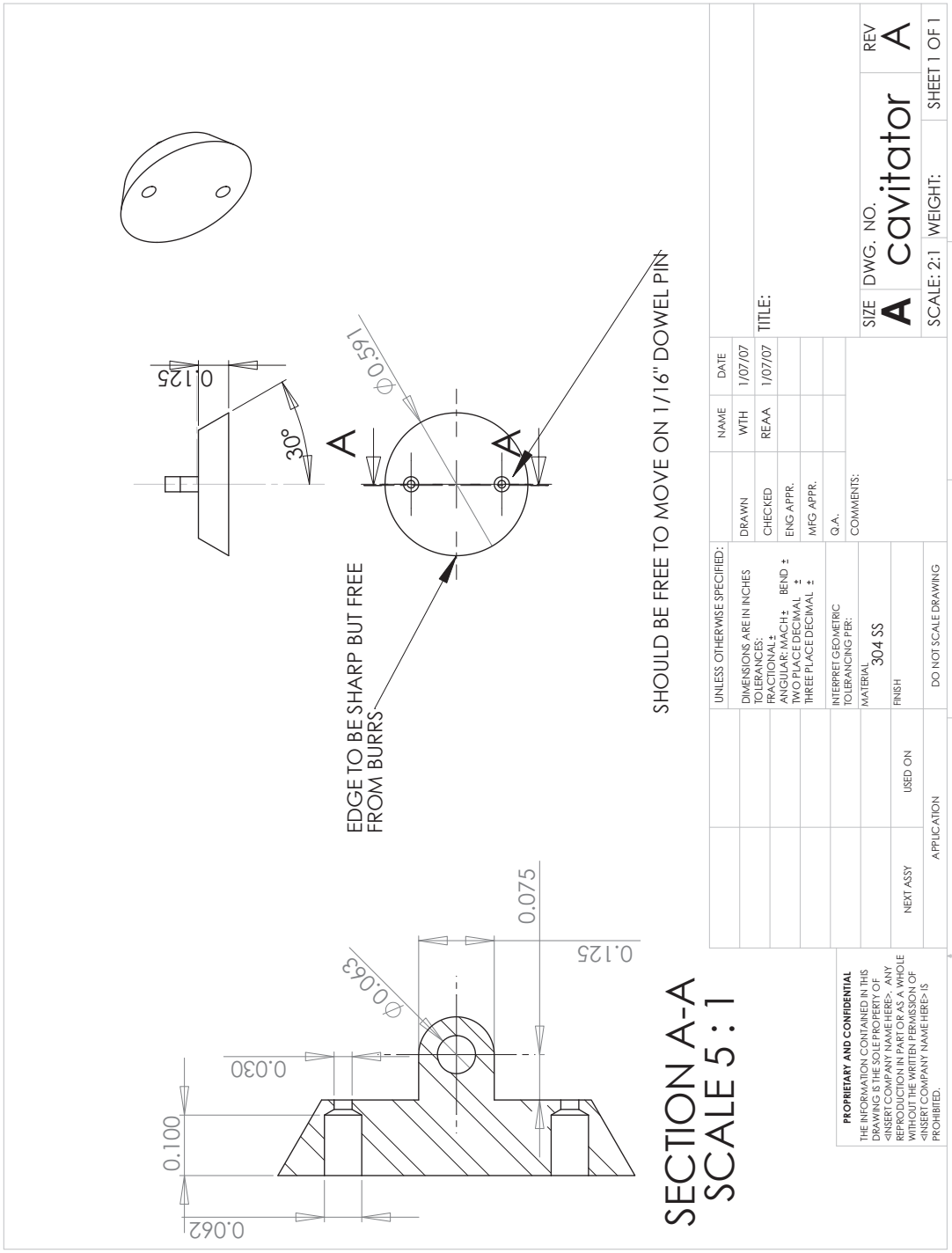

Figure A.2: A schematic of the CoSCIC cavitator.

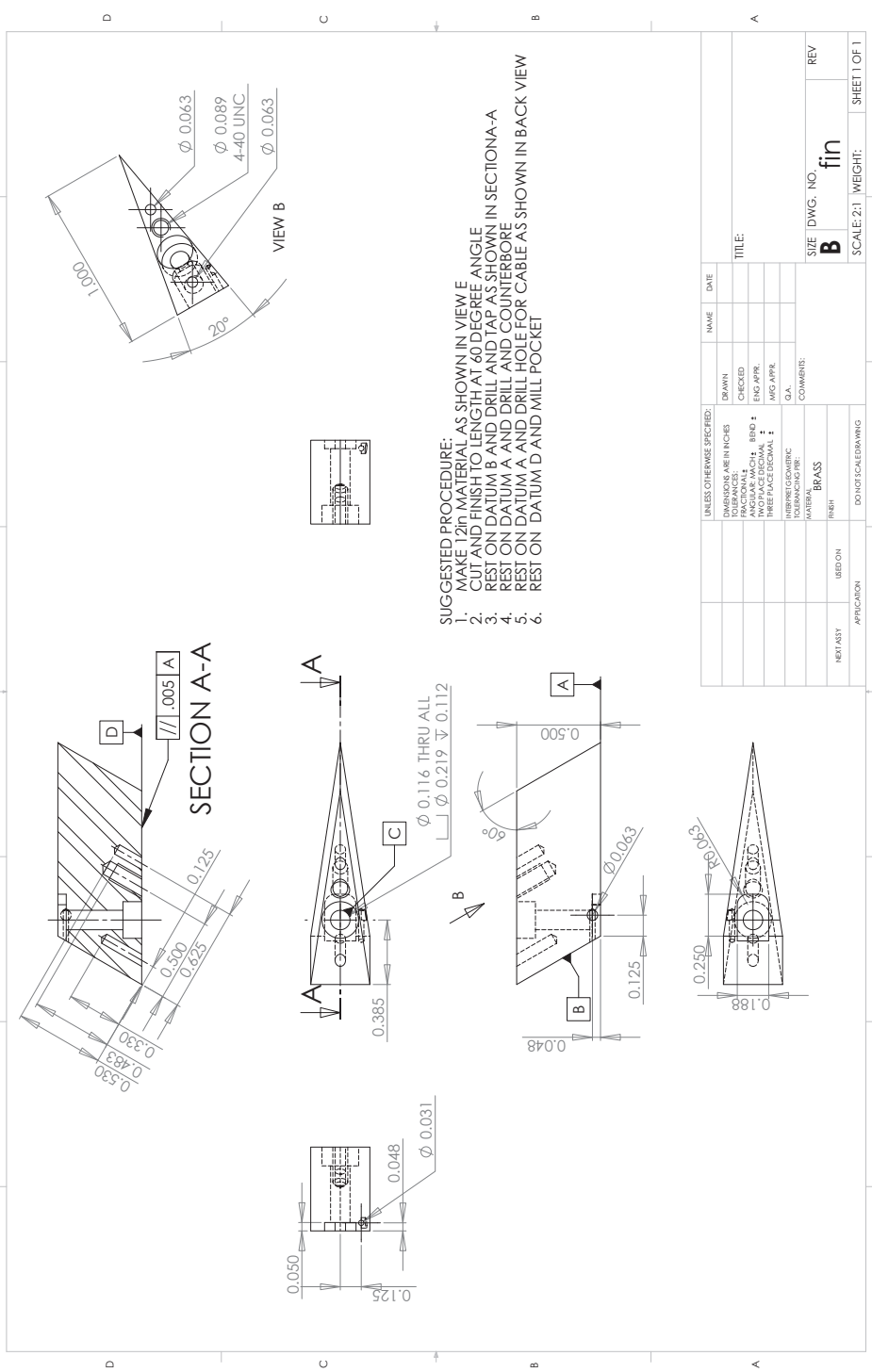

Figure A.3: A schematic of the CoSCIC fin.

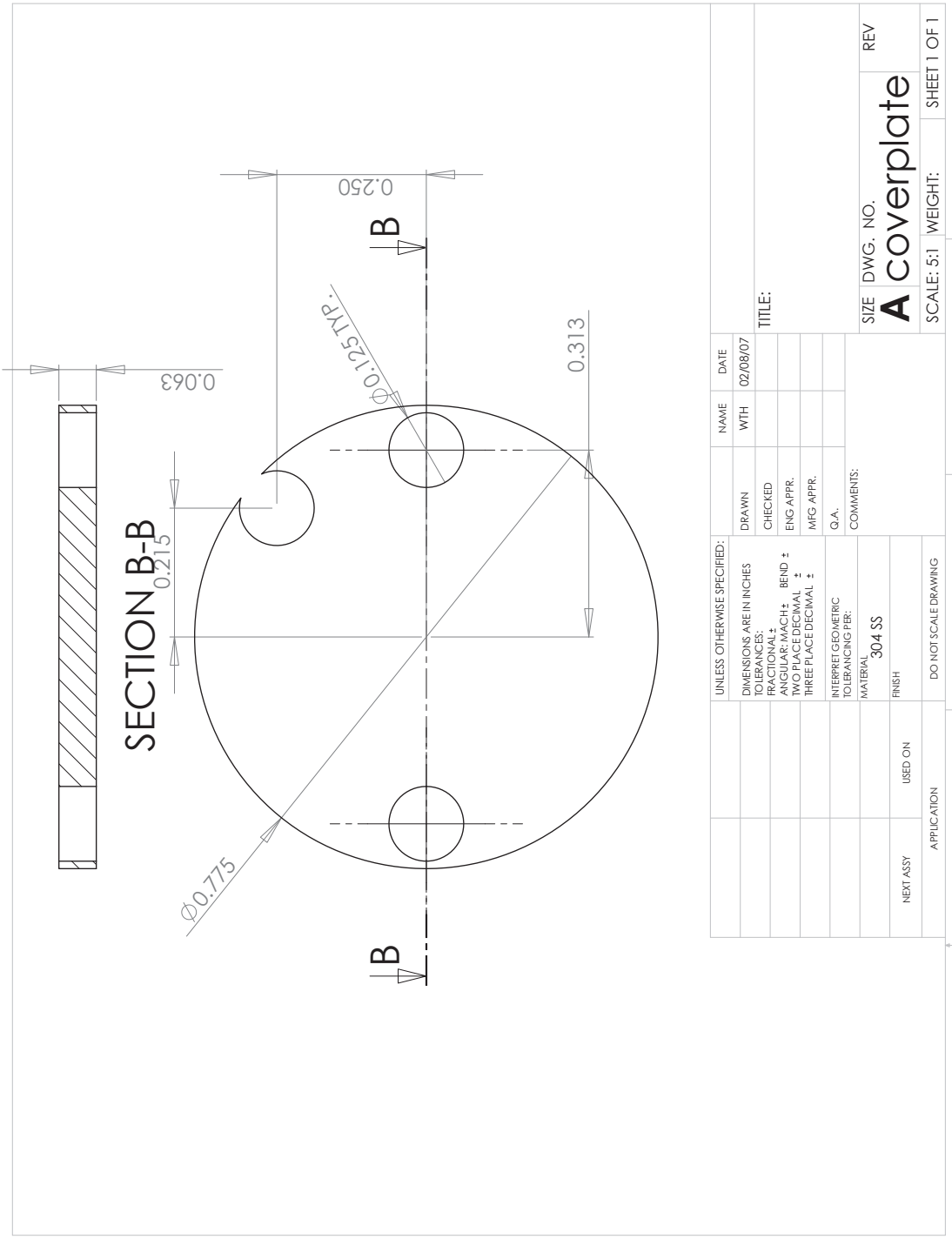

Figure A.4: A schematic of the CoSCIC coverplate.

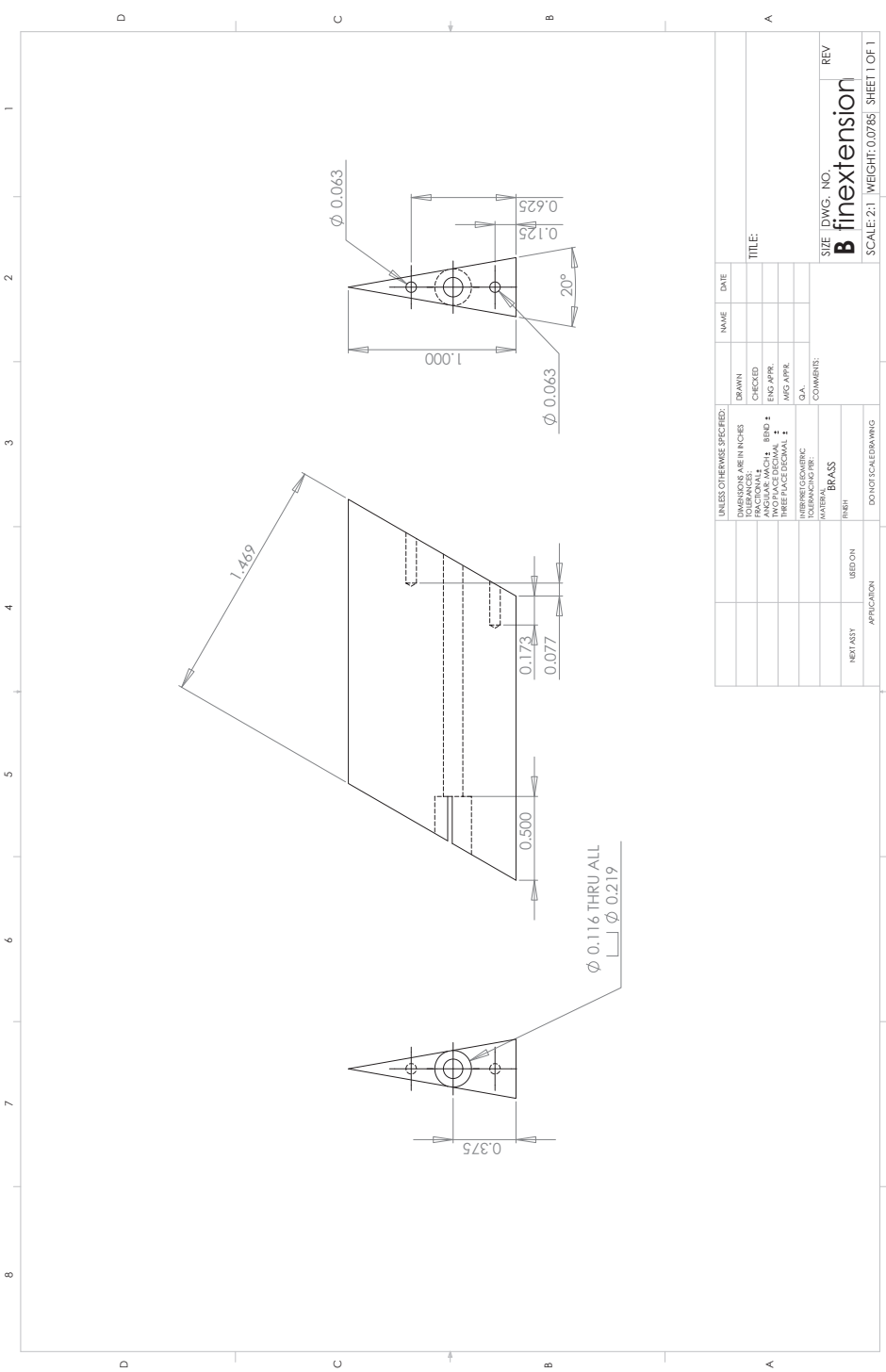

Figure A.5: A schematic of the optional CoSCIC fin extension.

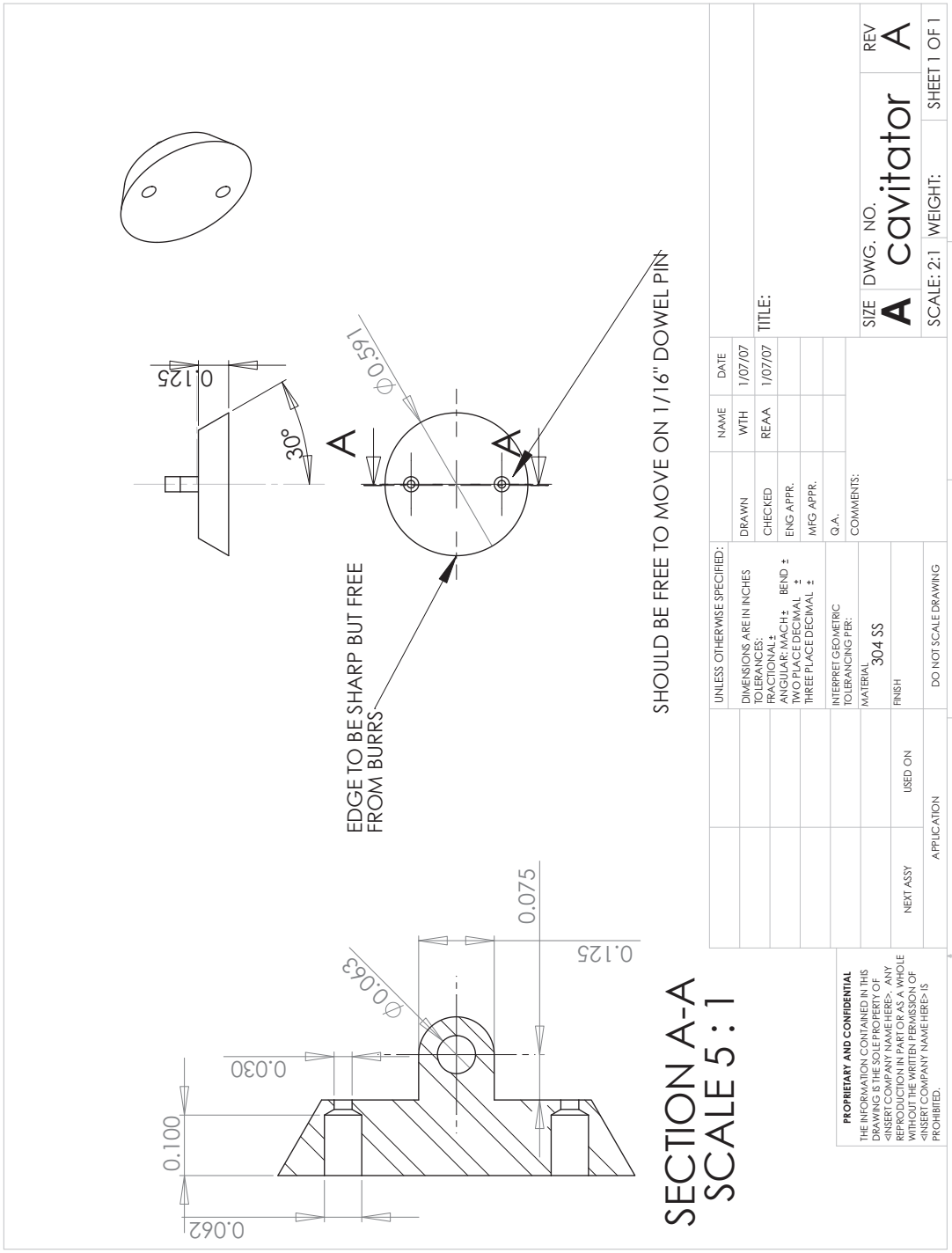

Figure A.6: A schematic of the CoSCIC finpin.

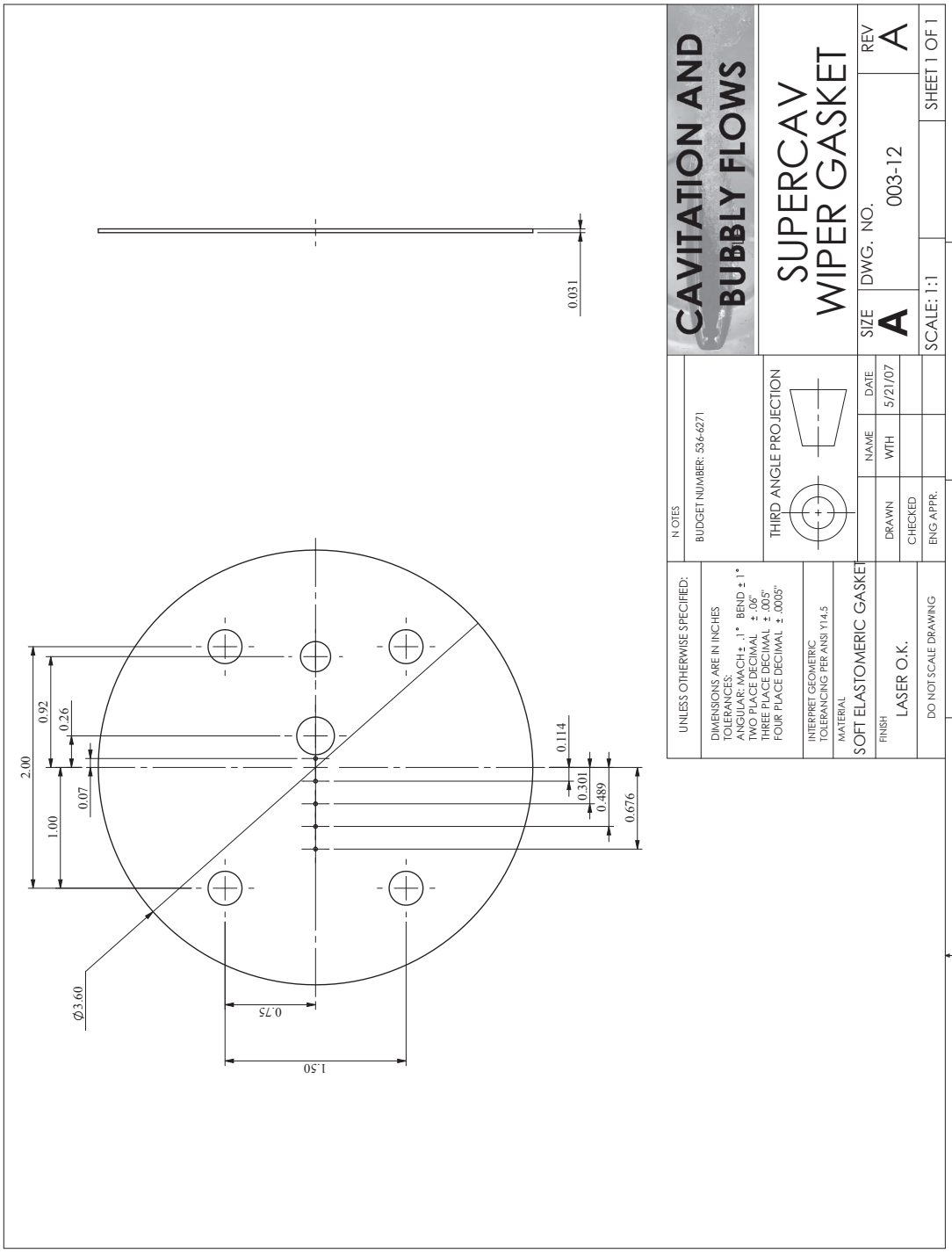

Figure A.7: A schematic of the CoSCIC gasket.

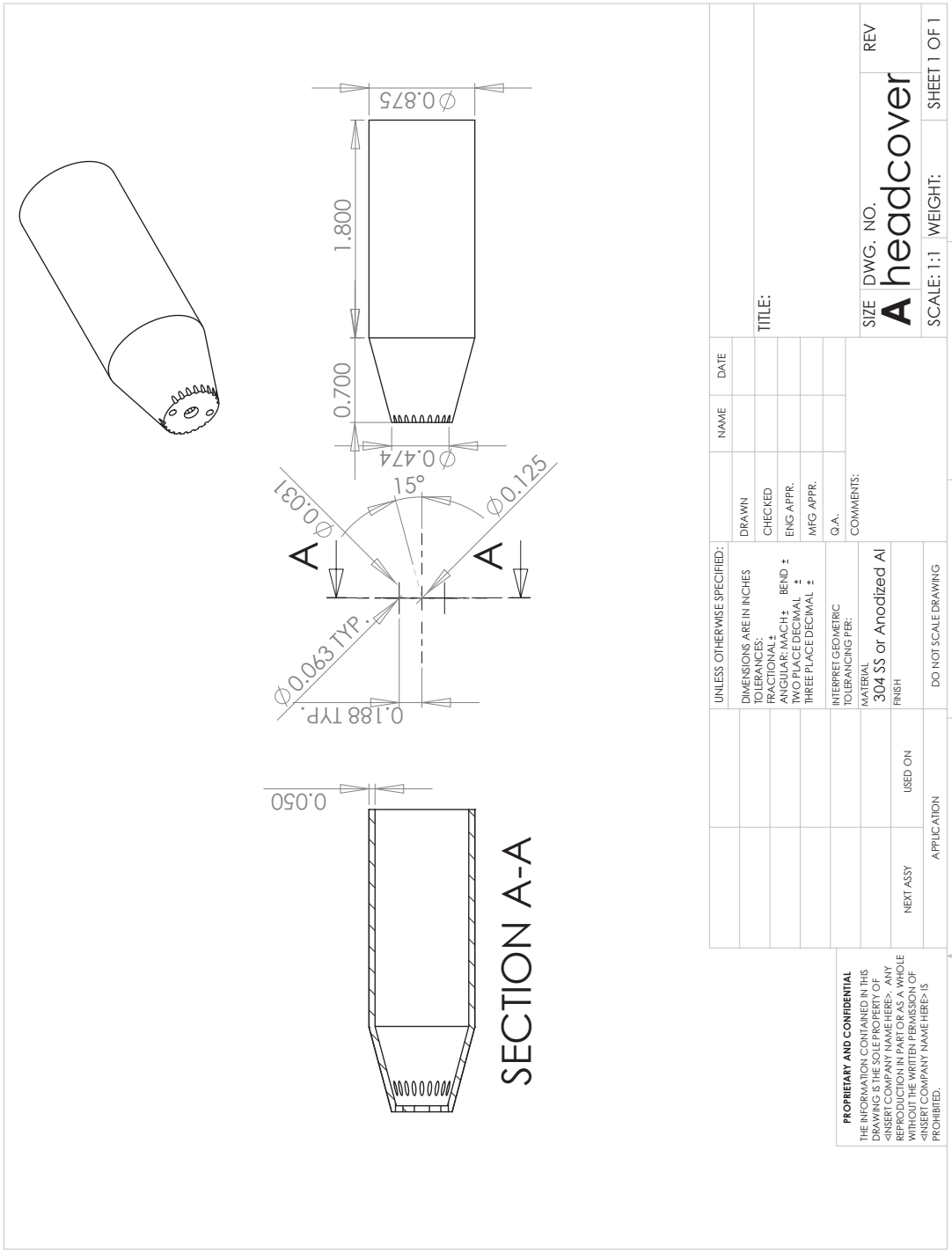

Figure A.8: A schematic of the CoSCIC headcover.

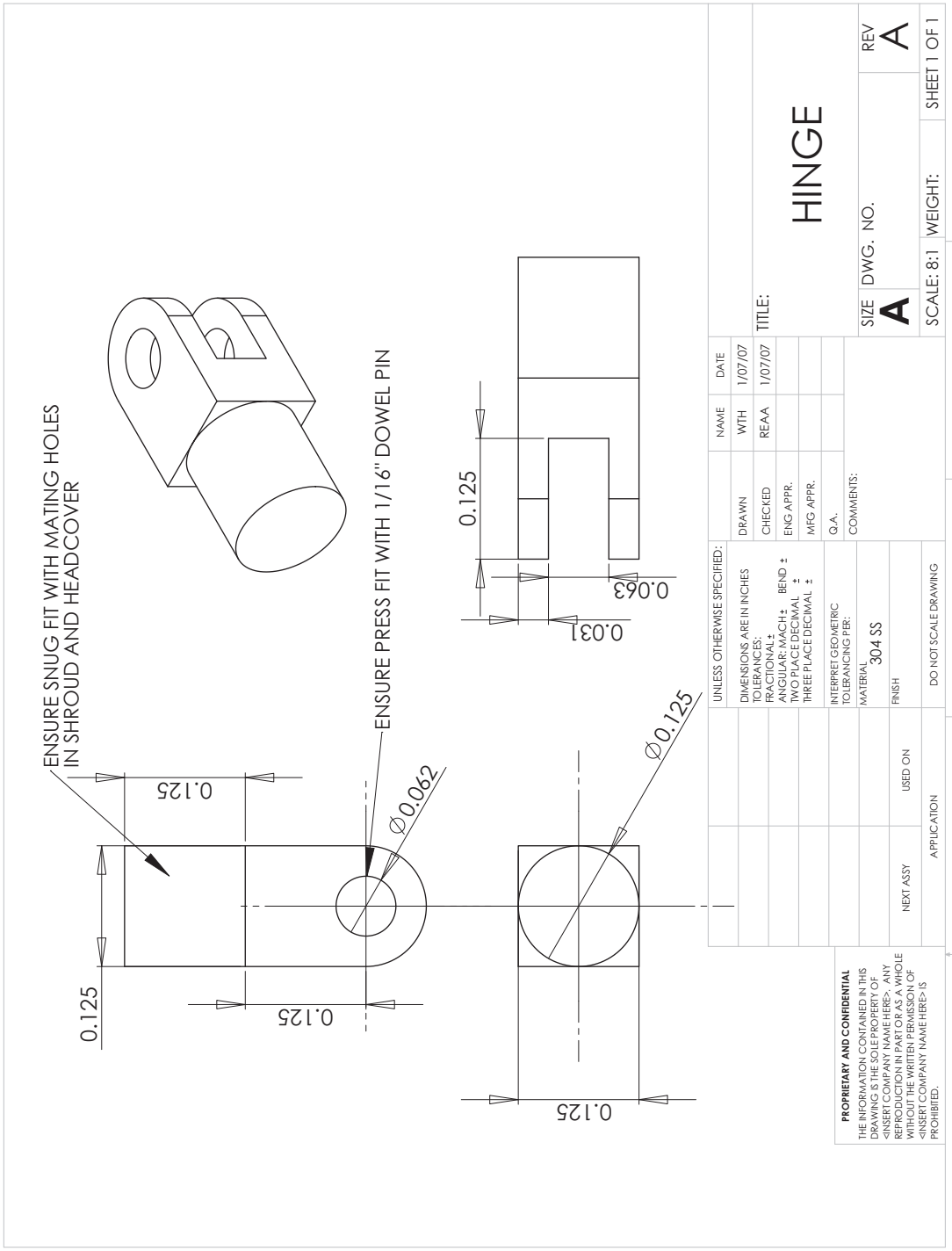

Figure A.9: A schematic of the CoSCIC hinge.

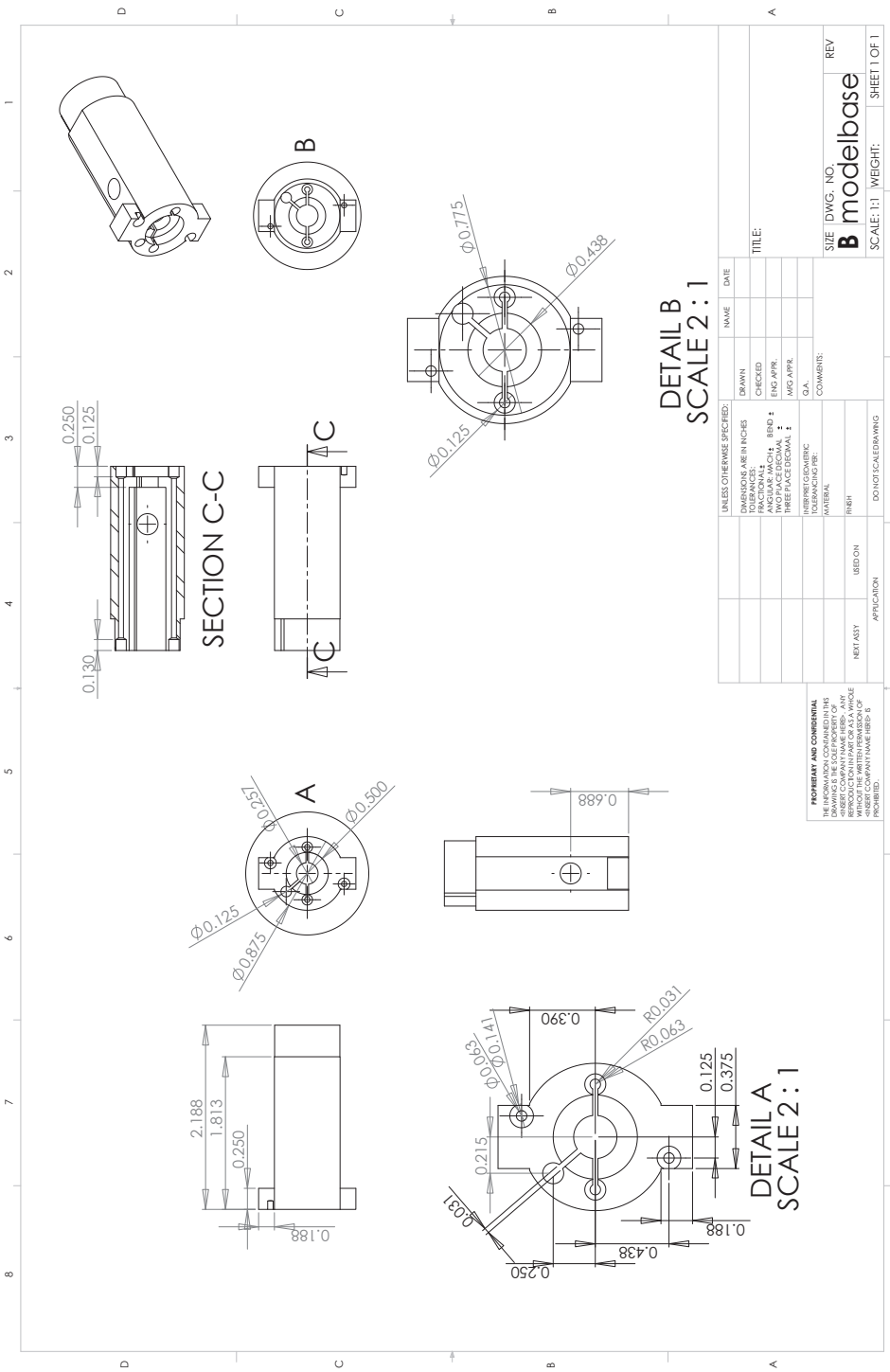

Figure A.10: A schematic of the CoSCIC modelbase.

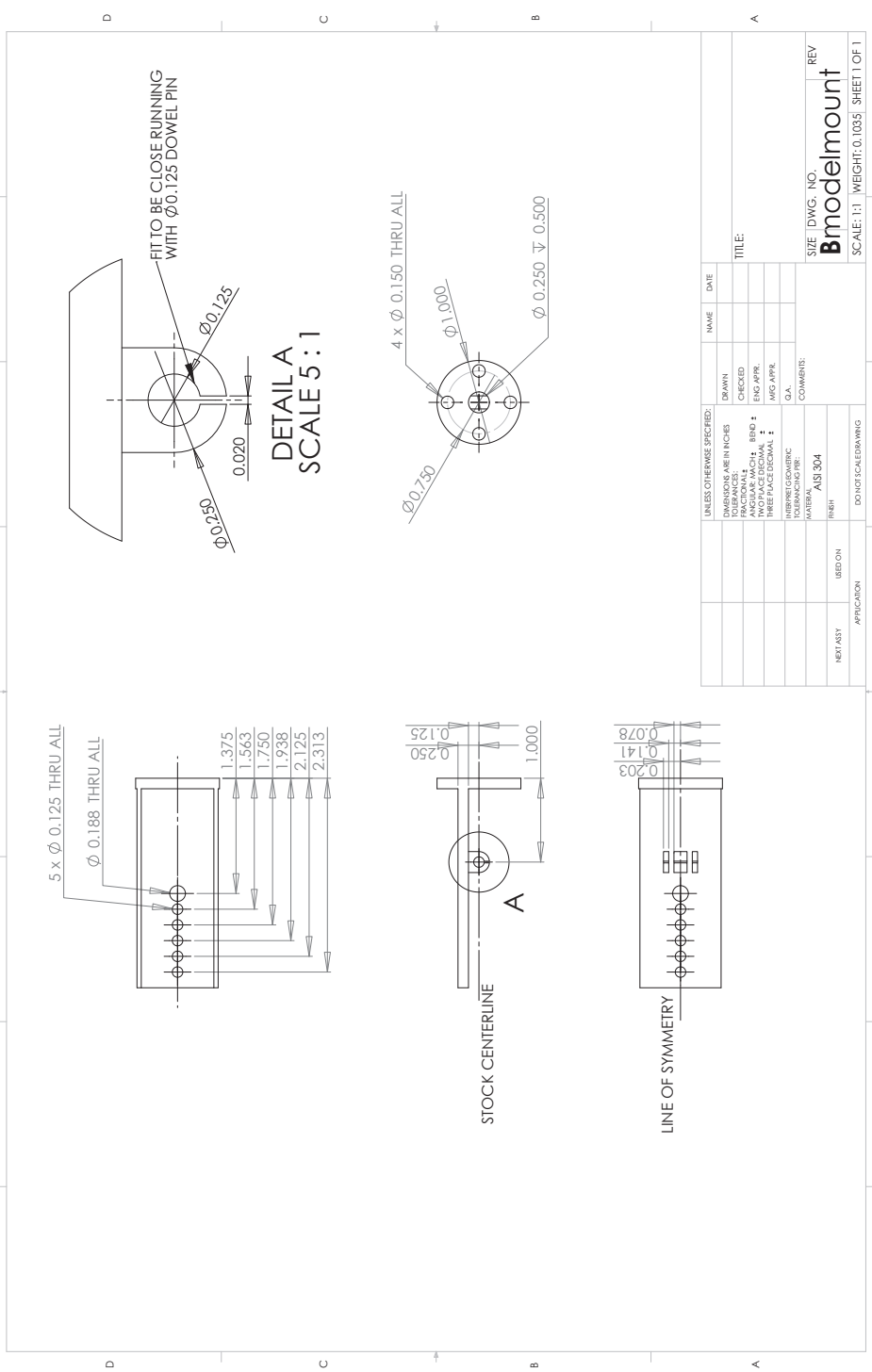

Figure A.11: A schematic of the CoSCIC modelmount.

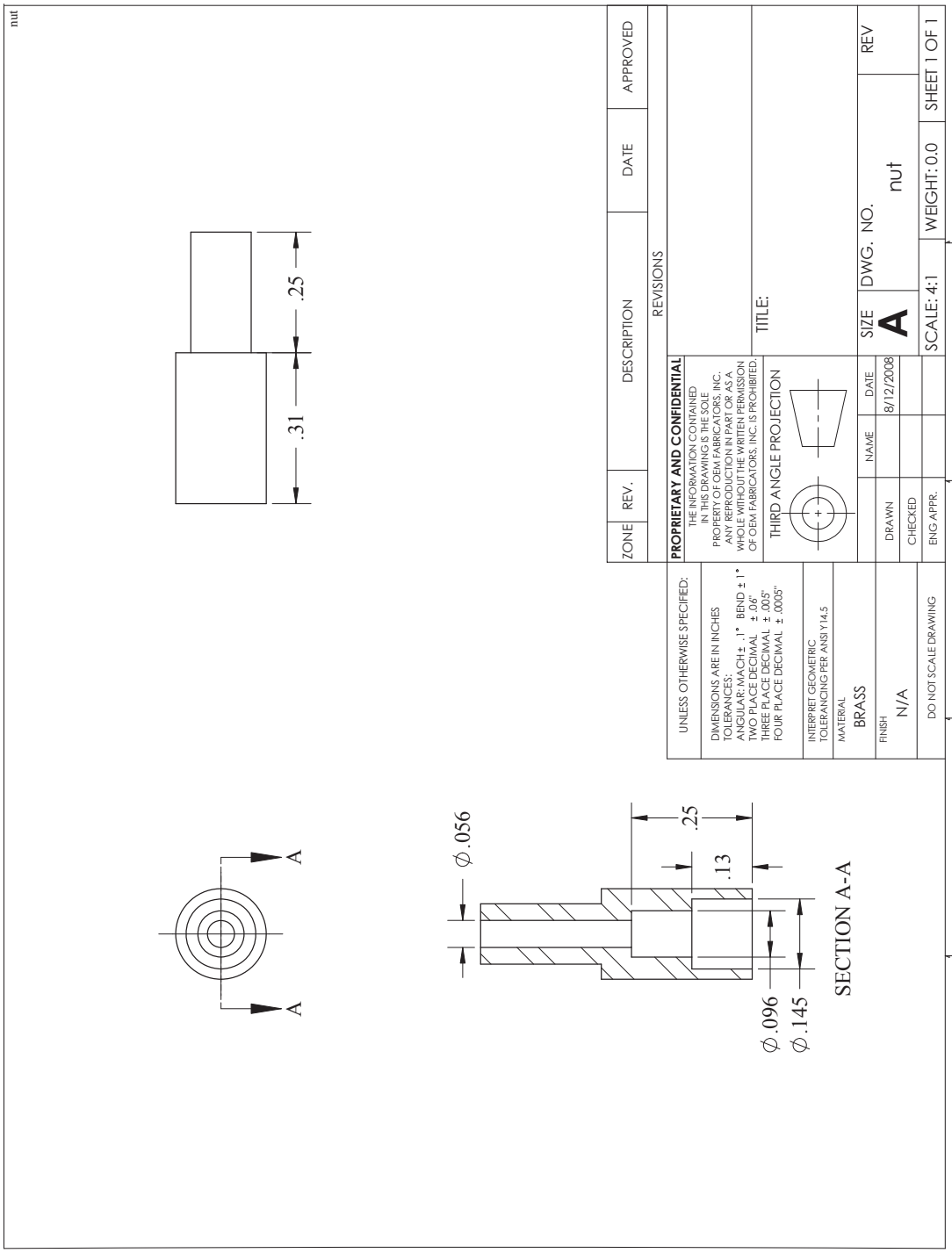

Figure A.12: A schematic of the CoSCIC nut.

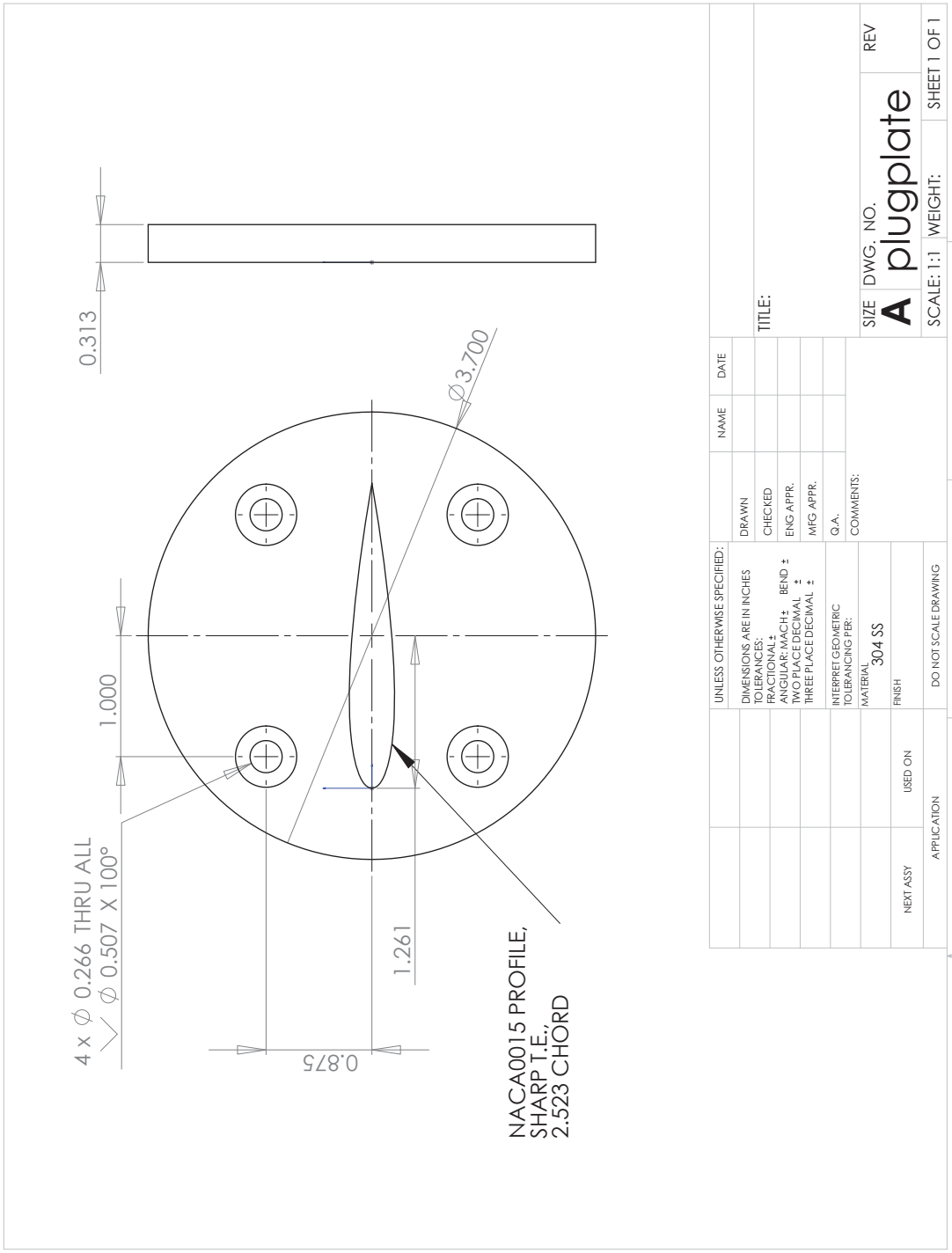

Figure A.13: A schematic of the CoSCIC plugplate.

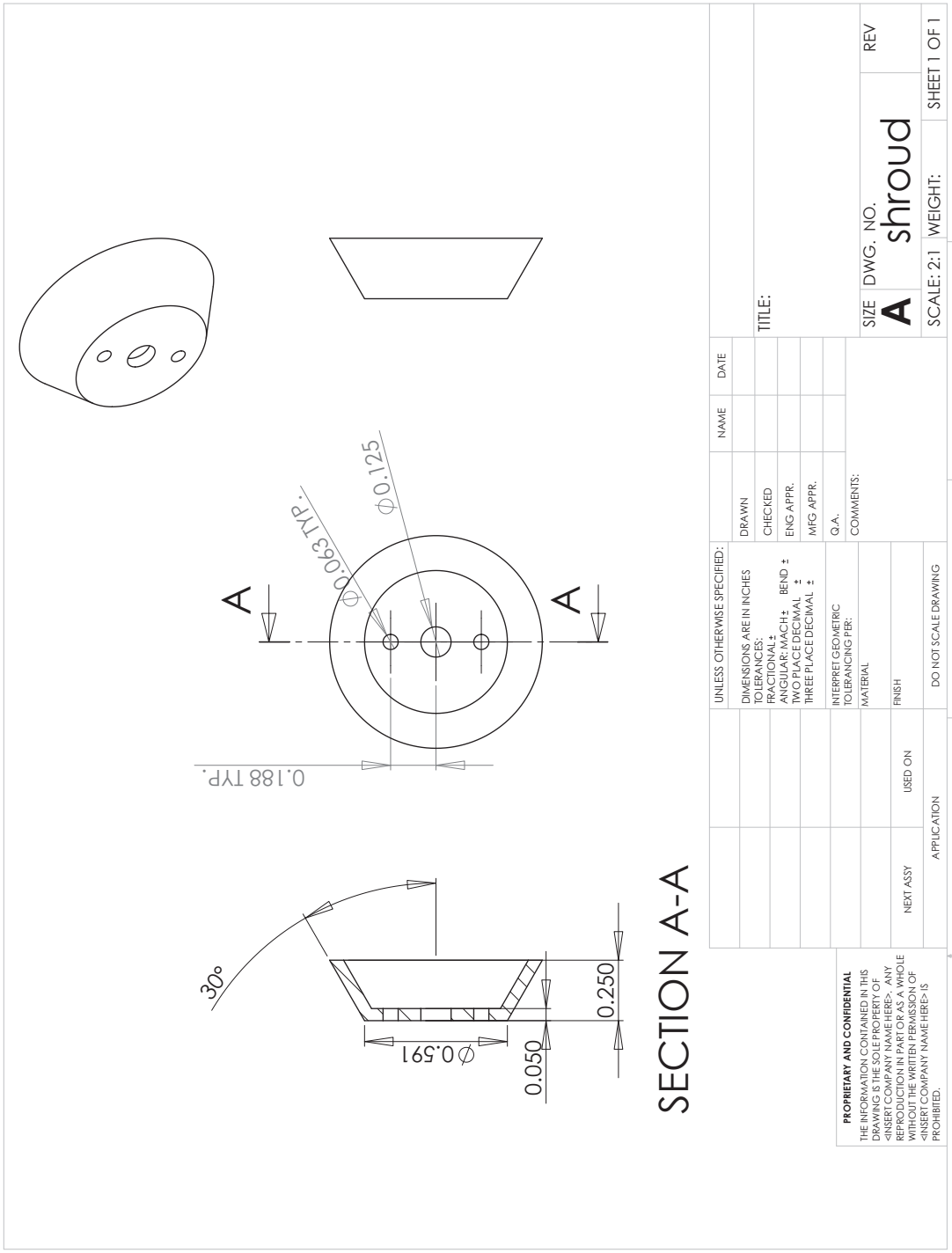

Figure A.14: A schematic of the CoSCIC shroud.

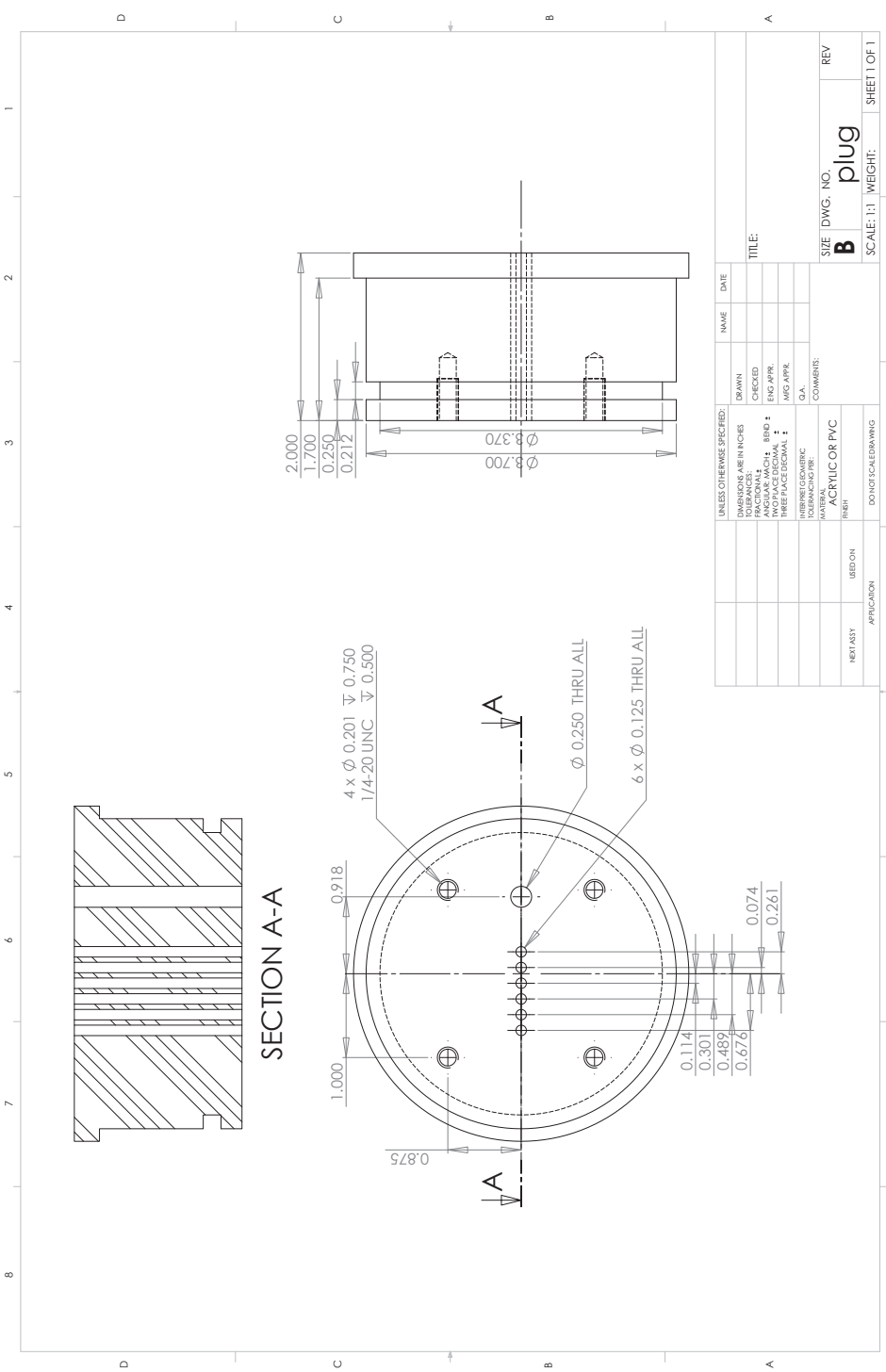

Figure A.15: A schematic of the CoSCIC plug.

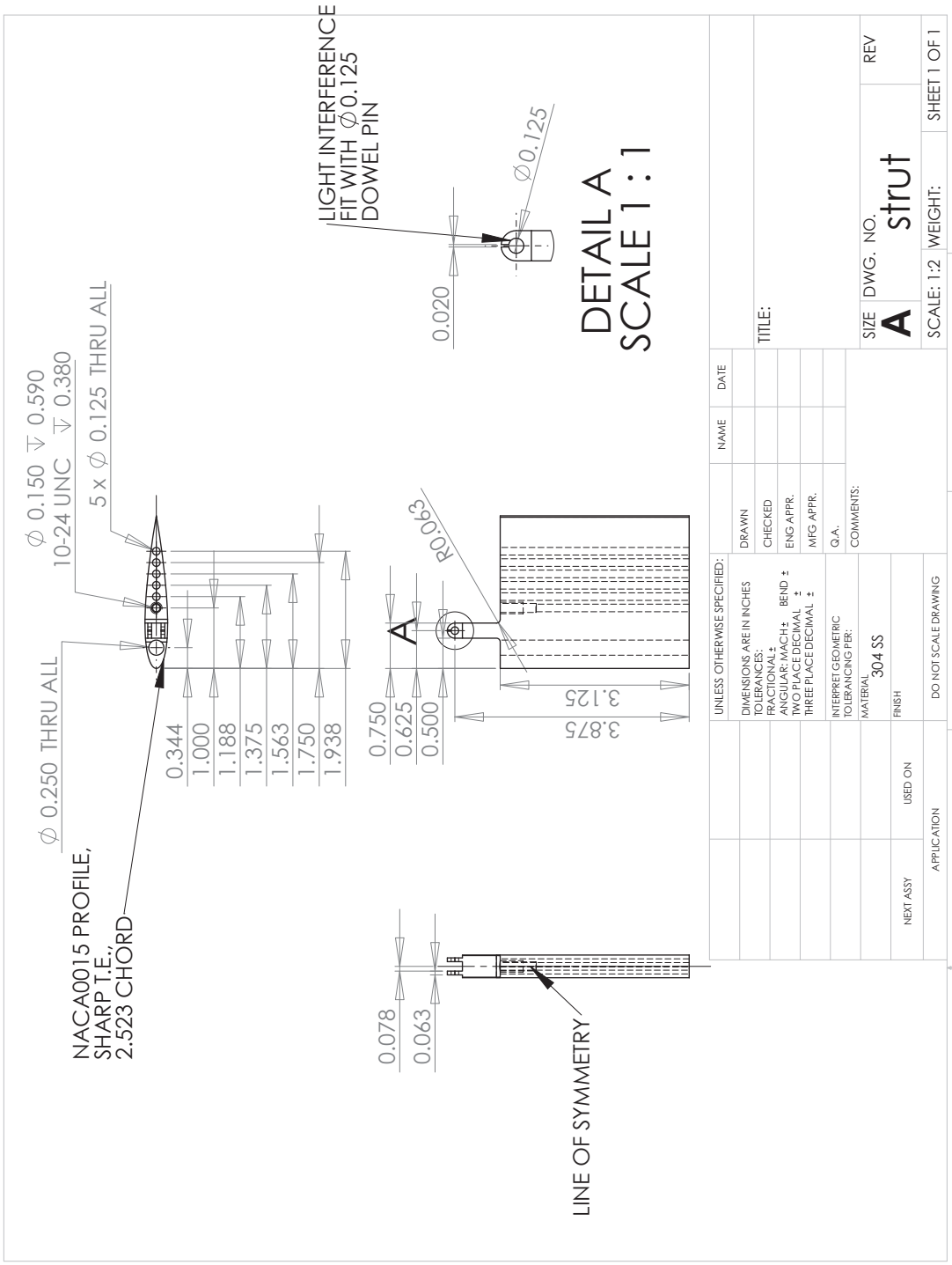

Figure A.16: A schematic of the CoSCIC strut.

Appendix B

K_{T_z} Controller

The K_{T_z} controller accepts a vector of inputs: $[\alpha,\ q]$, where α is the angle-of-attack of the vehicle in radians, and q is the pitch rate of the vehicle in rad/s. The controller outputs a thrust T_z in the z_{body}-axis of the vehicle. The T_z thrust is in units of Newtons. The K_{T_z} controller is defined as the state-space system:

$$K_{T_z} \triangleq \left[\begin{array}{c|c} A_{K_{T_z}} & B_{K_{T_z}} \\ \hline C_{K_{T_z}} & D_{K_{K_{T_z}}} \end{array}\right] \tag{B.1}$$

where

$$A_{T_z} = \begin{bmatrix} -276.7 & 20.45 & 14.04 & -292.4 & -1462 & 3.08 & 1.077 \\ -1.025 \cdot 10^5 & -1.012 \cdot 10^4 & -1.693 \cdot 10^4 & -1.09 \cdot 10^5 & -5.472 \cdot 10^5 & 1153 & 403.4 \\ -7.918 & 3950 & -62.83 & -8.683 & 7.132 \cdot 10^{-5} & -8.403 \cdot 10^{-8} & 0 \\ -1988 & -3.884 & 0 & -2192 & 1.89 & 8.203 \cdot 10^{-8} & 0 \\ 0.3208 & 0.0006231 & 0 & 0.3518 & -9.53 & -4.696 \cdot 10^{-11} & 0 \\ -0.0004117 & 4.143 \cdot 10^{-5} & 0 & -0.0004514 & -8.671 \cdot 10^{-8} & -25.13 & -9.253 \\ -0.000637 & -8.201 \cdot 10^{-5} & 0 & -0.0006985 & 1.26 \cdot 10^{-6} & 16 & 5.821 \cdot 10^{-11} \end{bmatrix} \tag{B.2}$$

$$B_{T_z} = \begin{bmatrix} 0.3031 & -5.937 \\ -4.685 & 2892 \\ 2.328 & -1161 \\ 584.4 & 1.142 \\ 9.314 & -0.0001832 \\ 0.000121 & 0.294 \\ 0.0001873 & 2.411 \cdot 10^{-5} \end{bmatrix}$$

$$C_{T_z} = \begin{bmatrix} -720.5 & -1.967 & -32.7 & -763.6 & -3832 & 8.075 & 2.825 \end{bmatrix} \quad D_{T_z} = \begin{bmatrix} 0 & 0 \end{bmatrix}$$

Appendix C

K_{δ_c} Controllers

C.1 State-Space Representation of $K^1_{\delta_c}$

The $K^1_{\delta_c}$ controller accepts a vector of inputs: $[A_{z,ref},\ A_{z,m}]$, where $A_{z,ref}$ is the acceleration reference command, and $A_{z,m}$ is a measurement of the z_{body}-axis acceleration of the vehicle. Both $A_{z,ref}$ and $A_{z,m}$ have units of m/s^2. The controller outputs a cavitator deflection command u_{δ_c} to the cavitator actuator. The cavitator deflection command u_{δ_c} is in units of radians. The $K^1_{\delta_c}$ controller is defined as the state-space system:

$$K^1_{\delta_c} \triangleq \left[\begin{array}{c|c} A_{K^1_{\delta_c}} & B_{K^1_{\delta_c}} \\ \hline C_{K^1_{\delta_c}} & D_{K^1_{\delta_c}} \end{array}\right] \tag{C.1}$$

where

$$A_{K^1_{\delta_c}} = \begin{bmatrix} -0.0681 & -0.201 \\ -0.146 & -3.129 \end{bmatrix},\quad B_{K^1_{\delta_c}} = \begin{bmatrix} 0.07125 & -0.06039 \\ 0.1429 & 0.002864 \end{bmatrix} \tag{C.2}$$

$$C_{K^1_{\delta_c}} = \begin{bmatrix} 0.0934 & 0.143 \end{bmatrix}\quad D_{K^1_{\delta_c}} = \begin{bmatrix} 0.0005089 & -0.0005212 \end{bmatrix}$$

C.2 State-Space Representation of $K^2_{\delta_c}$

The $K^2_{\delta_c}$ controller accepts a vector of inputs: $[A_{z,ref},\ A_{z,m}]$, where $A_{z,ref}$ is the acceleration reference command, and $A_{z,m}$ is a measurement of the z_{body}-axis acceleration of the vehicle. Both $A_{z,ref}$ and $A_{z,m}$ have units of m/s^2. The controller

outputs a cavitator deflection command u_{δ_c} to the cavitator actuator. The cavitator deflection command u_{δ_c} is in units of radians. The $K^2_{\delta_c}$ controller is defined as the state-space system:

$$K^2_{\delta_c} \triangleq \left[\begin{array}{c|c} A_{K^2_{\delta_c}} & B_{K^2_{\delta_c}} \\ \hline C_{K^2_{\delta_c}} & D_{K^2_{\delta_c}} \end{array}\right] \tag{C.3}$$

where

$$A_{K^2_{\delta_c}} = \begin{bmatrix} -2.422 & -4.492 \\ 0.6702 & -6.447 \end{bmatrix}, \quad B_{K^2_{\delta_c}} = \begin{bmatrix} -0.2684 & 0.3721 \\ 0.2896 & 0.2855 \end{bmatrix} \tag{C.4}$$

$$C_{K^2_{\delta_c}} = \begin{bmatrix} -0.4588 & -0.4066 \end{bmatrix} \quad D_{K^2_{\delta_c}} = \begin{bmatrix} 0.0006707 & -0.007033 \end{bmatrix}$$